UNIVERSITY OF GLASGOW

CHARACTERISING THE EFFECTS OF POWER ULTRASONIC DEVICES ON SURROGATE TISSUE MATERIALS

DONG WANG

A thesis for the degree of Doctor of Philosophy (PhD)

Submitted to the School of Engineering,
College of Science and Engineering,
University of Glasgow,
Glasgow, UK

2014

I. Abstract

Power ultrasonic surgical devices operating at low ultrasonic frequencies (20-100 kHz) have been shown to provide some advantages over reciprocating or manual devices in removal of tissue. Despite opportunities for widespread applications in orthopaedic, dental, ophthalmic and general surgical procedures, the mechanisms of interaction between high power ultrasound and human tissue is not well understood and little is known about the effects and safety implications for power ultrasonics in human tissue. Therefore, the effects of power ultrasonic devices on human tissue are investigated in this thesis.

From the limited literature on this topic, the basic effects caused by high power ultrasound on human tissue can be summarized into three main categories: mechanical response, thermal effects and acoustic cavitation. However, the relative contribution of each of these remains unclear. Thus, this study aims to analyse these responses and effects of tissue mimic materials subject to power ultrasonic excitation and hence investigate the potential to quantitively characterise the power ultrasonic damage on tissue. Due to the complexity of the interaction between cutting surface with tissue, the damage caused by cutting process was not covered. But the investigation of the damage by accumulated ultrasound energy in tissue was the main research topic in this thesis.

To substitute for human tissue, representative materials such as E-glass filled epoxy resin (ER), polyurethane foam (PUF) and transparent silicone elastomer (SE) were used in experimental studies to simulate the behaviour of cortical bone, cancellous bone and soft tissue respectively. Their mechanical properties were characterised using uni-axial compression and tensile tests to measure elastic modulus and dynamic mechanical analysis (DMA) to study the viscoelastic behaviour. Frequency and temperature dependent behaviour of tissue surrogates under power ultrasonic excitation were determined using the DMA data based on the time/frequency temperature superposition principle (TTS). The parameters relevant to thermal properties, including thermal conductivity and specific heat capacity were measured using the heat flow method and differential scanning calorimetry (DSC).

Ultrasonic horns were designed using the finite element (FE) method. The performance of the power ultrasonic system was then examined using experimental modal analysis (EMA)

with a laser Doppler vibrometer (LDV) to ensure the system met the experimental requirements.

To characterise the responses and effects of tissue mimics subject to power ultrasonic excitation, non-invasive field measurements have been developed for the fast and reproducible experimental assessment of ultrasonic displacement, strain, stress and temperature fields. An ultra-high speed camera and an infrared (IR) camera were used simultaneously for ER and PUF plate samples to obtain the imaging data which provided the displacement and strain fields with digital image correlation (DIC) technique and the steady-state temperature distribution with thermal imaging. The stress field in a transparent rectangular cubiod SE sample during power ultrasonic loading was mapped using a laser interferometer with acousto-optic effects. Due to the absorption of IR light by transparent SE, the temperature distribution of SE was not recorded by IR camera.

Numerical and analytical models were developed to simulate the ultrasonic wave propagation using ABAQUS FE software package and Mathematica respectively. These models incorporated frequency dependent mechanical properties of the mimic materials to verify experimental results. The results of the models matched well with the experimental findings of ultrasonic displacement, strain and stress fields. To assess the thermal effects of power ultrasound on the viscoelastic tissue mimics, thermo-mechanical FE models were created using the PZFlex FE software package. Furthermore, FE models for thermal analysis were parameterized in terms of dynamic modulus and acoustic damping coefficient with frequency and temperature dependency for determination of the heat generation and thermal conductivity and specific heat capacity for characterisation of the heat transfer. The FE results have close correlation with measurement results by an IR camera.

Based on the experimental and numerical studies, the damage of tissue mimicking materials under power ultrasonic excitation is related to accumulations of cyclic deformation and heating. Non-invasive full-field surface displacement, strain, stress and temperature measurements have the potential to be used to predict the damage of tissue samples interacting with the power ultrasonic devices. This study has provided confidence that the methodology can be applied to study tissue samples subject to excitations typical of ultrasonic surgical devices, including those for orthopaedic bone cutting.

II. Acknowledgments

Firstly, I would like to express my gratitude to my long-suffering supervisors: Professor Margaret Lucas and Professor Elizabeth Tanner. Without their input, advice, ideas, support and encouragement, I doubt I would have had the opportunity to begin a PhD and complete this study. Professor Lucas, a highly respected academician in the research field of power ultrasonics, gave me continuous support and guidance, led me through the difficulties and let me enjoy the great features of power ultrasonics. I truly appreciated her kind and infinite help during the long journey of my PhD study! Acknowledgements are extended to Professor Tanner, one of the leading experts in biomaterials, who has been a great advisor with invaluable knowledge and resourcefulness.

Special thanks go out to technical and research staff in University of Glasgow (in the Schools of Engineering, Chemistry and Physics) and University of Strathclyde (ACG and CUE) for their expertise and assistance throughout the studies. Without their help in preparation of experiments with advanced equipment, I could not finish this study alone.

Thanks are given to the Glasgow Research Partnership in Engineering, who provided the funding for this research and gave me the opportunity to explore this interdisciplinary field.

I would like to say thank you so much to lots of friends, who gave me good memories at Glasgow. What a wonderful stay here. The first one and the last one!

Finally, and more importantly, I would like to express my deep gratitude to my family including my great parents, beautiful wife and the baby son coming to birth. I am immensely indebted to them all. I have no words to express what I owe them for their continuous encouragement and patient love. What I can do is to be a stronger man, well-behaved son, sincere lover and trusted dad.

I love you all!

III. Table of Contents

IV. List of Table Captions

V. List of Figure Captions

VI. Abbreviations

AM	Analytical model
DIC	Digital image correlation
DMA	Dynamic mechanical analysis
DSC	Differential scanning calorimetry
EMA	Experimental modal analysis
ER	E-glass filled epoxy resin
FE	Finite element
FEA	Finite element analysis
FEM	Finite element model
FFT	Fast Fourier transform
FRF	Frequency response function
HIFU	High intensity focused ultrasound
IR	Infra-red
LDV	Laser Doppler vibrometer
Pk-pk	Peak-peak
PUF	Rigid polyurethane foam
PVDF	Polyvinylidene fluoride
PZT	Lead Zirconate Titanate
RTD	Resistance temperature detector
SE	Silicone elastomer
TTS	Time-temperature superposition principle
WLF equation	Williams-Landel-Ferry equation

1. Introduction

1.1 Research Background

1.1.1 Ultrasound

Ultrasound, where sound is defined as “energy in the form of vibrational waves in matter” [1], is sound waves having a frequency greater than the range of human hearing, generally considered as frequencies over 20 kHz. In general, ultrasonic waves vibrating or oscillating along or parallel to their propagational direction are referred to as longitudinal waves (Fig. 1.1). Transmission of longitudinal waves through a coupling medium produces alternating regions of compression and rarefaction, which create continually varying density in the medium. The cycles of compression and rarefaction in ultrasound waves exert positive and negative pressure or stress, which work on the molecules by first pulling them together and then pushing them apart. Energy transported via ultrasound waves results in changes in pressure or stress, temperature, density and particle displacement.

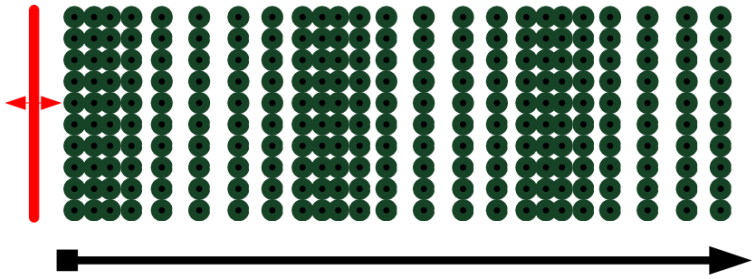

Fig. 1.1 A longitudinal wave show

There are various parameters to characterise ultrasound, such as frequency, amplitude, wavelength, speed, intensity and power. Depending on the power level, ultrasound can be divided into two broad categories, low power and high power. Low power ultrasound, usually in the range 0.1-10 W at a frequency typically above 1 MHz, is mainly used for non-invasive scans, such as medical imaging for diagnosis (medical ultrasonography) and non-destructive testing (NDT) such as crack-testing for materials and structures. Low power ultrasound leaves no permanent physical change in the coupling medium. These applications employ ultrasound to investigate boundary changes in a medium by ultrasonic wave propagation and reflection through the material. The obtained reflection signals provide information about acoustic impedance changes at boundaries between dissimilar materials, which cause the ultrasonic wave to be reflected back to the receiving transducer. In high power ultrasonic applications, the frequencies are at the lower end of the ultrasonic

spectrum, typically, 20-100 kHz and vibration amplitudes range from around 10 to 100 μm. Physical effects produced in the coupling solid, liquid or gaseous media change the structure of the medium irreversibly [2]. To utilise and study the effects of high power ultrasound, power ultrasonics is introduced.

1.1.2 Power Ultrasonics

Power ultrasonics is a research area where low frequency ultrasonic vibrations from around 20 kHz up to a few hundred kHz, and high power, normally in the range between tens of Watts and several kiloWatts, are applied to affect a desirable change in a material or medium. In order to maximise the desired effects, high vibration amplitude is normally used in power ultrasonic applications. In practical terms, typical amplitudes range from about 10 to 100 μm [3]. The fundamental research on power ultrasonics is to identify, model and characterise the mechanisms of ultrasound interaction with the medium in a particular application.

Generally, there are four main industrial applications: machining [4], welding [5], cleaning [6] and cutting [7]. Power ultrasonic techniques are applied to these existing processes to improve energy transmission, reduce or eliminate the need for chemicals, and increase effectiveness and efficiency. High power ultrasonic devices are also used in medical and clinical applications, for example, to cut and coagulate tissue. Surgical techniques using power ultrasonic devices offer surgeons some important benefits, which will be discussed in the next section.

A typical power ultrasonic system consists of a generator, a piezoelectric transducer, a horn and a working tip (Fig. 1.2). The ultrasonic generator is used to drive the transducer. Tuned at the resonant frequency, the piezoelectric transducer converts electrical to mechanical energy and provides a mechanical vibration along the axis. A horn, usually designed in a taper shape and tuned to the frequency of the transducer to amplify the vibration amplitude, is attached to the transducer by a threaded joint. A working tip, for contacting, cutting, or loading test samples, is incorporated with the horn.

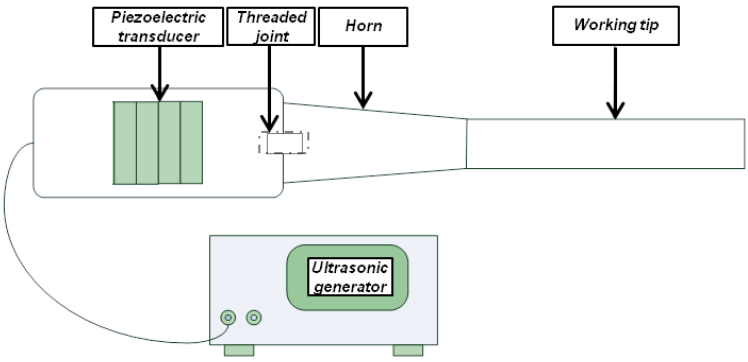

Fig. 1.2 Schematic configuration of generic power ultrasonic system

Several electric parts are incorporated in the ultrasonic generator system, including a wave generator and a power amplifier [8]. The ultrasonic generator is a high-voltage and high-frequency device, which is responsible for transforming a mains power supply from a frequency of 50 or 60 Hz to a high frequency alternating voltage or current required by the ultrasonic transducers. The generator supplies the required electrical signal to make the transducer work efficiently at transforming electrical power into mechanical vibration power.

Piezoelectric transducers are used in power ultrasonic systems due to being more efficient, having wider range frequency range and smaller size than magnetostrictive counterparts. The efficiency of piezoelectric transducers is over 90% and they are stable over a broad range of temperatures. The piezoelectric transducer produces a high frequency mechanical vibration through piezoelectric materials, such as crystals and certain ceramic materials. These materials have the ability to generate an alternating mechanical stress in response to an applied alternating voltage.

The horn fixed to the transducer amplifies the mechanical vibration and concentrates the energy into the working tip. Because the maximum amplitude of vibration provided by the transducer is usually insufficient for most power ultrasonic applications, a horn is necessary to act as an amplifier. The horn is tuned exactly to the transducer frequency. Horns are designed and manufactured in various geometric and material forms to meet the requirements of different applications.

In the applications of ultrasonic cutting, blades are required, which offer high precision cutting with very little debris. Ultrasonic blades can be made in different shapes for plunge and shear cuttings. Generally, a cutting blade operating at shear cutting mode is used in

most surgical applications, except ophthalmic surgery, in which plunge cutting is more appropriate for the removal of cataracts [9].

1.1.3 Power Ultrasonic Surgery

High power low frequency ultrasound has wide clinical applications from dental drilling to tissue removal. The use of high-power low-frequency ultrasound in surgery has been available for several decades since the introduction of cavitational tissue dissection in 1972 [10] and coagulation in 1991 [11]. Power ultrasonic surgical units have been widely used in many surgical procedures including dental [12], ophthalmic [13], orthopaedic [14] and neurosurgery [15] due to reduced tissue damage, decreased operating times, fewer instrument exchanges and more rapid healing. Moreover, when utilising ultrasonic energy to cut and coagulate tissue simultaneously, power ultrasonic surgery has been reported to achieve effective coagulation and safe cutting with relatively small thermal injury [16-18].

Operating in the high power and low frequency (20-100 kHz), ultrasonic surgical devices are used for biological tissue cutting, ablation, fragmentation and removal. In ultrasonic surgery, these are achieved through the surface application of high power ultrasound to the tissue. Although there are many research reports on the clinical effectiveness of ultrasonic surgical devices, little attention has been given to the interaction of ultrasonic devices and biological tissue, especially the responses of biological tissue to ultrasound exposure and ultrasonic wave or energy propagation through biological tissue. The power ultrasound effects on biological tissue are poorly understood and the mechanisms of ultrasonic wave interactions with viscoelastic biological tissues have not been clearly defined.

1.1.4 Effects of Power Ultrasound on Biological Tissue

Different effects can be induced by high power ultrasound. These effects depend on compound acoustic phenomena, which, in turn, are caused by primary vibratory inputs. Acoustic pressure causes cavitation and microstreaming in liquids, vibratory stress causes heating and fatiguing in solids and ultrasonic acceleration causes surface instability at liquid-liquid and liquid-gas interfaces [19].

From the limited literature, the effects of ultrasound on tissue can be summarized into three dominant aspects: acoustic cavitation, thermal effects and mechanical effects. Most power ultrasound applications rely on these vibration-induced phenomena occurring in the tissue.

However, the relative contributions of acoustic cavitation, thermal effects and mechanical effects on tissue types remains unclear [20]. Therefore, to assess the effects of ultrasonic surgical devices on tissue, these contributions need to be characterised quantitatively.

However, obtaining reliable information on these effects in power ultrasonic surgical applications is problematic at present. Conventional measurement methods have been used to investigate the effects of ultrasonic cutting of tissue by comparison between ultrasonic surgical devices and traditional saws or scalpels by varying parameters, such as vibration frequency, cutting force or application time. The research has focussed more on the ultrasonic cutting ability rather than the interaction between ultrasonic surgical devices and tissue. A better and more detailed evaluation of the device-tissue interaction is required.

1.1.5 Ultrasonic Field Characterisation

To provide an understanding of the ultrasonic effects in device-tissue interaction, the ultrasonic field in tissue during ultrasonic loading need to be characterised. Ultrasonic field characterisation is also useful for evaluating ultrasonic surgical instrument performance.

1.1.5.1 Surrogate Tissue Materials

The response of biological tissue to power ultrasound is variable due to the various biological properties. It is therefore necessary to characterise the properties of tissue for power ultrasonic applications. The complex geometry, availability and controls of living tissue often make its use impractical, as well as very expensive for laboratory based study. Additionally, its ultrasonic characteristics are not currently well defined, especially for transmission of high power and low frequency ultrasonic waves. Ideally, the creation of suitable surrogate tissue materials would solve many of the characterisation challenges. The mechanical, thermal and acoustic properties of surrogate tissue materials can be characterised using various tests to explain frequency and temperature dependent behaviour due to the intrinsic viscoelastic nature.

1.1.5.2 Non-invasive Ultrasonic Field Measurements

To characterise quantitatively the interaction between power ultrasound and tissue mimics, experimental work is required to measure ultrasound induced displacement, strain, stress and temperature fields in the materials. These measured fields can be used to understand

mechanical responses and thermal effects. The use of non-invasive measurement techniques with high sensitivity and fine resolution offer the opportunity to assess the full field ultrasonic effects on tissue. Compared to conventional disruptive measurements by manipulation of a probe to positions within the material, a non-invasive technique improves reliability and accuracy for detection of ultrasonic fields.

1.1.5.3 Numerical Models for Validation

To validate the experimental results, numerical models can be created to simulate the ultrasonic process in surrogate tissue materials. Accurate numerical simulations including finite element and analytical methods, which are adaptable to wide ranging design parameter changes, can be developed to build reliable predictive models. The models can be compared with the measurements to evaluate the interaction of ultrasound and tissue.

1.1.5.4 Methods for Characterising Ultrasonic Field

If the power ultrasonic input and the properties of tissue mimics are known, both the full-field non-invasive measurements and the subsequent development of reliable finite element and analytical models incorporating the material properties derived from various tests can be used as a platform to perform further evaluation of ultrasound effects on tissue to allow better understanding the performance of power ultrasonic surgical devices in cutting or vibrating tissue. Therefore, this work aims at characterising the effects of power ultrasonic devices on surrogate tissue materials using experimental and numerical methods.

1.2 Aims and Contributions of the Thesis

1.2.1 Aims of the Thesis

1. To extensively characterise the frequency and temperature dependent viscoelastic behaviour of tissue mimicking materials for use in high power ultrasonic applications.

2. To design a high power ultrasonic system, including ultrasonic horns, using finite element methods, for applying sufficient ultrasonic vibration to tissue mimicking materials.

3. To incorporate non-invasive measurement procedures in the characterisation of high power low frequency ultrasonic stress, strain and thermal fields within elastic and viscoelastic solids. The techniques can be used to provide accurate spatial strain, stress and thermal mapping without invasive damage caused by insertion of measurement sensors.

4. To develop finite element and analytical models which can be useful in providing a firm scientific basis for investigations of power ultrasound on elastic and viscoelastic solids and evaluation of the influence in the non-linear materials of ultrasonic wave propagation.

5. To perform damage analyses of tissue mimicking materials during power ultrasonic excitation by assessing the thermo-mechanical effects.

1.2.2 Contributions to the Research Fields

A comprehensive review of conventional measurement techniques for ultrasonic cutting tissue and their use in characterising ultrasonic cutting is presented. A literature review of full-field non-contact measurements to examine the mechanical response of specimens in the areas of fracture mechanics and materials is given, which serves to highlight some research on the behaviour of specimens under impact loading.

Power ultrasonic horns have been designed and manufactured for the experimental study. Their modal parameters are determined by experimental modal analysis. A novel triangular slotted ultrasonic horn has been made, which doubles the vibration amplitude from the transducer and can provide a contact surface for mounting tissue mimic samples, having a larger contact area than the output surface of the transducer. Moreover, a test rig is designed with features of providing high vibration amplitude uniformity at the horn contacting surface with samples. All horns are coordinated well with the commercial ultrasonic piezoelectric transducer, which is modelled using finite element method for validating its characteristics.

The time/frequency temperature superposition principle has been applied to experimental data from a dynamic mechanical analyser for estimation of frequency and temperature dependent behaviour of tissue mimicking viscoelastic materials. Furthermore, the behaviour of the viscoelastic materials during ultrasonic loading has been experimentally

characterised to validate the assumption of the time/frequency temperature superposition principle. Therefore, this validated principle provides a unique way of estimating material viscoelastic properties over time/frequency variations, which is applicable for power ultrasonic vibration.

Experimental procedures for non-invasive full-field displacement, strain, stress and temperature measurements of ultrasonic fields in the viscoelastic samples are described and developed. These techniques are based on digital image correlation, thermograpic and acousto-optic principles, which utilise an ultra-high speed camera, an infrared camera and a laser interferometer respectively to map displacement, strain, stress and temperature fields. Because conventional measurements by probe position within the material can alter the wave propagation within the materials, these non-invasive full-field measurements have the potential for accurate power ultrasonic field measurements.

Finite element models for simulating ultrasonic wave propagation in the materials and their thermo-mechanical behaviour during ultrasonic loading have been created. These models feature accurate representations of elastic and viscoelastic materials subject to power ultrasonic excitation. They can be used as rapid virtual prototyping tools with reliable knowledge of the transmission materials employed. Furthermore, analytical models are presented to analyse the ultrasonic wave propagation in elastic materials. The results from these analytical models are compared with the results from finite element models and experimental studies to show that experimental and numerical data correlate well in this application.

From the preliminary work described in this thesis, the full-field non-invasive measurement techniques and the numerical methods can be used as a solid basis for further investigation into power ultrasonic tissue interaction.

1.3 Overview of the Thesis

The project has five individual parts, including dynamics, materials, experiments, finite element analysis, and results and conclusions. The structure of the project is shown as follows:

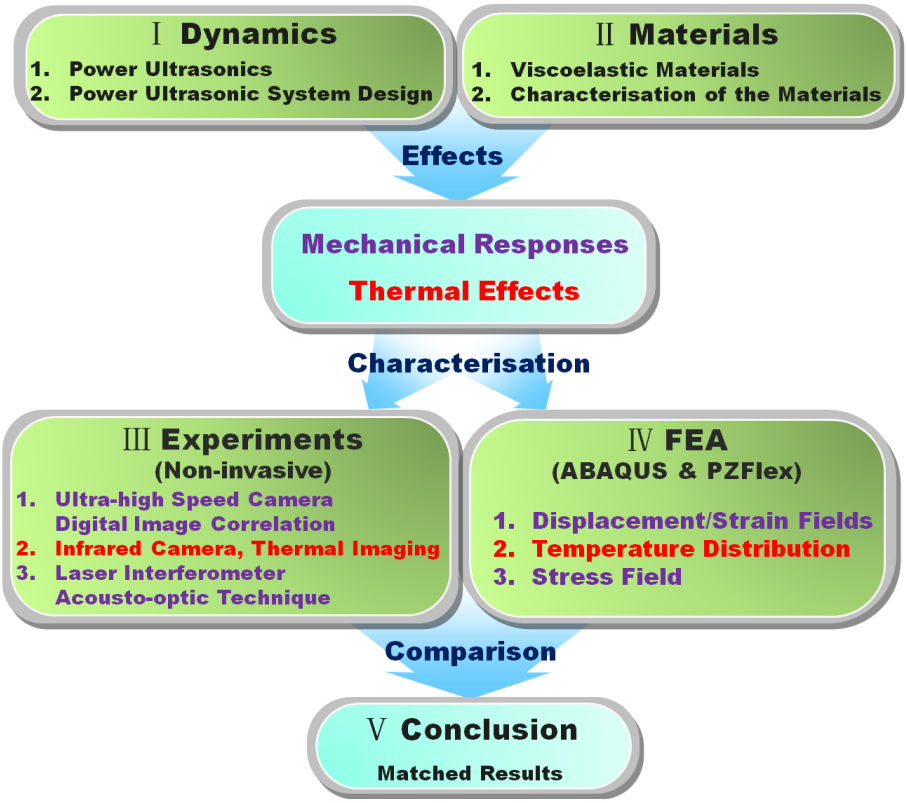

Chapter 2: **Literature Review**

This chapter presents a review of ultrasound, especially introducing common industrial and clinical applications of high power ultrasound and the effects of ultrasound on tissue. From this review, the thermal and mechanical interactions of power ultrasound with tissue emerge as the main mechanisms for the efficacy of the application. Invasive and non-invasive measurement techniques for characterisation of the power ultrasonic induced effects are described, which highlight the relative merits of non-invasive methods for quantifying high power ultrasonic fields.

Chapter 3: **Power Ultrasonic System Design**

This chapter describes the design procedure of power ultrasonic components by the use of finite element analysis for the ultrasonic experimental preparation. Firstly, a brief introduction and finite element analysis of the piezoelectric transducer are described. The finite element model of the transducer demonstrates a longitudinal mode at the resonance frequency and show a good match with experimental analysis. Next, the theoretical, finite element modelling investigation into the use of ultrasonic horns is developed and validated by experimental modal analysis using a laser Doppler vibrometer. The model accurately

predicts the performance of vibrating horns. Finally, a power ultrasonic test rig is made to facilitate the loading of samples.

Chapter 4: **Tissue Mimicking Materials**

Following the introduction of tissue mimics, Chapter 4 considers in greater detail the experimental characterisation of the viscoelastic behaviour of the materials during dynamic loading. Firstly, the biological tissue properties are presented. Next, tissue surrogates are manufactured and applied and their general properties are reviewed and summarised from the literature. Then, their mechanical and thermal properties, and frequency and temperature dependency are characterised by static mechanical, thermal and dynamic mechanical tests respectively. Finally, the experimental data is used to explain and model the behaviour of these tissue mimics under ultrasonic loading.

Chapter 5: **Non-invasive Field Measurement Techniques and Numerical Models**

Since the experimental set-up for ultrasonic loading of tissue mimicking materials was successful, non-invasive field measurement techniques are developed to quantitatively characterise the ultrasonic effects by measuring and calculating the displacement, strain, stress and thermal fields. An experimental investigation combining the use of digital image correlation and an ultra-high speed camera is described for the accurate characterisation of displacement and strain fields generated by the power ultrasonic system in hard tissue mimics. The experimental principles, requirements and procedures are illustrated. The detection of temperature increases occurring in the materials during ultrasound exposure using an infrared camera is presented as another non-contact method to display visually the images of thermal radiation. Thermo-mechanical effects are introduced to explain the temperature rise of the materials during ultrasonic loading. In addition, the application of the acousto-optic effect combined with laser interferometry for stress field quantification is presented to characterise the power ultrasonic wave propagation in transparent soft tissue mimics.

Finally, chapter 5 describes the creation of numerical models including analytical and finite element models. The analytical models created using Mathematica software provides full-field displacement and strain maps. The displacement, strain and stress produced by steady state longitudinal ultrasonic wave propagation in viscoelastic materials are

calculated using the finite element software packages ABAQUS and PZFlex. Due to the different time scales in mechanical and thermal simulation, it is hard to do a coupled thermo-mechanical analysis of the power ultrasonic vibration of viscoelastic materials by writing user subroutines with ABAQUS. Therefore, thermal responses are obtained using PZFlex by calculating the heat generation due to mechanical loss during ultrasonic loading and heat transfer due to convection. Material properties assigned to numerical models are determined from the experimental characterisation in chapter 4.

Chapter 6: **Measurement of Ultrasonic Fields and Correlation with Numerical Models**

This chapter presents the experimental results of non-invasive ultrasonic field measurements, which show excellent agreement with numerical simulations. The possible reasons for the material behaviour during ultrasonic loading are discussed and several factors affecting field profiles are investigated. Furthermore, accurate mapping of the mechanical and thermal fields can be achieved through finite element models created using frequency and temperature dependent material data.

Chapter 7: **Conclusions and Future Work**

It can therefore be stated that the accurate mapping of power ultrasonic fields within viscoelastic solids can be achieved through non-invasive measurements by a combination of digital image correlation with an ultra-high speed camera, thermal imaging techniques with an infrared camera and acousto-optic measurements with laser interferometry. Reliable finite element models for simulating ultrasonic mechanical and thermal responses can be created with consideration of the frequency and temperature dependent behaviour of the viscoelastic materials under ultrasonic loading. The platform for characterising the power ultrasonic effects on tissue can be built based on the experimental and numerical studies. Finally, practical suggestions for furthering the knowledge in this field are proposed.

2. Literature Review

2.1 Historical Background

Ultrasound has been present in nature for millions of years, where animals such as whales and dolphins use ultrasound for range-finding, target identification and communication over large distances by transmitting and receiving acoustic waves through water.

Felix Savart, a French physicist and medical doctor, designed the first ever ultrasonic generator (working at up to 24 kHz), the Savart wheel, in 1830 [21, 22]. The Galton whistle, which worked in the range 3 to 30 kHz, was invented in 1876, in an attempt to investigate the audio threshold of animals [23]. Tuning forks, producing frequencies from 16 to 90 kHz, were developed by Koenig in 1899 [24] for a more thorough study on the limit of human hearing.

1880 marks a milestone in the history of ultrasonics when Pierre and Paul-Jacques Curie discovered the piezoelectric effect [21, 25]. The development of ultrasonics was stimulated by the discovery of piezoelectricity, however it remained a laboratory curiosity for several decades afterwards. In 1896, pioneering work on the theory of sound was published by Lord Rayleigh, who defined fundamental discoveries in acoustics and optics. The research was fundamental to wave propagation and included atomization, surface (or Rayleigh) waves, molecular relaxation, acoustic pressure and bubble collapse which all have important influence within ultrasonics [21].

After the RMS Titanic collided with an iceberg mid-Atlantic on her maiden voyage, the potential of using ultrasonics as a viable means for detecting submerged objects became apparent. The beginning of World War I gave further impetus to development of underwater detection systems using ultrasonics. Chilowski designed an ultrasonic device for the French navy in 1914, but it had weak acoustic intensity. Langevin then adapted Chilowski's design to produce piezoelectric transducers working at resonance with high ultrasonic intensities for a joint U.S., British and French venture [26].

In the inter-war years, innovative work involving ultrasound continued with attention turning away from large scale inspection within vast regions of the oceans to small scale probing applications in specific regions of interest, such as applications in laboratories, factories and hospitals. Non-destructive testing was pioneered by Sokolov in 1920 who

investigated the possibility of ultrasonic detection of flaws and voids within manufactured components [27]. The potential of ultrasound in medicine as a diagnostic tool was investigated independently in the U.S. and Japan by 1948.

The destructive ability of ultrasound was first noted by Langevin. Initial pulse echo investigations at frequencies of 150 kHz were found to kill fish that were insonated with the ultrasonic beam [28]. Industrial processes using high intensity or power ultrasound then began.

2.2 Power Ultrasonic Applications

2.2.1 Power Ultrasonic Applications in Industry

Power ultrasound has been used in industry for materials processing (metals, ceramics and plastics) for almost century and in medical applications for dental and surgical procedures for more than half a century [20]. Early power ultrasonic applications in industry included machining, cleaning, metal and plastic welding and soldering [29].

Initially, material removal by ultrasonic energy was introduced by Wood and Loomis in 1927 [30]. High frequency vibration was applied to a vibrating tool for removing material from the workpiece, aided by fine abrasive grains in slurry that flows freely between the workpiece and the tool. [31]. The tool vibrates at a resonance frequency with low amplitude, which provides a velocity to the abrasive grains. Cyclic impacts of abrasive particles produce stresses, which cause microchiping and erosion of the workpiece surface. Ultrasonic machining has proved effective for machining hard, brittle materials, such as alumina, ceramics and glass [29].

Ultrasonic cleaning dated back to the early 1950s. Ultrasonic cleaners began being used in industry in about 1950, and came into use in relatively inexpensive household appliances in about 1970 [32]. In the ultrasonic cleaning process, the equipment, normally operating in the range of 20 to 50 kHz, produces ultrasonic waves in the cleaning fluid, where industrial components (metals, glasses, ceramics and plastics) were placed. Cavitation occurs when high frequency alternating pressure tears the liquid apart and leaves behind many microscopic voids which grow to a certain size, then collapse, causing high instantaneous temperatures and pressures. This implosion of cavitational bubbles removes surface dirt and contaminants on the workpiece [29].

The ultrasonic metal welding process was in the stage of research and development by 1955. It found original acceptance in the semiconductor industry for welding of miniature conductors. After that, the technique was used widely in many fields, such as automotive engineering and manufacturing processes. The main advantages of ultrasonic metal welds are low heating and thus relatively low distortion. As the welding temperatures are typically below the melting temperatures of the metal, the technique helps to avoid brittleness and formation of high resistance intermetallic compounds in dissimilar metal welds [29].

In the 1960s, the practical application of ultrasonic welding used for rigid plastics was developed. A patent was awarded in 1965 to Robert Soloff and Seymour Linsley, who contributed to the invention of ultrasonic welding [33]. Welding of plastics using ultrasonics is typically used for small parts in packaging, toys and many others. The process involves that ultrasonically induced heat melts the plastic workpieces precisely at the interface to join and bond them together without indiscriminate heating of the surrounding material.

The original work of ultrasonic soldering was done as early as 1936 and patents were issued in Germany in 1938 and 1939 [34]. Ultrasonic energy is used to solder materials to form a joint in the process of ultrasonic soldering. It is fundamentally similar to ultrasonic cleaning with cavitation in molten solder for eroding surface oxides and exposing the metal. The difference of ultrasonic soldering and welding is the presence or absence of a filler material.

Fig. 2.1 schematically illustrates the ultrasonic material processing in machining, cleaning and welding.

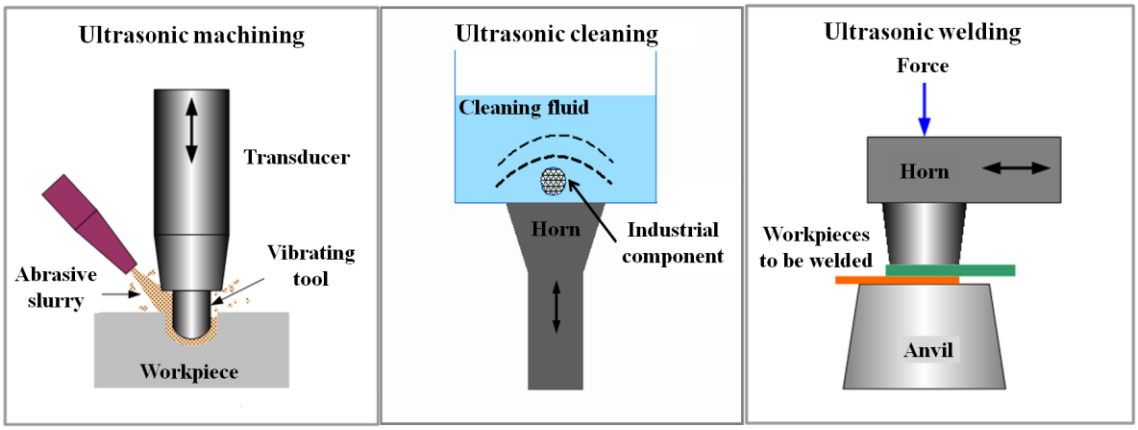

Fig. 2.1 Ultrasonic materials processing (a) machining [35] (b) cleaning (c) welding [35]

With advancements in materials, transduction methods and electronics, modern power ultrasonic applications have expanded, spanning from drilling, motors, food cutting, sonochemistry and many others.

The drilling-cutting action of ultrasonics was observed by Wood and Loomis in 1927, but it was not further exploited in the following years until the issue of British Patent 602801 to Balamuth in 1948. Ultrasonic drills were produced by several equipment makers by the early 1950s [36]. From 2000s, ultrasonic drilling devices were designed and used by NASA to bore through rock for a planetary exploration with advantages of their weight saving, miniaturisation and low axial load requirement [37]. An ultrasonic driller is a boring device, which utilise vibrations to hammer its bit through materials. Incorporation of torsional motion to the longitudinal ultrasonic vibration during drilling processes has shown improving cutting removal and increased rate of drill penetration. Cardoni et al. developed ultrasonic rock sampling devices by use of longitudinal-torsional vibrations (Fig. 2.2). The devices enhance drilling/coring performance during drilling and coring tests on sandstone [38]. The ultrasonic bit was designed for the attempt to generate combined longitudinal-torsional mode vibration.

Widely used in auto-focusing lens systems in cameras, small ultrasonic motors provide high holding torque with minimal noise, absence of electromagnetic interference and higher efficiency at low velocity compared with electromagnetic motors [39-41]. Ultrasonic motors are divided into two categories depending on the principle that generates the energy to move the drive: a travelling wave motor and a standing wave motor. By coupling longitudinal and torsional ultrasonic vibration, the standing wave motor uses one rotor and two stators to produce larger output torque. Two stators generate two orthogonal

vibrations excited by a longitudinal transducer (L-PZT) for longitudinal vibration and torsional transducer (T-PZT) for torsional vibration (Fig. 2.3) [42]. The surfaces of the stators transfer the generated vibrations through friction forces to the rotor, which produces the rotation.

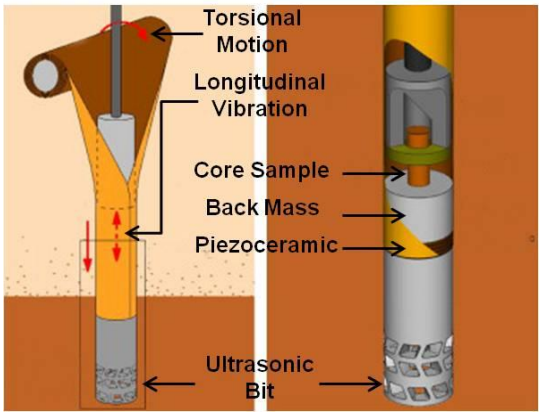

Fig. 2.2 The architecture of an ultrasonic drilling/coring system [38]

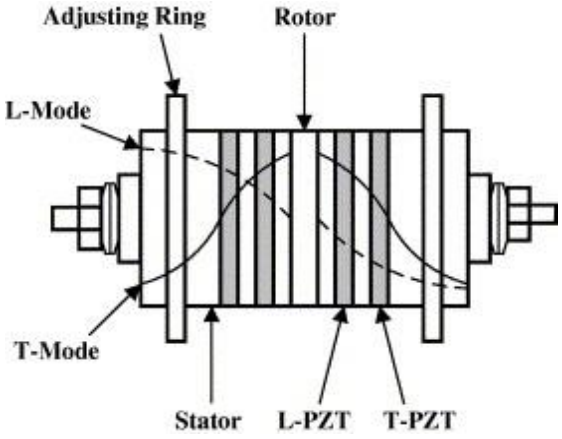

Fig. 2.3 Sketch of a longitudinal and torsional motor [42]

Power ultrasonic cutting systems revolutionised the food industry in 1990s by improving cut quality and accuracy with minimal wastage of food material [43]. Ultrasonic food cutting process involves a vibrating blade producing a nearly frictionless surface to which food products do not stick nor deform. Povey and Mason reviewed the ultrasonic cutting technique in the food industry, described the ultrasonic cutting process, driving machines and knife blades, and discussed the benefits of ultrasonic food cutting [44]. A superposition of the cutting movement of a blade and the vibrational movement generated by ultrasound makes cutting of food with several advantages such as reduced smearing, low product lost, less deformation, less tendency to shatter for brittle products and being able to handle sticky or brittle foods. It finds popular uses in cutting of fragile, heterogeneous, fatty and sticky foodstuffs such as cakes, pastry, bakery products and cheeses [45]. An ultrasonic cutting system designed by Sonics & Materials, Inc. with a guillotine blade to cut different kinds of food, is shown in Fig. 2.4 [46].

Sonochemistry is when power ultrasound is applied as an energy source to provoke chemical activity. In 1927, Loomis first observed the chemical effects of ultrasound [47], which derive principally from acoustic cavitation. During the 1950s and 1960s, many studies on cavitation culminated in a relatively detailed understanding of sonochemistry. Although the field of sonochemistry lay fallow for nearly 60 years, the renaissance of it

occurred with commercial availability of inexpensive and reliable power ultrasonic generators in 1980s. Sonochemical reactions do not generally take place during the ultrasonic irradiation of solids or solid-gas system, but occur in liquids, where cavitation effects can be produced by high frequency alternating pressure [48]. In Fig. 2.5, a titanium rod vibrating at 20 kHz gives rise to a cloud of cavitating bubbles that emit flashes of light and house an array of chemical reactions [49]. Micro-bubbles are formed at the beginning of cavitation and grow until they reach a critical size, several times larger than their initial size, before violently undergoing collapse. According to the generally more accepted hot spot theory, the diffuse energy of the sound is concentrated in chemically useful energy. The high temperature and large pressure caused by the localized "hot spot" where bubbles collapse induce sonication of water into H and OH radicals and the production of hydrogen peroxide (H_2O_2) [50, 51]. Power ultrasound can contribute to electrochemistry and green chemistry together with water and sewage treatment [52].

Fig. 2.4 An ultrasonic food cutting system

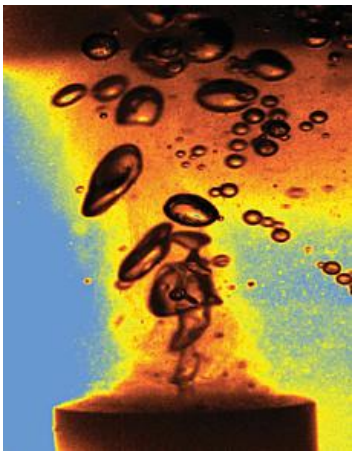

Fig. 2.5 Cavitating bubbles [49]

Other established industrial applications of power ultrasonics include metal working processes such as forming [53] and drawing [54], degassing [55] and homogenizing [56]. The power ultrasonic metalworking processes have lots of advantages such as force reduction, surface improvement and cost effectiveness. The techniques of power ultrasound make the applications of degassing and homogenizing reliable, of easy use and energy-saving.

2.2.2 Power Ultrasonic Applications in Medicine

Ultrasound is widely used in a variety of medical procedures including diagnostic, therapeutic and surgical procedures. Diagnostic ultrasound, as a non-invasive tool in

clinical medicine, is now applied extensively to visualisation of muscles, tendons and many internal organs to obtain their size, structure and to identify any pathological lesions [57]. Due to the low power (<0.5-3 W/cm^2) and high frequency (1-20 MHz), ultrasound employed in diagnostic applications such as obstetric sonography, B-scan ultrasonography, and Doppler echocardiography has no destructive effects on the scanned biological tissue. Therapeutic applications of ultrasound in physiotherapy have been extensively used in clinical practice and other therapeutic applications of ultrasound include treatment of tendon injuries, stimulation of bone repair, haemostasis and the targeted delivery of drugs [58, 59]. Similar to diagnostic ultrasound, therapeutic ultrasound in these applications are high frequency and at low or intermediate intensity levels (Table 2.1) and causes minimal damage. In contrast, high power ultrasound in medicine tends to permanently affect the biological tissue.

Table 2.1 General characteristics of ultrasound used for different therapeutic applications [60]

Therapeutic Applications	Frequency (MHz)	Intensity (W/cm^2)	Pressure (MPa)
Physiotherapy	1-3	1	<0.5
Haemostasis	1-10	100-5000	5
Bone growth stimulation	1.5	0.03	0.05
Drug delivery	Up to 2	Various	0.2-8

Lithotripsy has been a growing application of ultrasound since 1980 [61], for the physical destruction of hardened masses such as kidney stones and gallstones. The ultrasonic waves used in lithotripsy (frequency at 0.25 or 0.5 MHz [60]), called high-energy shock waves, are targeted at the stones from outside the body causing them to fragment. The stones are broken into tiny sand-like pieces, which usually pass easily through the ureters and the cystic duct. Due to being the least invasive stone treatment method, it has become a standard treatment [62].

High intensity focused ultrasound (HIFU), an application of ultrasound with an intensity over 1000 W/cm^{-2} and a frequency of 0.8-3.5 MHz, is a non-invasive surgical technique for the ablation of regions of target tissue such as tumours, without adversely affecting healthy surrounding tissue. The first work to consider potential HIFU applications was published in 1942 [63], and demonstrated that focused ultrasound beams could produce regions of highly localized biological effect. Fry et al. [64] used HIFU for treatment of Parkinson's disease in the 1950s. Tissue damage using HIFU (Fig. 2.6) encompass two

main processes: conversion of mechanical energy into heat and acoustic cavitation. Focused ultrasound beams from the concave oscillating piezoelectric transducer are concentrated on the target tissue. As the ultrasound beams propagate through the tissue, part of ultrasonic energy is absorbed by tissue and converted to heat. With focused ultrasound beams, a very small focus can be achieved deep in tissues. Significant energy deposition at the focus leads to coagulative necrosis of tissue causing irreversible cell death. Cavitation results in cell necrosis induced through a combination of mechanical stress and thermal injury [65, 66]. The use of HIFU for treatment of cancer was first suggested by Burov in 1956 [67]. Now, it is widely used in various cancer therapies of liver, prostate, bladder, kidney, and breast etc [65, 66, 68]. From the clinical outcomes, HIFU has been demonstrated to be effective in tumour ablation and has a lower side-effect profile than the traditional surgery.

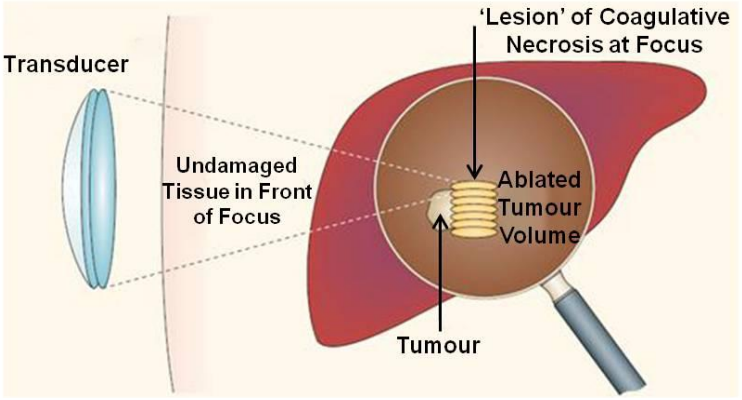

Fig. 2.6 A schematic representation of HIFU lesion production [65]

Studies on the potential use of power ultrasonics in clinical procedures such as soft and hard tissue cutting, or dissection and dental hygiene procedures were first undertaken during the 1950s [69, 70]. The power ultrasonic devices were used to cut, shatter or scale hard tissue or to dissect and emulsify soft tissue in surgery. Conventional surgical instruments for bone cutting such as burrs, saws and chisels, offer limited accuracy and manoeuvrability to surgeons [71], and electro-surgery for soft tissue dissection vaporizes the tissue with excess heat generation, which can damage adjacent tissue [72]. Ultrasonic surgical tools are safer and more effective than other instruments, because of the precise control, accurate and high quality cut, reduced cutting forces, limited debris, reduced bleeding and avoidance of surrounding tissue damage.

2.2.2.1 Dentistry

The use of ultrasound in dentistry is one of the most widespread power ultrasonic surgical applications. Power ultrasonic devices are capable of refining cavity preparation [73], removing deposits from the tooth structure [74] and assisting endodontic treatment such as locating calcified canals, removal of intracanal obstructions and root-end preparation [75]. An industrial ultrasonic drilling machine was first used to cut cavities in extracted teeth in 1952 [76]. Based on pioneering work by Balamuth [77], oral prophylaxis using ultrasound was first reported by Zinner in 1955 [74], while Richman first introduced ultrasonics to endodontics in 1957 [78].

The early uses of an ultrasonic drill required an abrasive slurry of aluminium oxide to assist the process of cutting or grinding enamel and dentine was reported by Postle in 1958 [79]. At that time, due to relatively slow action and the absence of efficient suction apparatus, ultrasonic cavity preparation did not compete with the more effective and convenient high speed drill [80]. The potential of ultrasound was exploited by Zinner as a scaling instrument for the removal of dental plaque and calculus from the surface of teeth [74]. By 1957, widely accepted dental use was established by Johnson et al. who made ultrasonic scaling as a rapid and simple alternative [81, 82]. In endodontic therapy, power ultrasonic instruments were also not recognised until Martin demonstrated their ability in the cleaning and preparation of root canals before filling and obturation [83]. Currently, although ultrasonic cleaning baths are available for the cleaning of dental instruments before sterilization, the main use of power ultrasound in dentistry is for dental scaling to remove calculus from teeth, root planning of teeth, and root canal therapy [84-86]. A modern ultrasonic dental scaling system from Mectron is shown in Fig. 2.7 [87].

Fig. 2.7 An ultrasonic dental scaling system from Mectron [87]

2.2.2.2 Soft Tissue cutting

For cutting and ablation of soft tissues, such as blood vessels, the acknowledged advantages of an ultrasonic surgical instrument are safety [88], precision [89] and

improved haemostasis [90] [20]. Especially in minimally invasive surgery, the technique of ultrasonic dissecting without blood loss is of paramount importance [91]. There are two main types of ultrasonic devices used for soft tissue cutting or ablation including ultrasonic cavitational aspirators for removing cataracts in the eye and debulking solid tissues, and ultrasonically activated dissecting and coagulation devices with sharper tips operating at 55 kHz for directly cutting and coagulating tissue in general or laparoscopic surgery [11].

In 1967, Kelman reported the use of a combination of power ultrasound and aspiration for fragmentation of human tissue and removal of the fragmented particles, which is the first study describing lens phacoemulsification in cataract surgery [13]. In 1978, Flamm et al. studied the effects of ultrasound on cat brain and spinal cord tissue, and concluded that ultrasonic cutting was effective in fragmentation of tissue with significant water content [92]. In the 1980s, Wuchinich et al. developed ultrasonic aspirators, which were suitable for endoscopic surgery [93] and extended the technology to the removal of tissue, such as brain neoplasms and other tumours, previously resistant to attack from vibration [94]. In 1994, Amaral developed an ultrasonically activated scalpel for laparoscopic use using an animal model and proved the efficacy of a hook-spatula blade on producing both cutting and coagulation [88]. Nowadays, an ultrasonic surgical system (Fig. 2.8) facilitates difficult procedures, minimises intraoperative blood loss, causes minimal tissue injury, improves intraoperative visualisation with absence of smoke, reduces cost, time and intraoperative instrument exchanges by combining grasping, cutting and coagulation into one integrated tool set, and is safe to both the surgeon and patient. The popularity of ultrasonic surgical systems is growing. Fig. 2.9 illustrates the clinical procedures with the highest growth in the application of ultrasonic surgical systems between 2003 and 2008 [95, 96].

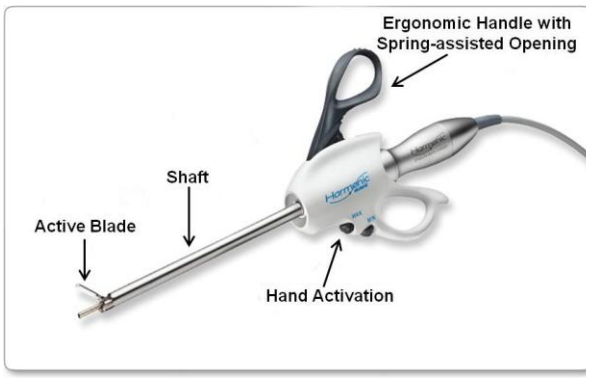

Fig. 2.8 An ultrasonic surgical system from Ethicon [95]

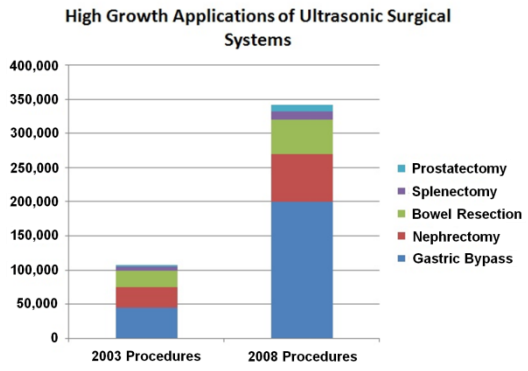

Fig. 2.9 High growth applications of ultrasonic surgical systems [96]

2.2.2.3 Bone Cutting

Ultrasonic surgical devices for cutting bone can be used for osteotomy, osteoplasty, drilling, shaping, and smoothing of bones in a variety of surgical procedures, including general, orthopaedic, maxillofacial, oral, hand, foot, neurosurgical, spine and plastic/reconstructive surgery. The advantages of the ultrasonic device in bone cutting include high precision cut, less damage to both soft and hard tissues, quicker recovery times than traditional saws or burs and safe use.

Longitudinally vibrational cutting tools operating at high frequency (6-12 kHz) for biological materials were made and described by Vang dating back to 1955 [70]. The first ultrasonic cutting instrument (named as URSK 7N, designed by Loshilov) used in bone surgery was reported by Giraud [71]. The instrument operating at a frequency of 25-30 kHz with amplitude of 50 μm was tested for transaction, rejoining and sawing of biological tissue by Volkov and Shepeleva in 1974 [97]. They concluded that orthopaedic procedures could be facilitated with the help of ultrasonic cutting devices after conducting 311 operations [97]. Polyakov did cutting comparison tests on bone using the instruments with and without superimposed ultrasonic vibration and found that ultrasonic vibration exciting the instrument in longitudinal resonant conditions could greatly increase the cutting rate and reduce the applied pressures [98]. Since the 1980s, scientists have been developing ultrasonic bone cutting instruments and bone cutting systems (eg. Fig. 2.10). These have interchangeable tool tips and an irrigation system to limit cutting temperature. The advantages of these devices identified the successful use through studies in small bone cutting [99, 100] include precise bone osteotomy [14], reduced cutting damage to bone [101, 102] and adjacent soft tissue [102, 103], reduced bleeding by promoting coagulation [104] and ease of use at the surgical site [105]. The claimed limiting factor of ultrasonic bone surgery is that it increases operative time compared to traditional techniques [105, 106].

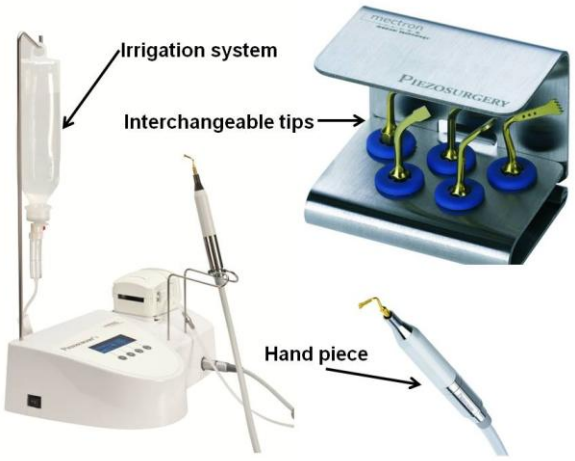

Fig. 2.10 An ultrasonic bone cutting system by PIEZOSURGERY® medical, Mectron [107]

2.3 Power Ultrasonic Effects on Materials

2.3.1 Introduction

Physical effects can be created in various (solid, liquid and gas) media by ultrasonic waves. Although physical laws governing the propagation of ultrasound can be used to describe the effects of ultrasound in the media, the biophysical effects of power ultrasonic waves in nonlinear biological tissues are difficult to characterise. The interaction between an ultrasonic surgical device and biological tissue is poorly understood, although considerable efforts have been made towards studying aspects such as mechanical and thermal effects, and the cutting ability of devices [108-116].

2.3.1.1 Power Ultrasonic Effects of Solid, Liquid and Gas

Graff discussed the major physical effects of ultrasound on solids, liquids and gases in process applications of power ultrasonics [2]. When a vibrating tool is pressed against a solid material, physical effects of surface and bulk stressing occur. The most common surface stressing effect is that of friction reduction between the vibrating surface and the load in drawing and rolling processes. Bulk stressing has been considered as the basis for many power ultrasonic processes. The induced stress level may be the cause of brittle fracture in slurry drilling and enhance dislocation activity in certain forming. In welding of plastics, where melting is found, it can be considered that the heating of material comes from ultrasonic bulk stressing. The cavitation, referred as the growth and collapse of small bubbles in a liquid under the cyclic phases of rarefaction-compression occurred during ultrasonic vibration, is the main physical phenomena associated with ultrasound in liquid.

Acoustic streaming is another phenomenon in ultrasonic interaction with liquid, which is of lesser importance than cavitation. The phenomenon of acoustic streaming is the intense, local circulation and vortex flow fields observed near the contacting surface of the vibrating tool. These fields can enhance the rates of heat and mass transfer in ultrasonic processes. A net radiation pressure was the main finding for a power ultrasonic tool radiating into a gas [2].

The mechanism of material removal in ultrasonic machining, well documented by Thoe et al., was summarized as mechanical abrasion by direct hammering of abrasive particles against a workpiece surface, micro chipping by impact of the free moving abrasive particles, cavitation effects from the abrasive slurry and chemical action associated with the fluid employed. The effects of the above mechanisms result in material removal by shear and fracture and displacement of the material at the surface by plastic deformation in the ultrasonic machining process [4]. Similar mechanisms were found in tissue removal and damage using power ultrasonic devices.

Humphrey reviewed the physical interactions between ultrasound and various fluids and these were categorized into fundamental physical effects, ultrasonic heating, cavitation and secondary effects. The fundamental physical effects due to wave propagation included particle motion, energy deposition, transmission and reflection, and nonlinear propagation. Secondary effects involved radiation pressure and streaming. The main changes in a fluid medium produced by ultrasonic propagation were outlined as heating and cavitation [117].

2.3.1.2 Power Ultrasonic Effects of Biological Tissues

The response of biological tissue to ultrasound is quite variable and depends on the acoustic and biological properties of the tissue as well as location and function of the tissue [118].

Power Ultrasonic Effects of Soft Tissue

Both mechanical action and cavitation at the tip of the ultrasonic surgical device have been suggested as the mechanism of fragmentation during cataract surgery by Schafer [119]. Rosenschein et al. developed an experimental ultrasonic angioplasty device and concluded that mechanisms of ultrasound in percutaneous ultrasonic angioplasty primarily included direct mechanical effects and cavitation, but there may also be thermal effects and

generation of microcurrents at the cellular level [120]. Amaral found the mechanical and thermal effects of an ultrasonically activated scalpel in cholecystectomy on producing the best mix of both cutting and coagulation [88]. Bond and Cimino reported that the mechanism in soft tissues is predominantly related to mechanical impact of direct shear, pressure wave components and acoustic streaming [113]. It can be found that the main effects of soft tissue to ultrasonic vibration are mechanical effect, thermal effect and acoustic cavitation, while secondary effect includes streaming.

Power Ultrasonic Effects of Hard Tissue

Cimino and Bond described that the mechanism of bone and hard tissue removal in ultrasonic cutting applications cannot be the same as in soft tissues [110, 111]. The effects of ultrasonic vibration in bone surgery involved mechanical cutting, fatigue failure of osteotome parts and high temperature [71]. Micro fracture along with mechanical impact and shock waves in a fluid were also more likely to occur in the bone and hard tissue removal in ultrasonic cutting applications [20]. Therefore, the main effects of ultrasonic vibration of hard tissue are both mechanical (impact and wave propagation) and thermal effects.

Barnett et al. summarized that mechanical and cavitation effects are time independent biological responses to ultrasonic exposure but that the thermal effect is time dependent. However, the magnitude of the resulting effect is dependent on the duration of exposure for any mechanism once a threshold value has been exceeded [118].

2.3.2 Direct Mechanical effects

Direct vibrating contact between the oscillating horn or blade tip and biological tissue results in fragmentation and ablation of materials into microscopic particles. If the tissue is not fragmented in one vibration cycle, repeated impacts may occur. Micro-damage may be progressively induced in the tissue applying power ultrasonic vibration. Ultrasonic waves can be delivered to the tissue by direct contact with the oscillating horn or blade tip [20]. Therefore, the mechanical interaction of the ultrasound with the tissue can be considered as producing ultrasonic wave propagation and effect of mechanical forces.

2.3.2.1 Ultrasonic Wave Propagation

Small amplitude ultrasonic waves propagating through media as linear elastic waves result in particle oscillations about their equilibrium position. In ideal fluids and gases, only a longitudinal mode exists, where particle displacements are parallel to the direction of ultrasonic propagation. Elastic solids can accommodate transverse waves (where particle displacements are perpendicular to the direction of propagation) as well as longitudinal waves.

Biological tissues are viscoelastic solids, where both longitudinal and transverse waves can propagate. However, similar to fluids, only longitudinal waves are of significance in soft tissues, because shear waves are highly attenuated at ultrasonic frequencies. In hard tissues, such as bone, both longitudinal and transverse waves should be considered [117, 121].

The equations of longitudinal and shear waves propagation in an isotropic linear elastic solid can be obtained as following,

$$\rho \frac{\partial^2 u}{\partial t^2} = (K + 2G) \cdot \Delta u \quad \textbf{2.1}$$

$$\rho \frac{\partial^2 u}{\partial t^2} = K \cdot \Delta u \quad \textbf{2.2}$$

$$\Delta = \frac{\partial^2}{dx^2} + \frac{\partial^2}{dy^2} + \frac{\partial^2}{dz^2} \quad \textbf{2.3}$$

where u denotes the elementary particle displacement vector, K (bulk modulus) and G (shear modulus) are elastic constants and Δ denotes the Laplacian operator.

If the cross-sectional dimensions are much smaller than the wavelength, only a longitudinal stress component is considered along the propagation direction of a slender bar (a bar whose cross-sectional area is considerably smaller than its length). The mathematical expressions for the transmission of plane waves through inviscid fluid medium are very similar to transmission of longitudinal waves along the bar. The governing differential equation is

$$\rho \frac{\partial^2 u}{\partial t^2} = E \frac{\partial^2 u}{\partial x^2} \quad \textbf{2.4}$$

where u is the longitudinal displacement of a particle in the bar and x is the particle displacement at the reference orientation.

Under the assumption that the cross-sectional dimensions of the bar are much smaller than the wavelength, the longitudinal wave propagation velocity c_l can be obtained by

$$c_l = \sqrt{\frac{E}{\rho}} \quad \textbf{2.5}$$

where E is the Young's modulus of the material and ρ is the density [122].

If the cross-sectional dimensions are comparable with the wavelength, wave propagation velocities corresponding to the case of longitudinal and shear wave modes are given by:

$$c_l = \sqrt{\frac{K + 2G}{\rho}} = \sqrt{\frac{E(1-\nu)}{\rho(1+\nu)(1-2\nu)}} \quad \textbf{2.6}$$

$$c_s = \sqrt{\frac{G}{\rho}} = \sqrt{\frac{E}{\rho(1+\nu)}} \quad \textbf{2.7}$$

where c_l is the longitudinal wave propagation velocity, c_s is the shear wave propagation velocity and ν is the Poisson's ratio [123].

Equation 2.5 has been used extensively to predict the elasticity of cortical (compact) bone [124]. It has also been suggested that in a cancellous bone a wave travels along each trabecula with the bar longitudinal wave velocity [125].

2.3.2.2 Effects of Mechanical Forces

Tissue fragmentation and ablation are related to the effects of mechanical forces which include direct mechanical impacts and shearing stress [111, 126]. For phaco-emulsification, it is thought that repeated impacts (a mechanical 'jack-hammer' effect) at a higher frequency (40 kHz) can make the cutting smoother than at a lower frequency (i.e. 20 kHz) [20]. In neurosurgery with the help of power ultrasonic vibration, the tissue

fragmenting action occurs without significant manually applied pressure, which can minimise unwanted damage and the pulling and distortion of surrounding tissue [108]. It was observed by Cimino et al. that the horn-tip peak-to-peak displacement, which influenced the applied pressure, was one of the most significant operating parameters affecting the rate of soft tissue fragmentation. By adjusting the tip amplitude, the surgeon could choose a sufficient level of fragmentation [110]. Khambay et al. recorded the applied force during bone cutting by an ultrasonic chisel and concluded that low force was a contributor to optimum cutting with high precision [112, 113]. The use of vibration forces to create a 'microchipping' effect is described by Balamuth et al. for tissue removal in dentistry [73]. In various soft tissues, the effect of mechanical forces in tissue ablation is thought to be shear forces, which result from difference in force levels across the boundary between horn-tip and the surface of soft tissues [20]. Frost and Fill described that ultrasonic penetration by high shearing stresses near the horn tip can lead to flow and creation of a viscous fluid layer [127]. Further tissue disruption may be due to the induced shear forces, particularly in the presence of acoustic streaming where forces will be greatly magnified [126].

It is found that the mechanism of soft tissue removal for ultrasonic applications mainly includes mechanical effects of direct shear and impact and ultrasonic wave components. The mechanism in hard tissue is predominantly related to the mechanical impact and micro-fracture induced by stress waves.

2.3.3 Thermal effects

Another effect observed in the power ultrasonic surgery is ultrasonic heating, which is due to the absorption of the ultrasound wave energy and the mechanical friction between an ultrasonic surgical tip and tissue. Thermal effects are significant contributors to tissue damage, such as protein denaturation and necrosis [20]. Denaturation occurs when proteins in tissue and blood undergo an irreversible physical change at an elevated temperature of more than 40 ℃. Changes in protein folding arrangements occur when tissue is heated and then denaturation happens when the heating is severe, causing gross shrinkage, changed hydration levels and other properties changes [128]. Protein loses its tertiary structure, enzymes are no longer able to support vital chemical reactions and cell death or necrosis occurs [129]. Denaturation and coagulation of the protein in sectioned tissue may be

desirable in certain applications for closing vascular structures and haemostasis, supporting the cutting process [88].

In the process of ultrasonic surgery, an acoustic field is generated by the tip-tissue interaction. The ultrasonic energy is transmitted across the contacting surface of the tissue and into the bulk and a thermal effect is generated due to the ultrasonic energy being absorbed by the biological tissue. Goldman et al. discussed energy absorption during ultrasound propagation in tissue. The absorption coefficient of bone was found to be many times greater than soft tissue in their study [130]. In ultrasound-assisted lipoplasty, the thermal effect by absorption of ultrasonic energy in fatty cells spreads to surrounding tissues which can be infiltrated by liquids at ambient temperature [131]. Humphrey [117] gave expressions to calculate the ultrasonic heating. The acoustic energy removed from the ultrasonic wave by absorption is deposited in the tissue in the form of heat at a rate q_v per unit mass,

$$q_v = 2\alpha_a I \tag{2.8}$$

where I is the intensity of the wave at the measurement location, α_a is the absorption coefficient of the tissue. When the wave propagates through a homogeneous media, its intensity diminishes with distance as a result of acoustic absorption. Attenuation coefficient α and absorption coefficient α_a can be generally used interchangeably. The ultrasonic wave, in the case of a harmonic plane wave, can be characterised in terms of its intensity

$$I = \frac{1}{2}\frac{\sigma^2}{\rho c} \tag{2.9}$$

where σ is the stress/pressure amplitude of the wave, ρ is the density and c is the wave velocity. As a result of the heat deposition, the temperature T at a point in the field initially rises at a rate given by

$$\frac{\partial T}{\partial t} = \frac{2\alpha I}{\rho C_p} \tag{2.10}$$

where C_p is the specific heat capacity at constant pressure. Once the temperature of the medium rises above the ambient value, a number of processes come into play that result in

heat being transferred from warmer to cooler regions mainly by heat conduction. The process can be described by

$$\rho C_p \frac{\partial T}{\partial t} = \nabla \cdot (k \nabla T) + q_v \qquad \textbf{2.11}$$

where k is the heat conductivity.

The ultrasonic cutting process is accompanied by high temperature on the cutting tool surface, which is due to the generation of frictional heat between the tissue and the vibrating tip. It was observed by Brooks et al. that the temperatures produced by power ultrasonic devices penetrating the bone are no higher than the temperatures generated by high speed drills [132]. Koch et al. studied the temperature distribution in soft tissue dissection using a harmonic scalpel. The maximum temperature elevation was detected near the blade [115]. Amaral concluded that the energy produced by a high power ultrasonic dissection system in a laparoscopic application is frictional energy, proportional to both the vibration frequency and the displacement of the instrument tip [88]. Klapper et al. conducted orthopaedic revision arthroplasty using ultrasonically driven tools. The clinical studies indicated that the absorbed energy due to the friction at the interface of ultrasonic tip and polymethylmethacrylate (PMMA) cement and intermolecular friction within the cement mantle alters the structure and mechanical properties of the cement in contact with the surface of the working tool bit and softens the cement. The friction heat can facilitate accelerated cement removal [133]. Dominici et al. analysed the heat generation for post removal in endodontics. The temperature change produced by the ultrasound may be enough to cause damage to the periodontal tissues and the main temperature increase was observed at the contact surface during ultrasonic vibration [134]. Similarly, Nicoll and Peters found the increased temperature was mainly on the dentinal surface during ultrasonic periodontal scaling procedures *in vitro* [135]. Thermal mapping of soft tissues during ultrasonic dissection was performed with an infrared thermal camera by Emam and Cuschieri [114]. The results demonstrated that the frictional heat produced during ultrasonic dissection results in histologic injury of tissues, which depends on the power setting and activation time of the ultrasonic system.

2.3.4 Acoustic Cavitation

When the ultrasonic tip is vibrating with sufficient amplitude and frequency, acoustic cavitation occurs in tissue, typically in liquids and soft tissue because of the large amount of contained water. The expansion and collapse of gas bubbles results in the generation of shock waves [20]. Within a reverberant environment, it is possible to initiate the phenomenon of acoustic cavitation, because threshold conditions for the onset of cavitation are reached easily. Exceptionally high localized pressures and temperatures are produced due to the formation and collapse of bubbles in aqueous tissue.

Propagation of the ultrasonic wave causes alternating compression and rarefaction cycles within tissue. Cavitation occurs during the rarefaction cycle, for example, when the tip is retracted and the particles within the tissue are farther away from one another. If the negative pressure exceeds the tensile strength of the liquid or tissue, the average distance between molecules reaches the critical molecular distance necessary to keep the tissue intact, the tissue tears apart and bubbles can be formed. If the amplitude of the ultrasonic wave is sufficient, bubbles in aqueous tissue will experience several rapid expansions to reach a critical size, several times larger than its initial size. After reaching the critical size a violent collapse of bubbles occurs [136]. Within the region of collapse, several extrme effects can occur, such as an internal bubble temperature of 3000 K, a pressure shockwave emission reaching 6 GPa [137] and a jet-like ejection with velocity up to 700-900 m/s [138].

Cavitational effects in fat tissue result in cell destruction and fat liquefaction during ultrasound-assisted lipoplasty [139]. Coleman et al. considered the violent collapse of the cavitation generated in lithotripsy as a contributor to stone disintegration, as well as contributing to undesirable biological effects such as tissue trauma [140]. Brock et al. found that the jetting effect of the collapsing cavitation bubbles is responsible for the break-down of the tumour in brain tumour surgery using ultrasonic aspiration [141]. Theoretical models were proposed by Brujan for pressures generated in cavitation jets when the bubble collapses close to biomaterials, resulting in fragmentation of dental tartar or intraocular lenses [142].

2.3.5 Other Effects

Other effects, such as acoustic streaming [110, 111] and radiation force [143], have been investigated in the literature. Acoustic streaming is a vigorous circulatory motion produced by oscillating bubbles in a sound field and radiation force is a time averaged force exerted by an acoustic field on an object. These are not direct effects, but secondary physical effects generated by an ultrasonic field in tissue [117]. Generally, although they can contribute to tissue ablation and fragmentation, these secondary effects influence tissue in a small scale producing small forces and motions.

2.3.6 Summary

Although ultrasonic effects on tissue can be categorized into several aspects mentioned above, the relative contribution of each of these remains unclear during power ultrasonic surgery. It requires more detailed evaluation, predictive modelling and experimental investigation of the tip tissue interaction especially in the cases of micro-fracture in hard tissues, energy absorption by tissue during ultrasonic propagation and the damage mechanism of cavitation.

2.4 Measurements of Ultrasonic Effects

Quantitative characterisations of power ultrasonic effects on tissue are required for assessing the performance of ultrasonic surgical devices. Many researchers have investigated the effect of mechanical forces from experimental work and obtained parameters relating to the damage mechanism [110]. These influential parameters include ultrasonic power, horn geometry, tip amplitude and tip pressure [20]. Temperature increases have been estimated using thermocouples to determine the thermal damage during ultrasonic surgical applications [116]. The power ultrasonic thermal effect on tissue is relevant to tissue type, onset of damaging temperature, ultrasonic power setting, type of horn tip used, length of application time and the effect of instrument pressure applied during ultrasonic use. Ultrasonic cavitation bubbles have complex dynamic behaviours, which have been experimentally studied by researchers using high speed cameras [144] or mathematic models [138]. The cavitation in tissue caused by power ultrasound are mainly dependent on tissue water content, applied frequency and power, and tip amplitude.

Apart from researches studying effect of mechanical forces, thermal effect and acoustic cavitation during ultrasonic surgery, it is necessary to study the power ultrasonic wave propagation in tissue, which could cause severe damage inside tissue. The stress field produced by wave propagation in tissue can influence its absorption of ultrasonic energy. The heat produced by the ultrasonic energy absorption can alter the mechanical properties of the tissue. Therefore, the visualisation of ultrasonic stress field and mapping of thermal distribution in tissue are necessary to characterise the damage mechanisms during power ultrasonic application.

2.4.1 Visualisation Techniques of the Ultrasonic Field

Power ultrasonic fields are extremely difficult to characterise, as not only can mechanical impacts cause damage to the measurement instrumentation being used, but cavitational bubbles can also destroy or scatter the acoustical signal under investigation. In particular, insertion or embedment of measurement instruments into tissue can change its structure and disturb the ultrasonic wave propagation. Thus measurements should be obtained under non-invasive conditions. Conducting non-contact optical measurements in tissue can be used to identify stress distribution experienced during power ultrasonic applications [145].

Firstly, existing methods of experimental characterisation of ultrasonic fields are reviewed. Secondly, non-invasive optical methods for visualising ultrasonic fields are introduced. These optical methods are helpful for understanding the physics of ultrasound wave propagation and the interaction of ultrasound and tissue.

2.4.1.1 Hydrophones

Traditionally, the principal devices for field characterisation of medical ultrasound are piezoelectric hydrophones, which operate based on piezoelectric effects that generate an electrical signal when subjected to a pressure change. Fibre optic hydrophones, one of the first application of fibre optic sensing in the late 1970s [146], are utilised to characterise ultrasonic fields by measuring the phase change of the light travelling in an optical fibre due to the strains developed in the fibre by the applied ultrasonic pressure. Therefore, the types of hydrophone for measuring and evaluating the ultrasonic wave emitted from an ultrasonic probe in gases and fluids include piezoelectric ceramic hydrophones, piezoelectric composites, piezoelectric polyvinylidene fluoride (PVDF) hydrophones and fibre optic hydrophones.

Piezoelectric Ceramic Hydrophones

A conventional piezoceramic hydrophone (Fig. 2.11) consists of lead zirconate titanate (PZT) as an active piezoelectric element, a backing block and a matching layer. The matching and backing layers are optimised to widen bandwidth and increase measurement sensitivity [147]. Two electrodes are deposited on opposite faces of the piezoelectric element to detect and sense the incident mechanical wave and generate the charge within the material. A visual representation of the acoustic waveform can be observed as a voltage on an oscilloscope by amplification of the acquired electrical signal.

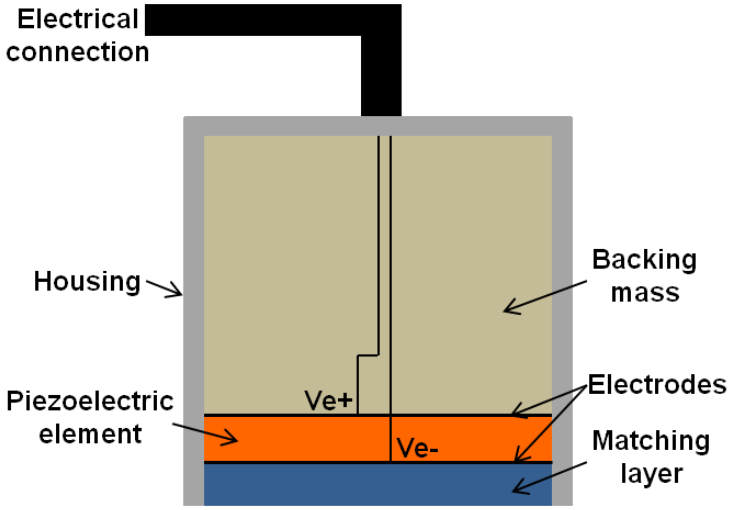

Fig. 2.11 Schematic of piezoelectric ceramic hydropone

The early use of piezoceramic hydrophones was during World War I, by convoy escorts in detecting U-boats, which greatly impacted on the effectiveness of submarines [148]. The hydrophone was designed to have features of relatively non-perturbation at higher frequency, uniform frequency response over the bandwidth, maintaining reasonable sensitivity and a good acoustic impedance match to water. However, the stiff and dense piezoelectric element also has the disadvantages of poor acoustic coupling to water, limited bandwidth and spurious modes dependent on physical geometry [145, 149]. Therefore, new materials with improved piezoelectric properties and better qualities for hydrophone applications, obtained by introducing inhomogeneities into piezoelectric ceramics and polymers have been investigated and tested.

Piezoelectric Composites

Typically, a piezoelectric composite is a combination of a piezoelectric ceramic as the active phase and a non-piezoelectric polymer as the passive phase to form a new piezoelectric material [150]. By changing the ceramic/polymer volume ratios, the piezocomposite transducer can efficiently transmit acoustic energy into the medium. Compared with conventional monolithic dense materials, piezocomposites have potential for increased bandwidth, lower acoustic impedance, higher piezoelectric constants and higher electromechanical coupling co-efficients [151]. The benefits of piezocomposites make it a preferential choice for many hydrophone applications, particularly at lower ultrasonic frequencies.

Coupled with matching layer and backing block technologies [147] piezocomposites can be fabricated in various connectivities such as 0–3, 1–3, 2–2 and 3–3 architectures. Connectivity is defined as the number of dimensions through which the material is continuous and the first digit refers to the piezoelectrically active phase. Smith reviewed piezocomposites in ultrasonic transducers on various arrangements of connectivities and found 1-3 and 2-2 connectivities are more useful for transducer applications [150].

Since it was invented by Newnham and Cross in the late 1970's, the 1-3 composite has been studied extensively. Today, it is the major piezocomposite on the market for ultrasonic transducers, actuators and sensors [152]. It can be manufactured by a dicing process of ceramic with a filled epoxy resin polymer. In 1-3 composites (Fig. 2.12), the ceramic is cut orthogonally in the form of elongated pillars or rods, connected continuously in only one direction, which were surrounded by the polymer matrix connected continuously in 3 directions [145].

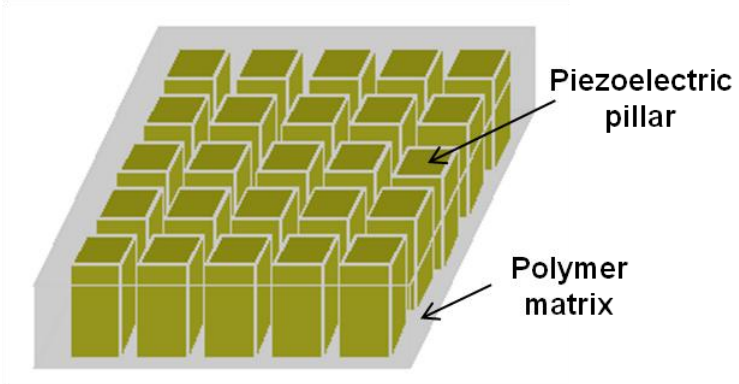

Fig. 2.12 Schematic of a 1-3 piezoelectric composite

Although it has improved piezoelectric properties and better qualities than the piezoceramic hydrophone, the piezocomposite hydrophone also perturbs the ultrasonic field when the hydrophone is inserted into the field. However, the problem can be overcome by the use of an alternative piezoelectric polymer, polyvinylidene fluoride.

Polyvinylidene Fluoride (PVDF) Hydrophones

The polymer PVDF has a strong piezoelectric effect for pressure to voltage conversion, which was discovered by Kawai in 1969 [153]. A small piece of piezoelectric PVDF film can be attached and electrically contacted to the surface of a hydrophone to work as the pressure sensitive element of the measuring instrument. The main advantages of a PVDF hydrophone over a ceramic one are better acoustic impedance matching condition to water and tissue, smaller physical size, configuration in flexible probe and membrane types, flat frequency response over a wide frequency. It is used as a "gold standard" in the characterisation of low intensity medical ultrasonic fields in water [145]. Due to minimal disturbance and diffraction effects to the investigated acoustic field, it can be used as an alternative in high power ultrasonic applications when used below the cavitational threshold.

PVDF hydrophones can be constructed using either membrane or needle designs (Fig. 2.13). One design of PVDF membrane hydrophone is known as the hoop-supported membrane approach. It consists of an annular frame with a diameter of 100 mm and a 9 μm thick sheet of PVDF stretched and mounted onto the frame. Gold or chromium electrodes are vacuum deposited at the centre of the film surface to work as active elements with diameters in the range of 0.2-1.0 mm [154]. Due to being thin compared to the acoustic wavelength and having a matched acoustic impedance with water, the membrane has a negligible effect on an ultrasonic field under investigation. A typical PVDF needle hydrophone has an active element made of PVDF film (500 μm diameter and 15 μm thickness) mounted onto the end of a hollow cylindrical tube, which has a diameter of 600 μm and is filled with an acoustically absorbing material. The backing material inside the hollow tube has a higher characteristic impedance than water and the membrane [154].

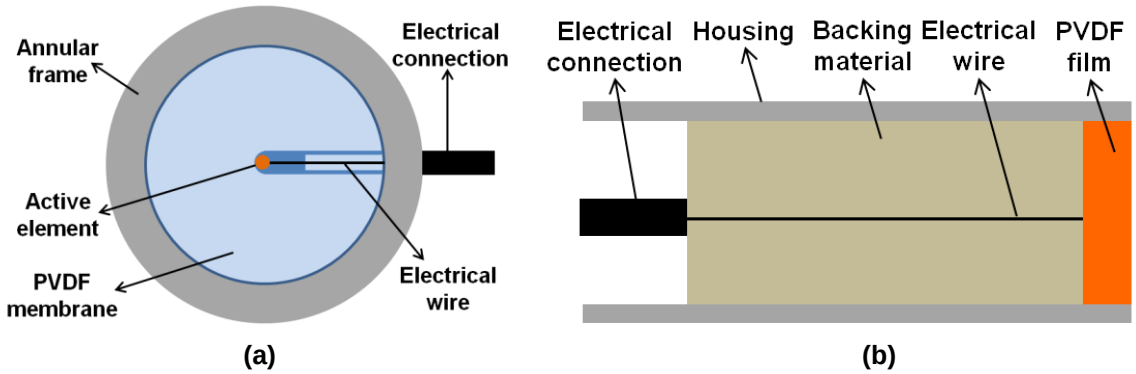

Fig. 2.13 Schematic of (a) needle type (b) membrane types PVDF hydrophone

An important advantage of the membrane hydrophone over the probe device is that the connecting cable does not pass through the ultrasound field. Consequently, the hydrophone neither perturbs the field nor adds to the received signal as a result of piezoelectric activity in the cable [155]. A needle hydrophone is more suitable for certain application *in vitro* and measuring field distribution in confined spaces [156].

The main drawback of PVDF as a hydrophone is its susceptibility to noise. The cavitational activity and temperature rises induced in power ultrasonic applications can readily damage PVDF hydrophones.

Fibre Optic Hydrophones

A fibre optic hydrophone consists of light from a laser diode coupled into a glass fibre with the end placed into the load medium. A fibre optic hydrophone is also referred to as a laser optic probe hydrophone, in which the ultrasonic pressure wave modulates the refractive index of the fluid in front of the tip of the fibre, leading to a change in reflectivity that can be measured with a photodiode at the other end of the fibre [154]. A more subtle design has a thin polymer film deposited onto the front of the tip of the fibre to sense the acoustic change. The photodiode detects the light reflected back along the core from the polymer/medium boundary. This type of fibre-optic hydrophone (Fig. 2.14) works on the principle of interferometric detection of changes in the optical thickness of a thin polymer film at the tip of the optical fibre sensor downlead [157].

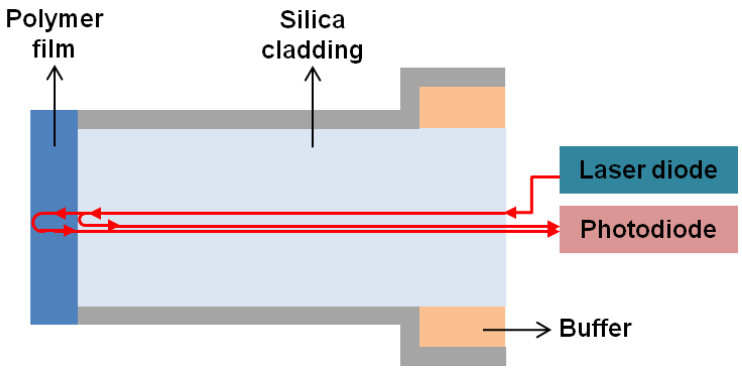

Fig. 2.14 Schematic of a fibre optic polymer film hydrophone

Power ultrasonic field measurement by fibre-optic hydrophones has the potential to overcome some problems associated with conventional ceramic, piezocomposite and PVDF hydrophones. A fibre optic hydrophone has small element size and significantly higher sensitivity than others of comparable dimensions. In addition, being capable of resistance to bubble collapse, it may withstand cavitation activity [157].

Summary

Although various hydrophones are available for ultrasonic field mapping, many hydrophones suffer from a lack of uniform response over a wide range of frequencies while still maintaining sensitivity, particularly below 200 kHz where power ultrasonic applications operate. Furthermore, any measurement device must be robust enough to withstand the vibration associated with high power ultrasound measurement. To attain increased levels of sensitivity, spatial resolution and non-invasiveness, hydrophone devices are generally quite delicate and fragile in nature, which can be easily damaged by power ultrasound. Thus there is limited literature on the use of hydrophones for the measurement of acoustic fields generated by high power applications [145]. Finally, as hydrophones are designed to be used in gases or fluid, they are poor for measuring ultrasonic fields in solids. Therefore, it is necessary to conduct the measurements using non-invasive techniques.

2.4.1.2 Non-invasive Techniques

To remove the perturbation caused by a hydrophone, quantification of the ultrasonic field can be performed without the insertion of a sensor. Several optical methods are available to provide information of ultrasonic fields without physical interaction, including Schlieren photography, interferometry and digital image correlation with an ultra-high speed camera.

Schlieren Photography

In 1935, Raman and Nath firstly proposed that ultrasonic waves behave like a phase grating to a propagating light wave [158]. The phase grating results from the fact that ultrasonic waves produce a periodic density variation in the medium and thus a change in the optical refractive index of the medium. As a traditional qualitative technique, Schlieren imaging of ultrasonic waves produces the visualisation of ultrasonic fields in a transparent medium, based on the detection of changes in the optical refractive index due to ultrasonic wave induced variation of the density of the medium. The intensity of the diffraction pattern is proportional to the integral of pressure along the light path. Appropriate optics can be used to allow the formation of an image of the phase grating on a film or a video array. The video gray level intensity in an image is related to the pressure (acoustic intensity) integrated over the light path [159].

Schneider and Shung did a quantitative analysis of pulsed ultrasonic beam patterns using a Schlieren optical system based on the principle of optical diffraction. The results of temporal average acoustic intensity over the light path were obtained, which were in good agreement with that obtained by the hydrophone [159]. Kudo et al. used Schlieren imaging to monitor ultrasonically induced changes in refractive index. The ultrasound field was visualised using a CCD camera and a simple image processing method instead of the complex Schlieren optical setup. Good agreement was found between the simple Schlieren imaging measurement and simulation [160].

Schlieren imaging offers a fast, accurate and non invasive detection of the whole pressure field and is an alternative to hydrophone measurement. However, the technique has limitation in accuracy for evaluating a 3D ultrasonic field because a 2D Schlieren image is given by the integral of 3D pressure intensities. In addition, due to its sensitivity to phase distortion of light, the Schlieren method requires high quality optical elements and a transparent medium which prevents its operation with an opaque load fluid or solid.

Interferometry

The principle of interferometry is based on the optical interference observed when two coherent light beams, reference and measurement, are made to coincide onto a photo detector. From the interference detected, the frequency and phase difference between the

measurement and reference beam can be determined. Hence, interferometry can be used as a measurement technique in quantify the phase alteration due to acoustic fields.

A laser Doppler vibrometer is typically used to determine time variant velocity of a reflective surface in motion by measuring the Doppler frequency shift of the reflected light to provide displacement amplitude measurements through the use of a phase detector. The laser vibrometer has been used with great success in experimental modal analysis which is a widely used technique to determine the parameters of resonant vibration in terms of modes of vibration, defined by natural frequency, mode shapes and damping factors. Through a laser scanning procedure, a laser vibrometer can be utilised to map the mode shapes of the whole resonant vibrating structure.

In addition, the signal of a laser vibrometer is sensitive to the strain of a transparent medium due to the acousto-optic effect. Another use of a laser vibrometer is to measure the average change in refractive index through the width of the laser beam. Through a complete scan, the technique can provide a reasonably accurate spatial representation of acoustic intensity distribution.

The use of a scanning laser vibrometer for sound measurements was proposed by Zipser and Lindner in 2000 [27, 161]. The acoustic field of an ultrasonic transducer in water was mapped by Mattei and Adler using a laser vibrometer based on the acousto-optic effect with a tomographic reconstruction of acousto-optic profiles [162]. Henderson et al. utilised the acousto-optic modulation of an optical path to measure the phase velocity and attenuation of a longitudinal plane elastic wave in a transparent solid media, polymethylmethacrylate (PMMA). The method provides averaged measurements inside the object not limited to the sample surface, which has the potential for use in acoustic tomography of a transparent solid medium [163].

This methodology also suffers from the same difficulties as Schlieren imaging as a transparent medium is needed. If the structure is not resonating in a steady state, the ultrasonic field is time dependent, thus due to data was not simultaneously collected during the scanning procedure, the full-field transient displacement and pressure/stress cannot be extracted using a laser vibrometer.

Ultra-high Speed Camera

Bond and Cimino [111] investigated the interaction between the ultrasonic horn tip and the surface of tissue using high-speed photography. Visual observations of the tip-tissue interaction and separation were obtained. In a study carried out by Simon et al., cavitation bubbles in a HIFU application of tissue fragment were observed using high speed photography [164]. These results were applications of high speed photography in capturing transient response of ultrasonic vibration. They did not use image processing analysis to investigate the ultrasonic field in the tissue.

There are many applications using ultra-high speed cameras with digital image correlation (DIC) technique, a kind of image processing analysis, for visually measuring and evaluating the high-strain rate impact loading of structures and resonant vibrating structures to track the deformation of specimens to impact loading and to study the mechanical behaviour of specimens to dynamic loading. Barthelat et al. [165] studied the response of nano-crystalline-coated thin-walled cylinders subjected to high strain rate torsional loading using an ultra-high speed camera along with two-dimensional DIC. Tiwari et al. [166] used this technique to track deformation in a split Hopkinson pressure bar during impact loading. Kirugulige et al. investigated dynamic crack growth behaviour of a polymeric beam subjected to impact loading by DIC combined with a rotating mirror type high speed digital camera [167]. These studies all focused on the high strain rate behaviour of test pieces, but characterisations of high frequency cyclic loading have not previously been reported. DIC has been used previously for vibration measurement by Helfrick et al. [168], in a study to determine the natural frequencies and mode shapes of a dryer-cabinet panel. The measurements were in a low frequency range and the DIC results were compared with those obtained using a scanning laser Doppler vibrometer. As well as successfully using DIC to record surface vibration responses, the authors of this study noted that the highest measureable frequency is largely dictated by the camera used and, importantly, the vibrating structure must excite displacements that are larger than the noise level of the measurements. Siebert et al. [169] carried out experiments using a high speed digital image correlation technique for vibration mode shape analysis at low harmonic loading frequencies (59.9 and 36.5 Hz). Wang et al. [170] applied high speed digital image correlation technique to measure displacement responses of a complex car bonnet surface under random excitation from 0 to 128 Hz for identifying modal properties. These vibration tests were not applications using ultrasonic frequencies. Therefore, it is necessary

to explore the possibilities for detection of power ultrasonic field using an ultra-high speed camera. Images were recorded in a short time to capture the motion of the vibrating structure. With the use of image processing technique, steady state or transient response of ultrasonic vibration can be characterised.

The ultra-high speed camera along with image processing analysis can be used to study both the steady-state response and transient build-up of vibration in a solid. Results are obtained for full field in a short time. However, there are some disadvantages in the use of this technique including requirements of additional image processing programs, surface preparation of the test sample and high intensity light.

2.4.2 Measurements of Temperature Field during Ultrasonic Vibration

Thermal damage occurring in ultrasonic surgery has been experimentally characterised by researchers using insertion of thermocouples or infrared thermography.

Huttula et al. measured root surface temperature changes when ultrasonic vibration was applied to cemented endodontic posts by positioning thermocouples at locations on the proximal root surfaces. A trend for higher temperatures was observed at thermocouples of non-irrrigated teeth. Irrigation had a significant impact on minimising the risk of thermal injury to the surrounding periodontium and bone during post removal with ultrasonics [171].

Goldberg et al. conducted bone cement removal with use of an ultrasound device during revision arthroplasty on cadaveric specimens. In their study, t-type thermocouples were placed on locations including the humeral cortex, the triceps muscle and the radial nerve around the ultrasonic cutting sites to measure temperature. They found the temperature in the humerus, the triceps and the radial nerve can reach to potentially dangerous levels, because cellular injury and necrosis had been established in the tissue. To limit the thermal damage, intermittent cold irrigation of the canal between passes of the ultrasonic device was applied [116].

In an attempt to prove the hypothesis that an ultrasonically activated scalpel provides a system that is able to enhance surgery without damage, infrared video thermography was used for *in vivo* and *in vitro* research studies. Temperature changes at and around the

ultrasonic activated blade or the tip of an electric cautery probe were investigated under various conditions. It is concluded that the risk of tissue damage is minimized by the use of an ultrasonic scalpel [91].

An infrared camera was used to record precise heat tissue mapping during ultrasonic dissections *in vivo* on a pig model by Emam et al. to investigate the effect of ultrasonic energy and the extent of residual tissue damage. They found that the regions with temperatures greater than 60 ℃ were located at the ultrasonic dissector shaft, cutting jaw and distances up to 25 mm from the instrument action spot during 10-15 second action. The thermal damage could be reduced when a low level of power is set and action time did not exceed 5 seconds at any one time [114].

Reduction of thermal damage during ultrasonic surgery is one of the main concerns of surgeons. Researchers measured the temperature elevation caused by mechanical friction, energy absorption and cavitation. Studies of heat generation during absorption of ultrasonic energy in ultrasound assisted surgery are lacking in the literature. Therefore, this project will focus on the study of thermal damage induced by absorption of ultrasonic energy. Due to interaction of the ultrasonic vibrations and the thermocouples not only causing erroneous measurements of test specimen temperatures but also producing localized heating in the specimen being monitored, the technique of non-contact thermal imaging was used in this study.

3. Power Ultrasonic System Design

This chapter introduces the work that was done on the design of the power ultrasonic system for this project. There are two sections in the chapter: introduction of piezoelectric transducer and the design of ultrasonic horns. In Sec. 3.1, a brief introduction of piezoelectric transducers, with special emphasis on high power ultrasonic transducers is given. Sec. 3.2 is related to the design of ultrasonic horns, which is based on finite element calculations (a modal analysis) of the designed resonance frequencies with corresponding eigenmodes of the horns. Dynamic modal analysis is discussed as the characterisation method to check experimentally the performance of ultrasonic horns. A test rig was designed to conduct the power ultrasonic vibration tests, which is discussed in Sec. 3.2.

3.1 Piezoelectric Transducer

3.1.1 Introduction

One of the most important parts in a power ultrasonic instrumentation system is the transducer, which is capable of converting electrical energy to acoustic energy for generation of ultrasonic waves. The two main types of transducers used in power ultrasonic applications are the magnetostrictive and piezoelectric transducers. The most commonly used are piezoelectric transducers.

The active element of the piezoelectric transducer is basically a piece of polarised material with electrodes attached to two of its opposite faces. When a voltage (V_e) is applied across the material, some parts of the molecule are positively charged, while others are negatively charged, therefore the polarized molecules will align themselves with the electric field generated by the voltage, resulting in induced dipoles within the material. The rearrangement of the molecules will cause the material to undergo a mechanical deformation. Conversely, a voltage can be produced as a result of an imposed mechanical stress (F) on the polarised material. These phenomena are known as the inverse and direct piezoelectric effects (shown in Fig. 3.1, where the poling axis represents the direction of piezoelectric effect), which are the basic functional principles of piezoelectric transducers. If a rapidly alternating voltage is applied, the piezoelectric material will vibrate at the same frequency as the applied voltage, which results in the production of ultrasonic vibration.

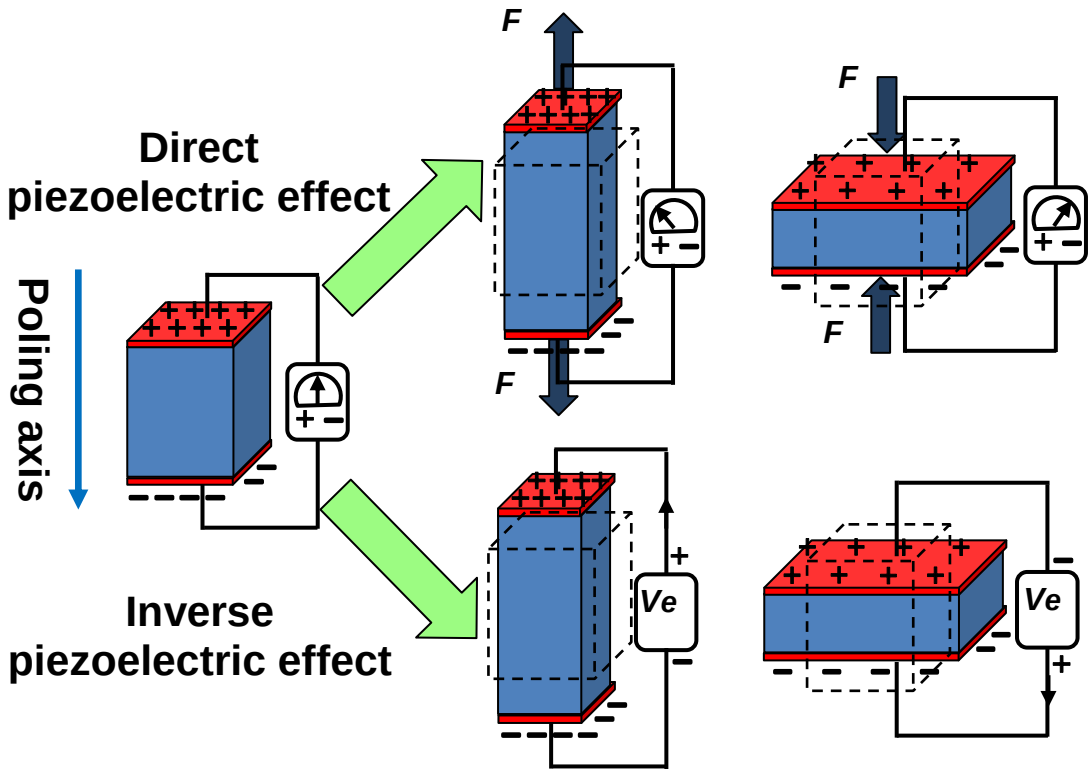

Fig. 3.1 The direct and inverse piezoelectric effect [172]

Materials demonstrating the piezoelectric effects include natural materials such as quartz and Rochelle salt or manufactured piezocomposite, such as lead zirconate titanate and barium titanate. Originally used in devices such as the very early types of underwater ranging equipment, quartz is not a particularly good material for power ultrasonic applications due to its mechanical properties, it is a somewhat fragile and difficult to machine. Currently, the PZT is one of the most frequently employed piezoelectric ceramics exhibiting better performance in power ultrasonic applications. To manufacture the piezoceramic, a suitable ferroelectric material, which is composed of a multitude of randomly oriented crystals, is firstly fabricated into the desired shape and attached to electrodes. Then, a strong direct current field is applied when the material is heated to Curie temperature. This is the process of polarisation. The polarisation of the material makes it into a piezoelectric ceramic with piezoelectric properties.

3.1.2 High Power Piezoelectric Transducers

Normally, piezoelectric transducers are designed to operate in a frequency range between 20-100 kHz to obtain higher output intensities in power ultrasonic application. Most transducers are designed to be driven at a resonance frequency for maximising vibration amplitudes and are generally half-wavelength units.

The piezoelectric transducer is a combination of different parts and materials. The most common type of piezoelectric transducer, called a Langevin transducer, is assembled in a sandwich form, in which piezoelectric components are embedded between electrodes and pre-stressed by two metals (front matching mass and backing mass) using a central bolt. Langevin transducers are specially designed for high power ultrasonic applications and mainly have two types of materials: piezoelectric materials representing the vibration generator and metals for the vibration transmitter.

For this high power application, PZT-8, a hard piezoceramic material with desirable properties, is used in the piezoelectric transducer. It can withstand high electrical driving and intensive mechanical load. It offers extremely high mechanical strength, high resistance to depolarization under mechanical stress, high electromechanical coupling factor and low dielectric losses under high electric excitation. The high Curie temperature of around 300 ℃ is also suited for high voltage and high power generator [173]. Several ring shape PZT-8 components are stacked in the Langevin transducer with a central pre-stressed bolt. The dimensions of these components are designed based on the output acoustic power required, the operating mode of vibration and the type of transducer model. The front and back materials are titanium alloys, which have high fatigue strength and good acoustic properties. These metals are designed to guide most of generated vibration towards the front mass rather than back mass achieving efficient transmission of acoustic energy from PZT ceramics.

The structure of a Langevin transducer is shown in Fig. 3.2, in which two polarised piezoceramic rings are sandwiched between front matching mass and back mass. The electrodes, used for applying the excitation voltage, are attached between the rings and the backing and matching layers. The polarisation directions of the pair of the rings are opposite to enable parallel switching under simultaneous opposing electric fields by the paralleled electrodes. The whole structure of the transducer is clamped by a bolt through the centre of the assembly. The central bolt is tightened to provide a precise amount of compression preventing the ring failure, reducing transducer losses and stabilizing the operating frequency, which are important to the proper operation of the transducer. A polymer is used as the insulating material to insulate electrically the central bolt from the rings. An ultrasonic horn or tool is fixed to the transducer by a stud.

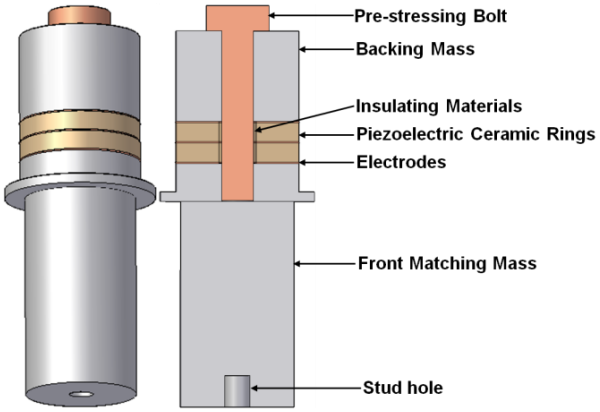

Fig. 3.2 A Langevin transducer

3.1.3 Transducer Characterisation

The power ultrasonic transducer used in this study was designed and manufactured by Sonic System Ltd, UK. The piezoceramic rings are made of PZT-8, and the backing and matching layers are titanium alloys, the electrodes are copper and the central bolt is steel. The tuned device operates in a longitudinal mode at the resonant frequency around 20 kHz. To characterise this transducer, the resonant frequency and the maximum output amplitude were measured when it was in harmonic excitation.

To obtain the resonant and anti-resonant frequencies, using an impedance analyser is a good method of measuring the specification of the transducer. The test was conducted using an Agilent 4294A precision impedance analyser (Fig. 3.3), which has sweeping frequency ranging from 40 Hz to 110 MHz and resolution down to 1 mHz. In this application, the sweeping frequency was set between 18 kHz to 34 kHz with resolution of 5 Hz and the experimental impedance-versus-frequency diagram is shown in Fig. 3.4, in which resonant and anti-resonant frequencies are both illustrated.

Fig. 3.3 Agilent 4294A precision impedance analyser

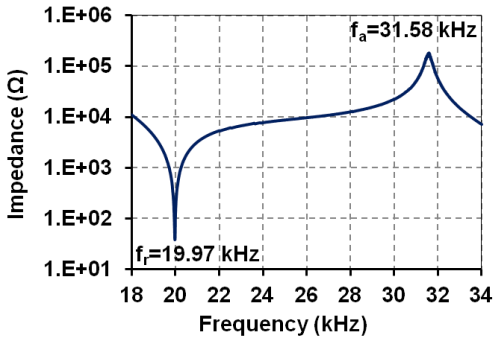

Fig. 3.4 Resonant (f_r) and anti-resonant (f_a) frequencies of the transducer

The resonant frequency of the transducer in 1st longitudinal mode obtained from the test is 19.97 kHz, which is quite close to the desired frequency, 20 kHz. Using a laser Doppler vibrometer, the measured maximum peak to peak output amplitude of the transducer is 12 μm, which is not sufficient for this power ultrasonic application.

3.2 Design of Power Ultrasonic Horn

3.2.1 Introduction

Generally, ultrasonic energy generated by a piezoelectric transducer is transmitted from the transducer to the test piece by an ultrasonic tool in a power ultrasonic system. Due to the transducer cannot excite sufficient vibration amplitude to load the test sample, the ultrasonic tool is a key component of the ultrasonic system, acting as a vibration amplifier by providing the necessary amplitudes of vibrations to induce desired effects on the test sample.

The component placed between the piezoelectric transducer and the test sample for augmenting vibration amplitudes is termed the horn. The ultrasonic horn is commonly a solid metal rod with a round transverse cross section. Commonly used ultrasonic horns driven at resonance are designed in tapered shapes such as conical, catenoidal, exponential, stepped, or more complex shapes (Fig. 3.5), with the tip area smaller than the base. These horns decrease in cross-sectional area to concentrate the ultrasonic energy in the direction of the load to amplify the vibration.

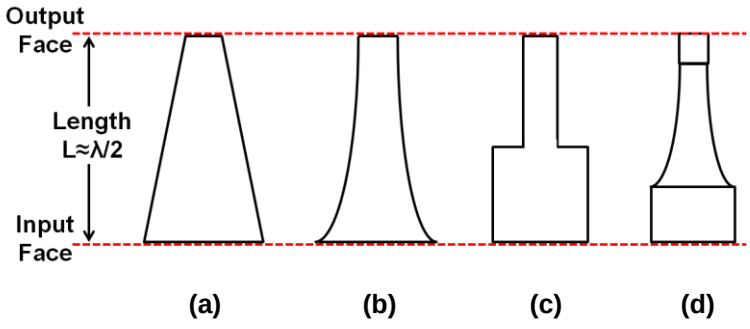

Fig. 3.5 Typical shapes of ultrasonic horns (a) conical (b) catenoidal or exponential (c) stepped (d) complex

The construction of each part of the horn is crucial for good performance. Generally, to drive longitudinal oscillation, the horn vibrates at longitudinal resonance frequency the same as the transducer, which is typically connected to the base (input surface) of the horn

using a threaded stud. The tip (output surface) of the horn is usually used for contact with the sample. The dimension of the base is restricted by the size of the transducer stack. The size of the tip depends on the dimensions of the test sample in contact with the horn. Although widely used and able to provide high ultrasonic amplitudes, the conventional rod-type horns mentioned above suffer from an important limitation: they are incapable of providing a large contact area to interface with the test sample. In this work, due to a large cross-sectional area of output face required, a novel rod-type horn was designed and manufactured with high magnification and large output surface to transmit efficiently ultrasonic energy into tissue mimicking materials.

3.2.2 Design of the Horn

Traditionally, the methods used for the horn design are based on the equilibrium of a element under elastic forces and integration over the horn length to achieve resonance. The applied excitation from the transducer can be effectively transmitted, when the designed horn vibrates at or particularly close to its resonance frequency. The horn should be designed properly and manufactured accurately to achieve satisfied vibration transmission.

To ensure a reliable performance of the horn, several performance criteria should be satisfied in the design of the ultrasonic horn including resonant frequency at close to the operating frequency of the transducer, high vibration amplitude of the operating mode, isolation of the operating frequency from close non-tuned modes and high amplitude uniformity at output surface.

3.2.2.1 Resonant Frequency

To effectively apply vibration on the test sample, the horn must be properly designed to vibrate at or particularly close to the transducer resonance frequency. In the case of longitudinal mode horn it is common to design the horn working at the first longitudinal vibration mode where the highest amplitude can be obtained. The resonance frequency of the horn is mainly determined by the length of the horn [173]. Normally, a horn is designed to be a half-wavelength in length. When designing an ultrasonic horn, the operating frequency of the transducer f can be used to calculate the horn length l. If the horn has a uniform cross section, it can be obtained by:

$$l = \frac{\lambda}{2} = \frac{c}{2f} = \frac{1}{2f}\sqrt{\frac{E}{\rho}} \quad \textbf{3.1}$$

where λ and c are the wavelength and the velocity of the longitudinal wave, and the velocity of the wave c is found:

$$c = \sqrt{\frac{E}{\rho}} \quad \textbf{3.2}$$

where E is the Young's modulus and ρ is the density of the material. However, for a non-uniform cross-sectional horn, such as an exponential horn, the horn length of half-wavelength pattern can be calculated:

$$l = \frac{\lambda}{2} = \frac{c}{4\pi f}\sqrt{(2\pi)^2 + (\ln n)^2} \quad \textbf{3.3}$$

where n is the ratio of the output surface to the input surface radius. For the horn with complex shapes, the equations cannot be utilised directly to calculate the exact overall length. Therefore, to ensure the resonant frequency of the horn at close to the operating frequency of the transducer, finite element analysis is now used for the design of the ultrasonic component.

There are several parameters to be considered in the design of the horn including output face area, gain, tuning frequency and output surface uniformity of vibration amplitude. For an optimal operation of an ultrasonic horn system, the maximum cross-sectional dimension of any part of the rod-type horn should be less than about a quarter-wavelength of the corresponding longitudinal acoustic wave at the horn's resonance frequency [174, 175].

3.2.2.2 Vibration Amplitude

Vibration amplitude can be defined as the peak-to-peak displacement of the horn at its output surface. In some power ultrasonic systems, the amplitude is a dependent variable related to the power applied to the system and gain factor. If the applied power is being set and controlled, an alternative approach to improving vibration amplitude is investigated by making the horn with high gain. The gain of the horn can be defined as the ratio in vibration amplitude between the output surface and the input surface. Normally, the gain is

dependent on the rate of change in cross-sectional area from the input surface to the output surface. The horn profile mainly affects the magnification. Therefore, modification of the cross-sectional area between the input and output surfaces of the horns leads to a change in vibration amplitude and subsequently induces an alternation of the gain.

The modal frequency of a column depends on its length, while vibration amplitude and gain are sensitive to width variation. It is possible to reduce the column widths whilst maintaining the horn global dimensions by incorporating a number of slots in the horn. For this application, requiring high vibration amplitude and large output surface, slotted rod type horns are designed and used, but these are prone to modal coupling at the operating frequency.

3.2.2.3 Frequency Separation

Modal frequency separation of the horn response is important in examining the performance of the horn. To avoid the coupling of the resonant frequency at the operating frequency, it is necessary to maximise the spread between the tuned and non-tuned modal frequencies of the horn. In this application, the horn requires a pure longitudinal vibration mode with a good separation from torsional and bending vibration modes. It is suggested that the frequency separation should be at least 1 kHz from the longitudinal mode frequency. Modal coupling at the operating frequency can induce distortion in horn movement, reduction of horn gain and poor uniformity of vibration amplitude at output surface. It is not easy to improve the frequency separation of the slotted rod-type horn due to the inclusion of additional slots, which may lead to a reduction of the separation by any change in dimensions of these slots. Finite element analysis can be used to design a horn with good frequency separation.

3.2.2.4 Uniformity of Vibration Amplitude

In order to operate the horn effectively with high amplitude gain, high uniformity of vibration amplitude should be achieved at the output surface of the horn. The vibration amplitude uniformity of the horn can defined as

$$Uniformity = \left[\frac{U_d}{U_D}\right] \times 100\% \qquad \textbf{3.4}$$

where U_D and U_d are the maximum and minimum amplitudes of the ultrasonic vibration on the horn output surface. The vibration amplitude uniformity requirement is estimated to be 80%. To achieve uniform amplitude distribution on the output surface of the horn, finite element analysis and optimum design can be used for the design of an ultrasonic horn [176].

3.2.2.5 Design of a Slotted Rod-type Horn

The first consideration in the horn design is the geometry. The length of a column, the first attempt of the horn, was calculated using equation 3.1, when the material properties and desired resonant frequency were determined. The resonant frequency of a column uniquely depends on its length, but vibration amplitude is sensitive to cross-sectional variation. Then, the column was cut into multi-element rods, which have cylindrical elements and elements of variable cross sections. The complex structure of the multi-element horn made its length from the base to the tip not only determines the frequency of resonance but also affects the gain. The rod model is well suited to determine the approximate vibration behaviour, provided that the maximum cross-sectional dimension of the horn is less than a quarter wavelength of the operating frequency. The cross sections of the horn's input and output surfaces are restricted by the transducer output surface, which is connected to the base of the horn and the dimension of the test specimen, which is contact with the tip of the horn. The horn input surface area with a diameter of 38 mm was same as the diameter of the transducer output surface, in order to achieve interface continuity and transfer ultrasonic energy efficiently. The output surface area with a diameter of 50 mm was designed to contact with the test sample, whose cross-sectional dimensions were 40 mm by 25 mm. The cross-sectional dimension of the output surface is larger than the input surface. To obtain high vibration amplitude at the output surface and high gain factor, thus it is possible to reduce the element cross-sectional area whilst maintain the horn global dimensions by incorporating a number of slots. Two symmetrical triangular cuts were taken from the cylindrical element to reduce the cross sectional area from the base to the tip. To avoid high stress concentrations, fillets were fabricated at the junction in the region where the diameter changes abruptly.

Another consider consideration is the material selection for the ultrasonic horn, which was very important to ensure it works correctly and achieves maximum efficiency [177]. Aluminium alloy (6082) was selected for the horn due to its high mechanical quality

factors, such as strength and durability. The properties of the material are listed in Table 3.1.

Table 3.1 The properties of the horn material [177]

Aluminium alloy 6082	
Ultimate strength	500 MPa
Endurance limit	225 MPa
Young's modulus	72 GPa
Density	2660 kg/m^3
Speed of sound	5200 m/s
Wavelength	252 mm
Acoustic impedance	13.86×10^6 kg/m^2 s
Quality factor	3333

For this application requiring high amplitude of vibration as well as high amplitude uniformity, a triangular slotted horn with multi-element rods was designed (shown in Fig. 3.6) which was operating at longitudinal resonant frequency close to 20 kHz, the operating frequency of the transducer.

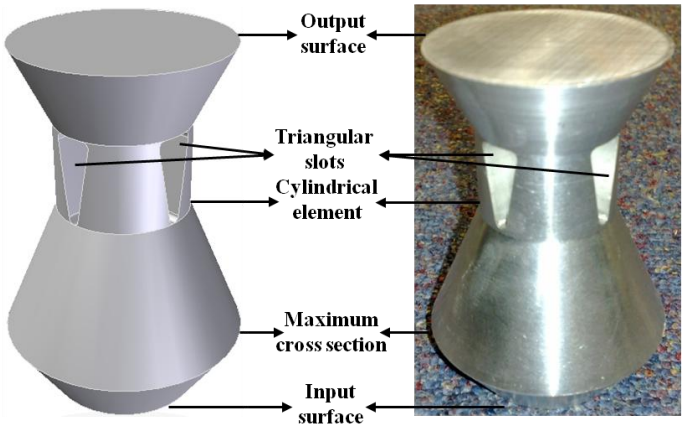

Fig. 3.6 The triangular slotted horn with multi-element rods (a) the drawing (b) as manufactured

To design the horn resonated at the desired frequency of longitudinal mode with high gain and uniformity, finite element models were created using ABAQUS software. Natural frequency and steady state dynamic analyses were used to predict the resonant frequencies, the mode shapes, the amplitude uniformity, gain factor, frequency separation and amplitude uniformity of the models. A multi-element rod type horn operating close to 20 kHz with the maximum lateral dimension less than a quarter wavelength and a length of around a half wavelength was designed and manufactured using aluminium alloy for this application. Experimental modal analysis (EMA) is then required to validate the results

found from the finite element models. The horn configurations were finalised when they satisfied the performance criteria in both the predicted models and the experimental tests. The process of ultrasonic horn design is detailed in Fig. 3.7.

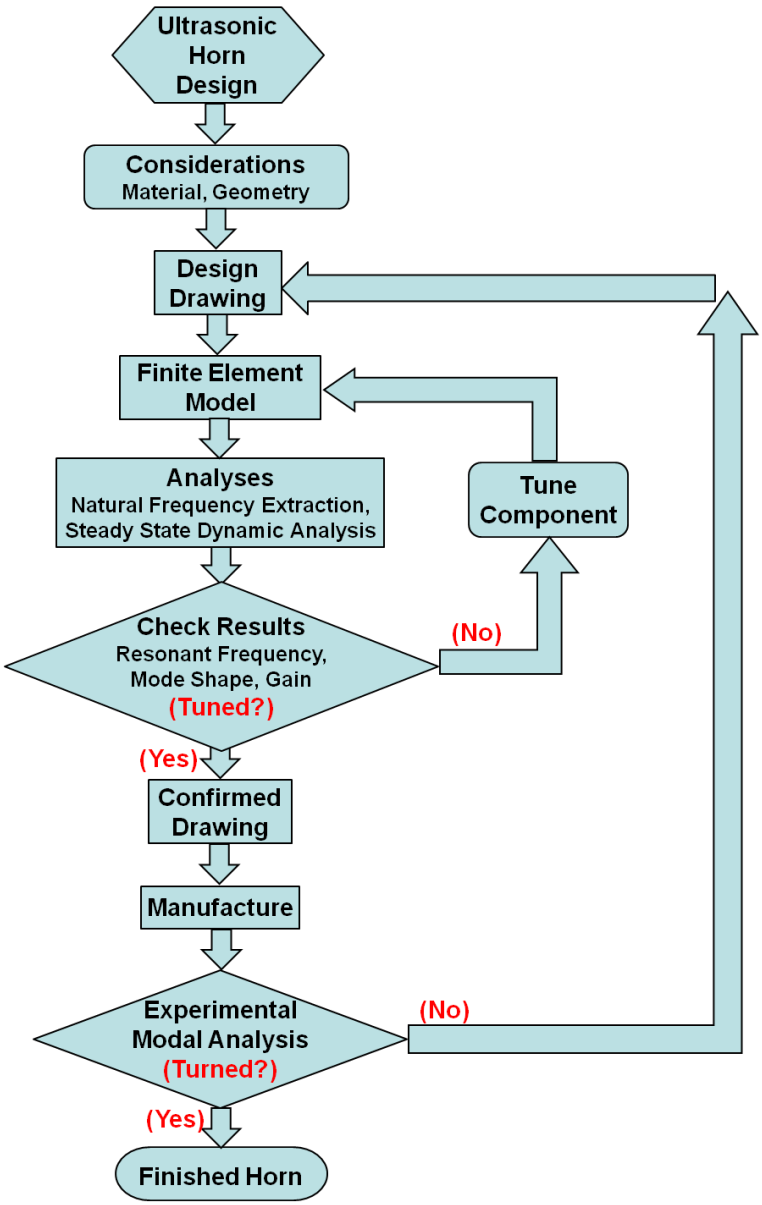

Fig. 3.7 The ultrasonic horn design process

3.2.3 Finite Element Analysis

3.2.3.1 Introduction

Finite element analysis is one of numerical modelling methods, which can be used to provide an approximate solution for the equations governing the system's behaviour. To find solutions to vibration problems, Courant introduced finite element analysis by utilising the Ritz method of numerical analysis in the 1940's [178]. Further development of FEA

followed for practical use in various industries, including defence, aerospace and automotive by the 1970's. With the rapid development of powerful computers, FEA became widely used to model complex structures under different loads. Many FEA and simulation software packages are commercially available to assist engineers in designing or troubleshooting.

As a numerical technique, finite element analysis is used to obtain approximate solutions of differential equations, which are the mathematical models of many physical, chemical and biological phenomena and include the heat equation and the wave equation. FEA solves problems by mesh discretisation of a continuous system into a set of discrete small elements, which have easy representation of the total solution. Assembled using nodes to define a complete system, the meshed elements are then modelled by applying material and structural properties to characterise the behaviour under certain loading and boundary conditions. A variety of numerical results can be provided by different analysis steps according to user defined parameters and requests.

3.2.3.2 Finite Element Modelling

In this application, the FE software package ABAQUS v6.9 (Simulia, France) was used to calculate the natural frequencies of the horn at the first step and the steady-state response, with displacement, strain or stress distributions obtained for the horn under power ultrasonic loading at the second step. In the FE models, the material properties of aluminium alloy used for the horn, were assumed to be linearly elastic with density and Young's modulus as listed in the Table 3.1. The horn models were analysed using the recommended element (C3D20R) which is for linear stress analysis with accurate results. C3D20R indicates a continuum (solid) element in 3D with 20-node quadratic brick and reduced integration, which reduces running time by reducing the integrating points from 27 (C3D20) to 8. The quadratic elements made the solution more accurate in modal behaviour investigations than linear elements. Sufficient element densities were defined for a fine mesh to obtain accurate results and converged solutions.

Firstly, frequency analysis was utilised to determine the natural frequencies and mode shapes of the horn. In this analysis step, no loading was applied to the models with free boundary conditions. The horn designed in FEA should be resonant as near to 20 kHz as possible with the mode shape of longitudinal vibration. If it was found not to be tuned to

longitudinal mode at 20 kHz, the horn geometry was modified. The accepted result, checked by frequency analysis, was transferred to the next analysis step.

Secondly, the horn's dynamic response to a predefined power ultrasonic loading at a specified frequency with harmonic excitation was prescribed in a steady-state dynamics direct step, which can be used to calculate the steady-state displacement amplitude, strain and stress. The response was recorded by performing a frequency sweep. The distributed pressure was applied on the input surface of the horn to maintain a specified input vibration amplitude. The results for the displacement amplitude, strain and stress of the horn were obtained for the applied loading at the desired frequency. The gain of the horn could then be estimated by comparison between the amplitudes of the output and the input surfaces.

3.2.3.3 Horn with Uniform Cross Section

The first FE model of the horn with uniform cross section in one mode of vibration, which can be bending, torsional or longitudinal mode was extracted in Fig. 3.8. Based on the equation 3.1, the FE model shows an accurate prediction of the longitudinal mode at 20 kHz.

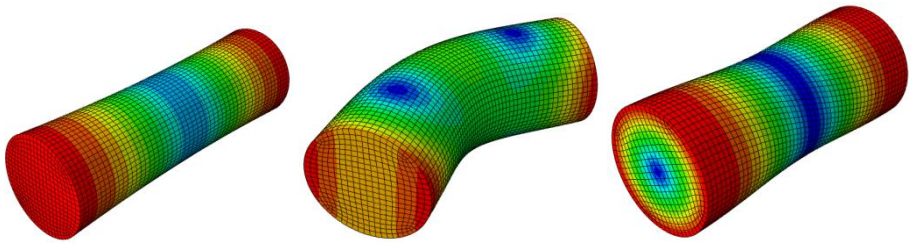

(a) **(b)** **(c)**

Fig. 3.8 Mode shapes with contour of displacement for (a) 1st longitudinal mode (b) 1st bending mode (c) 1st torsional mode of the horn with uniform cross section

3.2.3.4 Multi-elements Horn

Second attempt for the horn design is to create a FE model, which has a larger output surface than input's and a proper gain. Due to the vibration amplitude is related to cross-sectional variation, the initial horn with uniform cross section was cut into multi-element rods with variable cross sections. In this application, four-element horn was selected. To obtain a proper gain, the length of the horn is designed less than the half wave length and around 70% of the length of the horn with uniform cross section. The longitudinal mode of

the multi-element horn is shown in Fig. 3.9 and it is tuning at 24.3 kHz with the gain of 1.75. Based on the trial and error method, this model is the optimal model with a large gain, close to 20 kHz and a good frequency separation. The nearest bending mode frequency is 27.1 kHz.

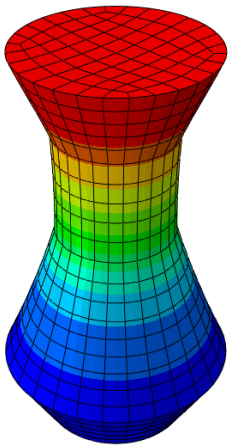

Fig. 3.9 The mode shape with contour of displacement for 1st longitudinal mode of the multi-elements horn

To increase the gain of the horn, it is necessary to decrease the cross sectional area of the rod elements. Triangular slots were introduced on the cylindrical rod element. Due to the bending mode frequency is proportional with the radius for the rod with uniform cross section, the decrease of the cross sectional area would decrease the gap between the longitudinal and bending mode frequencies. Therefore, modification of the triangular slotted horn was applied by creating a flange at the node plane of the horn and clamping the horn in a test holder. Finally, a test rig was designed by FEA with a complex structure of the multi-element triangular slotted horn, which met the design criteria. The FEA results of the designs were shown in the sections 3.2.5 and 3.2.6.

3.2.4 Experimental Modal Analysis

3.2.4.1 Introduction

Experimental modal analysis (EMA) is a widely used technique to determine the modal parameters of natural frequencies, mode shapes and damping factors of a linear, time-invariant structure using a set of frequency response measurements extracted from an excited structure [179]. EMA can be used to measure the response of the vibrating structure subjected to a vibrational load and to validate theoretical predictions (analytical or finite element models). Based on measuring frequency response functions (FRFs) on the

excited structure, EMA works when energy supplied to the structure with known of frequency content. It can be found that the response spectra of the resonance system are clearly amplified. The FRF can be then determined by analysis of the response and force spectra as a function of frequency. An FRF measurement isolates the inherent dynamic properties of a mechanical structure such as natural frequencies and mode shapes. Experimental modal parameters can be obtained from a set of FRF measurements.

The process of EMA is to measure the displacement, velocity or acceleration of the vibrating structure from a grid of points covering the vibrating structure surface. These vibration responses are obtained in the time domain. To convert them to the frequency domain, a fast Fourier transform (FFT) is performed to obtain the FRF, which is defined as a ratio of the Fourier transforms of an output response and the input force. FRFs, the complex transfer functions with real and imaginary components (magnitude and phase), are used to characterise modal parameters by curve-fitting procedures, which is described in detail by Ewins [180].

In this work, EMA was used to extract and characterise the dynamic properties of the horn and validate the FE simulations.

3.2.4.2 EMA Measurement System

Generally, the experimental testing equipment for modal analysis is composed of a signal generator for producing an excitation waveform, an amplifier for magnifying the generated signal, a transducer, which converts the amplified electrical signal into the mechanical vibration for vibrating the loaded structure, and a response measurement system, such as an accelerometer or a laser vibrometer.

In this application, the horn was excited by a transducer, which was driven by an amplified random signal. The desired input waveform was generated by a Data Physics SignalCalc Quattro analyser (Data Physics Corporation), which had two main functions, signal generation and data acquisition for analysing the dynamic signal. To measure the response of the horn, a 3D laser vibrometer (Polytec, 3D CLV-3D) was used. The measured signals were amplified, conditioned and collected by data acquisition hardware (the Quattro analyser), which was connected to a computer for further signal processing. The time domain data was recorded and transformed to the frequency using FFT to generate the

FRFs, which was produced in the computer consisting a digital signal analyser using data acquisition software (Signal Calc ACE, Data Physics Corporation).

The visualisation of the mode shapes of the horn was performed by the specialised modal extraction software ME'ScopeVES (Vibrant Technology Inc). Based on a curve fitting process, the software extracts a set of modal parameters, which are represented in a set of FRFs. Before mode shape extraction, measurements of vibration response are conducted from a set of a grid of points covering the whole surface of the horn. A schematic of EMA is shown in Fig. 3.10.

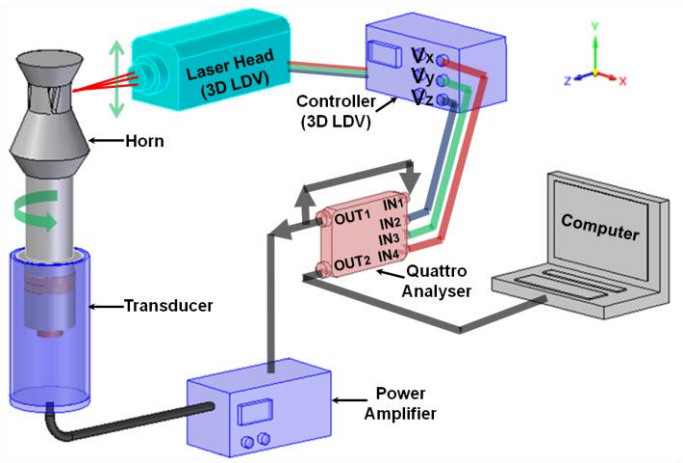

Fig. 3.10 Schematic of EMA

Excitation Signals

The signals used to excite the structure in modal analysis can be generated by various methods such as the periodic, transient and random methods depending on requirements of the test. However, EMA for exciting ultrasonic transducers uses a true random signal generated by the random method or a swept sine signal by the periodic method. Although the response of an ultrasonic transducer excited by the swept sine signal can be identically related to the excitation signal, the random excitation is more commonly used, because it excites all frequency at same time and can be easily implemented in EMA.

Response Measurement

Laser Doppler vibrometry is a well-established optical metrology tool, conventionally used to record surface velocity measurements from vibrating objects. To measure the response of the vibrating structure to the applied excitation for determining the FRFs, a laser

Doppler vibrometer (LDV) is used due to the requirements for non-invasive measurement of the vibrating structure and non disturbance of the structure. The experimental tests were carried out using a 3D LDV for response measurement in three mutually orthogonal directions as well as using a 3D scanning LDV, which can measure a designed grid of points on the target surface automatically over a short time period.

Basic principle of LDV

Based on the principles of the Doppler effects and optical interferometry, laser Doppler vibrometers can detect the instantaneous velocity response of a vibrating structure surface. The EMA tests were conducted using LDVs by shining a laser beam on a vibrating surface and analysis of the difference between the reflected beam from the target and reference beam from the source. As shown in Fig. 3.11, a LDV light beam from a helium neon laser is split into two coherent light beams, a reference beam and a measurement beam, by a beam splitter (BS 1). The measurement beam is focused onto the vibrating surface under investigation, reflected by the vibrating surface and deflected by BS 2. Through BS 3, the deflected beam is then collected and overlapped with the reference beam onto a photo detector. The resultant light intensity is not just the addition of the two beam intensities, but is modulated according to the formula

$$I_{tot} = I_1 + I_2 + 2\sqrt{I_1 I_2 \cos\left[2\pi(r_1 - r_2)/\lambda\right]} \qquad \textbf{3.5}$$

where I_1 & I_2 and r_1 & r_2 are respective light intensities and path lengths of the two splitting beams and r_2, the path length of the reference beam, should be constant. The phase difference between two coherent light beams is proportional to the difference in the respective path lengths transverse by the two light beams between their origin and the point at which they interfere. The optical interference of the two coherent light beams generate a dark and bright (fringe) pattern on the photo detector, which can be utilised to discern the frequency and phase difference between the measurement and reference beams. One complete dark and bright cycle on LDV means the displacement of the vibrating sample is half the wavelength of the used light. The change of LDV pattern with the modulation of the measurement frequency is proportional to the velocity of vibrating sample. To obtain the direction of the vibrating sample, a Bragg cell is placed in the reference beam, which introduces a shift of light frequency by 40 MHz. The modulation frequency is introduced

at 40 MHz when the vibrating sample is at rest. The presence of a Bragg cell makes it possible to not only detect the amplitude of movement but also clearly define the direction of movement by reduction or increase of the modulation frequency around 40 MHz due to vibrating sample moving toward or away the LDV [181]. A standard frequency modulated signal with the Bragg cell frequency and the modulation frequency is the photo detector's output signal, which can be demodulated to derive the velocity of the vibrating target.

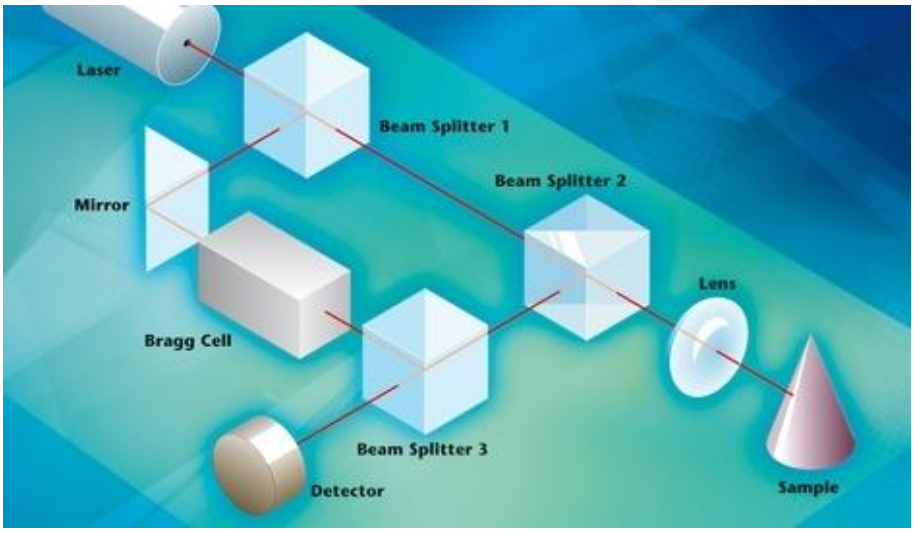

Fig. 3.11 Schematic diagram of LDV [181]

Signal Processing

The measurement signals at various locations on the horn surface obtained from the LDVs were collected by data acquisition equipment, the Quattro analyser, which can also be used as a spectrum analyser to extract and display the frequency response functions by digitising, sampling and transforming the measurement time domain signals to frequency domain and displaying them on the monitor. The sampling rate and resolution of the frequency spectrum of spectrum analysers can be varied depending on the requirements. In this work, the sampling rate of the spectrum analyser was set as 204.8 kHz and the resolution was 1.56 Hz over the frequency 0-40 kHz.

Initially, the measurement data collected from LDV are analogue signals, which need to be processed using a low pass filter as the anti-aliasing filter to ensure no aliasing of high frequency signals into the analysis frequency range. An analogue to digital converter (AD converter) is then used to digitise the data and control the resolution of the digitised signals to resemble the sampling rate parameter. The next step is to convert the signals from time domain to frequency domain using FFT for calculating the FRFs. The data for FFT was

required to be recorded as a finite length of time coupled with the periodicity principle, i.e. as periodic repetition data. The collected signals with the random excitation are non-periodic signals, which lead to a leakage problem when they are used directly in the FFT process. If the signal is ideal sampled and periodic, the resulting spectrum will display a single line at the frequency of the sine wave. However, because of the non-periodic signals used, the resulting spectrum in frequency domain displayed several frequency lines surrounding the resonant frequency line, which indicated the original signal possessing additional frequencies around the resonant frequency. To minimise the undesired effects, weighting functions (windows) can be applied to the sampled data in time domain prior to the Fourier transform calculation. The data are forced into a form more satisfactory to the periodicity requirements of the FFT by imposition of the windows.

This requirement was not met when a random signal was applied as input, which meant leakage occurred during FFT. Through the windowing technique, the measured signals were forced into the periodic signals to satisfy the FFT requirements. Many types of window are available for processing different types of time domain signals such as Gauss, Hanning, Cosine taper, Hamming, Dirichlet, and Exponential. A Hanning window was adopted in this application, which was commonly used for processing the continuous signal (random).

3.2.4.3 Visualisation of Mode Shape

After data collection and signal processing, the final step is to extract the modal parameters for each mode of vibration from the measurement data. There was one FRF per grid point for each of the three measurement directions in 3D LDV measurement. A set of FRFs were produced from the EMA of grid points over the horn structure. Modal parameters are identified by curve fitting the set of FRFs. The modes of vibration were visualised in a 3D model using the software ME'ScopeVES.

3.2.5 Results of FEA and Experiments

This study describes the modelling, design and fabrication of an ultrasonic horn which can be used to study the vibrational response of tissue mimic materials under power ultrasonic excitation. Characterisation of the vibration response of the horn is essential to ensure a reliable performance. Experiments including EMA were carried out to obtain the resonant frequency, the amplitude gain, the frequency separation between the operating frequency

and the close non-tuned modes and the uniformity of the vibration displacement amplitude on the output surface. It is necessary to compare the results of the FEA and experiments for validation.

3.2.5.1 Longitudinal Resonant Frequency

To ensure that the longitudinal resonant frequency and the mode shape predicted by FEA are consistent with those found through EMA, the designed horn were modelled using finite element method and analysed using experimental modal analysis.

In Fig. 3.12, the spectrum (raw data, presenting FRF traces) shows the resonant frequencies of the horn in the range between 0 and 40 kHz and the value of the longitudinal mode is clearly identified at 19.7 kHz. The FEA and EMA longitudinal mode shape results for the horn are shown in Fig. 3.13.

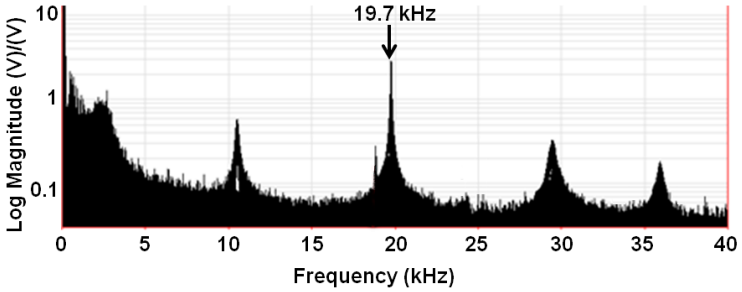

Fig. 3.12 Experimental FRF traces found through EMA

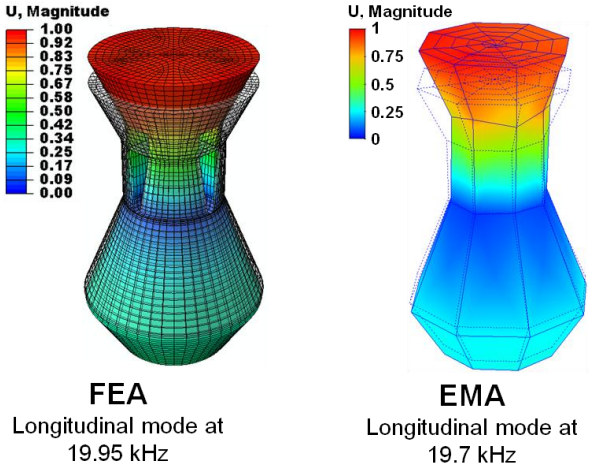

Fig. 3.13 Comparison of (a) FE predicted and (b) EMA measured longitudinal mode shape and modal frequency

It shows the FEA and EMA modal responses for the designed ultrasonic horn in the longitudinal mode at frequency close to 20 kHz. FEA predicted the longitudinal resonant frequency of the horn is 19.95 kHz, while EMA measured the frequency at 19.7 kHz. A percentage difference of 1.25% was found in longitudinal resonant frequency between the predicted FEA and the measured EMA. The slight variation in the natural frequency found between experimental and numerical results could be due to the accuracy of the input material parameters in the finite element model, errors in the manufacture of the horn or accuracy of FRF calculations using the FFT method.

3.2.5.2 Amplitude Gain

It is possible to design a rod-type horn with high gain while ensuring the cross sectional area of the output surface is larger than the input surface's. The displacement amplitudes were measured along a path of 19 equally spaced points positioned on the profile of the horn parallel to the axis of the multi-element rod using 3D LDV. The displacement amplitudes were measured along a path of 19 points positioned on the profile of the horn using 3D LDV. These points are equally spaced along the axis of the multi-element rod from the base to the tip of the horn. The normalised vibration amplitudes of these points from the FEA and the experiment are shown in Fig. 3.14. The predicted and measured amplitude gains of the horn were 2.65 from the FEA and 2.80 from the experiment respectively.

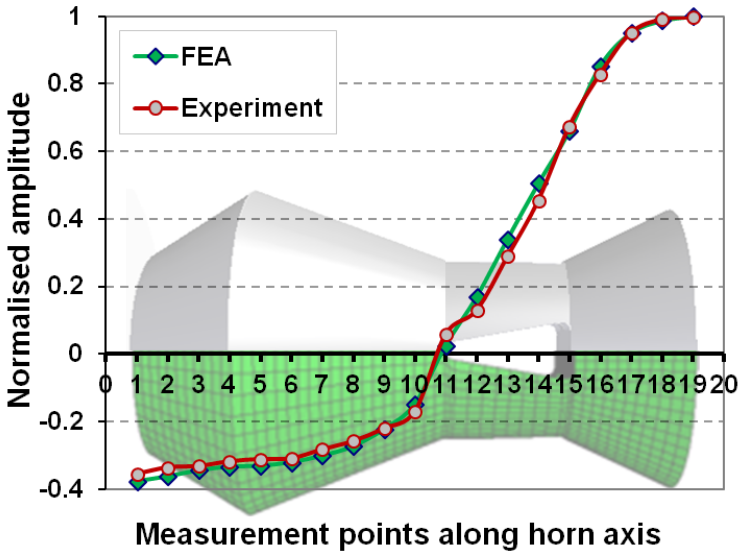

Fig. 3.14 The normalised amplitude distribution along the horn axis for both FEA and experimental results

3.2.5.3 Frequency Separation

For reliable operation of the horn in this application, the longitudinal mode frequency has to be isolated from other close modes which can participate in the response at the operating frequency. It is necessary to measure the spread between the tuned and non-tuned modal frequencies of the exciting horn in examining its performance. FEA and EMA were used to estimate and measure the separation of the horn frequencies. The longitudinal mode of the horn was determined to be at 19.95 kHz from FEA and 19.7 kHz from EMA, whereas a bending mode around the longitudinal mode was recorded at 18.86 kHz from the FEA and 18.8 kHz from the EMA (shown in Fig. 3.15). The tuned longitudinal frequency has a frequency separation of 1.06 kHz (FEA) and 0.9 kHz (EMA) from the bending mode, which makes the horn not satisfy the performance criteria of at least 1 kHz frequency separation in EMA. The coupling of longitudinal and bending modes may lead to a reduction in the vibration amplitude uniformity on the output surface the horn.

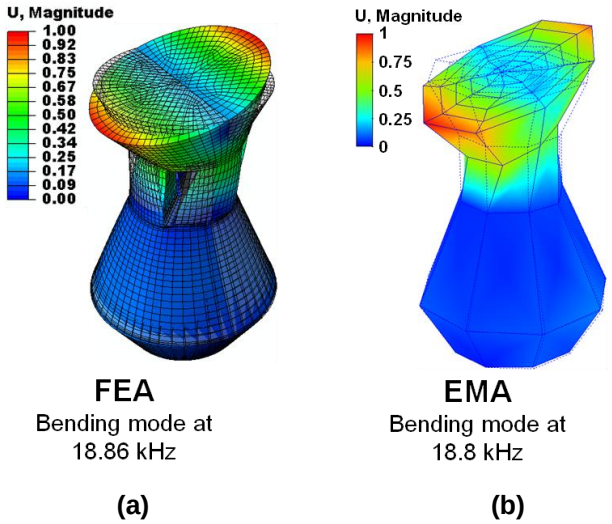

Fig. 3.15 (a) FEA predicted and (b) EMA measured bending mode shape and modal frequency

3.2.5.4 Uniformity of Vibration Amplitude

To measure the vibration amplitude uniformity, the output surface of the horn was scanned over a set of grid points using a 3D laser scanning vibrometer (Polytec PSV-400), when the horn was driven by the transducer at the operating frequency. The experimental set-up is shown in Fig. 3.16. Three laser heads simultaneously scanned the output surface of the horn to obtain the displacements at the grid points.

As shown in Fig. 3.17, the normalised vibration displacements over the output surface of the horn were obtained from the FEA and the measurement. The vibration amplitude uniformity can be calculated using the equation 3.4. The FEA predicts good estimation to the amplitude uniformity on the horn tip, which is about 95.5%. Due to the problem of modal coupling at the operating frequency, the measurement result is 77.8%. The vibration displacement on the output surface of the horn in 3 dimension predicted from the FEA and measured from the experiment are shown in Fig. 3.18. It is found that when the horn is driven at the operating frequency of 20 kHz, a coupled (longitudinal and bending) mode is excited.

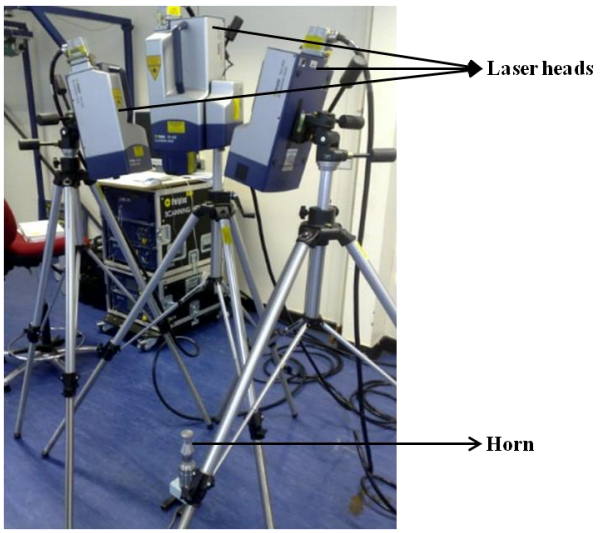

Fig. 3.16 The experimental set-up for measuring the vibration amplitude uniformity on the output surface of the horn using 3D scanning laser vibrometer

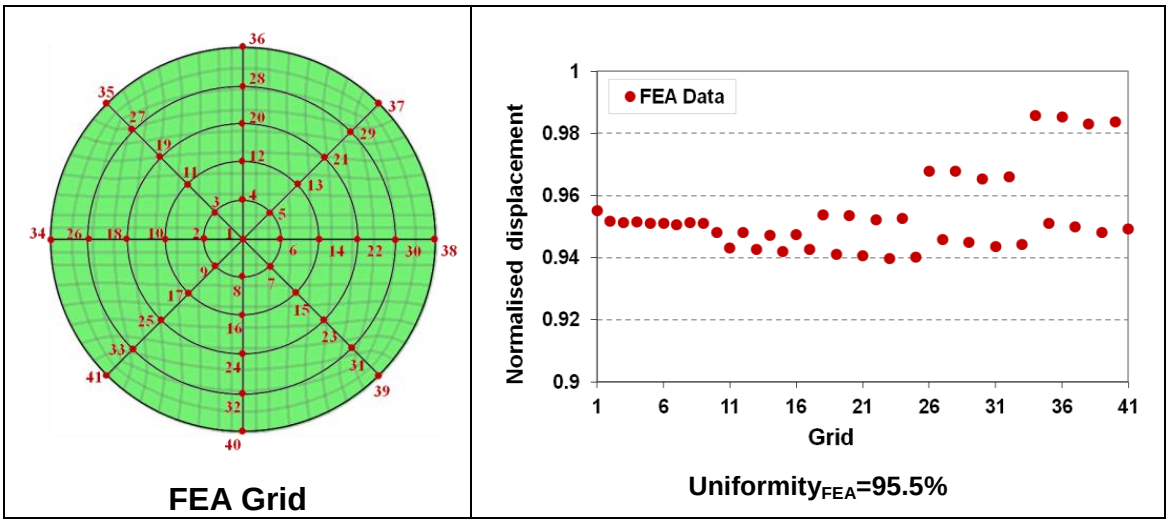

(a)

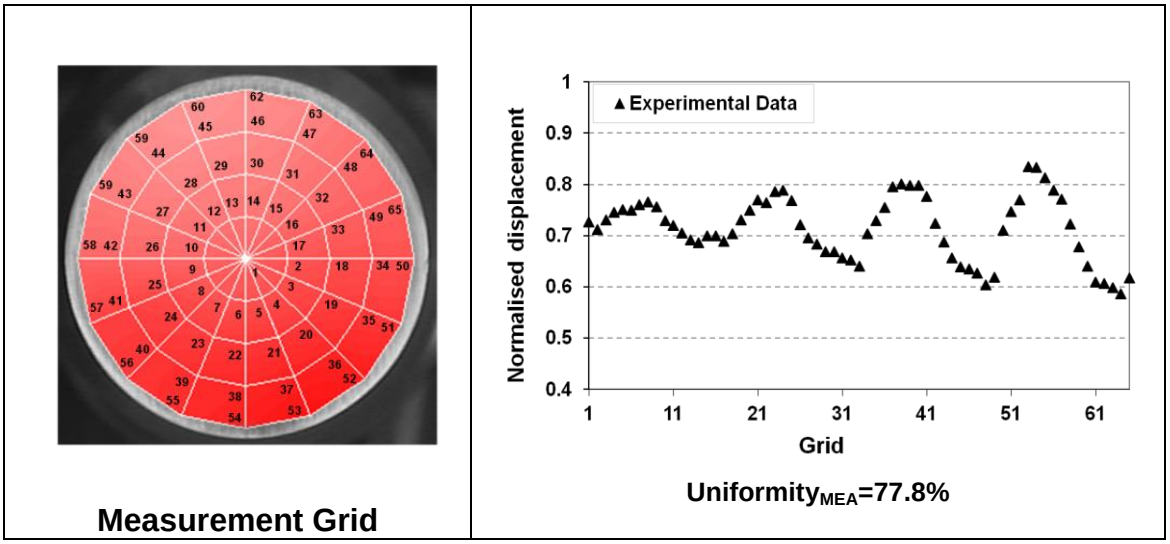

(b)

Fig. 3.17 The normalised displacement and amplitude uniformity on the output surface of the horn obtained from (a) the FEA and (b) the Experiment

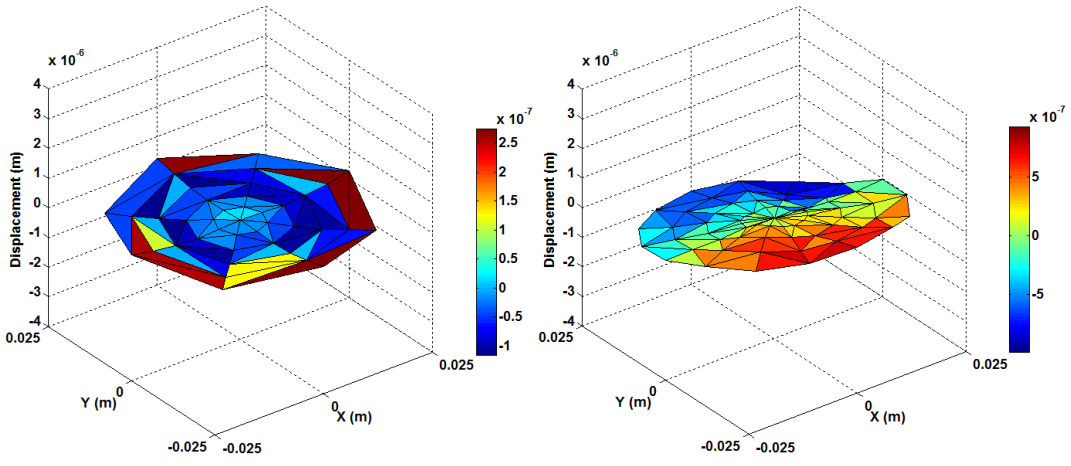

(a) (b)

Fig. 3.18 The vibration displacement on the output surface of the horn in 3D from (a) the FEA and (b) the experiment

3.2.5.5 Validation between FEA and Experiment

There is good correlation in terms of resonant frequencies and mode shapes between FEA and EMA. The small difference between FEA and EMA in the predicted modal frequencies and shapes can be used to verify that the finite element model is suitable for the design of the ultrasonic horn. However, it can be observed that the coupled mode due to poor frequency separation for the excited horn at the operating frequency is difficult to recognise in the FEA. In order to obtain a reliable operation of the horn at the operating frequency with high gain factor and high amplitude uniformity, it is necessary to improve the frequency separation of the horn.

3.2.6 Test Rig

To hold and test the tissue mimics subjected to ultrasonic vibration, a test rig (Fig. 3.19) was designed and manufactured, which could enabled tests to be performed on a stable platform. Due to the poor frequency separation of the triangular slotted horn, the test rig has to be designed with an improved feature in the frequency separation. The test rig consists of a holder structure and a modified triangular slotted horn designed with a fixing flange (Fig. 3.20), which is clamped within the test rig. The location of the nodal plane of the horn was used for determining the clamping position. The holder structure uses pillars and plates to make the ultrasonic excitation system work properly.

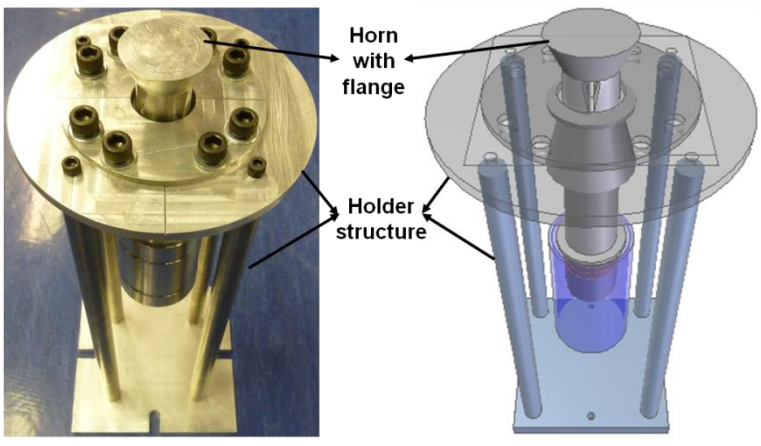

Fig. 3.19 (a) the manufactured test rig and the (b) drawing

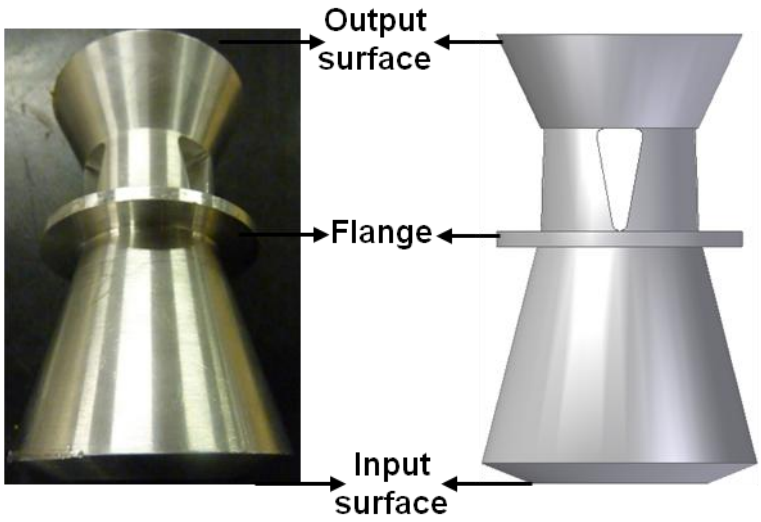

Fig. 3.20 The modified triangle slotted horn with flange (a) the manufactured horn and (b) the drawing

A finite element model of the modified horn with the clamping plate for simulation of the test rig was developed to find the resonant frequencies, the amplitude gain and the frequency separation. In the model, a fixed boundary condition was applied at the flange to implement no motion at this feature. The modal frequencies of the longitudinal and bending modes and the gain factor were calculated by the FEA and measured by the experiment using LDVs (Fig. 3.21). The results are shown in Fig. 3.22-4.

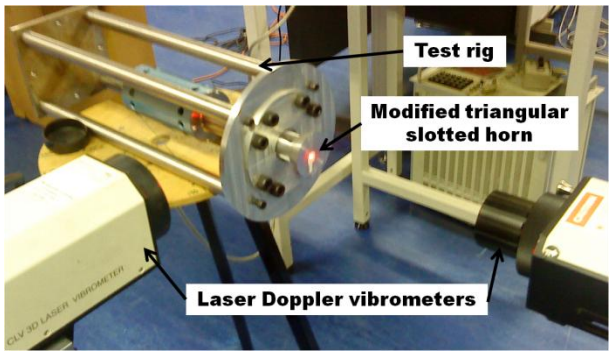

Fig. 3.21 Experimental characterisation of the test rig using LDVs

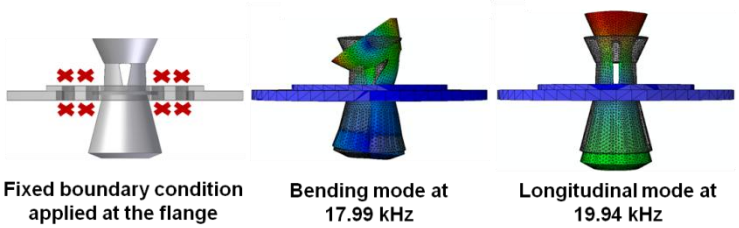

Fig. 3.22 The bending and longitudinal mode shapes of the test rig predicted by the FEA

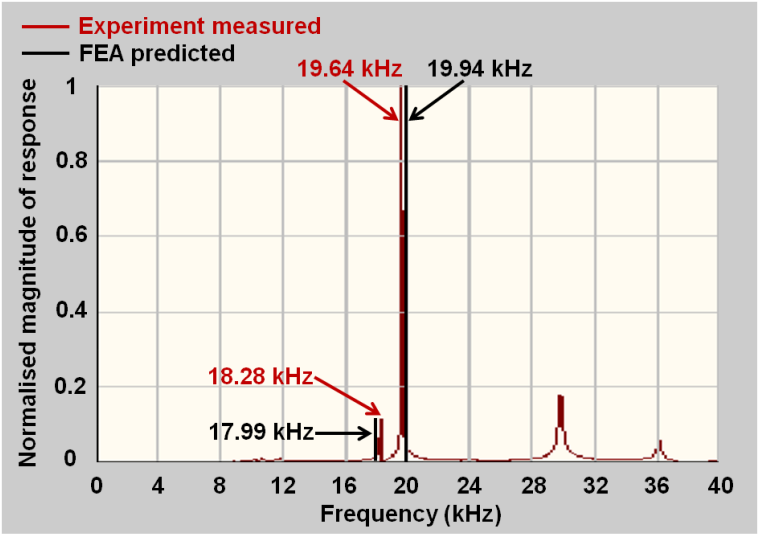

Fig. 3.23 The modal frequencies of the test rig obtained from the FEA and the experiment

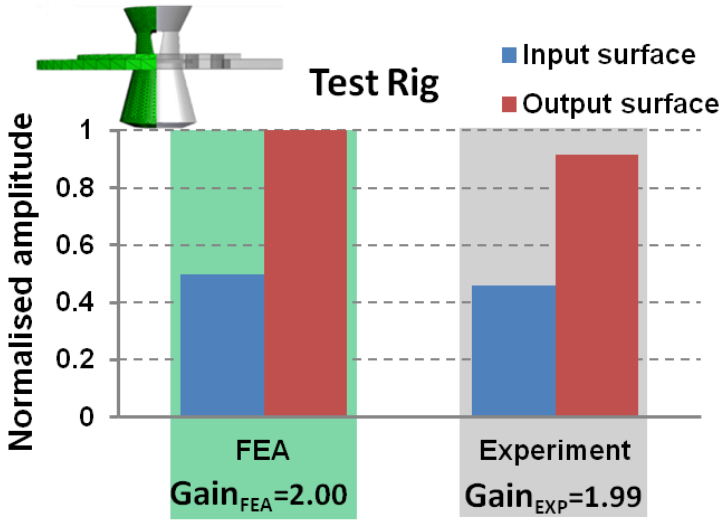

Fig. 3.24 The gain factor of the test rig obtained from the FEA and the experiment

It is found that the gain factor of the test rig is around 2, a small difference between the FEA and the experiment in prediction of resonant frequencies (tabulated in Table 3.2) and the frequency separation is greater than 1 kHz, which satisfy the performance criteria. Therefore, the designed test rig with power ultrasonic excitation system was used to do the vibration tests of tissue mimicking materials with large contacting surface in this work.

Table 3.2 The modal frequencies of the longitudinal and bending modes and frequency separation between them obtained from the FEA and the experiment

Modal frequency (kHz)	FEA	Experiment
1st Bending mode	17.99	18.28
1st Longitudinal mode	19.94	19.64
Frequency separation	1.95	1.38

3.2.7 Probe Horn

To provide large ultrasonic amplitude to the smaller cross-sectional area tissue mimicking samples, a probe horn was used, which has a higher gain factor than the test rig. The vibration response was characterised using a laser vibrometer. The probe horn (Fig. 3.25) was made from aluminium alloy with a 38 mm diameter base fixed to the transducer and a 22 mm diameter tip attached to the test samples.

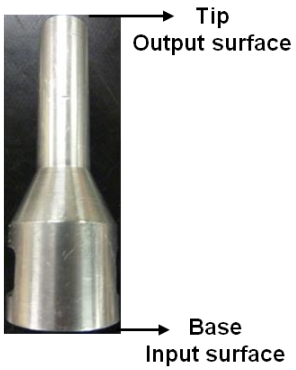

Fig. 3.25 The manufactured probe horn

The finite element model for the probe horn was created and the experiment was carried out to find the resonant frequencies and the gain factor. The resonant frequency of the probe horn in the 1st longitudinal mode was 20.51 kHz obtained from the FEA and 20.62 kHz from the experiment, as shown in Fig. 3.26. The gain of the probe horn (Fig. 3.27) was predicted as 2.99 by the FEA and 2.96 measured by the experiment.

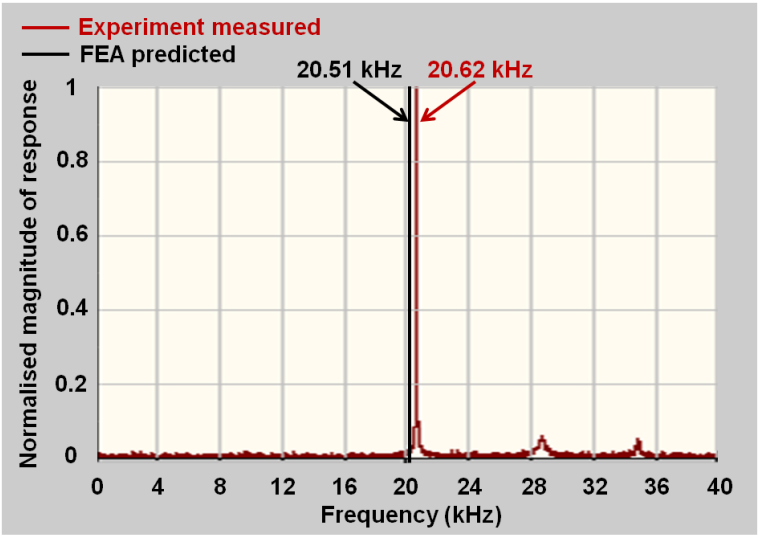

Fig. 3.26 The resonant frequencies and the 1st longitudinal resonant frequency of the probe horn obtained from the FEA and the experiment

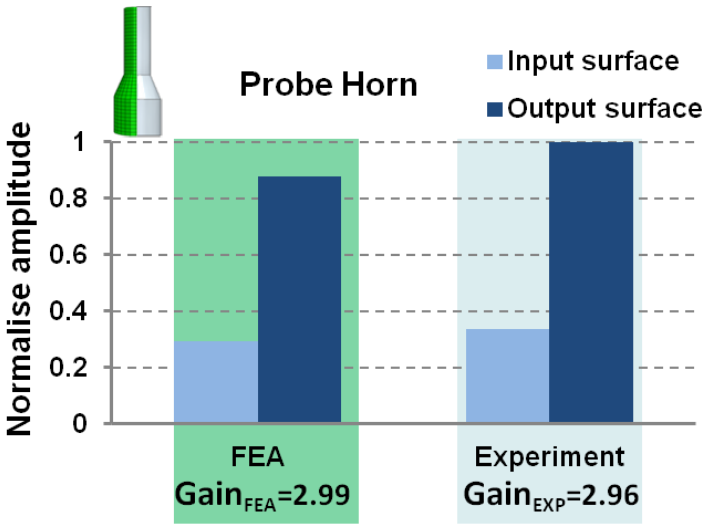

Fig. 3.27 The gain factor of the probe horn obtained from the FEA and the experiment

Good correlations can be obtained between the FEA and the experiment for these characterisations of the probe horn.

3.3 Chapter Summary

The design of a power ultrasonic system has been investigated, initially from a fundamental transducer, in which resonant and anti-resonant frequencies was predicted using a finite element model and measured using an impedance analyser, to ultrasonic horns and a test rig which rely on finite element models to ensure tuning and reliability. The performance of the power ultrasonic components was experimentally characterised by experimental modal analysis and experiments using laser Doppler vibrometers.

A rod-type triangular slotted horn with larger output surface was designed, using finite element analysis as part of the design process. Many performance criteria were examined in the design of the horns such as resonant frequency of the longitudinal mode, gain factor, frequency separation and vibration amplitude uniformity. Overall, a good correlation between the predicted and the measured resonant frequencies, mode shapes and gain factors of the designed component was achieved and ensured validity of the finite element models. To improve the frequency separation of the triangular slotted horn, the test rig was discussed, which satisfies the performance criteria. To obtain higher vibration amplitude, a probe horn with a higher gain was used to apply ultrasonic vibration on small cross-sectional area samples. These designed ultrasonic components provide reliable performance for power ultrasonic vibration tests on tissue mimicking materials.

4. Tissue Mimicking Materials

Tissue mimicking materials were used for experimental tests in the power ultrasonic application to evaluate the device-tissue interaction. E-glass filled epoxy resin (ER) and rigid polyurethane foam (PUF) were the alternatives for hard tissue (cortical bone and cancellous bone respectively) and silicone elastomer (SE) was the surrogate for soft tissue. In this chapter, the mechanical and thermal properties of surrogate tissue materials were accessibly characterised by performing several tests to determine the power ultrasound induced behaviour. The dynamic loading induced on the tissue mimics, because of its viscoelastic property, caused significant frequency and temperature dependent behaviour to be displayed. There are two sections in this chapter, an introduction and the characterisation of the thermo-mechanical properties of the viscoelastic surrogates.

The brief introduction is followed by section 4.1.2 covering the general properties of human tissue and the tissue mimicking viscoelastic materials. Section 4.2 characterises the properties of the tissue mimicking materials, which can be categorized into mechanical properties, thermal properties and frequency and temperature dependent thermo-mechanical properties. To do these characterisations further, several experimental tests were designed and illustrated in this section. The experimental data obtained from these tests was utilised in the finite element analysis to validate the behaviour of viscoelastic mimics during power ultrasonic vibration.

4.1 Properties of Tissue Mimicking Materials

4.1.1 Introduction

The mechanism of interaction for ultrasonic surgical devices is poorly understood, although considerable effort has been directed by many authors and organisations towards reviewing it from several aspects, such as, deleterious mechanical and thermal effects, and the cutting ability of devices [108-112, 115, 116, 182-184]. From the limited literature, the mechanism of ultrasound effects on biological tissue can be summarized into three main topics: direct mechanical effects, thermal effects and acoustic cavitation [20].

Although all of these effects often occur simultaneously in the presence of power ultrasound on tissue, the response of tissue to power ultrasound can be quite variable due to the range of biological properties. For power ultrasonic applications, the biological

properties of tissue have a strong impact on ultrasonic tissue interaction. A general discussion of the physical properties of biological tissue is given by Duck [185].

Biological tissue shows non-linear, anisotropic and viscoelastic behavior [186]. Many experimental studies on hard and soft tissues have done concentrating on the aspects of their elastic and viscoelastic behaviour. Tissue requires viscoelastic parameters (dynamic mechanical property) in addition to the elastic modulus (static mechanical property) to fully describe their mechanical behaviour. However, ultrasonic excitation gives a limited strain of tissue in a very small range. The equivalent strain-stress relationship could be linear, which could be assumed that tissue shows elastic behaviour when subject to ultrasonic vibration. The physical and elastic properties of tissue were given in the Table 4.1.

Table 4.1 Physical and elastic properties of tissue [185, 187, 188]

	Density (kg/m^3)	Young's modulus (MPa)	Poisson's ratio	Tensile strength (MPa)	Compressive strength (MPa)
Skin	1093-1190	4.6-20	0.48	3.7-11	
Muscle: Cardiac	1060	0.0062-0.11 (10% strain)	0.49 (average)	0.11	
Muscle: Skeletal	1038-1056			0.11	
Bone: Cortical	1990±27	16000-23000	0.40-0.62	130-160	150-210
Bone: Trabecular	1920±20		0.32 (bovine)		0.4-7.7
Cartilage	1092-1104	5.0 (costal) 0.79±0.36 (articular)		2.8 (costal)	7.8 (costal)
Fat	917-939				

Thermal damage in the ultrasonic exposure of tissue is related to ultrasound absorption and thermal conduction [118]. Ultrasonic absorption coefficient is relevant to conversion of the ultrasonic energy into tissue heat and thermal properties of tissue can reveal the heat transfer. Data about ultrasound absorption and thermal properties of tissue have been collected for reference shown in Table 4.2.

Table 4.2 Ultrasound absorption and thermal properties of tissue [185, 187, 188]

	Ultrasound absorption coefficient (dB/cm)	Thermal conductivity (W/m·K)	Specific heat capacity (J/g·K)	Heat of Ablation (kJ/g)
Skin	3.5±1.2 (1MHz)	0.293±0.016 0.385-0.393	3.15-3.71	4.27
Muscle: Cardiac	1.3-3.3, 4.7±0.44 (4.3 MHz)	0.492-0.562	3.72	1.51
Muscle: Skeletal		0.449-0.546	3.43 (bovine)	
Bone: Cortical	1.5-38.2 (1MHz)	0.373-0.496		
Bone: Trabecular	1.9-15.7 (0.5MHz)	0.27-0.33 (cow)	1.15-1.73 (bovine)	
Fat	1.8±0.1 (1MHz)	0.23-0.27	3.59 (bovine)	

Due to their availability, reproducibility and properties which are similar to biological tissue, three viscoelastic biomechanical test materials, ER, PUF and SE, were used for this study to represent hard and soft tissues. The materials are available to allow test data to be incorporated in the model making experimental validation achievable and offering a more consistent alternative to real tissue. Therefore, it is necessary to know the mechanical and thermal properties of the tissue mimics in this power ultrasonic application.

4.1.2 Properties of Tissue Mimicking Materials

4.1.2.1 Soft Tissue Mimicking Materials

To obtain reliable information on ultrasound tissue interaction, phantom studies are essential to mimic biological tissue. It is important to make the phantoms with the same mechanical and thermal properties of the corresponding tissue. Several soft tissue mimicking materials were developed for power ultrasound applications.

Hydrogels are similar to many biological tissues, due to their large water content. Hence, to explore the high temperature and stress regimes involved in power ultrasound applications, polyacrylamide gel (PAA gel, a hydrogel) containing egg white was made to facilitate the experimental work. The physical properties of PAA gel match well with those of soft tissue. Data on the physical properties of PAA gel were obtained from the literature and is shown in Table 4.3. To visualise the temperature rise for power ultrasound propagation in tissue, egg white, a protein, was added in the gel to work as a temperature sensitive indicator for promoting coagulation of organic tissue. The procedure to fabricate the PAA gel containing egg white is given in Appendix 1 [189].

Table 4.3 Properties of PAA gel [190, 191]

	Young's modulus (kPa)	Poisson's ratio	Tensile strength (MPa)	Glass transition temperature (℃)
PAA gel	Max. approx. 78	0.318-0.467	0.00271-0.01013	187.85

In the fabrication of PAA gel egg white mixture, too much egg white resulted in an opaque gel, while too little caused low sensitivity and low optical contrast. The phantom containing 30% egg white by mass was best for visualisation of temperature rise produced by power ultrasonic exposure. However, due to the poor laser transparency of the PAA gel with egg white preventing mapping of the stress field using the laser Doppler vibrometer, which was one of the experimental methods used in this study, therefore the PAA gel was not utilised as a soft tissue mimicking material.

Another soft synthetic material, silicone elastomer (Fig. 4.1), was an alternative for characterisation of ultrasonic effects. SE is cheap and easily formed into a solid shape at room temperature and is optically transparent, which made it an attractive candidate for this research. The mechanical properties of SE are summarized in Table 4.4 [190, 192].

Table 4.4 Physical and mechanical properties of silicone elastomer [190, 192]

	Density (g/cm^3)	Young's modulus (MPa)	Tensile strength (MPa)	Poisson's ratio	Thermal conductivity (W/m·K)	Specific heat capacity (kJ/kg ·℃)	Glass transition temperature (℃)
SE	1.3-1.8	0.005-0.02	2.4-5.5	0.5	0.3	1.3	-123

Samples of the silicone elastomer were made according to the manufacturer's instruction (ELASTOSIL® RT 601 A/B, Wacker Chemicals Ltd). There are two components: the platinum catalyst and the crosslinker. These material elements were mixed in 9:1 mixing ratio by weight to form the final elastomer at room temperature. After intensive mixing for several minutes in a fume hood, the mixture was poured into a prepared mould. The mould was then placed in a vacuum degas tanker above a horizontally levelled table to release air bubbles from the mixture and ensure parallel sample surfaces. Samples were left to cure either for 24 hours in a well-ventilated area or for 20 minutes in the oven at 80 ℃ before removing from the mould.

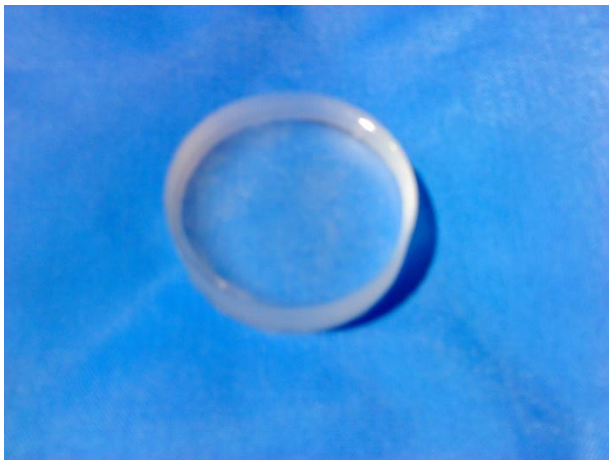

Fig. 4.1 A silicone elastomer sample

4.1.2.2 Hard Tissue Mimicking Materials

Samples of hard tissue mimicking materials were made from biomechanical test materials, Sawbones Europe, including E-glass filled epoxy resin (ER, Fig. 4.2a) for cortical bone and solid rigid polyurethane foam (PUF, Fig. 4.2b) for cancellous bone. They are primarily used as alternative testing medium to human bones, because they provide consistent and uniform mechanical properties in the range of human bone. The mechanical properties of the materials are listed in Table 4.5.

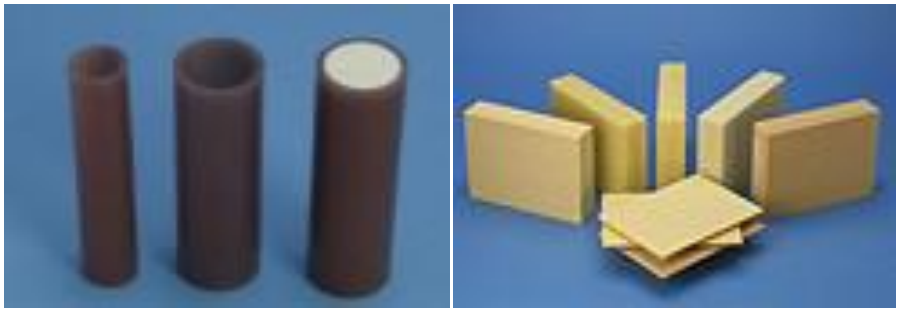

(a) **(b)**

Fig. 4.2 Hard tissue mimics (a) E-glass filled epoxy resin for cortical bone (b) rigid polyurethane foam for cancellous bone [193]

Table 4.5 Mechanical properties of hard tissue mimics [193]

	Density (g/cm^3)	Modulus (MPa)	Strength (MPa)	Poisson's ratio
ER	1.64	16,000	106	0.3
PUF	0.48	592	12	0.3

4.2 Characterisation of the Properties of Tissue Mimicking Materials

4.2.1 Introduction

Deriving properties data for tissue mimicking materials is a crucial factor for determining whether the performance assessment of ultrasonic surgical devices gave correct and realistic results. Reliable finite element analysis is required for engineering simulations, which are largely dependent on accurate and realistic material data. To model the materials accurately, the properties of tissue mimics were characterised mechanically and thermally using different parameters and experimentation. In this study, frequency and temperature dependent mechanical and thermal properties data were required in order to develop finite element models of power ultrasonic loading processes. Standard and specific materials characterisation techniques were assessed.

Three materials: ER, PUF and SE were used to determine their properties for implementation in FEA, particularly mechanical and thermal simulations during the power ultrasonic loading. These tissue mimicking materials were considered to be general representations of hard and soft tissue but are not considered to accurately represent the full spectrum of biological tissue. They have different mechanical and thermal behaviour and display diverse frequency and temperature dependencies.

4.2.2 Mechanical Properties

To extract the mechanical properties, such as Young's modulus and strength, tensile and compression tests were conducted using a test rig by loading a specimen with a predefined geometry until failure occurs. The elastic behaviour during the tests was derived from the linear region of the stress-strain relationship, which was calculated from the measured load and displacement data.

4.2.2.1 Characterisation of the Mechanical Properties of ER and PUF

Generally, to determine the mechanical properties well, it would be advantageous to characterise the material in tension as well as compression. In the application of ultrasonic surgical cutting or loading, samples are firstly compressed and then sheared. Failure occurs more often under compression than tension at the interface between the ultrasonic horn and

the material. Compression tests for ER and PUF were performed following the standard ISO 604:2003 to obtain compressive stress-strain data [194].

Principle of Characterisation of the Mechanical Properties of ER and PUF

ER and PUF were machined to a standard size of 50mm (Length) × 10mm (Width) × 4mm (Thickness). Machining operations were carried out by a milling machine ensuring smooth surfaces. Then, ER and PUF were tested in a uni-axial compression testing machine (Zwick Roell Z250) at temperatures of 22, 30, 40, 50 and 60 ℃ for ER and room temperature of 22 ℃ for PUF at crosshead velocities of 1 mm/min. The centre of each specimen was carefully positioned at the centrelines of the compression plate surfaces to ensure the compression force was applied axially and the specimen was parallel to the compression plate surfaces of the test machine. The specimen was placed in the temperature controlled chamber (Fig. 4.3) and allowed to soak for half an hour to ensure the whole specimen was at the desired testing temperature. A small preload of 100N was applied prior to the test and then the specimen was compressed to failure.

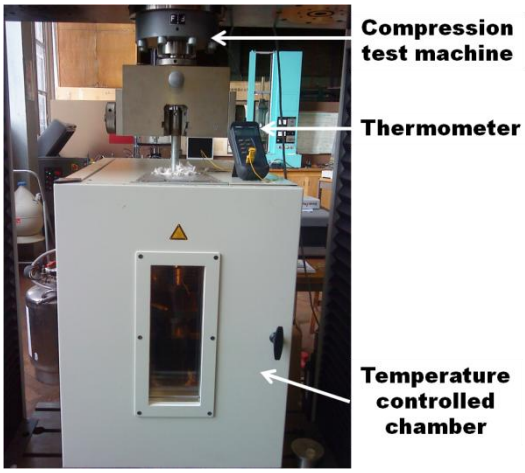

Fig. 4.3 Compression tests at different temperatures

Results of Mechanical Properties of ER and PUF

The nominal strain was determined by crosshead travel and compressive modulus was defined on the basis of two specified strain values at the strain of 0.05% and 0.25%. The stress-strain relationship in compression tests are shown in Fig. 4.4 for ER and Fig. 4.5 for PUF. The compression modulus were calculated and listed in Table 4.6 for ER and Table 4.7 for PUF. It could be assumed that the compression modulus of ER and PUF are identical to the tensile Young's modulus.

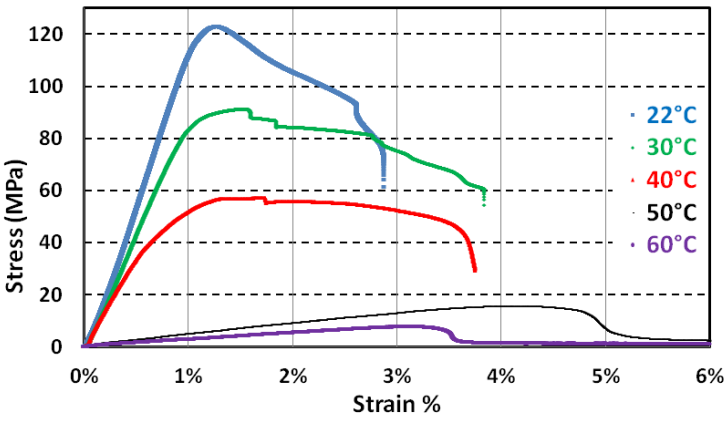

Fig. 4.4 Typical stress-strain curves of ER in compression at different temperatures

Table 4.6 Typical compression modulus of ER at different temperatures

Temperature (℃)	Young's modulus (MPa)
22	9962.3
30	8508.5
40	7493.8
50	540.88
60	354.38

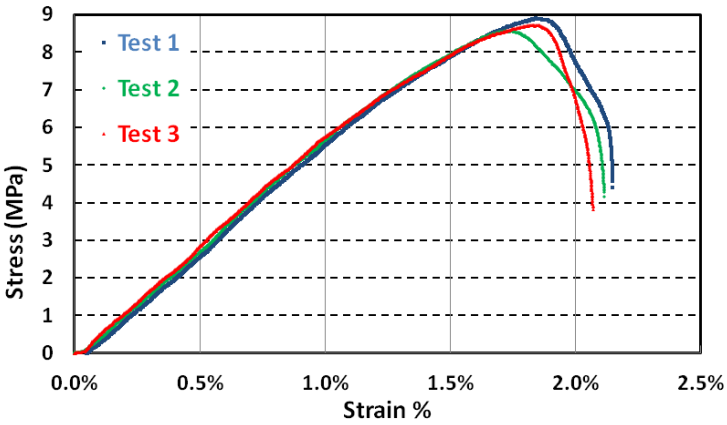

Fig. 4.5 The stress-strain curves of PUF for compression tests at room temperature 22 ℃

Table 4.7 The compression modulus of PUF

Test	Compression modulus (MPa)
1	556.5
2	562.2
3	571.5
Mean	563.4
Standard deviation	7.6

Due to the glass transition temperatures of ER is around 50 ℃ and PUF is above 120 ℃, which will illustrate in section 4.2.4, the mechanical properties of ER is more temperature dependent than PUF. Therefore, compression modulus of ER at different temperatures up

to 60 ℃ were obtained but the compression modulus of PUF at room temperature was calculated.

4.2.2.2 Characterisation of the Mechanical Properties of SE

The majority of mechanical tests for silicone elastomers use uni-axial tests, either a tensile test or a compression test, to determine the tensile and compressive stress-strain properties. Standard test pieces were prepared in advance. Dumb-bell shaped specimens (gauge length 20mm, type 1A) were made for tensile tests and cylindrical specimens with diameter 29 mm and height 12.5 mm were fabricated for compression tests. Standard test pieces were produced from polytetrafluoroethylene (PTFE) mouldings (Fig. 4.6 and 4.7), to allow the specimens to release easily. The test procedures were followed the standards ISO 37:2005 and ISO 7743:2008.

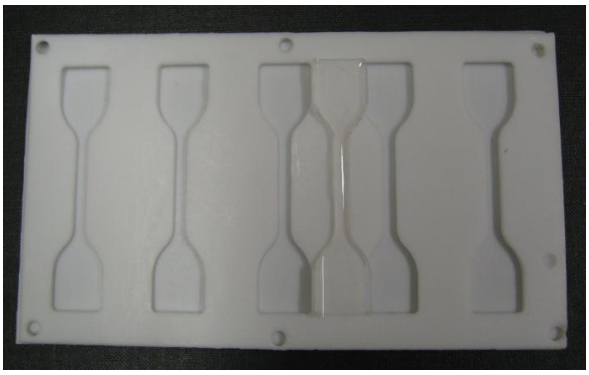

Fig. 4.6 Tensile test specimen moulds and SE specimen

Fig. 4.7 Compression test specimen moulds and SE specimen

Principle of Characterisation of Mechanical Properties of SE

In tensile tests at room temperature, dumb-bell test pieces were gripped by clamps and stretched in a tensile testing machine (Zwick Roell Z250) at a fixed rate (500 mm/min). Force and elongation data were collected until the sample broke. Due to the difficulties of griping the sample without clamp induced failure and making samples without flaws, tensile tests proved difficult to perform. Compression tests were simple to perform for SE. A standard test piece was lubricated by oil on the flat top and bottom surfaces, which were contacted with the metal plates of test machine. The lubricant was used to reduce friction with the loading platens, where the specimen attained a barrel shape. In the compression test, the lubricated test sample was pressed between two compression platens of the test machine (Zwick Roell Z250) at a constant speed of 10 mm/min until a reduction of

specimen's height of 25% reached. The strain was released at the same speed and the compression release cycle repeated three more times. The four compression cycles form an uninterrupted sequence. The measured load and displacement data were recorded to determine the force-deformation relationships for calculating the compression modulus during the four cycles. The experimental set-ups for characterisations of the mechanical properties of SE are shown in Fig. 4.8.

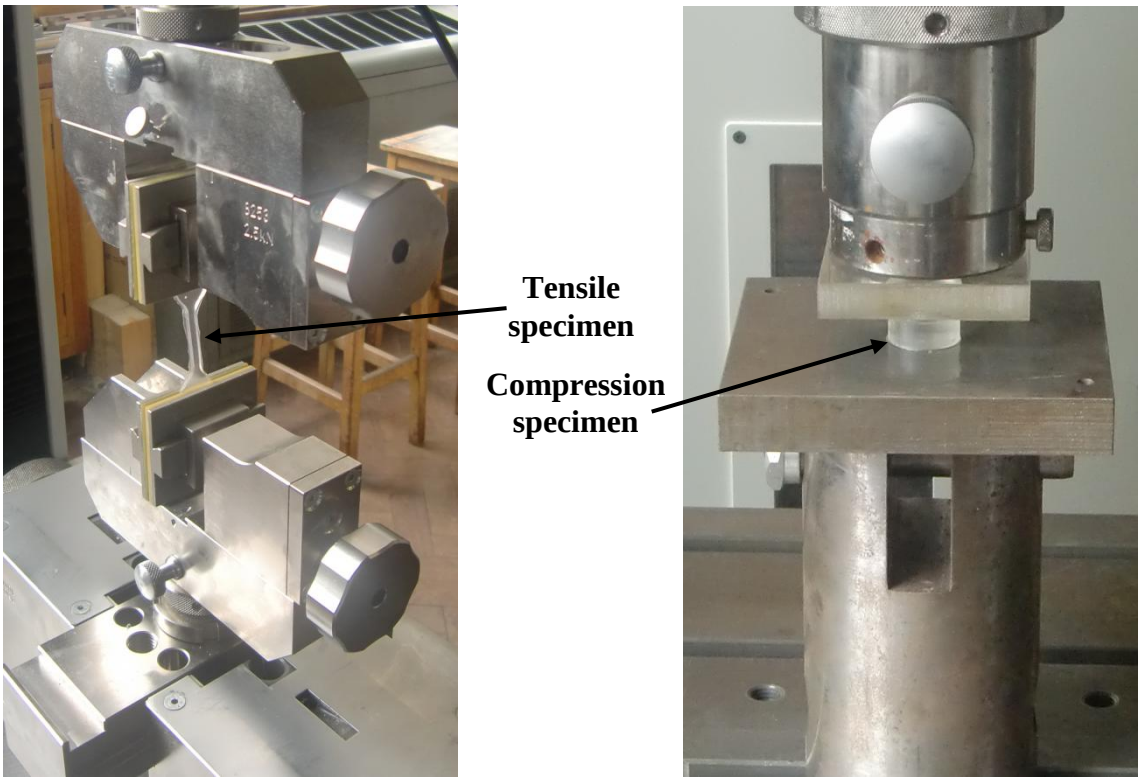

Fig. 4.8 Mechanical experimental set-ups for (a) tensile test (b) compression test

Results of Mechanical Properties of SE

The test specimens were all moulded from the same batch. Although the specimens were manufactured from the same mixture, small variations occurred during setting and test preparations. It was difficult to obtain consistent values for their mechanical properties. The tensile stress-strain results for SE from three tests obtained to provide Young's modulus and tensile strength are plotted in Fig. 4.9. The strain was determined by the displacement travelled by the crosshead of the machine, which produced similar results at low strain but as the strain increased the results diverged when compared with the results from the more accurate laser extensometer. In this thesis, for the purpose of finite element modelling, the strain calculated using the change in displacement of the crosshead can be

considered accurate but future considerations of materials testing should employ optical extensometry techniques to improve the accuracy.

Three compression results were derived from the recorded force-deformation diagrams (Fig. 4.10). There were four compression loading cycles in each test, where the strain was measured from the point at the curve in the last (fourth) cycle and the compression modulus is calculated between 10% and 20% deformation. The compression tests of SE show that the material is stiffer in compression than in tension. The compressive elastic modulus is higher than the tensile (Table 4.8).

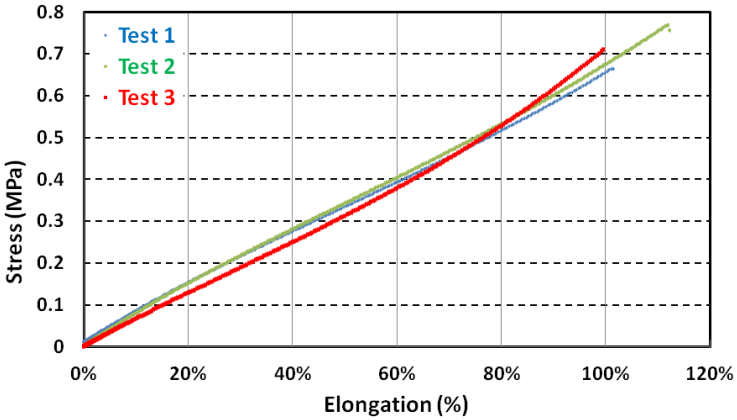

Fig. 4.9 Results of tensile tests for SE

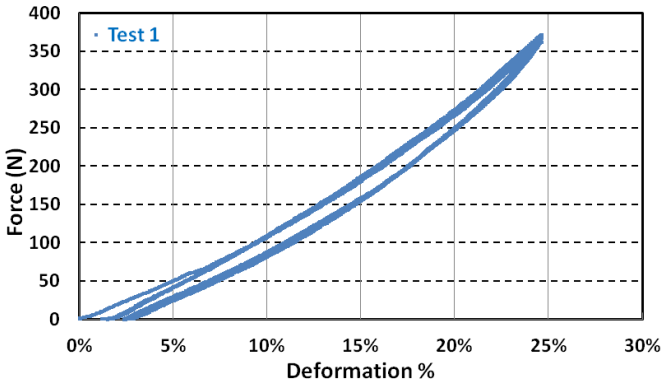

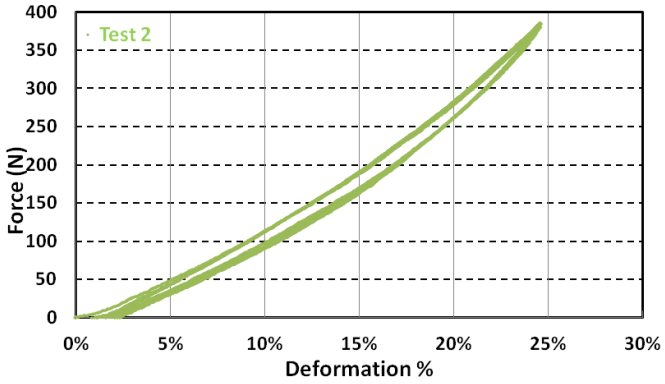

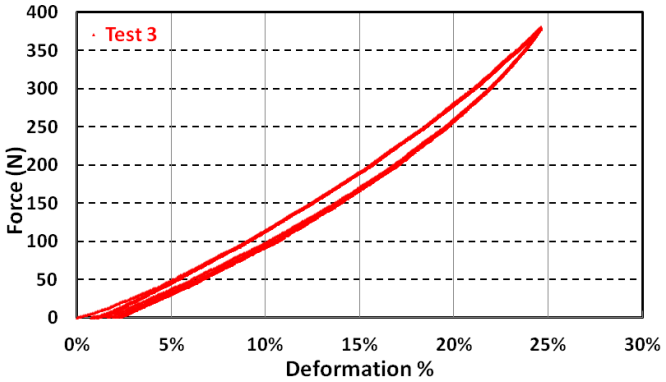

Fig. 4.10 Results of compression tests for SE

Table 4.8 Results of mechanical tests for SE

Test	Young's modulus (MPa)	Tensile strength (MPa)	Elongation at break	Compression modulus (MPa)
1	0.83	0.66	101.50%	2.31
2	0.79	0.77	112.25%	2.28
3	0.79	0.86	99.58%	2.35
Mean	0.80	0.76	104.33%	2.35
Standard deviation	0.02	0.10	0.07	0.09

4.2.3 Thermal Properties

Heat induced by rapid strain cycling is another effect of power ultrasound on biological tissues. To map the thermal distribution during power ultrasonic loading, it was necessary to obtain the thermal properties of the tissue mimics. In addition, heat transfer in the specimen during ultrasonic vibration can be modelled with FEA, if the thermal properties of the materials are available. These parameters include thermal conductivity and specific heat capacity, which can be used to predict heat build-up with time.

4.2.3.1 Measurement of Thermal Conductivity

When an object is placed between two different temperature parts, heat flows from the hot part to the cold part of the object occurs through thermal conduction. To measure heat flows through the object, the guarded heat flow meter method was applied in the experiment following the International Standard ISO 22007-1:2009 [195].

The Principle of Thermal Conductivity Measurement

The test apparatus is shown in Fig. 4.11 (a) and the schematic in Fig. 4.11 (b).

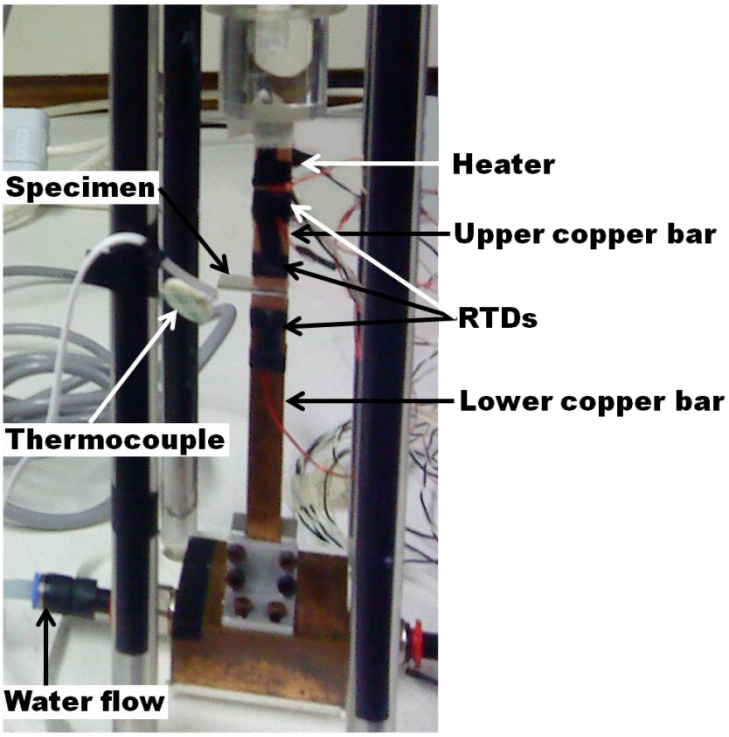

(a)

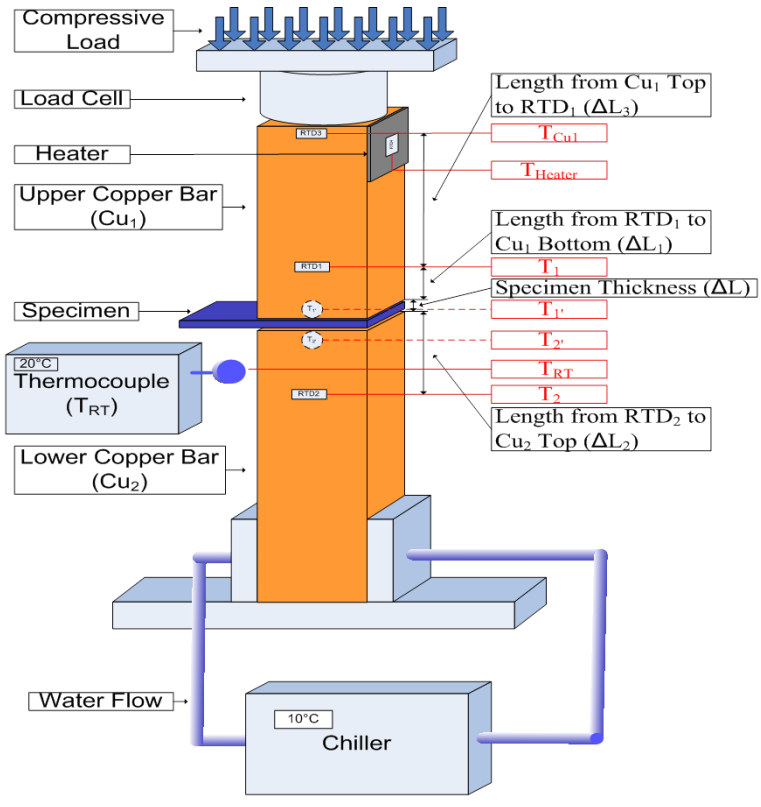

(b)

Fig. 4.11 Setup for thermal conductivity measurement (a) experimental (b) schematic apparatus

A plate heater attached on the lateral surface of a copper bar works as a heat source. The sheet of solid specimen was clamped tightly under a compressive load between the two copper bars with known geometry, thermal conductivity and thermal emissivity. A load cell sitting on top of the upper copper bar (Cu_1) was used to measure the compressive load. The lower copper bar (Cu_2) was maintained at a constant lower temperature by a liquid cooled chiller. For higher accuracy and to check repeatability, resistance temperature detectors (RTD) with four-wire configuration were attached on the copper bars for precise temperature measurement. Two calibrated resistance temperature detectors (RTD_1 and RTD_2), placed on the two copper bars (Cu_1 and Cu_2), were used to measure the total temperature drop ($T_1 - T_2$) between RTD_1 and RTD_2, including the temperature drop through the specimen ($\Delta T, T_{1'} - T_{2'}$) between the top ($T_{1'}$) and bottom ($T_{2'}$) surfaces of the sample, temperature difference ($T_1 - T_{1'}$) from RTD_1 to Cu_1 bottom edge and temperature difference ($T_{2'} - T_2$) from Cu_2 top edge to RTD_2. The average temperature between T_1 and T_2 was kept at room temperature to minimize lateral heat flow. Temperature measurements, performed by the calibrated RTDs at the heater (T_{Heater}) and top edge of Cu_1 (T_{Cu1}) were used for calculation of emitted heat radiation to ambient environment. The ambient environment temperature (T_{RT}) was recorded by a digital thermocouple. All temperatures were measured in ℃ but converted to Kelvin.

After reaching thermal equilibrium, an axial temperature gradient was established through these components and the temperature drop (ΔT) across the specimen was determined from measurements and calculations as follows:

$$\Delta T = T_{1'} - T_{2'} = T_1 - \frac{(Q_H - Q_{RH} - Q_{RCu1T} - Q_{RCu1B}) \times \Delta L_1}{k_{Cu} \times A} - T_2 - \frac{(Q_H - Q_{RH} - Q_{RCu1T} - Q_{RCu1B}) \times \Delta L_2}{k_{Cu} \times A} \quad \textbf{4.1}$$

Q_H is the power of the heater, which is the product of supplied voltage (V) and current (I), Q_{RH} is the radiation emitted by the heater (T_{Heater}), Q_{RCu1T} is the maximum radiation emitted by the upper part of Cu_1 at T_{Cu1}, Q_{RCu1B} is the maximum radiation emitted by the lower part of Cu_1 at T_1, ΔL_1 is the length from RTD_1 to Cu_1 bottom edge, ΔL_2 is the length from Cu_1 top edge to RTD_1, k_{Cu} is the thermal conductivity of copper, A is the cross-sectional area of the copper. It was assumed that there was no emitted heat radiation from the thin sheet specimen. Because a hot object is radiating energy to its cooler surroundings at T_{RT}, the radiation loss takes the form:

$$Q_R = e\sigma A(T^4 - T_{RT}^4) \quad \textbf{4.2}$$

where Q_R is the total emitted radiation, e is radiation emissivity, σ is the Stefan–Boltzmann constant equal to 5.67×10^{-8} W/m^2·K^4, A is the radiating surface area. The amount of heat that flows through the specimen (Q_S) can be obtained by:

$$Q_S = Q_H - Q_{RTotal} = Q_H - Q_{RH} - Q_{RCu1T} - Q_{RCu1B} - Q_{RCu2} \quad \textbf{4.3}$$

where Q_{RTotal} is the total emitted radiation, Q_{RCu2} is the maximum radiation by the upper part of Cu_2 at T_2. Q_S is dominated by thermal conductivity (k_S), thickness (ΔL) and cross-sectional area (A) of the specimen and the temperature drop (ΔT) through the specimen according to the Fourier equation:

$$Q_S = k_S A \frac{\Delta T}{\Delta L} \quad \textbf{4.4}$$

Thermal conductivity of the specimen was calculated from:

$$k_S = \frac{Q_S \times \Delta L}{A \times \Delta T} \quad \textbf{4.5}$$

The thermal conductivity of the specimens (ER, PUF and SE) were tested using the setup described above at the School of Physics and Astronomy, University of Glasgow. After allowing 30 minutes to reach thermal equilibrium, the temperature data from RTDs was recorded using a LabView controlled system for 10 minutes. Thermal conductivities of the specimens were obtained by a combination of their measurements and equations.

Results of thermal conductivity

The measurement results of thermal conductivity for three materials: ER (k_{ER}), PUF (k_{PUF}), and SE (k_{SE}) are listed in Table 4.9. Two tests for each specimen were conducted and average results were taken as the inputs for finite element models.

Table 4.9 Results of thermal conductivity for ER (k_{ER}), PUF (k_{PUF}) and SE (k_{SE})

	k_{ER} (W/m·K)	k_{PUF} (W/m·K)	k_{SE} (W/m·K)
Exp. 1	0.57	0.029	0.18
Exp. 2	0.57	0.027	0.19
Average	0.57	0.028	0.185

4.2.3.2 Measurement of Specific Heat Capacity

Specific heat capacity, a measurable physical quantity, is the quantity of heat required to raise the temperature of a material per unit mass by one degree. The specific heat capacity of the material was determined using differential scanning calorimetry, a thermal testing method for measuring the response of a specimen over a temperature range. Differential scanning calorimetry (DSC) was used to measure the physical properties of a sample change (material transition) as a function of time and temperature. Following the stepwise-scanning method in British Standard BS ISO 11357-4:2005, the specific heat capacity of the materials at different temperatures was obtained [196].

The Principle of Specific Heat Capacity Measurement

To measure specific heat capacity of a sample, the scanning calorimeter monitored the temperature and heat flow from the quantity of heat (energy) absorbed or dissipated by the sample when subjected to a temperature profile. A standard reference sample was in the same controlled atmosphere. Based on a temperature difference between the sample and the reference material, the variation in heat flow was measured against temperature, to determine the endothermic heat absorbed and exothermic heat expelled by the sample and hence obtain the specific heat capacity.

A differential scanning calorimeter Q100 (Fig. 4.12 (a)) from TA Instruments was used in this study. The sample of mass of approximately 20 mg was encapsulated in a pan and an empty pan (Fig. 4.12 (b)) was used for reference. These pans were placed on a thermoelectric disk surrounded by a furnace, which was heated at a heating rate of 5 ℃/min from 0 ℃ to 150 ℃. In the furnace, the heat energy was transferred from the thermoelectric disk to the sample and the reference. The temperature difference between the sample and reference, caused by heat capacity of the sample, was measured by thermocouples on the underside of the thermoelectric disk. The specific heat capacity of the sample was calculated from the results of the temperature difference.

(a) (b)

Fig. 4.12 The instrument for measuring specific heat capacity (a) DSC Q100, TA Instruments, (b) DSC system components [197]

Results of Measurements of Specific Heat Capacity

The results of specific heat capacity of the materials (ER, PUF and SE) are shown in Fig. 4.13, which were obtained from the School of Chemistry, University of Glasgow. The values were used for thermal properties data in finite element models.

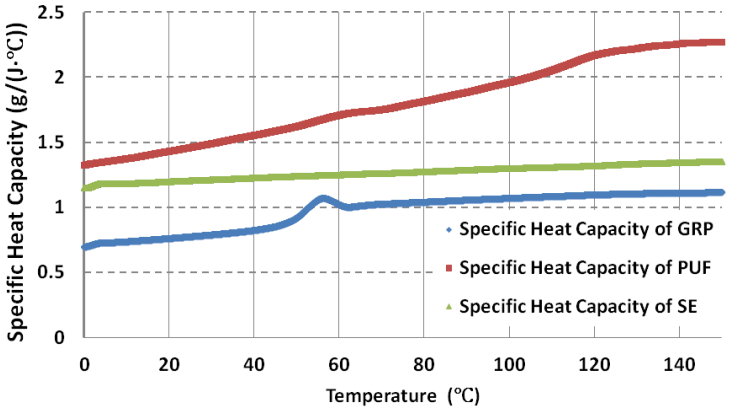

Fig. 4.13 The specific heat capacities of ER, PUF and SE between 0 ℃ and 150 ℃

4.2.4 Frequency and Temperature Dependency of the Materials

The tissue surrogates ER, PUF and SE are all polymers, which belong to a class of substances known as viscoelastic materials [198]. Because of the long-chain nature of polymeric materials, polymer viscoelasticity is a type of inter-relationship between elasticity, flow and molecular motion. The deformation of the materials includes some elements of both elasticity and flow, in other words, the materials respond to external

forces in a manner somewhere between the behaviour of an elastic solid and a viscous liquid thus known as viscoelastic [198, 199].

The mechanical properties of tissue mimics were obtained using uni-axial tests at a constant rate of strain similar to those used for other materials, such as metals. If mechanical tests were performed at different strain rates or temperatures, the stress-strain response varied. The response of polymer based materials is time/frequency and temperature dependent, which is inherent due to the intrinsic viscoelastic nature of the material. For characterisation of viscoelastic behaviour of polymeric materials during ultrasonic loading, tests and analysis approaches should be adopted for the tissue mimics to determine the manner in which properties vary with time/frequency and temperature.

4.2.4.1 Viscoelastic Materials

For elastic materials, stress is proportional to strain under small strain condition, which is a linear relationship known as Hooke's law. The relationship between stress σ and strain ε can be expressed as:

$$\sigma = \varepsilon E \neq f(t) \quad \textbf{4.6}$$

where E is the elastic modulus and t time. When the elastic solid is subjected to an external load, it will deform into a new equilibrium condition which stores all of the external energy. It will return to the original shape immediately the load is removed. No energy dissipation occurs in the elastic deformation regime.

In viscoelastic materials, the behaviour during deformation is dependent on both time (frequency) and temperature. For example, if the viscoelastic material is deformed by a constant load, which means the stress is held constant, the strain will increase with time. The mechanical behaviour of viscoelastic materials can be represented in terms of stress-strain as

$$\sigma = f(\varepsilon, t) \quad \textbf{4.7}$$

Stress is a function of time and strain. If strain and strain rate are infinitesimally small, the viscoelastic materials will behave linearly, which can be written as

$$\sigma = \varepsilon \cdot f(t) \quad \textbf{4.8}$$

where stress is proportional to a product of strain and a function of time. Energy is dissipated in viscoelastic materials when they are deformed under cyclic stresses.

In this application, power ultrasonic tests of the viscoelastic materials are based on time varying deformations or cyclic loading. When a viscoelastic material is subject to a force varying sinusoidally with time, a sinusoidal stress is developed and a sinusoidal strain is generated but lags behind the corresponding stress by a phase angle δ. The stress and strain can be express as follows,

$$\sigma = \sigma_0 sin\omega t \quad \textbf{4.9}$$

$$\varepsilon = \varepsilon_0 \sin(\omega t + \delta) = \varepsilon_0 sin\omega t cos\delta + \varepsilon_0 cos\omega t sin\delta \quad \textbf{4.10}$$

There are two components in the strain expression, the one ($\varepsilon_0 sin\omega t cos\delta$) in phase with strain and another ($\varepsilon_0 cos\omega t sin\delta = \varepsilon_0 sin\delta \sin(\omega t + \frac{\pi}{2})$) out of phase of stress by $\frac{\pi}{2}$. Because of phase lag and stiffness, the dynamic modulus of viscoelastic materials is regarded as a complex modulus E^*, represented by ordinary dynamic elastic (storage) modulus E' , measuring the material's elastic behaviour and mechanical loss modulus E'', measuring the viscous component of the modulus.

$$E^* = \frac{\sigma^*}{\varepsilon^*} = E' + iE'' \quad \textbf{4.11}$$

In terms of energy, the storage modulus is used to measure energy stored per cycle of sinusoidal deformation, and the loss modulus is used to measure energy dissipation or heat loss. The ratio of the loss modulus to the storage modulus is called damping or damping tangent, expressed as

$$tan\delta = \frac{E''}{E'} \quad \textbf{4.12}$$

The tangent of the phase angle is primarily used for calculating the energy dissipation in viscoelastic materials.

Applying sinusoidal strain ($\varepsilon_0 sin\omega t$) to a viscoelastic sample, the total work done in one cycle W can be calculated as:

$$W = \oint \sigma d\varepsilon = \oint \sigma \varepsilon dt \quad \textbf{4.13}$$

Because the stress can be related to the strain using the expression

$$\sigma = \sigma_0 \sin(\omega t + \delta) = \sigma_0 sin\omega t cos\delta + \sigma_0 cos\omega t sin\delta = E'\varepsilon_0 sin\omega t + E''\varepsilon_0 cos\omega t \quad \textbf{4.14}$$

$$W = \int_0^{\frac{2\pi}{\omega}} E'\, \varepsilon_0 sin\omega t(\varepsilon_0 cos\omega t)dt + \int_0^{\frac{2\pi}{\omega}} E''\varepsilon_0 cos\omega t(\varepsilon_0 cos\omega t)dt = 0 + \pi E''\varepsilon_0^2 \quad \textbf{4.15}$$

The average energy dissipated by heat loss per unit time, Q_{avg}, is calculated by,

$$Q_{avg} = \frac{W}{2\pi/\omega} = \frac{\omega\varepsilon_0^2 E''}{2} \quad \textbf{4.16}$$

4.2.4.2 Experimental Determination of Viscoelastic Properties

Dynamic mechanical analysis (DMA) is one of the fundamental methods to characterise the viscoelastic time/frequency and temperature dependent behaviour of a polymer. The time/frequency and temperature dependent behaviour of can be determined when a material sample with a known geometry is loaded with sinusoidal deformation. The monitored force at different temperatures is used to calculate the storage modulus, loss modulus and phase difference. These are related to the sample's stiffness, ability to dissipate mechanical energy and information on the relationship between the elastic and inelastic components respectively. The modulus-frequency and modulus-temperature behaviour for the tissue mimicking materials was determined using DMA to characterise their responses to cyclic loading.

The principle of DMA

DMA was used to measure the material response to sinusoidal stress under specific temperature conditions. A controlled sinusoidal deformation was applied to a sample of known geometry. By measuring both the amplitude of the deformation at the peak of the sine wave and the phase lag between the sinusoidal stress and strain, dynamic properties of the viscoelastic materials, quantities such as modulus and damping, were obtained [200].

As the dynamic modulus is a function of temperature and frequency, each time a sine wave is applied, the result of a modulus can be obtained by scanning a temperature or frequency range. This allows a series of data to be recorded. Traditionally, experiments are performed by cooling or heating the sample to a temperature, equilibrating, performing the experiments at each strain rate, and then loading a new sample and repeating them at the new temperature. Compared with traditional approaches, the modulus as a function of temperature and frequency can be obtained from DMA faster.

It is important for the application of power ultrasound to viscoelastic solids to map modulus or viscosity as a function of frequency. Modulus-frequency plots can show the change of a material's properties as frequency changes. Based on the time-temperature superposition principle and under certain conditions, experimental data obtained from frequency sweeps at a range of temperatures can be used to predict the behaviour of the material at high frequencies, which are not directly measurable by DMA. This will be discussed in detail in the next section.

Time temperature superposition principle

The time temperature superposition principle (TTS) provides a unique way of estimating material viscoelastic properties over time (frequency) for specific end-use applications. For viscoelastic solids, it states that time and temperature are equivalent so that the dynamic modulus at one temperature can be superimposed upon the modulus at another temperature by shifting the curves horizontally along the log time or log frequency scale [201].

Using the idea of time/frequency temperature equivalence, it was assumed that the changes seen by altering the temperature were similar to those caused by frequency changes. Therefore, to estimate the material properties at high frequencies where it is impossible to measure experimentally, modulus data, collected by DMA at different temperatures over smaller ranges of frequency, was used to build a master curve, which extends to the higher frequencies range. The frequency scan data was overlapped to construct the master curve. The master curve was created by selecting a series of frequency scan data, which was collected at specific temperatures in the vicinity of the glass transition temperature (T_g) over a short frequency range, to use as a reference curve. Other frequency scan data at other temperatures were then shifted to the reference curve with respect to frequency to

perform the superposition. After shifting the curves, the resulting master curve covered a range much greater than that of the original data [201].

There are two mathematical models commonly used for shifting a given set of data upon a temperature reference curve with respect to temperature. The theory of the models is based on considering the effect of temperature on relaxation time and the properties of viscoelastic solid. The time-temperature shift factor (α_T) reveals the relationship between the relaxation time at a given temperature $\tau(T)$ and the relaxation time at a reference temperature $\tau(T_0)$, which is expressed as

$$\alpha_T = \frac{\tau(T)}{\tau(T_0)} \quad \textbf{4.17}$$

For most polymers, the shift factor is calculated using the Williams-Landel-Ferry (WLF) equation as

$$\log(\alpha_T) = \frac{C_1(T - T_0)}{C_2 + (T - T_0)} \quad \textbf{4.18}$$

In this equation, C_1 and C_2 are constants, T is the measurement temperature, T_0 is the reference temperature. Therefore, the relevant modulus data at 20 kHz can be estimated using the resulting master curve after shifting a series of multiplexed frequency scans to a reference curve using TTS, which was described by Ferry as a "method of reduced variables" [202].

DMA experimental set-up

The Q800 Dynamic Mechanical Analyser (Fig. 4.14 (a)) from TA Instruments (Crawley, UK) is a thermal analysis instrument used to test the dynamic properties of the materials. By use of a dynamic force to deform a sample, viscoelastic behaviour can be derived. Dynamic mechanical analysers consist of several parts controlling the deformation, the temperature and sample geometry and environment. In this application, the fixture for controlling the deformation was dual cantilever (Fig. 4.14 (b)), which clamped both ends of the specimen but allowed the middle to flex. The dual cantilever bending mode is an appropriate general-purpose mode for evaluating thermoplastics and elastomers. The test samples of ER and PUF were cut to a size of 60 (length) ×10 (width) × 3 (thickness) mm.

To ensure accuracy, a digital calliper was used to measure the specimens' width and thickness prior to testing and the measured data was used as the input in the analyser. During the experiments, the sample was mounted on the dual cantilever clamp in a standard furnace, where the temperature was precisely controlled. The analyser was operated in multi-frequency, step-temperature mode, which assessed viscoelastic properties as a function of frequency, while the oscillation amplitude was held constant at 15 μm maximum. The test was run at multiplexed frequencies of 0.1, 0.2, 0.5, 1, 2, 5, 10, 20, 50, 100 Hz in temperature step experiments. In total, 10 frequencies were swept at set temperatures ranging from -20 to 100 ℃ for ER and -20 to 170 ℃ for PUF, increasing in 10 ℃ steps. Cold nitrogen gas was supplied by controlled heating of liquid nitrogen and programmed during the run to make the analyser operate at subambient temperatures.

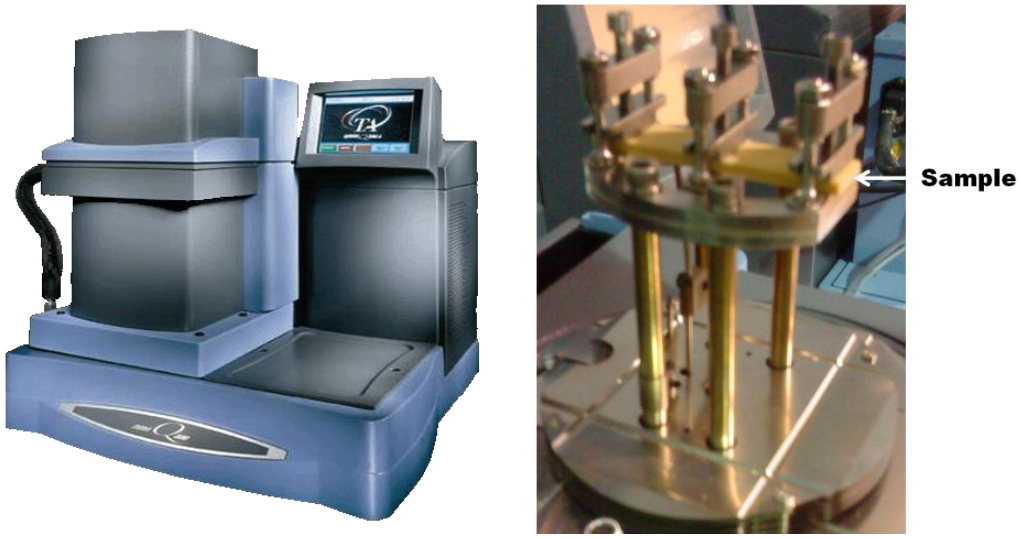

(a) (b)

Fig. 4.14 Dynamic mechanical analyser (a) Q800 and (b) dual cantilever clamp [197]

The DMA tests for SE were different from the tests for ER and PUF, due to the use of a compression clamp (Fig. 4.15) instead of a dual cantilever. The compression clamp fixture was designed for elastomers with low Young's modulus. The prepared sample for compression DMA was moulded into a cylinder 8 mm thickness and 15 mm diameter. In the compression mode, the sample was placed on a fixed flat surface and a top oscillating plate applied the force. The test was run at multiplexed frequencies in temperature step experiments (from -60 to 60 ℃). Other experimental settings were the same as for ER and PUF.

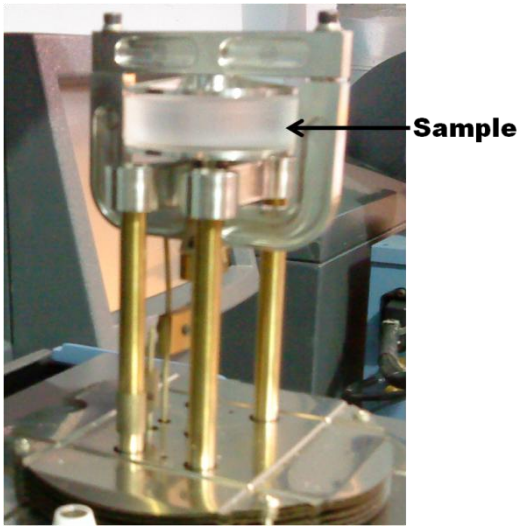

Fig. 4.15 The compression clamp of the dynamic mechanical analyser for SE

DMA experimental results

The frequency and temperature dependent behaviour of ER, PUF and SE were measured using frequency multiplexing techniques (0.1-100 Hz) in the temperature ranges -20 to120 ℃ for ER, -20 to 160 ℃ for PUF, and -60 to 60 ℃ for SE by the dynamic mechanical analyser at the Department of Mechanical and Aerospace Engineering, University of Strathclyde.

As shown in Fig. 4.16, the storage modulus of ER decreased with increasing temperature, and a critical change of mechanical properties was observed between 40 and 50 ℃ with reduction in the storage modulus by 85%-90%, which corresponds to the glass transition temperature. To align the individual experimental data points with points on the reference temperature curve, TTS generated the master curve of storage modulus (Fig. 4.17) by shifting the points using the equation 4.18. A commercial software package, TTS Rheo Advantage Data Analysis from TA Instruments was used to determine the constants C_1=146.8, C_2=655.4 K, standard error: 10.72, shown in Fig. 4.18. The shift factor was calculated based on a reference temperature of 19.9 ℃. The storage modulus of ER was obtained around 13.9 GPa at 20 kHz from the master curve in Fig. 4.17. The damping tangent was not constant in the temperature range from 20 to 100 ℃, shown in Fig. 4.16.

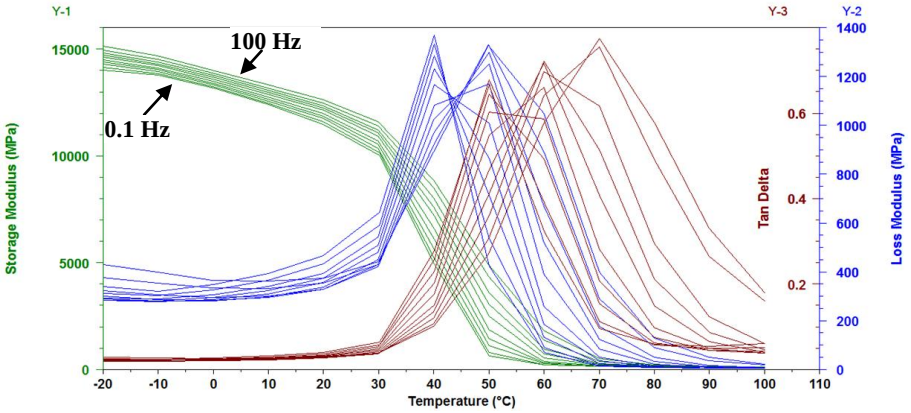

Fig. 4.16 The storage modulus, loss modulus and damping tangent of ER at multiplexed frequencies in different temperatures between -20 ℃ and 100 ℃

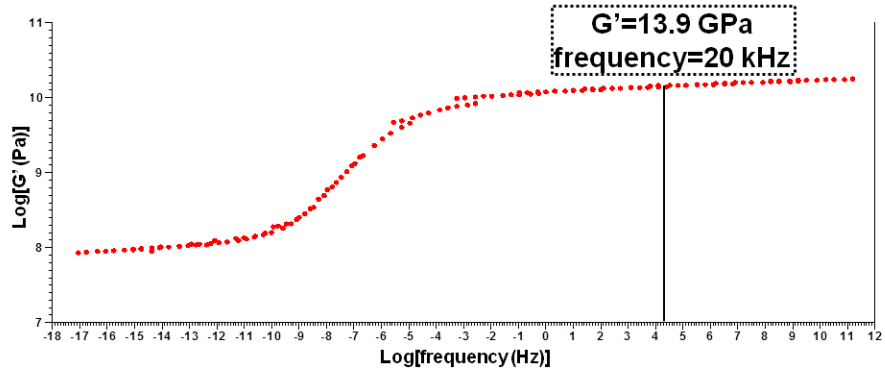

Fig. 4.17 The master curve of storage modulus generated for ER at reference temperature of 20 ℃ and frequencies between 10^{-18} and 10^{12} Hz

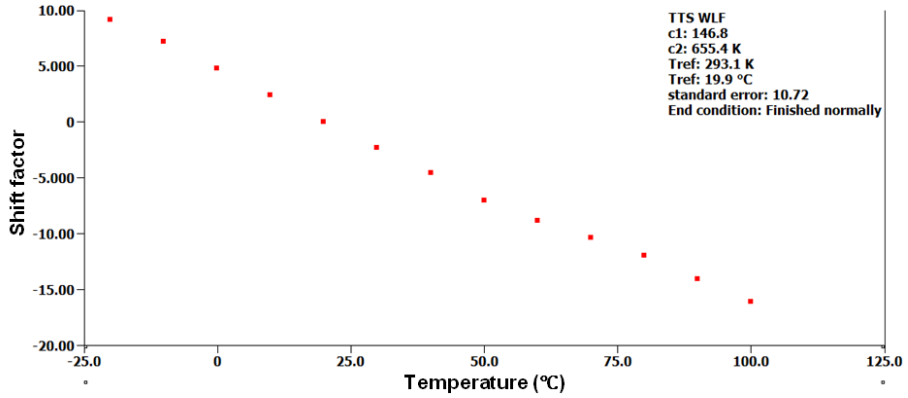

Fig. 4.18 The WLF equation of storage modulus shift factor kit for ER at temperature between -25 ℃ and 100 ℃

The storage modulus, loss modulus and tan delta of PUF are shown in Fig. 4.19. The glass transition temperature of PUF was around 130 ℃, which was much higher than room temperature. Compared with ER, the frequency and temperature dependent behaviour of PUF is not obvious. It was not possible to obtain the master curve at room temperature for reference using TTS, because the glass transition temperature was not near room temperature. At high frequencies and low temperature, the storage modulus increased into

the glassy range. As the frequency increases beyond the capability of the polymer chains to respond, the polymer glassifies with a nearly constant storage modulus. Therefore, the value of the elastic modulus obtained from static compression tests was constant in ultrasonic application around room temperature. The elastic modulus was considered to be the storage modulus in the high frequency low temperature applications. The damping tangent was obtained from the master curve of damping at frequency 20 kHz and 120 ℃, which was around T_g (Fig. 4.20).

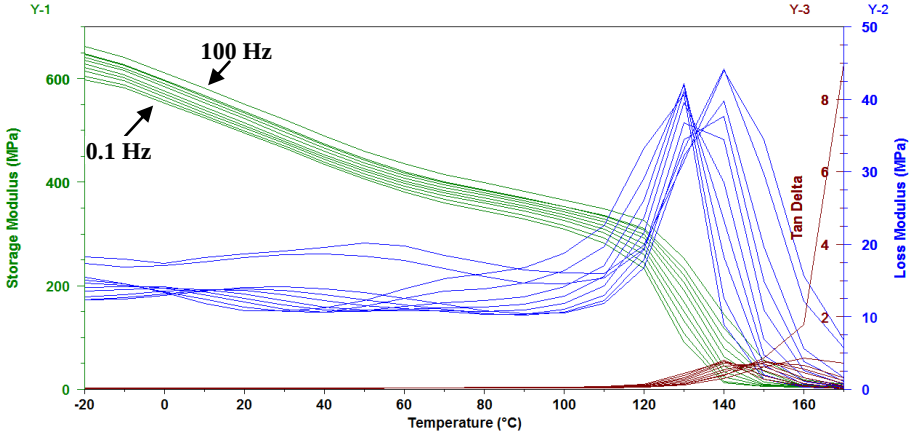

Fig. 4.19 The storage modulus, loss modulus and damping tangent of PUF at multiplexed frequencies at temperature between -20 ℃ and 170 ℃

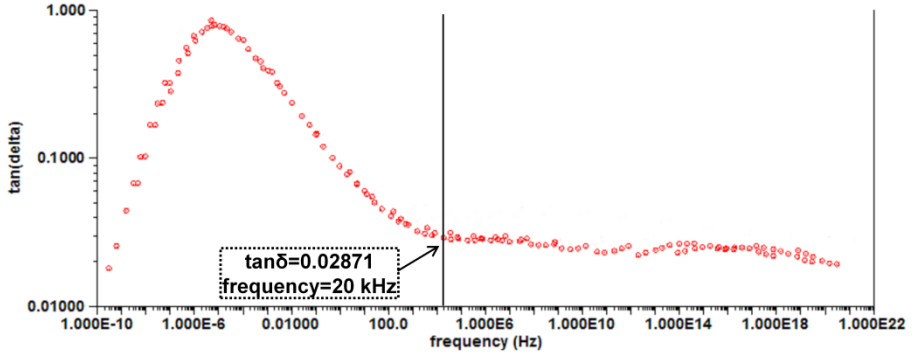

Fig. 4.20 Damping tangent of PUF at frequency 20 kHz and temperature 120 ℃

From the DMA results of SE (Fig. 4.21), the storage modulus was not dependent on the surrounding temperature in the range of -60 to 60 ℃, but increased with loading frequency from 0.1 to 100 Hz. The master curve of SE cannot be generated based on the WLF equation and so the modulus of SE used in the finite element model for ultrasonic loading was not determined from the DMA tests.

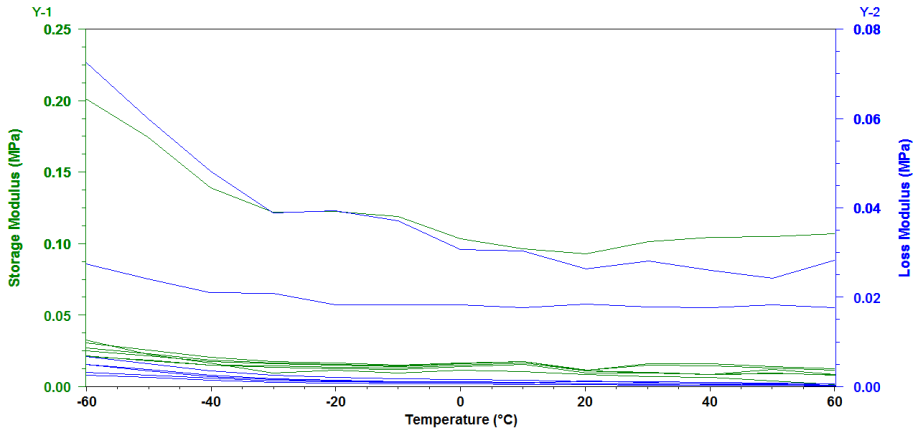

Fig. 4.21 The storage modulus and loss modulus of SE at multiplexed frequencies at temperatures between -60 ℃ and 60 ℃

Extensive measurements in the frequency and temperature domains of ER and PUF and subsequent deduction of the master curves establish the mechanical and thermal behaviour for cyclic deformations over a frequency range of several decades, not all of which can be accessed realistically at any one temperature and frequency. To examine the applicability of the TTS principle for this ultrasonic application, experiments and FE models were carried out and created. The comparisons between experiments and FE models determined by the experimental materials characterisation and with the aid of TTS principle could provide the confidence in determination of viscoelastic behaviour in ultrasonic application using DMA and TTS principle.

4.2.5 Extracting Material Properties for Finite Element Modelling

Once the thermal and mechanical properties of the specimen had been characterised, it was necessary to determine the material response to power ultrasonic loading using finite element analysis. Material models in the finite element packages were used to represent the experimental data in a convenient form, which was used in the solution of the finite element problems.

An elastic material model was available in ABAQUS to simulate the harmonic vibration response at 20 kHz using displacement and strain fields. The elastic material model describes the material behaviour using fundamental engineering properties including density, Young's modulus and Poisson's ratio. Due to the frequency effect on modulus, the Young's modulus for ultrasonic loading at 20 kHz for ER was calculated from the DMA data instead of from static compressive test data. In contrast, the Young's modulus for PUF during ultrasonic loading used in the finite element models was from the data by static

compressive test data operating at room temperature. In the tests of ultrasonic loading, the sample was vibrated at 20 kHz. Because the glass transition temperature of PUF was measured up to 130 ℃ and the loading frequency was high, the storage modulus was in the glass range beyond the capability of the polymer chains to respond. In contrast, due to the rubber region of SE being at room temperature, the storage modulus of SE was heavily dependent on loading frequency. The Young's modulus used in the finite element model for SE was not from compressive tests but calculated from the shear relaxation modulus data measured by Lu et al. using a dynamic nanoindentation test following the equation

$$E = 2G(1 + \upsilon) \quad \textbf{4.19}$$

where E is the Young's modulus, G is the shear modulus, and υ is the Poisson's ratio [203-205].

To obtain the thermal response during ultrasonic loading, another finite element package PZFlex was adopted with a thermo-mechanical model, which was represented by density, Young's modulus, Poisson's ratio, damping Q factor, thermal conductivity, and specific heat capacity. The damping Q factor was calculated from DMA tanδ data following [206]

$$Q = \frac{1}{tan(\delta)} \quad \textbf{4.20}$$

to extract internal heat generation by ultrasonic vibration induced heat dissipation. Thermal conductivity and the specific heat capacity were used for mapping the temperature field by thermal conduction. Because it is not measureable for transparent SE using non-contact IR camera, the thermal response was not recorded for SE.

The parameters of materials properties for finite element models (listed in Table 4.10) will be explained in chapter 5.

Table 4.10 The parameters of materials properties for finite element models

	PZFlex Models					
	ABAQUS Models			Q Value	Thermal Conductivity (W/m·K)	Specific Heat (kg/(J·K)
	Density (kg/m^3)	Young's Modulus (MPa)	Poisson's Ratio			
ER	1640	13.9	0.3	36.62*	0.57	760
PUF	500	563	0.3	34.8	0.028	1573
SE	1100	13	0.495	-	-	-

*Damping loss Q value for ER is temperature dependent and the value 36.62 is measured at room temperature.

5. Non-invasive Field Measurement Techniques and Numerical Models

5.1 Introduction

Measurements of a wave front using a hydrophone, a traditional device for ultrasonic pressure field characterisation, have shown to be extremely difficult in solid materials. Thus, it is necessary to develop other methods to study the power ultrasonic effect on biological tissue. Compared with conventional ultrasonic field measurement techniques involving hydrophone or sensor probe insertion into the medium, non-invasive field measurement techniques are a more attractive option for development in this project.

In this chapter, non-invasive field measurement techniques instead of traditional contact measurement techniques are introduced and developed to evaluate the power ultrasonic mechanical and thermal effects on solids, and numerical models are created to compare with the experimental findings with the aim of validating the approach.

First, a brief introduction of the ultra-high speed camera system and image techniques, with special emphasis on 2D in-plane full-field digital image correlation (DIC) is presented. In addition, the experimental preparation and set-up are presented, which included specimen preparation, set-up of the power ultrasonic system, and camera configuration and lighting set-up. The displacement and stress/strain fields of the solids during power ultrasonic loading can be characterised by the DIC technique with an ultra-high speed camera.

Next, a non-contact temperature measurement technique, thermal imaging, using an infra-red (IR) camera is presented. Under ultrasonic loading, heat generation can take place in the specimen leading to high temperatures in the zones where stresses are concentrated. The heat generated in the specimen due to conversion of mechanical energy to thermal energy was detected by the IR camera, which provides the results of temperature distribution. The fundamental process by which ultrasonic wave energy is converted to thermal energy and thermal imaging techniques are discussed.

Then, an optical measurement technique is described for characterising the power ultrasonic field generated in a transparent viscoelastic solid using the acousto-optic effect, with a laser Doppler vibrometer and full-field scanning techniques. The experimental

arrangement by precise manipulation of the laser scanning of the transparent specimen is presented followed by an introduction to the basic principle of acousto-optic theory.

Finally, the numerical models for verification of and comparison with experimental results were created based on analytical and finite element methods. Ultrasonic fields including displacement and stress/strain fields were simulated by numerical analyses. Temperature distributions in the process of ultrasonic loading on materials were modelled by a coupled thermo-mechanical finite element analysis.

5.2 Digital Image Correction & Ultra-high Speed Camera

5.2.1 Introduction

The primary aim of this study was to find techniques to detect the stress/strain and temperature fields in surrogate tissue specimens, which are excited at ultrasonic frequencies. Traditionally, contact extensometery is used to measure the strain between two points, which provides the average strain over the gauge length. However, the extensometer can influence small or delicate test specimens due to being attached to the specimen thus applying additional mechanical loading.

A non-contact and full-field strain measurement system with high accuracy is required for this application for dynamic testing at ultrasonic frequencies. The advent of digital imaging at ultra-high frame rates now allows recording of the response of vibrating samples using laboratory or commercial systems. Post-image processing can be used to measure vibration displacements and calculate the associated strain in full-field. By this non-contact imaging technique, it is possible to image vibrating samples at ultrasonic frequencies and, specifically, visualise the mechanical deformation during ultrasonic excitation of tissue surrogate samples. Experimental setups were developed to facilitate the manipulation of the displacement and strain/stress fields under evaluation.

5.2.2 Digital Image Correlation

5.2.2.1 Description of the Digital Image Correlation Method

Digital image correlation (DIC), a non-contact displacement measurement technique, is a full field image analysis method, which is based on a comparison between grey-scale digital images of a test piece at different stages of deformation under load. By tracing

blocks of pixels, 2D DIC determines the surface displacements of the test piece in order to create in-plane surface strain maps.

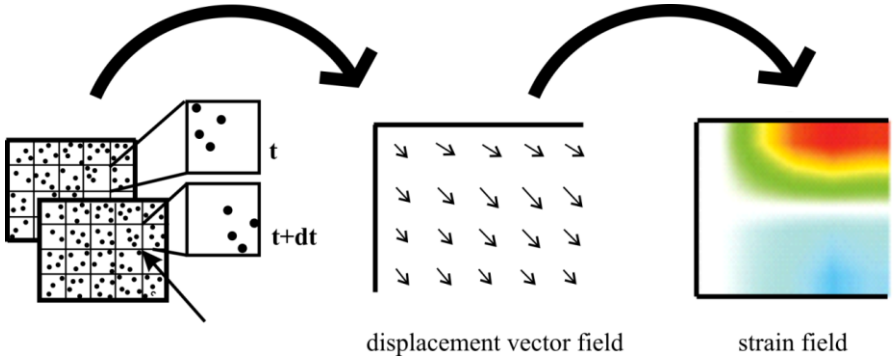

Fig. 5.1 The principle of 2D digital image correlation showing the relative motion of pixels between frames that are used to calculate the displacement vector field and thus the strain field [207]

The basic principle of 2D DIC (Fig. 5.1) is to match the same pixels between sequential images, which are recorded in different states of deformation at different times. The recorded images are divided into overlapping subsets, which are formed by adjacent pixels. The pixels contain a numerical grey-scale value, which is related to the digitized light intensity. The distribution of pixel intensity is used to correlate the images. Because the subset has a wider variation in grey levels, it can be more uniquely identified and can be used in a correlation procedure more accurately than an individual pixel. During the DIC process, the undeformed image is adopted as a reference image and is then compared with subsequent images after deformation using pattern recognition and matching procedures to search for and recognise a specific subset in the series of images.

The numerical correlation procedure is a feature of the software (Fig. 5.2). In an undeformed reference image, there is a square reference subset, inside which a point P with coordinates (x_i, y_j) is located. The intensity of the reference subset pixels is represented by $F(x, y)$ and the point $F(x_0, y_0)$ is located at the centre of the reference subset. After deformation, the reference subset has moved to a new location means that point P has moved to P' of coordinates (x_i', y_j') and centre point from F to F' of coordinates(x_0', y_0'). The coordinates of point P'can be obtained from equations 5.1 and 5.2,

$$x_i' = x_i + u + \frac{\partial u}{\partial x}\Delta x + \frac{\partial u}{\partial y}\Delta y \quad \textbf{5.1}$$

$$y_j' = y_j + v + \frac{\partial v}{\partial x}\Delta x + \frac{\partial v}{\partial y}\Delta y \quad \textbf{5.2}$$

where u and v are the horizontal and vertical components of the displacement of the centre marker $F(x_0, y_0)$. By solving the variables u and v, the in-plane (subset) deformation in the x direction and y direction can be obtained respectively. Using the intensity of the reference subset $F(x, y)$ and target subset $F'(x', y')$, the best match between the reference and target subset to find the values u, v and $\partial u/\partial x, \partial u/\partial y, \partial v/\partial x, \partial v/\partial y$ (subset distortion) can be achieved by minimizing the correlation function S, which is expressed as follows,

$$S = 1 - \frac{\sum_i \sum_j F(x_i, y_j) F'(x_i', y_j')}{\sqrt{\sum_i \sum_j F^2(x_i, y_j) \sum_i \sum_j F'^2(x_i', y_j')}} \quad \textbf{5.3}$$

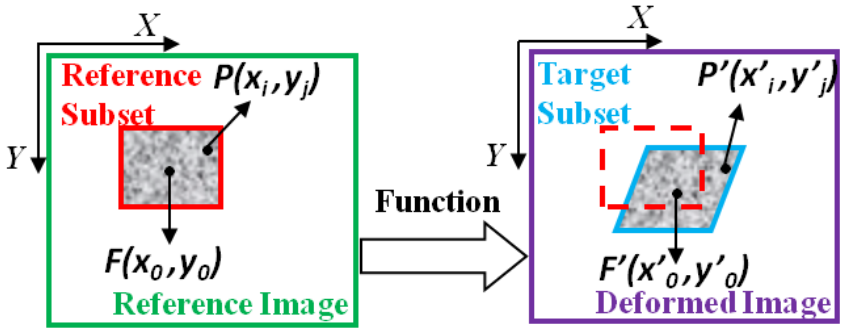

Fig. 5.2 The numerical scheme of the correlation procedure

To obtain better distinguishing subsets in each image, a high-contrast speckle pattern is applied to the sample prior to imaging. A comprehensive review of the 2D DIC process has been presented by Pan et al. [208].

5.2.2.2 DIC Analysis for the Application

In this application, the DIC analysis was conducted using a Matlab based program developed at Johns Hopkins University [209, 210]. The software was based on the implementation of the Matlab image registration function CPCORR, which performs normalized cross-correlation to track user-defined marker positions between the undeformed reference and subsequent deformed images. Each marker point is centred on the subset (region-of-interest). Displacement vectors for each marker can be determined by the difference between the pixel coordinates of the reference and deformed subset centre

points. Using a grid of equally spaced marker positions, displacements can be interpolated to give full-field displacement measurements. The strain was calculated by differentiation of the displacement field. During the process of correlation, since the subsets are tracked, rather than individual pixels, highly accurate measurements can be obtained at sub-pixel resolution.

The ultrasonic vibration amplitude within the surrogate bone samples used in this study was of the order of a few microns. These displacements are less than the maximum traceable displacement (up to 4 pixels) in the range of the subset, and therefore DIC could track the displacement in the subset by correlating consecutive images using the undeformed image as a reference. Another consideration is the density and size of the grid. Markers were used on the grid to represent the position of each image subset to be tracked. A grid with a marker spacing of 10 pixels in the horizontal and vertical directions of the image was created, using a subset size of 20×20 pixels, giving sufficient accuracy and sufficient subset size for the limited camera resolution, which defined by the camera (Shimadzu HPV-1 hired from EPSRC engineering instrument pool). The size of grid markers should be selected to avoid marker overlap and smoothing effects.

5.2.3 Ultra-high Speed Camera

Ultra-high speed photography was used to monitor the deformation of the specimen during ultrasonic vibration. The introduction of the charge coupled device (CCD) revolutionized imaging technology from film to digital and sped up the development of high speed photography. There is a new technique for capturing images at extremely high speeds with an ISIS-CCD chip (in situ storage image sensor CCD), a typical interline transfer CCD chip, which can quickly transfer each pixel into its register in microseconds by integrating the memory on board into the CCD chip [211].

In order to capture in detail the initial transient interval where the cycles of vibration amplitude build-up can be characterised for power ultrasonic excitation at 20 kHz, an image acquisition rate of more than 200 kHz is required, which is dependent on the performance of the ISIS-CCD camera. The Shimadzu HPV-1, ultra-high speed camera (Fig. 5.3 (a)) is capable of up to 1 million frames per second (fps), recorded image data at 250 kfps. The camera resolution is limited to 312×260 pixels with a 10 bit dynamic range. The number of acquired frames at any frame rate was fixed at 102. The digital frame was 8

bit images, which provided pixel intensity with 256 greyscales. To provide adequate lighting, two photographic flash guns, Nikon speedlight SB 900 (Fig. 5.3 (b)), were used for specimen illumination. To improve the quality of images, the aperture of the camera lens was set at f2.8, using a Nikon 24-85mm macro zoom lens, and the camera exposure time was fixed at $1/8^{th}$ of frame rate, which was the minimal setting for the camera.

(a) **(b)**

Fig. 5.3 Ultra-high speed photographic system: (a) Shimadzu HPV-1, high speed camera and image control and display system [212], (b) flash gun: Nikon speedlight SB 900 [213]

5.2.4 DIC & Ultra-High Speed Camera for Dynamics

Due to the availability of ultra high speed cameras at high resolution and new developments of computer technology, DIC has a wide range of applications in experimental mechanics and is being used in transient dynamic events. There have been a number of published studies using DIC with ultra-high speed cameras for full-field measurements to examine the mechanical response of specimens to dynamic loading, which were reviewed in section 2.4. The vibration measurements reported previously mainly illustrated the observed full displacement field of the test pieces. The strain field, relevant in investigating internal heat generation, was not extracted from the displacement field. To extract the vibration response including displacement and strain distributions from test-pieces excited at ultrasonic frequencies, it is possible to use an ultra-high speed camera. In this study, the Shimadzu HPV-1 with 2D DIC was used as described by Reu [211], allowing full-field measurement of the vibrational response of surrogate bone material specimens excited by a power ultrasonic device.

5.2.5 Experimental Set-up

5.2.5.1 Specimen Preparation

To compute the specimen full field deformation under dynamic load, the surface of the sample should have a random speckle pattern for image tracking. The pattern should be non-repetitive, isotropic and high contrast. Normally, the surface should be coated by spraying a black and white pattern of adequate spot size, which should cover several pixels (3-5 pixels) on images, avoiding too fine pattern elements.

The sample size was 50×10×4 mm and the sample surface was prepared with a random speckle pattern (shown in Fig. 5.4), achieved by spraying first with white paint and then adding black paint such that the random black dots met the required size of several pixels [214]. It was essential that adequate contrast was applied to the sample, to allow for precise measurement of the changes in grey scale distribution. Matt paints were used to avoid specular reflections and ensure all areas were covered by the speckles.

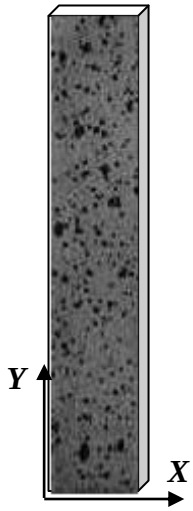

Fig. 5.4 The prepared sample captured using Shimadzu HPV-1

5.2.5.2 Image Acquisition by Camera Setting

The vibration response of samples to excitation at 20 kHz by the ultrasonic horn as described in chapter 3 was measured using 2D DIC with an ultra-high speed camera. The DIC experimental setup is shown in Fig. 5.5 (a), with the schematic in Fig. 5.5 (b). The test sample was bonded to the output face of the tuned ultrasonic horn, which was excited by a longitudinal mode Langevin transducer incorporating a piezoceramic PZT stack tuned at 20 kHz. The PUF sample vibrated in resonance in its second longitudinal mode, as

predicted by finite element analysis. The ER sample was not vibrating in resonance due to the single excitation frequency being some way from the natural frequency of the sample.

During ultrasonic excitation of the specimen, the Shimadzu HPV-1 ultra-high speed camera captured images, while two Nikon SB 900 flash guns were utilised simultaneously with the camera to illuminate the specimen, which was planar, parallel to and at a constant distance from the camera. The trigger was controlled to initiate image acquisition and flash exposure with a delay of 400 μs, giving stable lighting during image acquisition. Since the flash exposure lasted over 1 ms, which is longer than the frame integration time, 102 frames could be obtained during one exposure. The camera control unit allowed control of the camera set-up and stored the images for DIC analysis.

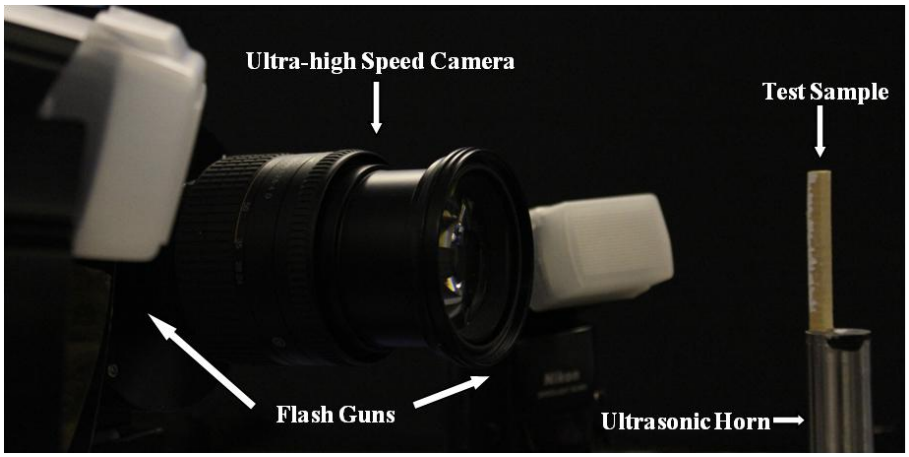

(a)

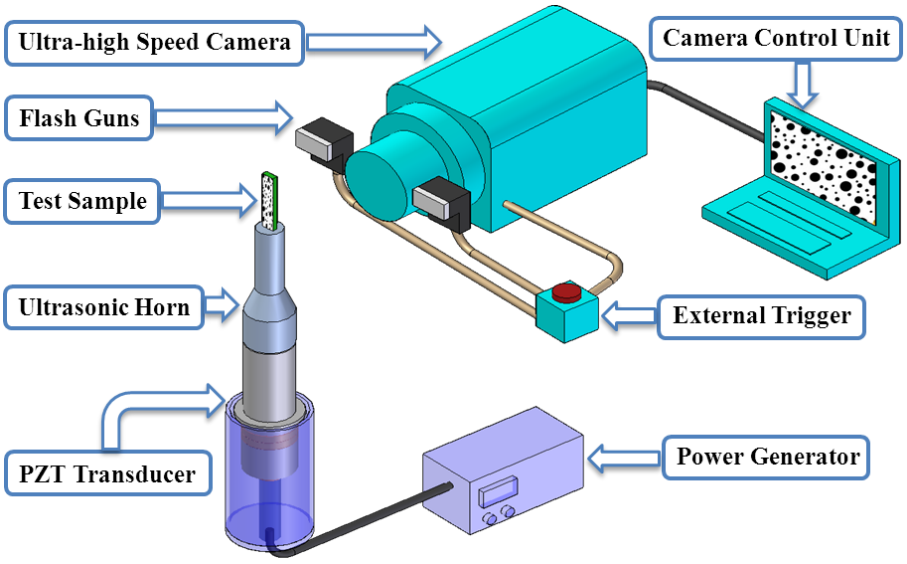

(b)

Fig. 5.5 (a) DIC Experimental set-up and (b) schematic of DIC experimental set-up

To record images of the planar surface of the specimen before and after loading, two sets of images were acquired. The first set was acquired from the undeformed specimen, providing the reference image. During ultrasonic excitation, acquisition of a second set of images was controlled by the external trigger, which was used to capture images when a steady-state vibration in the sample was achieved.

5.3 Thermal Imaging by Infra-red Camera

5.3.1 Introduction

Mechanical vibrations at sufficiently high amplitude can influence the physical properties of materials. In power ultrasonic applications, high frequency mechanical oscillations generate heat inside the materials as a result of absorption of the ultrasonic wave energy. Damage to the materials can be caused by cyclic loading and internal heating induced by the high temperature. It is therefore necessary to obtain the temperature distribution to assess the ultrasonic effects on materials.

The temperature of specimens subjected to power ultrasonic vibration rose due to heat generated during cyclic deformation [215]. Since the thermal effects of ultrasonic excitation are also critical in characterising the potential benefits or hazards of ultrasonic surgery, thermal analysis using thermal imaging is also adopted as a noncontact system that displays thermal radiation visually. An IR camera is suitable and the device, that detects and displays the amount of infrared energy emitted, transmitted and reflected by the sample. It means that the temperature distribution of the sample under ultrasonic vibration can be determined.

5.3.2 Infra-red Camera

Thermocouples, often used to detect temperature, can either be attached to or inserted into the samples being measured. However, these methods are invasive, altering both the geometry and dynamic behaviour of the sample, and are subject to other limitations, including difficulty in locating the peak temperature and mapping the thermal distribution and producing localized heating in the sample. Therefore, for full-field surface temperature detection, IR thermography can produce images of specimen surface temperature due to ultrasonic excitation using a thermographic camera.

The IR camera (T425, Flir, Wilsonville, US) was chosen as a noncontact instrument to provide a visual display of specimen heating. The camera, shown in Fig. 5.6, measures temperature in the range -20 to 1200 ℃ and captures thermal images at 9Hz, which is sufficient for recording the heating accumulated from ultrasonic excitation. The thermal sensitivity is 50 mK and the image resolution is 320×240 pixels.

Fig. 5.6 Infra-red camera, Flir T425 [216]

5.3.3 Thermo-mechanical Effects

Several thermo-mechanical effects are activated when mechanical cyclic loading is applied to a sample material. Temperature changes observed in the material during cyclic loading are caused by a combination of thermoelasticity (temperature variation due to thermoelastic effects), heat generated by reversible anelastic damping and irreversible plastic deformation (temperature variation due to heat dissipation) and internal friction [217].

During elastic loading, the temperature change varies in proportion to applied stress due to thermoelastic effects. It is related to the thermal expansion coefficient, specific heat capacity and initial temperature. Detection of thermoelastic effects requires high resolution due to small temperature changes. A small amount of dissipated heat energy due to anelastic thermal effect is generated by the energy loss in the mechanical hysteresis loop, which induces the temperature changes. As the stress amplitude approaches the yield strength, large amounts of dissipated heat are observed due to additional micro-plastic or

plastic deformations. Almost all the irreversible mechanical energy due to the anelastic deformation will be converted into heat.

Excitation of the thermo-mechanical effects at ultrasonic frequencies at low stress levels results in different damping mechanisms [217]. Because stress in the specimen is below the elastic limit, the dissipated energy mainly comes from internal material damping and the local plastic deformation at a microscopic scale.

The energy loss of ultrasonic waves passing through a medium increases with travel distance. The ultrasonic wave experiences attenuation (mainly induced by internal material damping) which is a type of viscoelastic response in the material. A distributed temperature field can be produced due to attenuation of the waves when the ultrasound is propagating in a solid.

5.4 The Acousto-optic Effect and its Measurement

5.4.1 Introduction

By detecting optically the change in refractive index, which is due to the change in density of transparent medium during the propagation of ultrasound, a non-invasive method based on the acousto-optic effect has been developed for stress field characterisation in a viscoelastic solid. A laser Doppler vibrometer, producing a laser beam passing through an acoustic field generated by an ultrasonic horn, is used to detect ultrasonic stress induced optical phase shifts. The total phase change induced in the laser beam is representative of the average stress value along the laser path. Stress can be calculated from the optical phase change across the width of the acoustic field. Scanning routines and image reconstruction algorithms combine together to map the stress field from the acquired phase modulated data [218].

5.4.2 Acousto-optic Effect

The interaction between low-frequency ultrasound and light waves provides a method to visualise the acoustic field, which modulates the amplitude and phase of light in a transparent medium. The basic principle of the visualisation of a sound field by light is known as the acousto-optic effect, which was first predicted by Brillouin in 1921 [219] and experimentally confirmed by Debye and Sears [220] and Lucas and Biquard in 1932 [221].

Raman and Nath in 1936 [158] and Phariseau in 1956 [222] presented theoretical models to explain this phenomenon. The developments of laser technology in the 1960s and signal processing technologies benefited the broad applications of acousto-optics.

The technique for the non-invasive measurement of acoustic fields is to characterise the acoustic stress fluctuation due to ultrasonic vibration. For a harmonic low-frequency ultrasonic wave, in this case a longitudinal wave oscillating along its propagational direction, the longitudinal displacement $u(x,t)$ in the medium can be described by:

$$u(x,t) = Asin[\omega\left(t - \frac{x}{c}\right) + \varphi] \qquad 5.4$$

where A is amplitude, ω is angular frequency, φ is phase angle at $x = t = 0$, c is phase velocity.

When the wave propagates through the medium, a series of alternating regions of compression and rarefaction (Fig. 5.7) are produced under the action of the mechanical strain. Compression regions have greater number of molecules per unit volume than rarefaction regions, which means the compression and rarefaction phases change the permittivity of the medium, alter its density and cause the inhomogeneous distribution of refractive index, in this case dynamically by the oscillating ultrasonic wave. The compression phase results in a stress increase to the ambient stress in the medium, whereas the rarefaction phase results in a stress deficit.

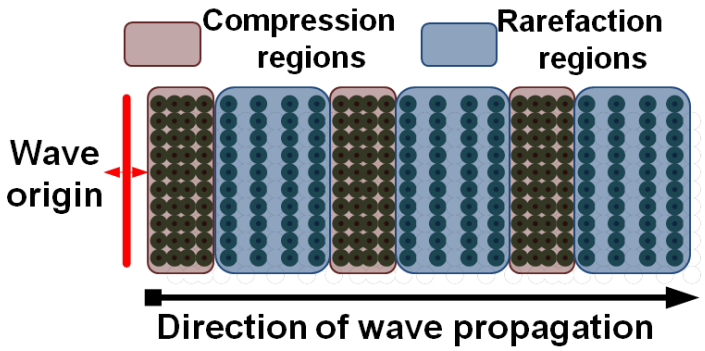

Fig. 5.7 Compression and rarefaction regions due to longitudinal wave propagation through a medium

In general, the refractive index of the transparent medium which is a function of permittivity (equation 5.5) increases with its density. The variation of the transparent refractive index of the medium diffracts the incident light and influences its amplitude and

phase. Practically, diffraction of light by an acoustic field can be neglected due to the small amplitudes of acoustic field in the low ultrasonic frequency application [223].

The refractive index is defined as

$$n = \sqrt{\varepsilon_r \mu_r} \quad \textbf{5.5}$$

where n is the refractive index of the medium, ε_r is the relative permittivity of the medium, μ_r is the relative permeability (for most materials, μ_r is very close to 1 at optical frequencies [224]).

The relative permittivity is expressed as:

$$\varepsilon_r = \frac{\varepsilon}{\varepsilon_0} \quad \textbf{5.6}$$

where ε is the absolute permittivity of the medium, ε_0 is the permittivity of free space approximately 8.85×10^{-12} F/m.

As discussed above, in a transparent coupling medium, acoustic stress fluctuations induce alternations in local density, which modulates the refractive index of the medium. In this case, the viscoelastic properties of the medium, silicone elastomer, which has a sufficiently low refractive index to prevent light loss, is similar to a incompressible liquid. Therefore, the applied acoustic stress to the incompressible medium makes it without changing its shape. The density of the medium goes up as the stress increases. The relationship can be considered linear between acoustic stress and refractive index, shown in equation 5.7, when the acoustic wave propagates in the medium.

$$\mu_{op} = \frac{\delta n}{\delta \sigma} \quad \textbf{5.7}$$

where δn is the variation in ambient refractive index, $\delta \sigma$ is the variation in ambient stress, $\mu_{op} = 2.7 \times 10^{-9}$ Pa^{-1} in air.

The refractive index of the compression and rarefaction regions can be defined as:

$$n = n_0 \pm \delta n \quad \textbf{5.8}$$

where n_0 is refractive index when there is no acoustic wave present.

As demonstrated above, the variations of refractive index, δn, due to harmonic wave propagation can be presented as:

$$\delta n(t) = n_1 \sin\left[\omega\left(t - \frac{x}{c}\right)\right] \quad \textbf{5.9}$$

where n_1 is the maximum change in refractive index, c is the speed of ultrasound wave in the medium.

Under such conditions, as light travels through the ultrasonic wave field, due to change in refractive index, the path length of the light r is modified according to equation 5.10, which means the light travels faster or slower depending on the stress fluctuations.

$$r = dn \quad \textbf{5.10}$$

where d is the geometric length of the path light follows through the medium.

The change in the optical path length produces variations in phase of emerging light from the unchanged incident light (Fig. 5.8), when the light travels through the transparent medium with different refractive index at different parts.

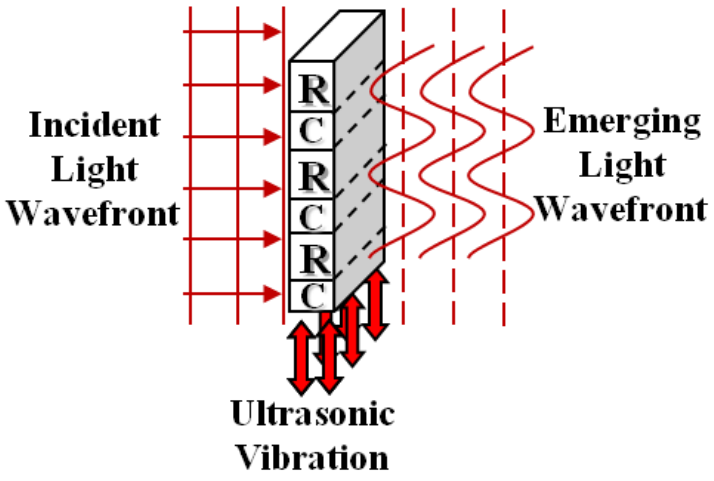

Fig. 5.8 Light wavefronts impinging on a refractive index variation due to ultrasonic wave propagation where 'C' represents compression and 'R' represents rarefaction

To quantify the variations in phase, a laser Doppler vibrometer has been used to perform the measurements, which is a non-invasive method of measuring the acoustic field in the transparent solid caused by ultrasonic vibration.

5.4.3 Laser Doppler Vibrometer

The LDV is designed to make measurements of the velocity and displacement of a vibrating surface. Based on the principle of LDV discussed in section 3.2, the displacement of a vibrating surface can be determined by measuring the phase difference between the measurement and reference laser beams. Hence, phase variations introduced by an ultrasonic wave in the transparent medium are readily attainable using LDV. Hence, the laser Doppler Vibrometer was used to measure ultrasonic stress distribution by quantitative analysis of the acousto-optic modulation of the optical path.

5.4.3.1 Quantification of Phase Variations

As discussed above, due to the sinusoidal wave generated by the ultrasonic transducer, the pressure or stress change in the homogeneous isotropic medium can be considered as a harmonic function [218] given by:

$$\delta\sigma(x,y,z,t) = \sigma(x,y,z)\sin\left[\omega\left(t-\frac{z}{c}\right)+\theta_c\right] \qquad \textbf{5.11}$$

where $\delta\sigma$ is the change in ambient stress, θ_c is the constant phase front

Changes in the refractive index δn will modulate the optical path and phase of the light [225, 226] according to:

$$\varphi(t) = \frac{2\pi\delta n(t)L}{\lambda} \qquad \textbf{5.12}$$

where $\varphi(t)$ is the phase change of the light, L is the width of the specimen through which light passes, λ is optical wavelength.

Combining equation 5.11 with equation 5.12, the phase change induced by stress variation: $\varphi(t) \propto \sigma(t)$ can be represented in a harmonic function by

$$\varphi(t) = \frac{2\pi\mu_{op}\delta\sigma(t)L}{\lambda} \quad \textbf{5.13}$$

For the experimental arrangement depicted in Fig. 5.9, where the laser beam passes through the ultrasonic field of width L twice following reflection from a reflective surface to the sample. Therefore, the phase change will be representative of the average stress along the path of the light and the total phase change must be doubled:

$$\varphi(t) = \frac{4\pi\mu_{op}}{\lambda}\int_0^L \delta\sigma(x,y,z,t)dx = \frac{4\pi\mu_{op}}{\lambda}\int_0^L \sigma(x,y,z)\sin\left[\omega\left(t-\frac{z}{c}\right)+\theta_c\right]dx \quad \textbf{5.14}$$

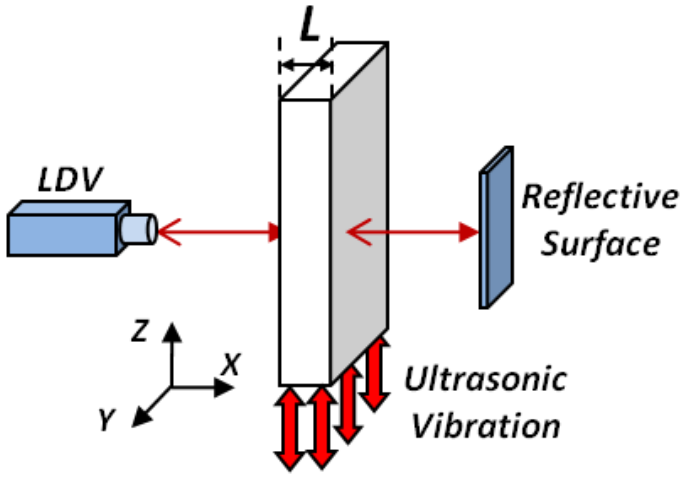

Fig. 5.9 Experimental arrangement of stress field detection by laser Doppler vibrometer

It is can be found that the phase component of laser light is proportional to the frequency and the 'average' rate of change of ultrasonic stress along the optical beam. Based on the principle of LDV, the phase change causes an additional modulation to the intensity of light incident upon the photo detector, which can be written as:

$$I = \frac{I_L(1+\cos(\varphi(t)+\varphi_{REF}-\varphi_0))}{2} \quad \textbf{5.15}$$

where I_L is the light intensity at source, φ_{REF} is the phase of the reference beam and φ_0 is the phase of the measurement beam [145]. Since the reflective surface is assumed to be stationary, phase variation measured by the LDV is due to a change in refractive index inside the transparent medium. Therefore, the output from the LDV is purely a function of the phase variation caused by stress. The spatial distribution of the ultrasonic field in the plane perpendicular to the laser beam can be mapped using a LDV with scanning manipulation.

5.4.4 Experimental Arrangements

Silicone elastomers have a long history of excellent performance in very demanding applications. Due to high optical transmittance in the UV-visible region, stable thermo-mechanical properties upon exposure to heat and humidity and easy processing into arbitrary 3D solids, a two-component silicone elastomer (Elastosil RT 601, Wacker-Chemie GmbH, Munich, Germany) was chosen.

5.4.4.1 Specimen Preparations

For the preparation of the silicone block, a SE specimen (Fig. 5.10 (a)) (117×26×35mm) was manufactured in a rectangular parallelepiped mould made of polished Perspex® (Fig. 5.10 (b)). The specimen had parallel transparent surfaces, which allowed a laser beam to traverse the thickness of the specimen without reflecting or refracting. Special care must be taken during placement of the specimen. The front and back surfaces of the specimen should be exactly parallel and perpendicular to the laser beam, otherwise, significant error will be induced, due to the loss of reflected laser beam.

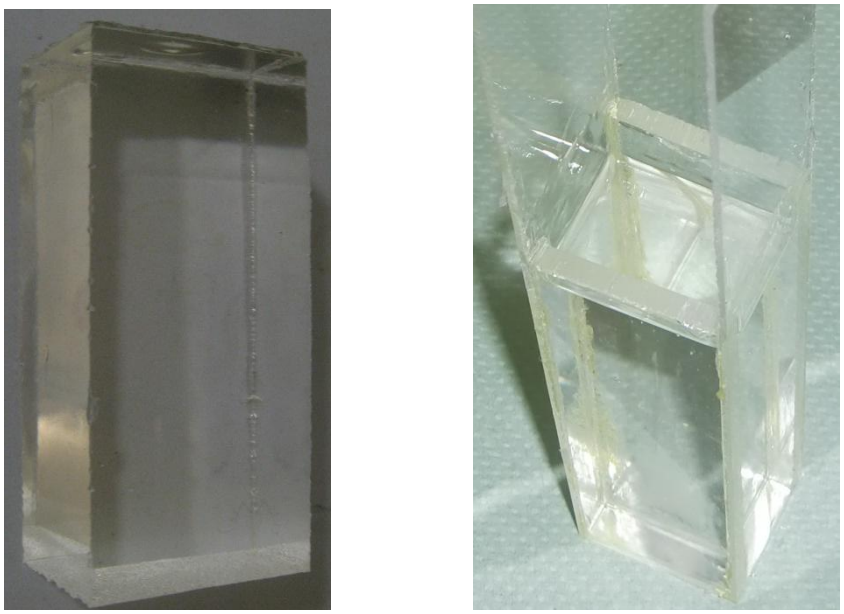

(a) **(b)**

Fig. 5.10 (a) the specimen of silicone elastomer and (b) the Perspex parallelepiped mould with the specimen

5.4.4.2 Experimental Set-up

The experimental set-up and the schematic for detection of the ultrasonic field using a LDV with the acousto-optic principle are illustrated in Fig. 5.11. The cuboid prepared

specimen was affixed on the top of the ultrasonic horn using same uncured silicone, which then vulcanised with time. The ultrasonic horn was fixed on the holder and rigidly connected to the ultrasonic transducer using a threaded stud.

The experiment for ultrasonic field mapping was performed at the Centre for Ultrasonic Engineering, University of Strathclyde using the LDV system including an optical head (Polytec OFV 303) and a modular vibrometer controller (Polytec OFV-3001) incorporating an OVD-01 velocity decoder. The high sensitivity measuring head produces a CW 2mW helium-neon laser focussed to below 40 μm diameter spot size. The controller provides power for the optical head and processes the vibration signal, which is decoded to achieve velocity information. The velocity decoder converts the frequency seen by the photo detector into a voltage proportional to the vibration velocity and can measure from DC (0 Hz) to ultrasonic signals (1.5 MHz) with high linearity (0.5%) and low noise level. Due to the small amplitude of the signals and the use of a low ultrasonic frequency (19.6 kHz) device, a velocity decoder in the measurement range 5 mm/s/V would be suitable for this application.

A sinusoidal waveform generator (Tiepie, Handyscope HS3) was used to excite a continuous vibration signal, which was amplified by an RF power amplifier (Kalmus 155LCRH) and then input to a power ultrasonic system, including a transducer and an ultrasonic horn, with a resonant frequency of 19.6 kHz.

In order to obtain the full-field stress distribution, a customised scanning facility was used. The sensor head and a reflector were mounted on the linear positioning unit which had controllable motion in the vertical and horizontal axes. The linear positional stage providing a horizontal plane of motion was a PI M521 DG from Physik Instrumente (Karlsruhe/Palmbach, Germany), controlled by a PI C842 ISA controller capable of 1μm resolution. The vertical plane of motion was provided using custom built scanning equipment by Phoenix ISL, which can resolve vertical motion to less than 0.5 mm. To make the laser beam pass through the specimen and reflect back along the same path, the sensor head and reflector were aligned parallel on opposite sides of the specimen and their motion was synchronised by the positioning unit.

The output signal of the LDV was acquired by an Agilent 54622 oscilloscope controlled by a PC. To enhance the SNR, signal averaging of 10 measurements was carried out and the

output data at each sampling position was stored as the peak to peak value. To re-construct the image in terms of stress, the data was analysed in the Matlab plotting tool.

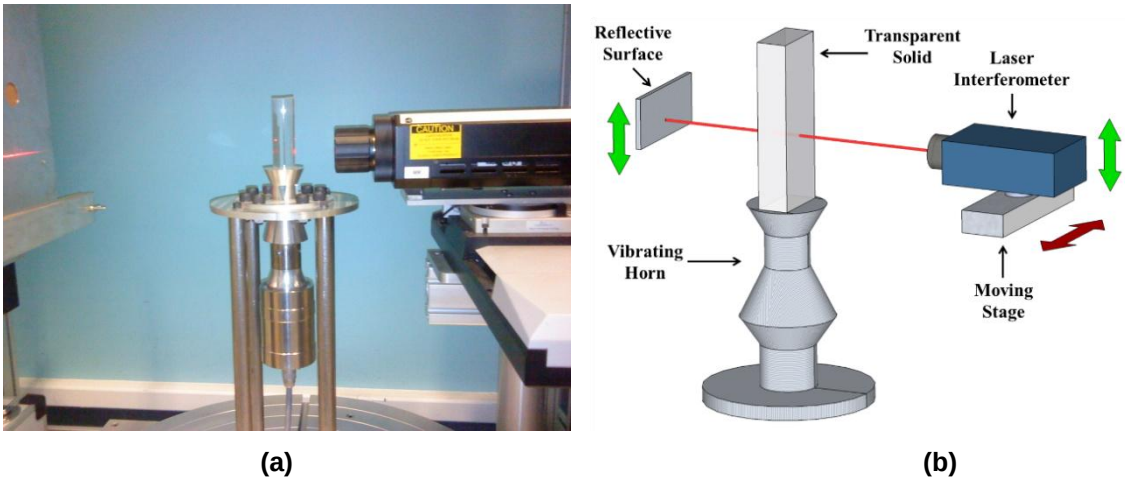

(a) (b)

Fig. 5.11 Scanning LDV setup for measurement of ultrasonic field in a vibrating transparent solid (a) experimental (b) schematic

5.5 Numerical Models

5.5.1 Introduction

To assess the performance of ultrasonic surgical devices on tissue, it is important to simulate the thermo-mechanical effects using numerical models, which allow for an accurate description of thermal and mechanical behaviour by calculating the displacement, stress, strain and temperature. Validated numerical models provide the potential to predict the effects of ultrasonic devices on tissue at the design stage.

Analytical modelling of wave propagation in acoustic media is employed as an alternative method to obtain the steady state wave pattern of a sample. It is widely used in one-dimensional (1D) vibration theory when the longitudinal dimension of the test sample is greater than its lateral dimension. The method considers the longitudinal modes of vibration and it assumes that a plane stress wave propagates in the axial direction of the test sample.

Engineering analysis of mechanical systems have been addressed by deriving differential equations relating the variables through basic physical principles such as equilibrium, conservation of energy, conservation of mass, the laws of thermodynamics, Maxwell's equations and Newton's laws of motion. To solve engineering problems concerning the mechanical deformation and heat conduction, FEA is one of the most flexible and powerful

computational tools, which can make the resulting mathematical models tractable. As a discretisation technique in structural mechanics, the finite element method subdivides the mathematical model into non-overlapping components of simple geometry called finite elements. Simplifying complex profile shapes with simple boundary conditions is achieved using meshing, in which each element is connected or assembled by a grid of nodes. The response of each element is expressed in terms of a finite number of degrees of freedom characterised as the value of functions at a set of nodal points. The material and structural properties are assigned to the mesh to define how the model reacts to the applied loading conditions. The response of the model is then considered to be approximated by that of the discrete model obtained by assembling the collection of all elements.

5.5.2 Analyses of Mechanical Response

5.5.2.1 Analytical and Finite Element Models

Analytical models (AMs) and finite element models were created to the study the ultrasonic effects on ER and PUF. Numerical analyses were performed for a rectangular sample, which is benchmarking the technique.

Analytical Model for PUF

As the test sample has longitudinal dimension greater than its lateral dimension, for the AM, the sample can be treated as a uniform beam vibrating in the longitudinal direction (Fig. 5.12) and it is assumed that the stress, $\sigma\ (y,t)$, is uniformly distributed in the cross-section [227] and the cross-section remains plane during deformation. In general, this approximation holds for vibration where the wavelength is long compared with the width of the beam [228]. Since only longitudinal vibration is applied, only the displacement component, $w(y,t)$, in the longitudinal direction is considered.

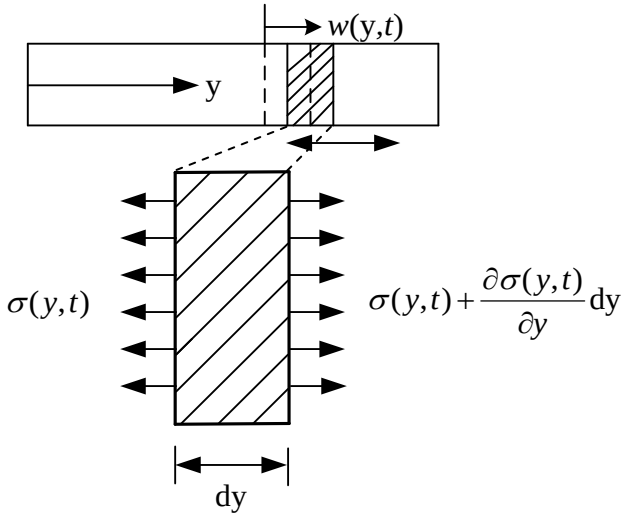

Fig. 5.12 Longitudinal vibration of a beam

By considering an element of the beam of length dy, we have

$$S(y)\left[\sigma(y,t)+\frac{\partial\sigma(y,t)}{\partial y}dy\right]-S(y)\sigma(y,t)=\rho S(y)\frac{\partial^2 w(y,t)}{\partial t^2}dy \qquad \textbf{5.16}$$

where $S(y)$ is the cross-sectional area and ρ is the density of the material.

Since,

$$\sigma(y,t)=E\varepsilon(y,t)=E\frac{\partial w(y,t)}{\partial y} \qquad \textbf{5.17}$$

where E is the Young's modulus.

The solution for harmonic vibration is given by

$$w(y,t)=\tilde{w}(y)[Acos(\omega t)+Bsin(\omega t)] \qquad \textbf{5.18}$$

where A and B are dependent on initial conditions, ω is the circular frequency and $\tilde{w}(y)$ is the mode shape function.

In this case the equation of motion can be written as

$$\tilde{w}''(y) + \frac{\rho\omega^2}{E}\tilde{w}(y) = 0 \qquad \textbf{5.19}$$

where prime denotes differentiation with respect to y. This provides the equation for calculating the longitudinal mode shape function.

In this application, the ultrasonic excitation frequency at 20.7 kHz is also the modal frequency of the second longitudinal mode for the specimen. When the specimen vibrates in one of its natural modes of vibration, all points of the specimen will undergo synchronous simple harmonic vibration, which means that all points will pass simultaneously through their equilibrium positions [229]. Hence the analytical solution for the mode shape, which is stationary, can be used to calculate the specimen's steady-state response to the dynamic loading.

Considering the mechanical properties: density $\rho = 500\,\text{kg/m}^3$, and Young's modulus $E = 563$ MPa and boundary conditions: $\tilde{w}(0) = 1.2 \times 10^{-5}$ m and $\tilde{w}'(L) = 0$, the equation 5.19 can be solved using the method of separation of variables to obtain $\tilde{w}(y)$. As a continuous wave is emitted by the ultrasonic transducer, the wave pattern in the sample is a standing wave in steady-state.

Finite Element Model for PUF

In the FEM, a direct-solution steady-state dynamic analysis was adopted, where a linear perturbation procedure is used to calculate the system's linearised steady-state response to harmonic excitation.

The specimen is excited by an oscillatory force such that a steady-state response is achieved, and the vibration displacement amplitude response of the specimen at 20.7 kHz longitudinal vibration is calculated. All computations are performed using the commercially available finite element modelling software ABAQUS.

The main aim of the FEA is to calculate the steady state dynamic response of the specimen under harmonic excitation at the tuned frequency. The analysis was performed as a frequency sweep, recording the response at a set of discrete frequencies. In order to capture fully the specimen surface deformation and associated stress/strain fields, a fine mesh was employed in the 2D model, incorporating a total of 3125 4-node, bilinear plane-strain

quadrilateral, reduced integration, hourglass control elements. Free boundary conditions were used for the model except from the excitation input plane.

The material properties, determined from tests or obtained from references [230], for rigid polyurethane foam were: elastic modulus $E = 563$ MPa ; density $\rho = 500$ kg/m^3; Poisson's ratio, $\nu = 0.3$. The material was assumed to be isotropic and linear. For this model, free boundaries were set on all sides of the PUF sample. The sample was subjected to a sinusoidally varying pressure along its base to excite a peak-peak (pk-pk) vibration amplitude of 24 μm at a frequency of 20.7 kHz.

Analytical Model for ER

The differential equation 5.16 is based on the assumption that the cross-section of the specimen remains plane and the motion of the cross-section is only in the axial direction of the specimen. The longitudinal vibration of the ER specimen, which is a thin uniform beam, can be described using this equation. As the cross-sectional area of the specimen is constant, equation 5.16 can be written:

$$\frac{\partial \sigma(y,t)}{\partial y} = \rho \frac{\partial^2 w(y,t)}{\partial t^2} \qquad \textbf{5.20}$$

Since

$$\sigma(y,t) = E\varepsilon(y,t) = E\frac{\partial w(y,t)}{\partial y} \qquad \textbf{5.21}$$

and

$$c = \sqrt{\frac{E}{\rho}} \qquad \textbf{5.22}$$

equation 5.20 can be expressed as

$$\frac{\partial^2 w(y,t)}{\partial t^2} = \frac{1}{c^2}\frac{\partial^2 w(y,t)}{\partial y^2} \qquad \textbf{5.23}$$

where c is the velocity of propagation of the displacement or stress wave in the specimen.

The longitudinal wave equation can be solved by separation of variables and assuming a solution of the form

$$\partial w(y,t) = F(x)G(t) \tag{5.24}$$

Substituting this solution into the wave equation gives

$$\frac{1}{F(y)}\frac{\partial^2 F(y)}{\partial y^2} = \frac{1}{c^2}\frac{1}{G(t)}\frac{\partial^2 G(t)}{\partial t^2} \tag{5.25}$$

From equation 5.25, the partial derivatives are no longer required, the left hand side is a function of y only and the right hand side is a function of $t$only. For convenience of solution, $-(\omega/c)^2$is applied to each side as a constant. Then

$$\frac{d^2F(y)}{dy^2} + \left(\frac{\omega}{c}\right)^2 F(y) = 0 \tag{5.26}$$

and

$$\frac{d^2G(t)}{dt^2} + \omega^2 G(t) = 0 \tag{5.27}$$

Hence, the solution can be given as

$$F(y) = Asin\left(\frac{\omega}{c}y\right) + Bcos(\frac{\omega}{c}y) \tag{5.28}$$

and

$$G(t) = Csin\omega t + Dcos\omega t \tag{5.29}$$

where A and B are dependent on the boundary conditions of the vibrating specimen, and C and D on the initial conditions.

Therefore, the displacement component for the wave equation is

$$\begin{aligned} w(y,t) &= \left(Asin\left(\frac{\omega}{c}y\right) + Bcos\left(\frac{\omega}{c}y\right)\right)(Csin\omega t + Dcos\omega t) \\ &= \left(\sqrt{A^2+B^2}\sin\left(\frac{\omega}{c}y+\theta\right)\right)\left(\sqrt{C^2+D^2}\sin(\omega y+\varphi)\right) \end{aligned} \tag{5.30}$$

where θ and φ are phase angles dependent on A and B, and C and D respectively.

Considering the boundary conditions $w'(L,t) = 0$ and input vibration amplitude at the specific time point, when $w(L,t_1) = 0.012$ mm, the vibration shape of the specimen at $t_1$can be obtained and considered as the wave pattern in the steady-state. In the analytical model for ER, Young's modulus E and density ρ were 13.9 GPa and 1640 kg/m^3 respectively.

Finite Element Model for ER

The simulating procedure of 2D FEM for ER was similar to PUF using ABAQUS. The direct-solution steady-state dynamics analysis was used to calculate the steady state dynamic response of the specimen under harmonic excitation. The same calculating step was adopted using the same frequency sweep, type of elements, specimen geometry, boundary conditions and outputs, but with different material properties and excitation input.

The material properties, determined from tests and references [231, 232], for ER were: elastic modulus $E = 13.9$ GPa; density $\rho = 1640$ kg/m^3; Poisson's ratio $\nu = 0.3$. The material was assumed to be isotropic and linear. For this model, free boundaries were set on all sides of the ER sample. The sample was subjected to a sinusoidally varying pressure along its base to excite a pk-pk vibration amplitude of 24 μm at a frequency of 20.8 kHz.

Finite Element Model for SE

To model the SE specimen under ultrasonic excitation, a FEM with density, Young's modulus and Poisson's ratio of SE was created using ABAQUS. The specimen was modelled as excited by an oscillatory force at 19.6 kHz and in steady-state response by coupling a direct-solution steady-state dynamics step.

The analysis was performed as a frequency sweep, recording the response at a set of discrete frequencies. In order to capture the deformation of the specimen, a fine mesh was employed in the 2D model with dimension of 115×40 mm, incorporating a total of 4600, 4-node, bilinear plane-stress quadrilateral, reduced integration, hourglass control elements. Free boundary conditions are applied to the model except the plane of input vibration.

The material properties, obtained from references, for SE were: elastic modulus $E = 13$ MPa [203]; density $\rho = 1020$ kg/m^3 [233]; Poisson's ratio $\nu = 0.495$ [205]. Lu et al. measured the viscoelastic properties of SE using nanoindentation tests, which provided the shear relaxation modulus of SE as 4.4 MPa. The results from nanoindentation tests can be used to characterise the frequency dependent dynamic properties of SE. The elastic modulus (dynamic) can be obtained from [234]:

$$E = 2G(1 + \nu) \quad \textbf{5.31}$$

where E is elastic modulus, G is the shear modulus, ν is Poisson's ratio.

The material was assumed to be isotropic and linear. For this model, free boundaries were set on all sides of the SE sample. The sample was subjected to a sinusoidally varying pressure along its base to excite a peak-peak vibration amplitude of 20 μm at a frequency of 19.6 kHz.

5.5.3 Finite Element Models for Thermal Response Calculation

5.5.3.1 Introduction

Finite element models were developed to aid in the analysis of the coupled mechanical thermal problems using the finite element software PZFlex (Weidlinger). The model calculates damping losses per vibration cycle in the mechanical analysis. This then constitutes a steady-state event for the thermal analysis such that a constant thermal input results for each thermal time-step. Hence, the thermal analysis solves for the temperature field [235]. The temperature dependence of material properties is not significant for PUF, but significant for ER. The damping losses calculated by mechanical analysis are coupled with the general heat transfer module in thermal analysis to provide predicted temperature distribution.

5.5.3.2 Finite Element Model of Thermal Response for PUF

In the finite element model, the internal loss is modelled as visco damping. In the model for PUF, a wave velocity of 1231 m/s was calculated based on the density, Young's modulus and Poisson's ratio of the PUF and a mechanical Q value of 34.8, which was calculated by equation 4.20 [206]

The damping tan (δ) at 20 kHz was obtained using the TTS generated master curve based on the damping results from experimental dynamic mechanical analysis, shown in Fig. 4.20. A 2D model was employed and time steps of 5 nanoseconds were used in the mechanical analysis to provide sufficient steps per cycle. The oscillation amplitude of 24 μm (pk-pk) excited by the horn at the contacting end of the PUF sample was simulated in the mechanical analysis model by applying an oscillating pressure. Free boundary conditions were used in the PUF mechanical model except the contacting end with the horn.

In the thermal analysis, the initial temperature was 20 ℃, which was the specified temperature boundary conditions for the specimen model and, in this case, the time step was 0.5 seconds. Ultrasonic excitation was applied to the specimen for 14 seconds. A specific heat of 1573 J/kg·K and conductivity of 0.028 W/m·K were incorporated based on experimental measurements. Table 5.1 lists the parameters used in the finite element thermal models.

Table 5.1 The parameters of finite element thermal models for PUF used in PZFlex analysis

Mech. analyses	Density (kg/m^3)	Poisson's ratio	Q value	Pressure (MPa)	Wave speed (m/s)	Young's modulus (MPa)
	500	0.3	34.8	0.827	1231	563
Thermal analyses	Time (s)	Environment Temp. (℃)	Specific heat capacity (J/Kg·K)		Thermal conductivity (W/m·K)	
	0-14	20	1573		0.028	

5.5.3.3 Finite Element Model of Thermal Response for ER

During ultrasonic excitation, the temperature of ER increases with time. Due to the low glass transition temperature of ER around 60 ℃, the mechanical properties of ER are heavily temperature dependent. Accurate finite element models of ER are challenging in this application. Compared with heat generation by damping losses, a small amount of heat was transferred by convection. The thermal response of ER is dominated by the internal heat generation other than heat convection during power ultrasonic loading. The detected peak temperature due to heat generation in the specimen is associated with viscoelastic damping, which is temperature dependent. In a short spell of ultrasonic excitation, the temperature rise is limited, which means the value of viscoelastic damping is held relatively constant. Therefore, the goal of the finite element models of thermal response for ER was to find a peak temperature and include several iterations with different viscoelastic

damping assumptions. The models were divided in time sequence, which meant that the damping coefficient of each new iteration was based on the peak temperature obtained in the previous model. In this study, due to nonuniform distribution of temperature in the whole sample, the other temperature dependent mechanical properties were ignored. The viscoelastic damping is the only consideration with temperature and frequency dependencies. The finite element ER models were created using the same material properties, with density $\rho = 1640$ kg/m^3, Young's modulus $E = 13.9$ GPa and Poisson's ratio $\upsilon = 0.3$ but with different damping loss Q value.

Model A was to simulate the thermal response from the start of ultrasonic excitation up to 1s. The surrounding temperature was measured at 25.1℃. The Q value, valued at 36.63, was predicted by the master curve of $\tan(\delta)$ at the reference temperature of 20 ℃ and 20 kHz from the results of experimental dynamic mechanical analysis. The Q value in model B was obtained by the master curve of $\tan(\delta)$ at a reference temperature of the peak temperature in model A and 20 kHz. The following models were all created based on this assumption. The values of Q at 20 kHz at different reference temperatures are listed in Table 5.2.

Table 5.2 The Q values at 20 kHz at different temperatures for FEA in PZFlex

Temperature ℃	Tan (δ)	Q value
20	0.02731	36.62
30	0.02962	33.76
40	0.03719	26.89
50	0.1005	9.95
60	0.2023	4.94
70	0.4114	2.43

As discussed above, finite element simulation of thermal response in PZFlex has separate mechanical and thermal analyses. The model with damping loss Q value calculated damping losses per vibration cycle in the mechanical analysis. The constant thermal input results obtained by damping losses were used in thermal analysis to provide the steady-state temperature field.

Time steps of 5 nanoseconds were employed in the mechanical analysis to provide sufficient steps per cycle. The oscillation amplitude of 24 μm (pk-pk) excited by the horn at the contacting end of the ER sample was simulated in the mechanical analysis model by applying an oscillating pressure. The boundary conditions applied to the ER models were same with the PUF models.

In the thermal analysis, the specified temperature of 20 ℃ was applied to all boundaries of the thermal models. The time step was set at 0.5 seconds. A specific heat of 760 J/kg·K and conductivity of 0.57 W/m·K were incorporated based on experimental measurements.

5.6 Chapter Summary

To minimize any detrimental impact on the ultrasonic field profile, non-invasive field measurements were developed for the fast and reproducible experimental assessments of ultrasonic displacement, stress/strain and temperature fields in solids. This chapter described several non-invasive techniques utilising the digital image correlation technique with an ultra-high speed camera, the thermo-mechanical effect with an infrared camera, and the acousto-optic effect with a laser Doppler vibrometer that were implemented to characterise the ultrasonic fields generated by low-frequency power ultrasonic transducers operating on different (elastic, viscoelastic and transparent) solids. Measurement principles and experimental arrangements with specimen preparations were used to show how and why they work to make non-invasive field measurements possible.

Numerical models, including analytical and finite element models, were developed to analyse the power ultrasonic mechanical effects on tissue mimics. The finite element mechanical analyses provided the damping losses of the viscoelastic materials, which were used to calculate the thermal response during power ultrasonic loading. Due to the frequency and temperature dependent behaviour of the materials, the finite element models were created with the help of the time/frequency temperature superposition principle.

Both experimental and simulation results will be utilised to assess the ultrasound interaction with tissue in the next chapter.

6. Measurement of Ultrasonic Fields and Correlation with Numerical Models

6.1 Introduction

Previous chapters have outlined non-invasive measurement techniques for displacement, strain/stress and temperature fields in viscoelastic solids under power ultrasonic excitation and detailed the numerical models for use in simulations of these fields.

This chapter assesses the veracity of results from both the non-invasive measurement methods and the detailed finite element models. Firstly, the behaviour of the bone surrogate materials, PUF and ER, subject to power ultrasonic vibration excitation were studied, by combining the use of an ultra-high speed camera and 2D in-plane DIC techniques to provide a non-invasive methodology for investigating the effects of ultrasonic surgical devices applied to biological tissue materials. These materials were then modelled by analytical and finite element methods for the prediction of and subsequent comparison with the experimental results. Following this, thermal effects of power ultrasound on ER and PUF were evaluated using an IR camera and verified by coupled thermo-mechanical finite element models. Based on the experimental and numerical findings, ultrasonic damage mechanisms in hard tissue mimics are discussed. Additionally the ultrasonic fields of transparent SE were characterised using LDV, based on the acousto-optic effect and a full-field scanning technique and then simulated by finite element models using dynamic material properties.

6.2 Mechanical Effects for PUF and ER

6.2.1 Introduction

During ultrasonic excitation, the mechanical deformations of both PUF and ER samples were determined utilising an ultra-high speed camera with the digital image correlation technique. This technique is new for full-field measurements in power ultrasonic applications. Due to the high frequency vibrations with small amplitude, it was first necessary to analyse the noise and sensitivity of the measurements. Deformation of the samples under ultrasonic excitation was then measured by correlating the displacement field of a set of images, which were taken over a single vibration cycle. Finally, the experimental results were compared with the numerical models.

6.2.2 Ultrasonic Field Measurement

6.2.2.1 Noise Analysis and Sensitivity

The vibration amplitude of the output surface of a nominal 20 kHz ultrasonic transducer is controllable up to a few tens of microns and therefore it is essential to determine that the sensitivity of the measurement system allows for detection of the ultrasonic vibration response above the measurement noise floor. A group of images from a sample surface without ultrasonic excitation was captured by the ultra-high speed camera in order to investigate the noise floor. A set of 102 images was recorded for the sample surface of 10×50 mm via a pixel array, each pixel representing 0.2174 mm for PUF and 0.2 mm for ER in the digital images. Fig. 6.1 shows the displacement field from correlation of the PUF images and Fig. 6.2 is for the ER sample in an unexcited state. The y-direction is in the direction of proposed excitation through longitudinal mode vibration of the ultrasonic transducer. From these results, it is clear that displacement measurements below 1.1 µm for PUF and 0.7 µm for ER are noise, largely as a result of camera noise plus imperfections and variations in the lighting conditions [168]. However, these displacement noise floors do not preclude measurements of the displacement of the specimens due to ultrasonic excitation in this study, which are well above this noise floor.

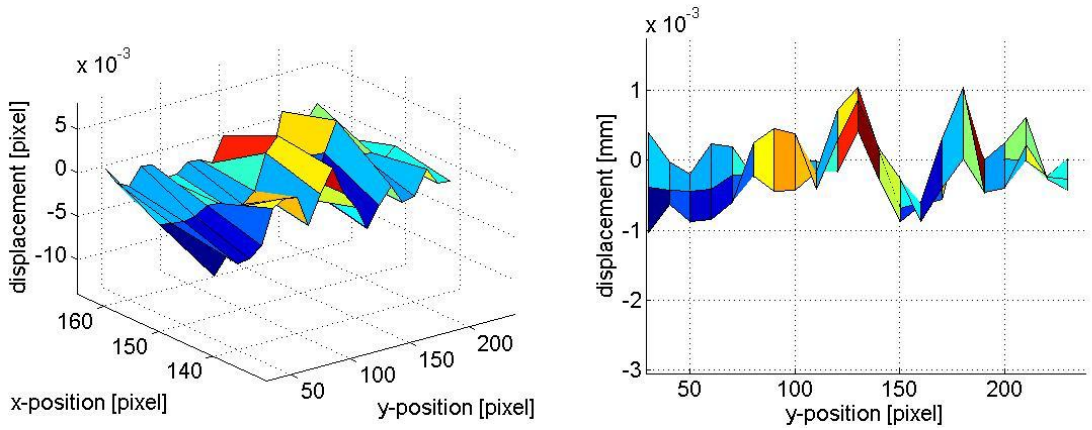

(a) **(b)**

Fig. 6.1 PUF displacement field in Y axis in the undeformed state to demonstrate noise floor (a) in 3D in pixels, (b) 2D in millimetres

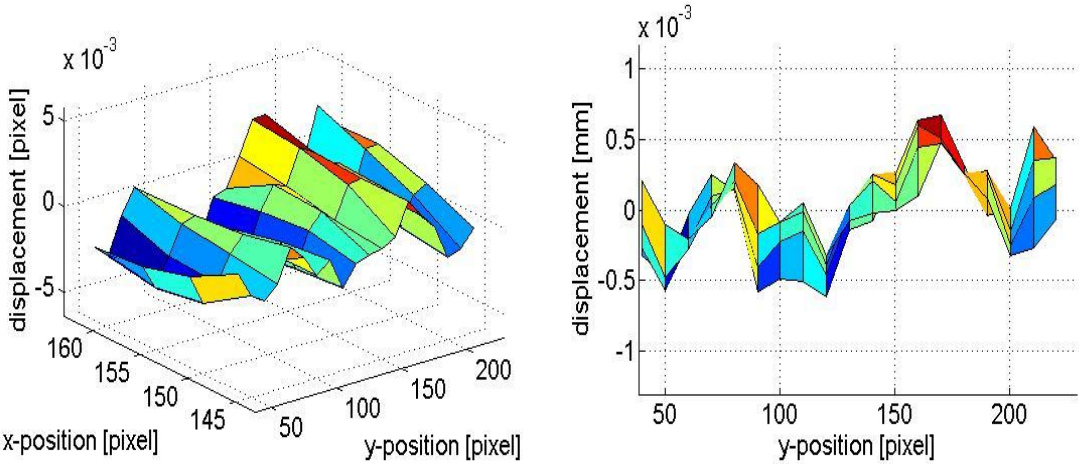

Fig. 6.2 ER displacement field in Y axis in the undeformed state to demonstrate noise floor in (a) 3D in pixels, (b) 2D in millimetres

6.2.2.2 Deformation Measurement of PUF and ER Samples

Capturing a Single Vibration Cycle for PUF

The capability of DIC measurements for providing an accurate characterisation of the displacement field under ultrasonic excitation was demonstrated initially by capturing the vibration response from the PUF specimen surface during one vibration cycle. Fourteen images are presented in Fig. 6.3 (1)-(14), with (1) being the undeformed reference image, and the evolution of the displacement response in the y-direction (the axial vibration displacement) is shown in each subsequent image. The results of measurements are displayed as a 3-dimensional model for the full field information. The colours represent the amplitudes of displacements in the y-direction, the direction of the input vibration. From the 4 μs fixed time between successive images, the vibration frequency, 20.83 kHz can be estimated from the DIC measurements, as compared to the known vibration frequency of the transducer with the horn, verified by LDV measurement, of 20.7 kHz.

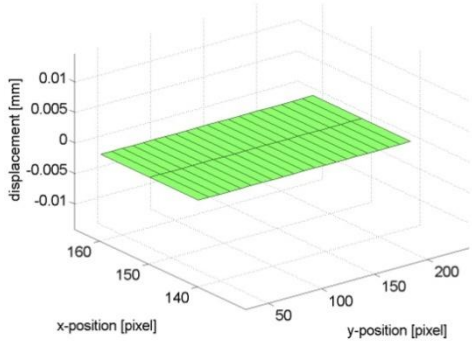
displacement [mm]
0.01
0.005
0
-0.005
-0.01
160
150
140
x-position [pixel]
50
100
150
200
y-position [pixel]

(1)

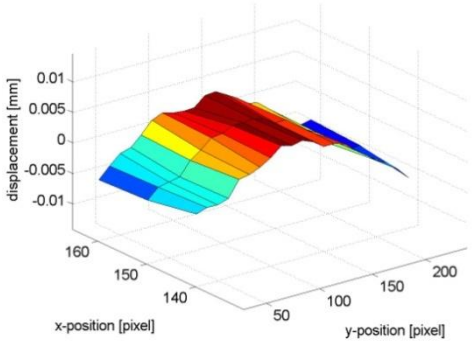
displacement [mm]
0.01
0.005
0
-0.005
-0.01
160
150
140
x-position [pixel]
50
100
150
200
y-position [pixel]

(2)

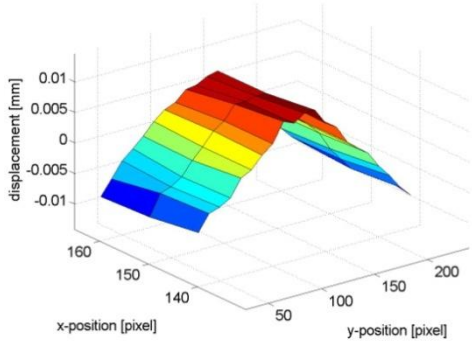
displacement [mm]
0.01
0.005
0
-0.005
-0.01
160
150
140
x-position [pixel]
50
100
150
200
y-position [pixel]

(3)

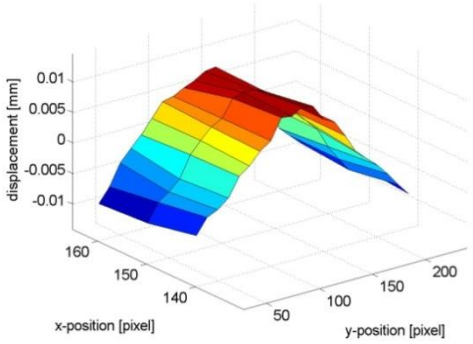
displacement [mm]
0.01
0.005
0
-0.005
-0.01
160
150
140
x-position [pixel]
50
100
150
200
y-position [pixel]

(4)

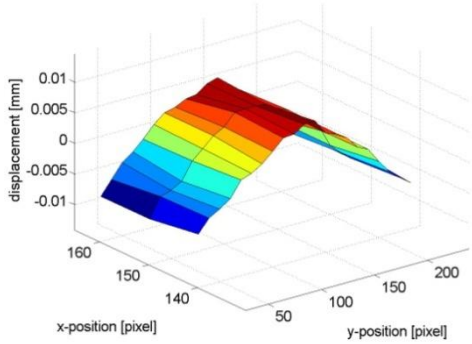
displacement [mm]
0.01
0.005
0
-0.005
-0.01
160
150
140
x-position [pixel]
50
100
150
200
y-position [pixel]

(5)

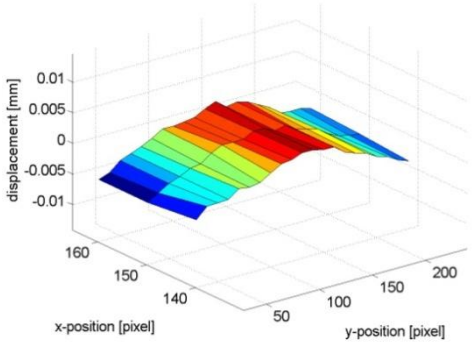
displacement [mm]
0.01
0.005
0
-0.005
-0.01
160
150
140
x-position [pixel]
50
100
150
200
y-position [pixel]

(6)

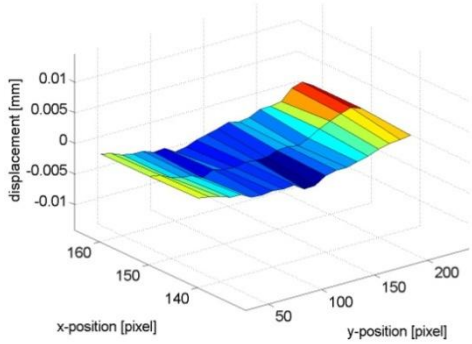
displacement [mm]
0.01
0.005
0
-0.005
-0.01
160
150
140
x-position [pixel]
50
100
150
200
y-position [pixel]

(7)

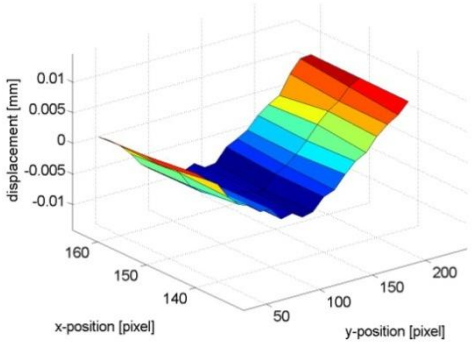
displacement [mm]
0.01
0.005
0
-0.005
-0.01
160
150
140
x-position [pixel]
50
100
150
200
y-position [pixel]

(8)

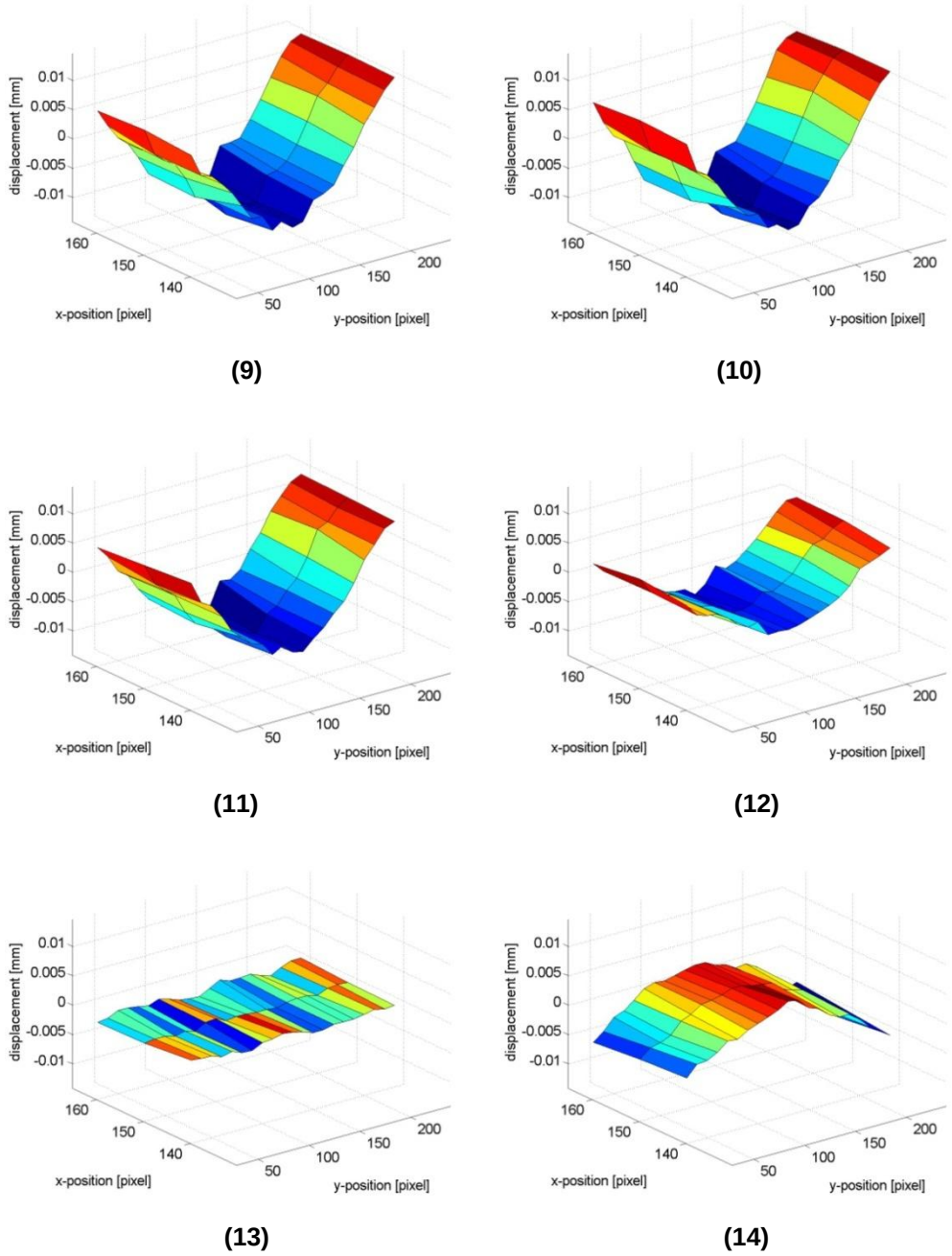

Fig. 6.3 Evolution of displacement field in one cycle of vibration for PUF

Capturing a Single Vibration Cycle for ER

The DIC experimental data for ER was collected after 3 seconds of ultrasonic vibration and captured the vibration responses from the specimen surface for the displacement field in the y-direction. There are 14 images in Fig. 6.4 displaying the evolution of displacement during one vibration cycle. The displacement contour information in image (5) shows the deformation of the ER specimen at the maximum distortion during one vibration cycle in the test. The image acquisition rate was 250,000 frames per second and the frequency of

vibration was around 20.7 kHz, giving about 12 images per cycle. Therefore, the true peak vibration amplitude was not necessarily captured with this sampling rate.

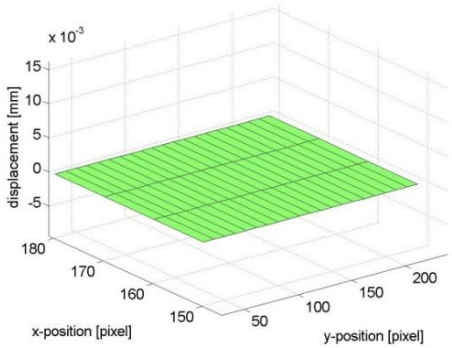

(1)

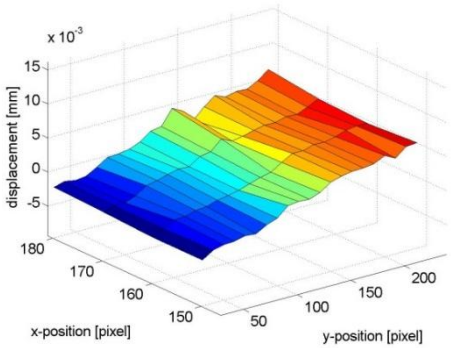

(2)

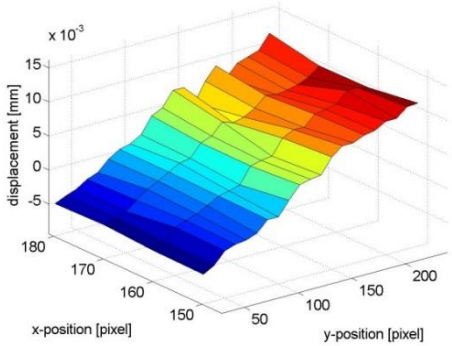

(3)

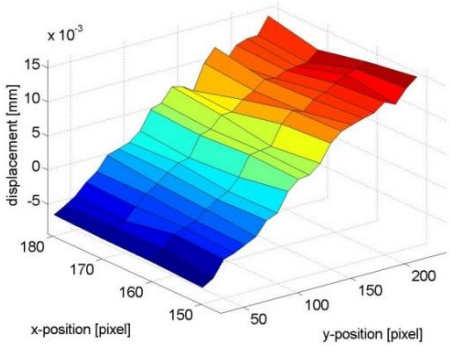

(4)

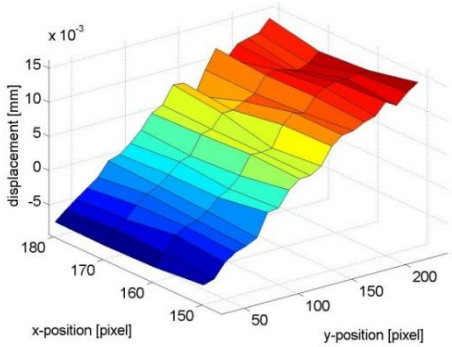

(5)

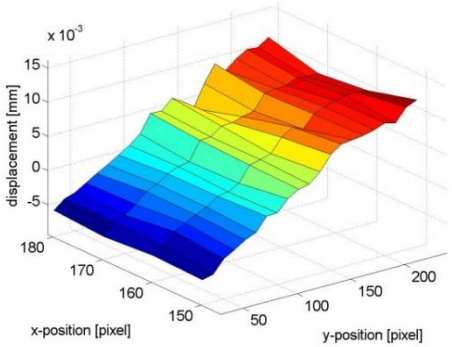

(6)

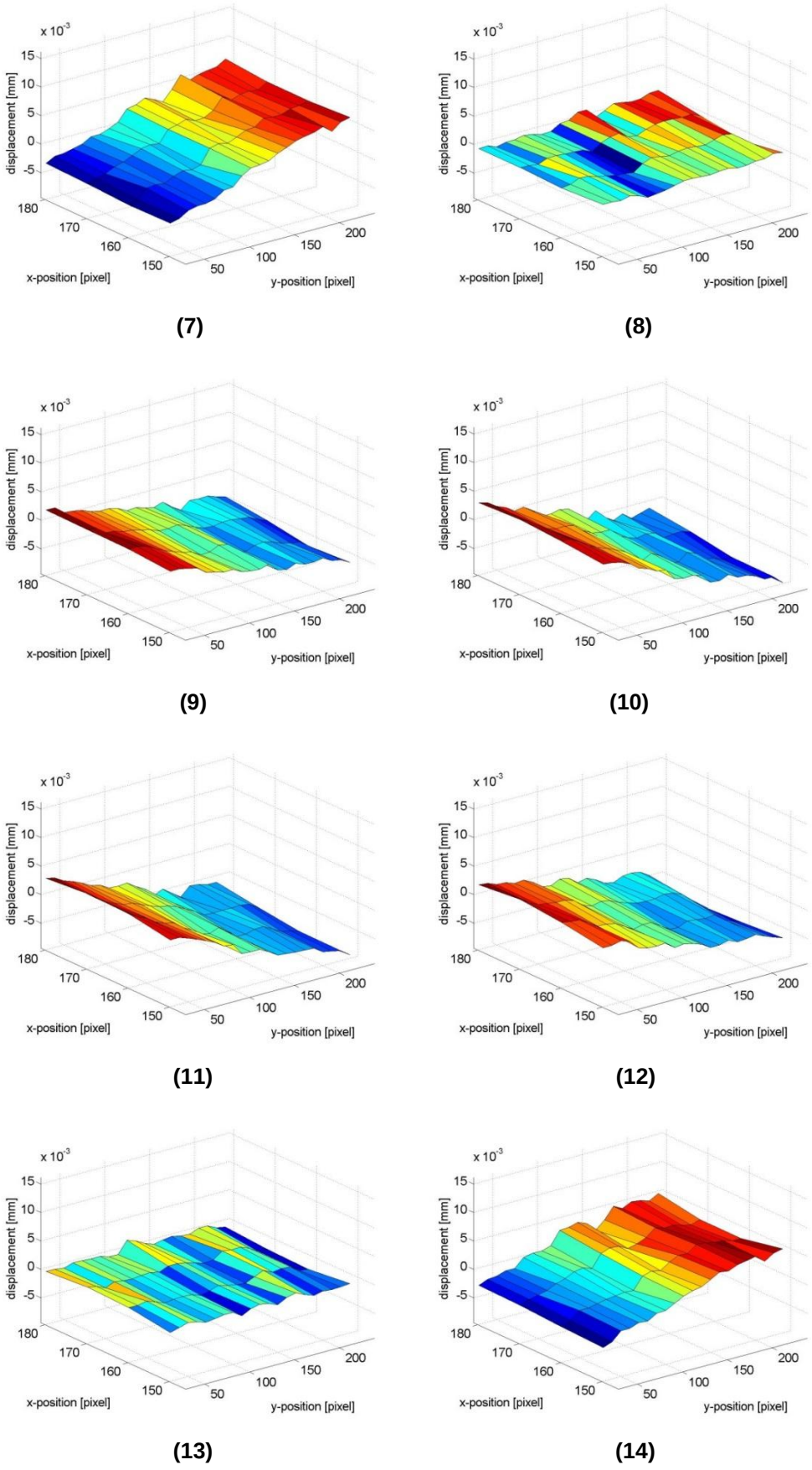

Fig. 6.4 Evolution of displacement field in one cycle of vibration for ER

Since the data of all surface points were recorded simultaneously, the technique of DIC with an ultra-high speed camera could be advantageously used for the study of ultrasonic vibration, the transient behaviour and vibration shape could easily be obtained and analysed. In comparison, point by point scanning measurements across a grid, for example using a laser vibrometers, cannot capture full field data simultaneously and rely on each point on the grid having a time invariant response. This is rarely the case for surface responses of tissue materials under ultrasonic excitation, where heating and material properties changes mean that vibration response change with time.

6.2.3 Correlation between Experiments and Simulations

Experimental displacement results were compared with the numerical models for validation. Strain fields derived from the displacement results were also compared with the numerical simulations.

6.2.3.1 Displacement and Strain Fields for PUF

Displacement Response in the Y-axis

The displacement amplitude (Fig. 6.5) of the longitudinal wave, in the y-direction, was obtained from the AM, and compared with that predicted by the FEA (using ABAQUS) and the peak displacement in Fig. 6.3, image (10) from DIC measurements.

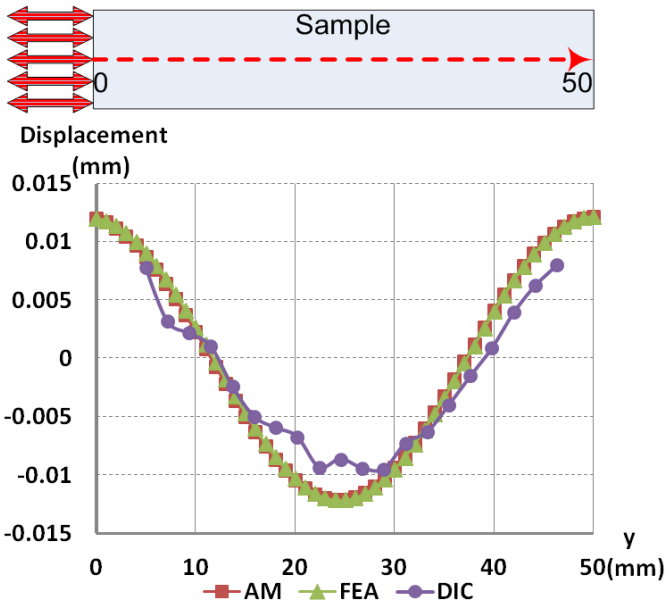

Fig. 6.5 Measured (DIC) and predicted displacement amplitude (AM and FEA) along the centre-line for PUF sample

Comparison of Displacement and Strain Fields by AM, FEA and DIC

Fig. 6.6 shows a comparison of contour plots of the displacement field estimated from the AM, FEA and DIC measurements. The vibrational response in the sample clearly exhibits the second longitudinal mode for all methods used. For clarity, the contour plot of the displacement field in the region of interest from the DIC measurements, with images captured after 2s of excitation, is overlaid on the surface of the sample in Fig. 6.6 (c).

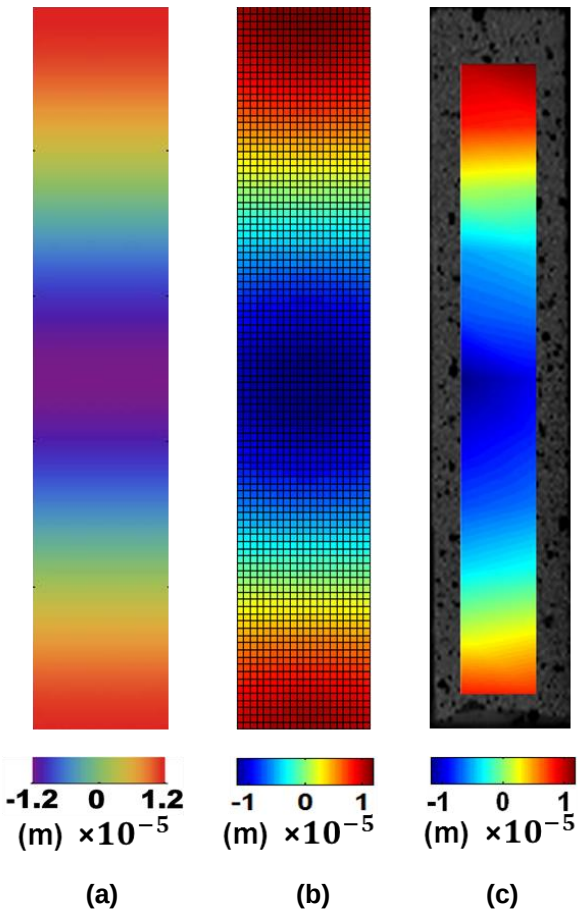

Fig. 6.6 The results of displacement field by (a) AM (b) FEA and (c) DIC for PUF excited at around 20 kHz and 24 µm

The full-field strain maps were calculated directly from the displacement fields and are shown in Fig. 6.7 (c). Comparing the two numerical model results (AM and FEA in Fig. 6.7 (a), (b)), the strain maps were a very close match.

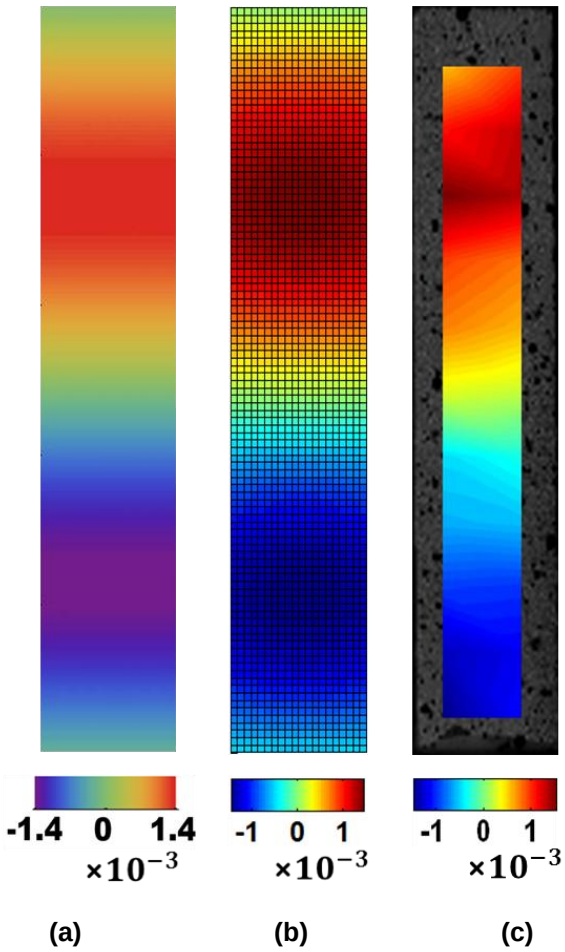

Fig. 6.7 The results of strain distribution by (a) AM (b) FEA (c) DIC for PUF excited at around 20 kHz and 24 µm magnitude

The displacement and strain contour plots obtained from the DIC measurements, shown in Fig. 6.5 (DIC), 6.6(c) and 6.7(c), illustrate two problems associated with the measurements. First, the data at the highest amplitude locations, which in this case are the anti-nodes located at the upper and lower ends of the specimen, are lost due to difficulties with extending the measurements out to the specimen boundaries. The correlation errors of displacements at boundaries are larger than those from other locations on the specimen and therefore, the results at boundaries were discarded and not shown in the contour plots. Second, although Fig. 6.3 image (10) is the maximum amplitude measurement image in the cycle, the image is not captured precisely at the time in the cycle associated with peak vibration amplitude. Capturing the peak vibration amplitude more precisely relies on synchronization of the ultrasonic vibration cycle and image capture triggering, along with even higher fps capabilities. Although this was not achievable in this experiment, it is not necessarily a limiting factor in the technique. However, the mode shape is clearly captured and the correlation of displacement is, at the worst, over 90% at the peak of the vibration cycle as clearly shown in Fig. 6.5. The agreement between model and DIC measurement

data is much closer if images away from peak vibration are compared but the images themselves are less sharp with a lower signal to noise ratio.

To measure the response of a sample to an ultrasonic excitation frequency, the DIC technique provides an advantage of being able to capture the full-field surface displacement and strain, however more precise triggering is required to enable capture of the exact peak response in the vibration cycle, which can be more easily captured using, for example, LDV. However, a very significant advantage of DIC with an ultra-high speed camera over LDV is the ability to map the surface strain without having to deal with the significant influence of changing temperature in the sample due to absorption of ultrasonic energy for the duration of the scanning point-by-point LDV measurement process. The DIC measurement technique also enables full-field characterisation during transient events, such as amplitude build-up during the first few vibration cycles, even at high frequencies.

Comparison of Displacement Fields from FEA and DIC in the X-axis

The displacement fields in the transverse direction from FEA and DIC are shown in Fig. 6.8. The grid used was 5×15 pixels and the markers are shown as green dots in Fig. 6.8 (b). The result for DIC was recorded at maximum displacement during ultrasonic vibration. The FEA result was used for correlation with the DIC experimental data. Over 150 points were correlated in the DIC test and over 3000 nodes were created in the FEA model. The data from these two methods matched very well in the x-axis.

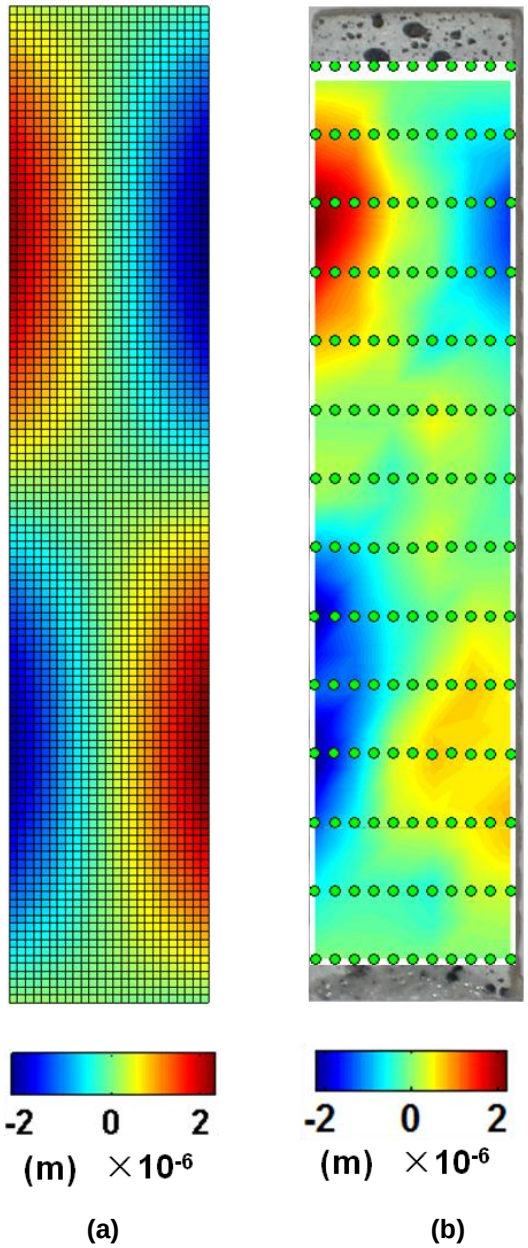

Fig. 6.8 Displacement fields in x-axis by (a) FEA (b) DIC for PUF excited at around 20 kHz and 24 µm magnitude in y-axis

6.2.3.2 Displacement and Strain Fields for ER

Displacement Response in the Y-axis

The displacement amplitude (Fig. 6.9) of the longitudinal wave, along the centre line of the ER specimen in the y-direction, was obtained from the AM, and compared with those predicted by the FEA and the maximum deformation from DIC measurements (Fig. 6.4, image (10)).

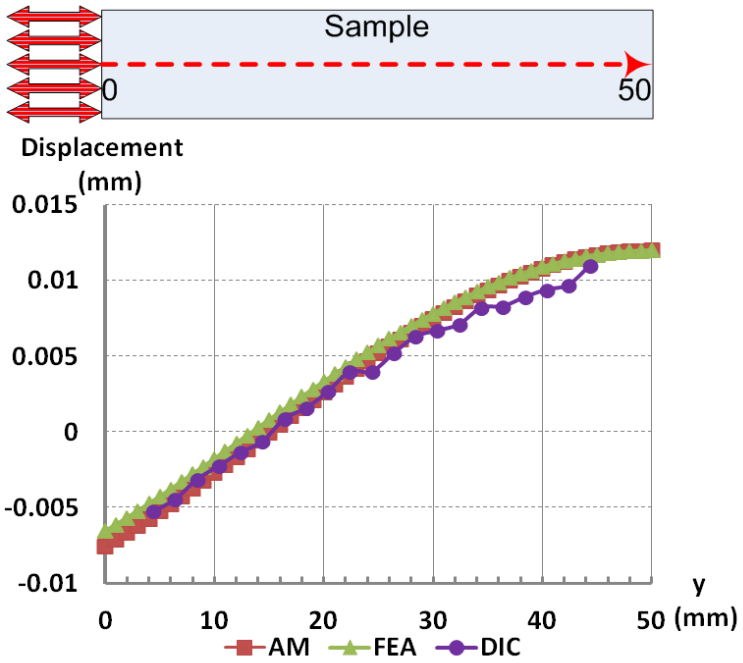

Fig. 6.9 Measured and predicted displacement along the centre-line of the ER sample

Comparisons of Different Elastic Modulus by Static Compression Test, DIC and TTS

The centre-line displacement of ER in the y-direction from DIC measurement is shown in Fig. 6.10. The wavelength (λ) of the longitudinal wave, propagating in the y direction, can be obtained from:

$$\lambda = 38.4 \times 4 = 139.2\ mm \tag{6.1}$$

Based on longitudinal wave propagation in a bar, the wave speed can be calculated by

$$c = \lambda f = \sqrt{E/\rho} \tag{6.2}$$

Therefore, the elastic modulus E can be expressed as:

$$E = (\lambda f)^2 \rho = 13.75\ GPa \tag{6.3}$$

where density $\rho = 1640$ kg/m^3 and frequency $f = 20.8$ kHz.

In comparison, the elastic modulus from a standard static compression test was found to be 9.96 GPa. The storage modulus calculated from the master curve of TTS using DMA data is 13.9 GPa, which is comparable with the results obtained by DIC. Therefore, ER has frequency dependent behaviour, in which the dynamic response cannot be described by the static modulus in a power ultrasonic application. The master curve of TTS is a good predictor for ER under ultrasonic excitation.

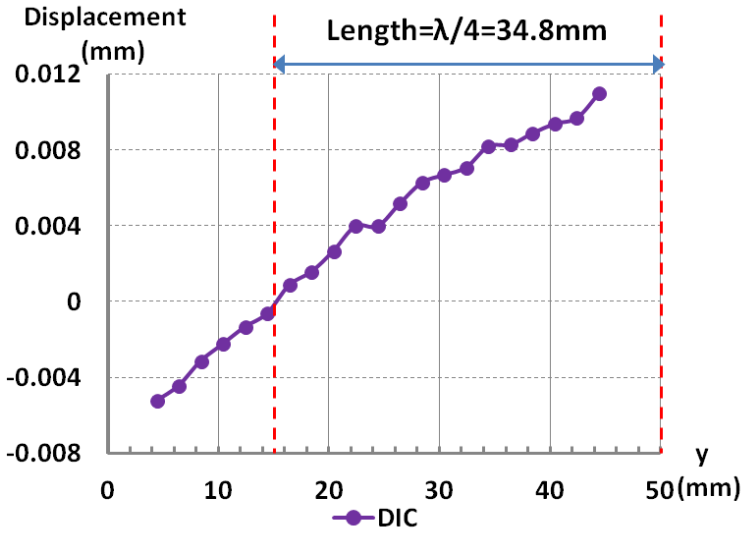

Fig. 6.10 Measured displacement along the centre-line of the sample at its maximum amplitude by DIC

Comparisons of Displacement and Strain Fields by AM, FEA and DIC

A comparison of contour plots of the displacement field estimated from the AM, FEA and DIC measurements is illustrated in Fig. 6.11. The displacement fields were captured at the measured maximum deformation of the specimen during one ultrasonic vibration cycle. The results from the DIC test for a transient response are very promising. There are strong correlations with the results of the analytical and finite element models. From the time/frequency temperature superposition principle explained in Chapter 4, it is clear that the specimen will be stiffer under dynamic loading at the ultrasonic frequency, where the elastic modulus increases from 9.96 GPa (static measurement) to 13.75 GPa (dynamic measurement).

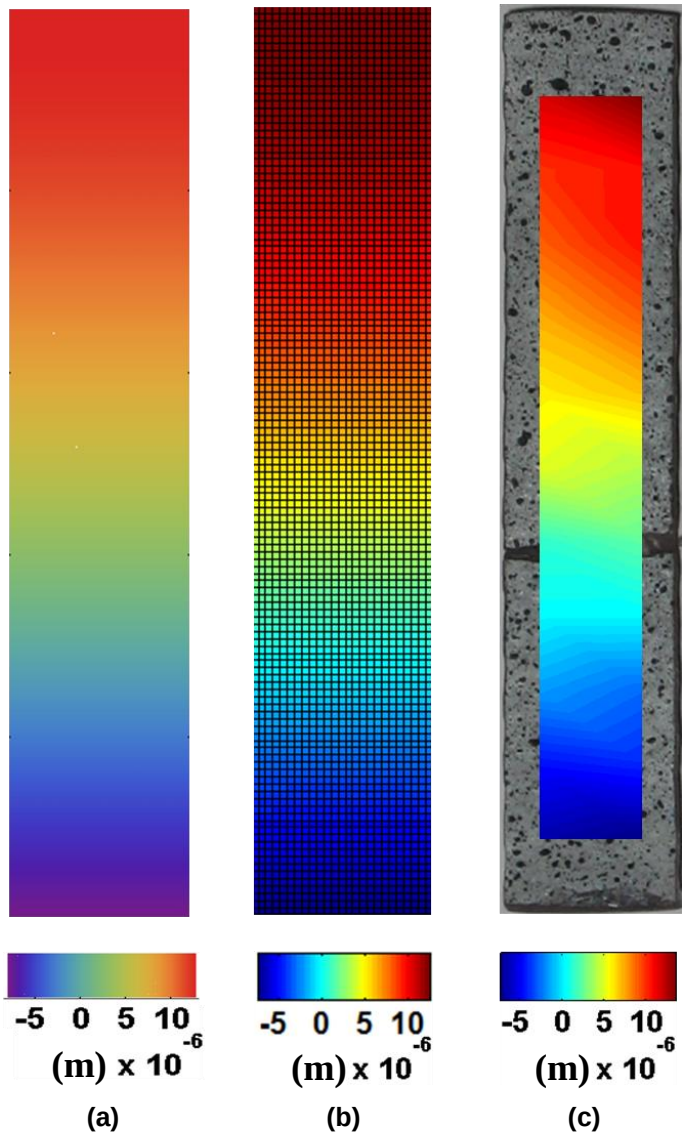

Fig. 6.11 The results of displacement field by (a) AM (b) FEA and (c) DIC for ER excited at around 20 kHz and 24 μm

The estimated strain field (shown in Fig. 6.12) can be calculated by a numerical differentiation process from the displacement gradient. However, in DIC measurements differentiation can amplify the background noise which is contained in the displacement gradient, leading to inaccurate strain results. Due to the small deformation during ultrasonic excitation of the ER specimen and the uncompensated noise in the measurement, the strain field is computed not accurately by the DIC method. The maximal strain is only 0.06% predicted by the analytical and finite element models. Hence, the errors of displacement estimation caused by noise can hide the underlying strain information. So, it is believed that the accuracy of strain estimation would be improved in future work by implementation of a smoothing algorithm on the displacement field.

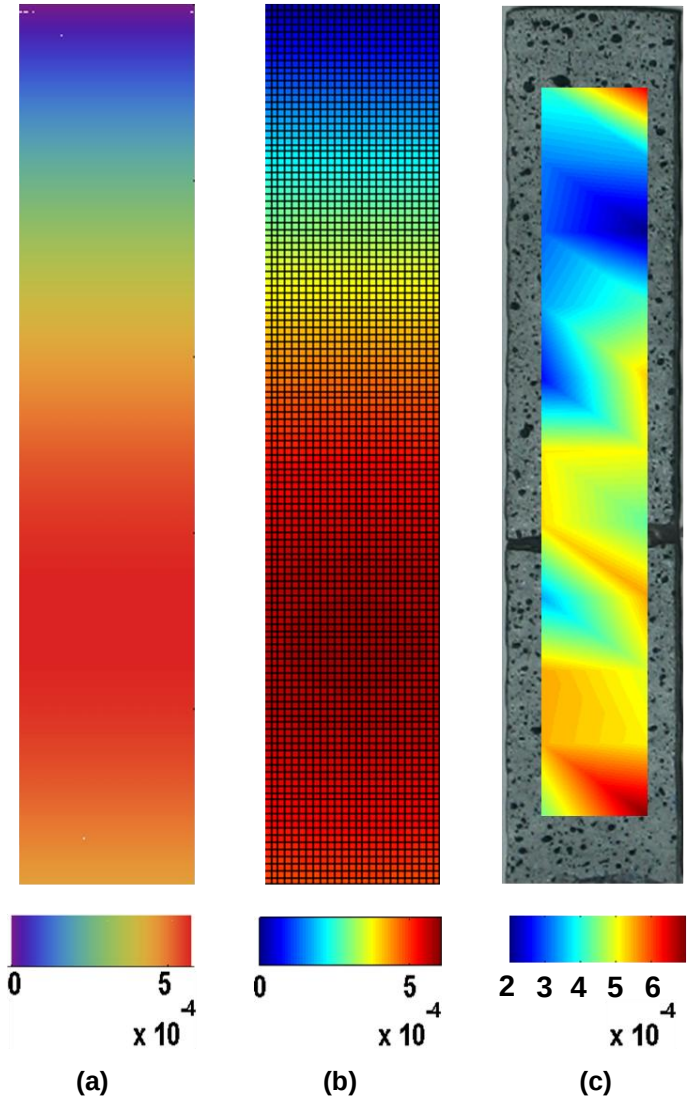

Fig. 6.12 The results of strain distribution by (a) AM (b) FEA (c) DIC for ER excited at around 20 kHz and 24 μm

6.2.4 Conclusions

The feasibility of using an ultra-high speed camera with a 2D digital image correlation technique to examine the dynamic behaviour of bone mimic materials (PUF and ER) under excitation from an ultrasonic device has been demonstrated. The full-field surface displacement evolution can be obtained using a high speed DIC system, enabling the capture of both the steady state response and cycles during the transient build-up of ultrasonic displacements. For PUF, the experimental results of displacement and strain show close correlation with analytical and finite element models, however a more accurate measure of the peak displacement amplitude requires some further refinement of the DIC triggering or measurement of a large number of images per cycle. For ER, the experimental data of the displacement field from DIC correlates well with the analytical and finite element models. However, due to the small deformation of the sample and uncompensated

background noise in the images, the strain field was not accurately computed by the differentiation process of the displacement field using the DIC technique. The significant benefit for characterising the response under ultrasonic excitation using the ultra-high speed camera with the DIC technique over current measurement techniques, such as point-wise LDV measurements, is that it provides significant mitigation of temperature effects. Also, the scanning process during LDV measurements makes it impossible to capture transient events. Full-field surface strain measurements can be used to predict regions where tissue damage can occur close to or remote from the site where the ultrasonic surgical device is interacting directly with the tissue.

Compared with other techniques used for deformation measurement, the technique of DIC with an ultra-high speed camera for dynamic measurements has many advantages and several disadvantages. Experimental setup and specimen preparation are straightforward. The ultra-high speed camera requires secure mounting and will record the images if enough light is available during ultrasonic excitation. The preparation of specimens is a simple process, which involves spraying a random speckle pattern on a flat surface of the specimen. In addition, there is no contact with the measurement system and the results can be obtained for full field in one snapshot. Finally, based on a non-contact full field method, the technique of DIC with ultra-high speed camera allows the determination of displacement amplitudes and vibration phases with high spatial and temporal resolution. Displacements down to a few microns and frequencies up to several tens of kHz can be covered, giving rise to applications of displacement and strain measurements in a large dynamic range. The application of high frequency vibration can be demonstrated with accurate full-field measurements of displacements, especially for mode shape analysis.

Nevertheless, the application of this technique for power ultrasonic applications also suffers from some disadvantages. Because the estimation of strain by a numerical differentiation process can amplify the background noise contained in the extracted displacement, it is not recommended as an effective method for very small deformation measurement, where the noise floor cannot be ignored. For vibration at high frequency and low amplitude, the results are heavily dependent on the quality of the imaging system which requires a high quality CCD sensor and a high level of constant light.

6.3 Thermal Effects for PUF and ER

6.3.1 Introduction

In power ultrasonic applications, high frequency mechanical oscillations generate heat inside the materials as a result of absorption of the ultrasonic wave energy. Damage is possibly caused by internal heating as a result of local strain and material damping. It is therefore necessary to obtain the temperature distribution to assess the thermo-mechanical effects.

The temperature of the specimen subjected to ultrasonic excitation was captured by an IR camera. Images from the whole sample surface were recorded, from the initiation of ultrasonic excitation until failure, and the resultant thermal field was also calculated by finite element models.

6.3.2 Thermal Measurements

6.3.2.1 Thermal Measurement of the PUF Specimen

Thermal mapping of the PUF sample during ultrasonic excitation was performed with an infra-red thermal camera in real-time. Thermal images were obtained from the starting time of vibration excitation (0 s) up to the failure of the sample (16 s). Fig. 6.13 shows that the maximum temperature in the sample reached 160 ℃ at 16 seconds, when the sample failed and the peak temperature captured in the thermal image at 14s was around 120 ℃, which is the T_g of PUF. The test sample illustrates that the local temperature increases sharply, especially at displacement node positions. During the ultrasonic excitation, the maximum temperature was generated at the high strain locations. Thus, the material failures were located at the thermal damage positions where the temperature also increased sharply.

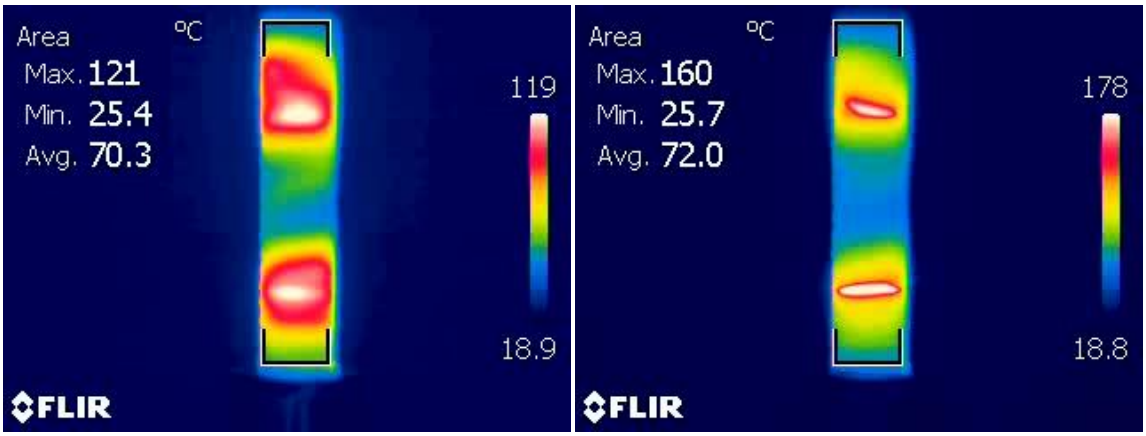

Fig. 6.13 Thermal image of PUF during ultrasonic excitation at 14s and 16s showing surface temperature in ℃

6.3.2.2 Thermal Measurement of the ER Specimen

The temperature distribution on the ER sample during ultrasonic excitation was recorded with the IR thermal camera in real-time. Data was recorded from the start time of vibration excitation (0 s) up to failure of the sample at around 20 s. Fig. 6.14 shows the evolution of temperature distribution for ER during ultrasonic vibration from 0 to 11 s. The recordings illustrate that the local temperature increases sharply especially at the displacement node (Fig. 6.15). During ultrasonic excitation, the highest temperature was generated at the highest strain location, which is a local stress concentration (Fig. 6.15). Thus, sample failure is located at the cyclic loading induced fracture damage position where the temperature is highest.

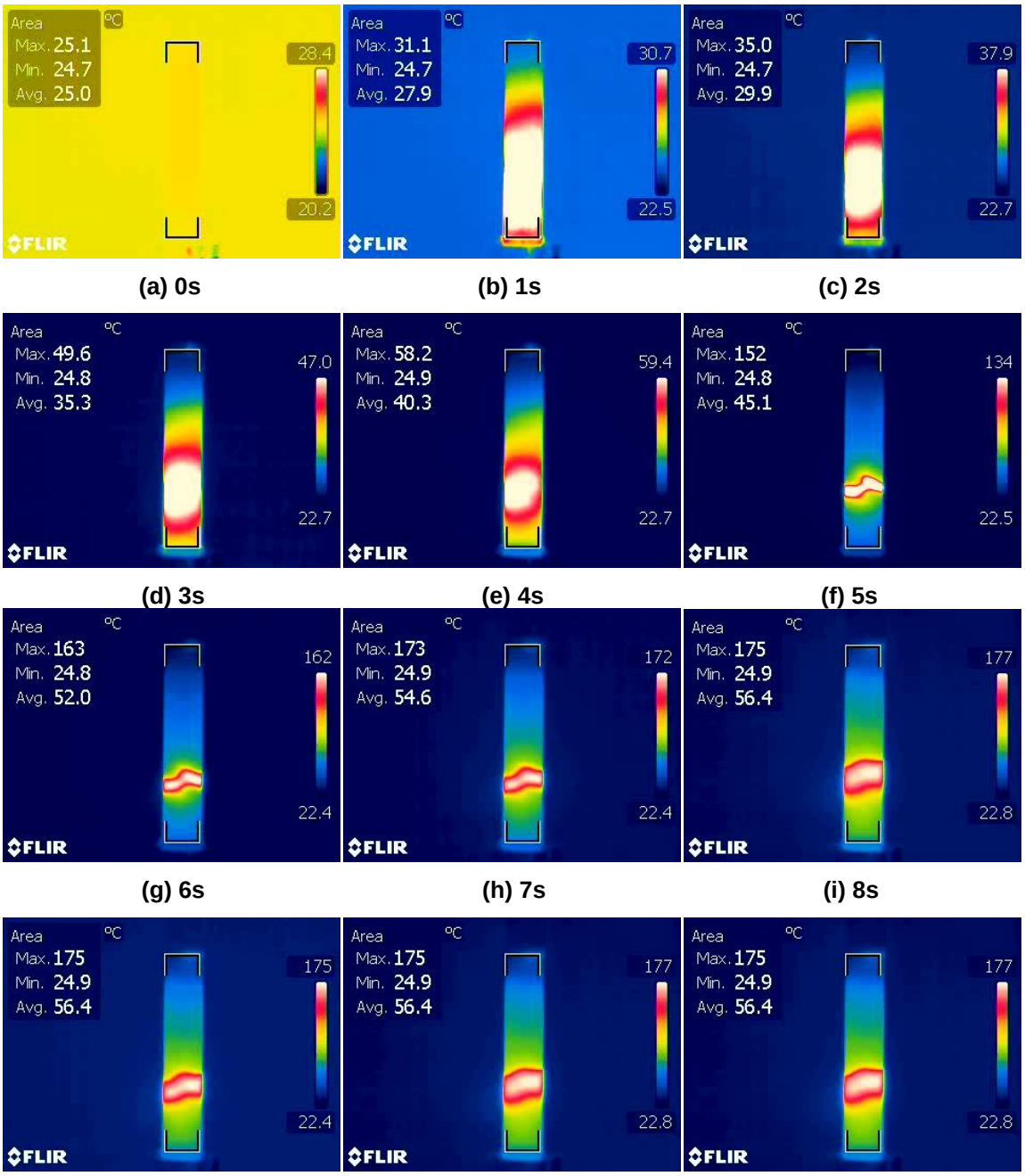

Fig. 6.14 Evolution of temperature distribution on ER sample during ultrasonic vibration showing the temperature in ℃ between (a) 0 second and (l) 11 second

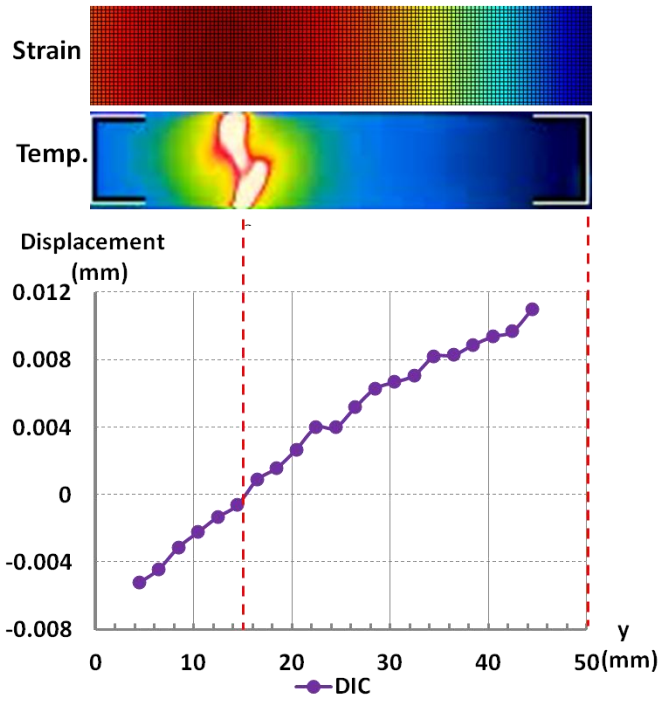

Fig. 6.15 Correlations between thermal measurement and DIC data and strain field from FEA

6.3.3 Correlation between Thermal Measurement and FEA

6.3.3.1 Temperature Distribution for PUF

The temperature field in the PUF sample as predicted by the finite element model using PZFlex is shown in Fig. 6.16 (b). The thermal map data was extracted 14s after the start of ultrasonic excitation, consistent with the results of thermal imaging measurement (Fig. 6.16 (a)) obtained at the same time. From Fig. 6.16 (c, d), ultrasonic damage to the PUF sample during the test was found at the same maximum temperature locations as predicted in the measurement. The results of the thermal maps in Fig. 6.16 matched well between the experiments and FEA.

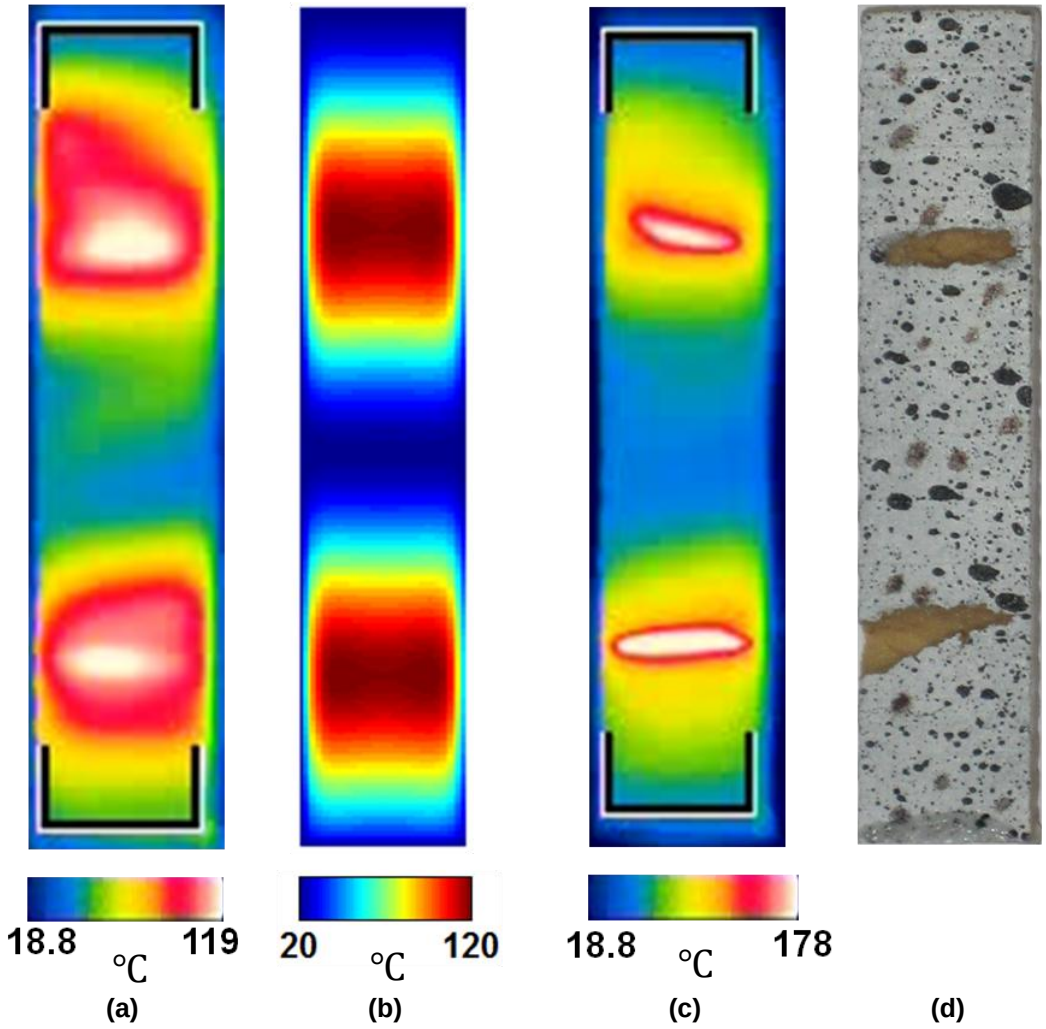

Fig. 6.16 Thermal distributions in PUF from (a) thermal imaging at 14s (b) FEA at 14s, and (c) thermal imaging at 16s, (d) the sample after the test

During ultrasonic excitation, the maximum heat generated in the PUF specimen was located at displacement nodes, which were captured by the IR camera and verified by FEM. The evolution of maximum temperature from measurements and FEA are illustrated in the Fig. 6.17. From 0 s to 14 s of ultrasonic loading, the peak temperature increases linearly with time from the FEA data due to the heat conduction effect being small enough to be ignored. During vibration cycles, the rate of heat generated is significantly higher than the rate of heat loss. The nearly adiabatic conditions result in a linear increase in temperature with time. A similar trend can be found in the thermal imaging results. The temperature increases almost linearly up to the glass transition temperature T_g is reached around 120 ℃, thereafter it rapidly rises to 160 ℃. A significant increase of damping loss tan (δ) at T_g can be observed in Fig. 6.18, which means a large amount of heat is generated at that temperature. Although the stress applied to the specimen is lower than the elastic limit, the dissipated energy comes from internal material damping and local plastic

deformation at a microscopic scale, which can be considered as contributors to the material failure.

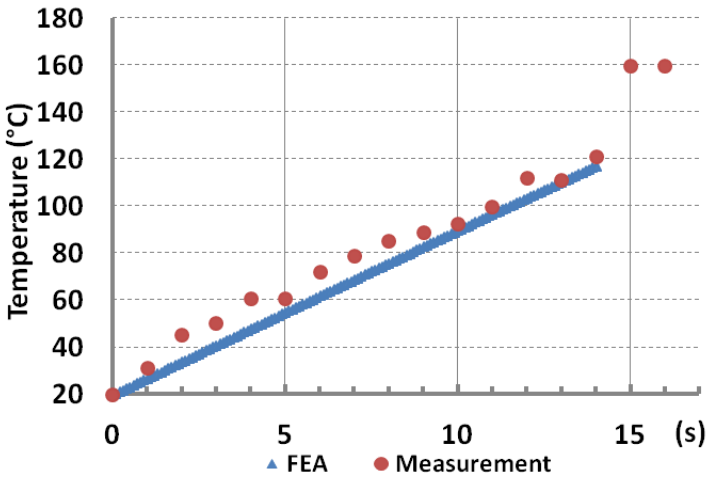

Fig. 6.17 Evolution of temperature at the position of displacement antinodes for PUF specimen during ultrasonic exciation obtained from FEA and IR camera

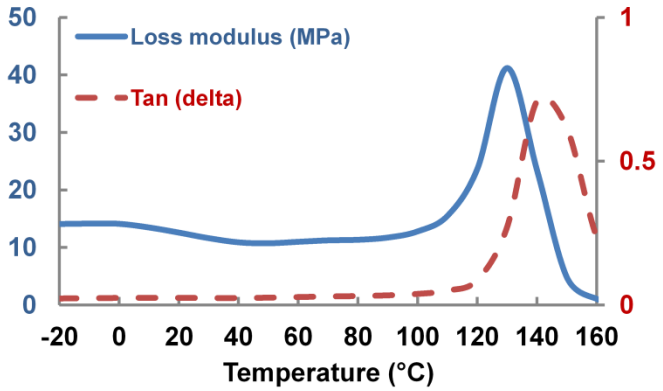

Fig. 6.18 The loss modulus and damping cofficient of PUF at 1Hz at different temperatures

6.3.3.2 Temperature Distribution for ER

Due to the nonlinear heat generation in ER during ultrasonic excitation, the finite element simulation of ER for thermal response was divided into several time period sub-models. Results of peak temperature from each model were used as the input in the next iteration to evaluate damping loss.

For the initial 1s time period, the thermal distribution in the ER sample was predicted by the finite element model, identified as model A in the Table 6.1, using a damping factor Q at 20 kHz for a reference temperature of 20 ℃. The thermal field at a time of 1s is shown in Fig. 6.19 (b), which is compared with the experimental result in Fig. 6.19 (a). Due to the peak temperature in model A being 32.2 ℃, the damping factor Q of model B for

simulation of the next 1s time frame was valued at 33.76, which is the Q value at a reference temperature of 30 ℃. The result of model B for simulation of the thermal response at time 2s is shown in Fig. 6.19 (d) and is compared with the corresponding experimental results in Fig. 6.19 (c) from thermal imaging. Based on this procedure for FEA, the thermal responses of ER during ultrasonic excitation from 0 s to 5 s are shown in Fig. 6.19 and the parameters for the models are listed in Table 6.1.

Table 6.1 The parameters for finite element thermal models

Model	Ultrasonic loading time period (s)	Initial peak temperature (℃)	Q value	Peak temperature (℃)	Results
A	0-1	25.1	36.62	32.2	Fig.6.19 (b)
B	1-2	32.2	33.76	40.2	Fig.6.19 (d)
C	2-3	40.2	26.89	50.2	Fig.6.19 (f)
D	3-4	50.2	9.95	75.9	Fig.6.19 (h)
E	4-5	75.9	2.43	166.7	Fig.6.19 (j)

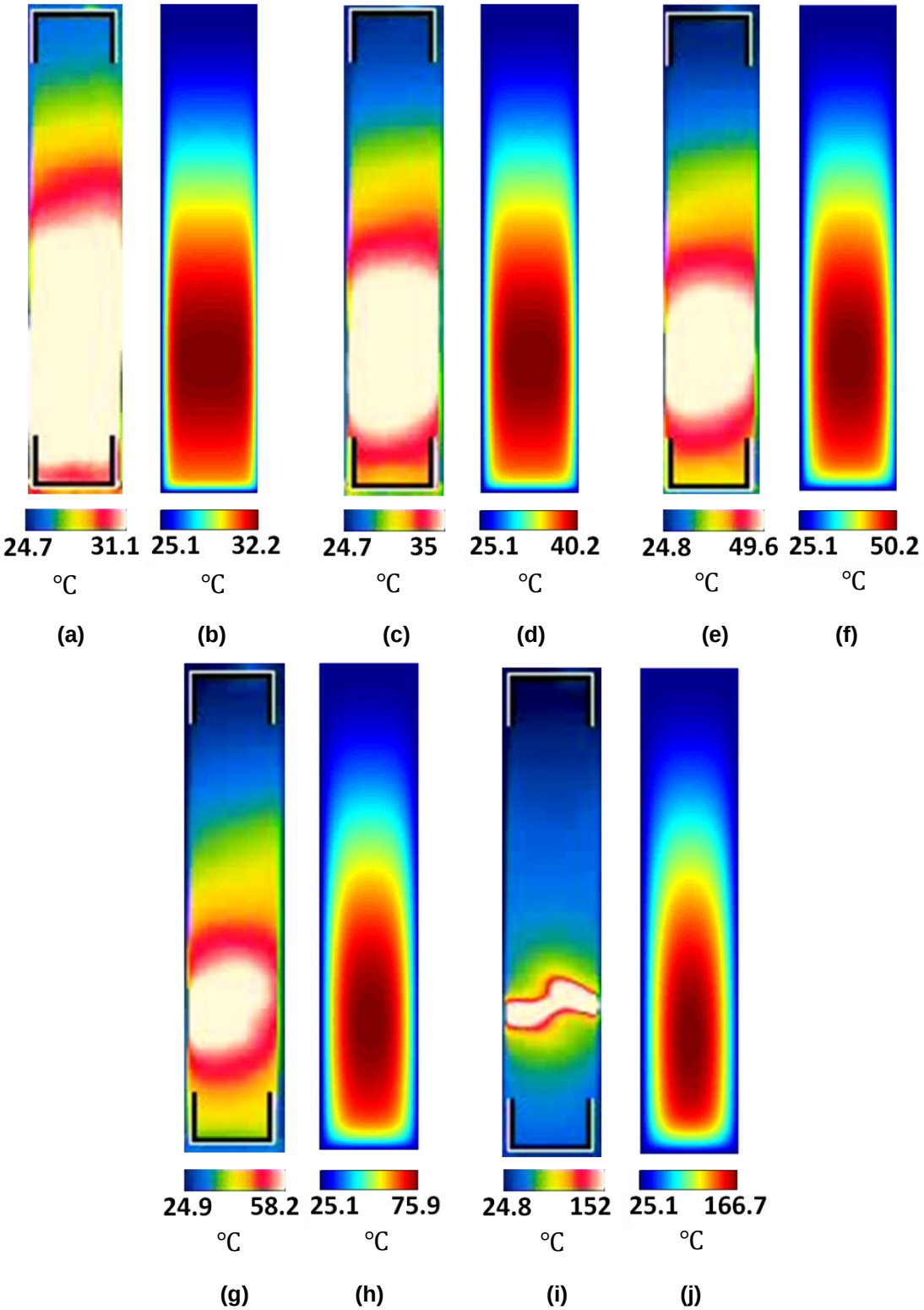

Fig. 6.19 Correlation of (a, c, e, g and i) thermal measurement and (b, d, f, h and j) FEA at times between 0s and 5s

In FEA, after an ultrasonic excitation time of 5s, the peak temperature is over 160 ℃, at which temperature the damping loss Q value cannot be extracted from the DMA tests. Therefore, subsequent thermal finite element models were not possible in this study but

should be considered for further work. The temperature distributions in FEA were correlated with the thermal data from IR camera during the initial 5 s.

During continuous ultrasonic excitation, the peak temperature in the ER sample did not increase linearly, due to the temperature dependent properties of ER. The evolution of peak temperature in FEA compared with experiment data is illustrated in Fig. 6.20. At the beginning of ultrasonic excitation, the peak temperature increases steadily to the region of glass transition temperature T_g at around 60 ℃, then there is a rapid increase up to 175 ℃. The temperature is then constant with time due to the decrease in damping Q at high temperature, such that the rate of heat generated is equal to the rate of heat convected. Finally, the specimen failed at around 190 ℃, which can be possibly considered to be due to a combination of plastic deformation induced by crack initiation and material melting.

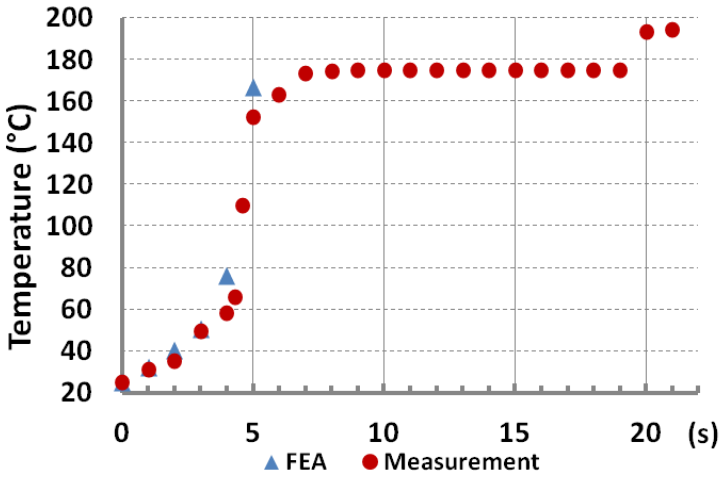

Fig. 6.20 Peak temperature evolution of ER specimen during ultrasonic loading experiment detected by IR camera and modelled by finite element method

6.3.4 Conclusions

The temperature distributions in PUF and ER during application of ultrasonic excitation were measured using an IR camera. The use of thermal imaging has provided good correlation with FEA predictions in the location of damage sites in hard tissue mimic materials and offers opportunities to initiate studies for a range of ultrasonic surgical devices.

Heat generation in hard tissue mimic materials was determined using temperature and frequency dependent damping losses, which were characterised by dynamic mechanical analysis. The important material parameters for modelling the thermal response during

ultrasonic excitation were wave velocity, applied stress, damping Q, density, Young's modulus, specific heat and heat conductivity. Due to the complexity of tissue mimic materials, the finite element models were updated with temperature dependent properties, in an iteration manner.

6.4 Mechanical Effects on SE

A non-invasive method based on the acousto-optic effect, using a LDV, has been developed for stress field characterisation in the transparent viscoelastic soft tissue mimic SE. By a combination of basic scanning routines and image reconstruction algorithms, accurate full-field stress information is presented. The experimental result is validated by finite element analysis using ABAQUS. The technique was introduced in Chapter 5.

6.4.1 Experimental Results

Experiments were conducted with the setup according to Fig. 5.11. The normalised measured and finite element generated harmonic stress fields through the specimen are shown in Fig. 6.21, and comparison of the normalized axial stress profiles from the measured and FEA predicted data is presented in Fig. 6.22.

In Fig. 6.21 (a), the incident ultrasound wave was from the vibrating horn to the PUF sample as shown at distance 0. Measurement proved problematic up to a distance of 7 mm from the excited end, where some extra silicone rubber was used to affix the sample on the top of the horn. The surfaces between distance 0 and 7 mm were not perfectly perpendicular to the laser beam and therefore laser scanning was employed only from 7 to 115 mm above the vibrating horn surface.

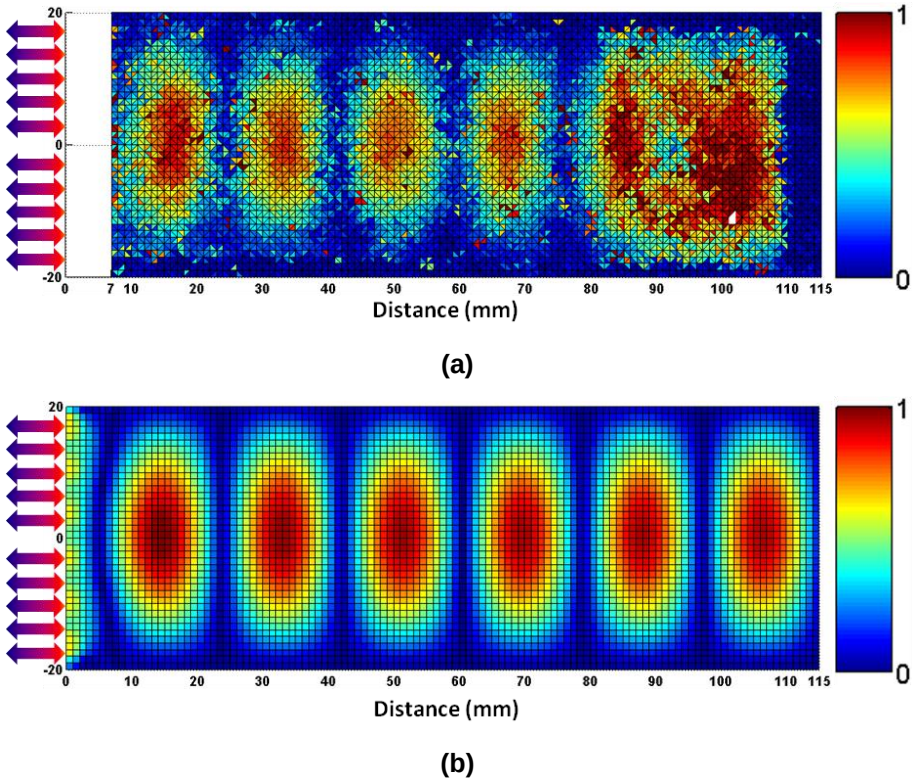

Fig. 6.21 Normalised stress map of SE under ultrasonic exciation (a) experimentally measured, (b) FEA predicted

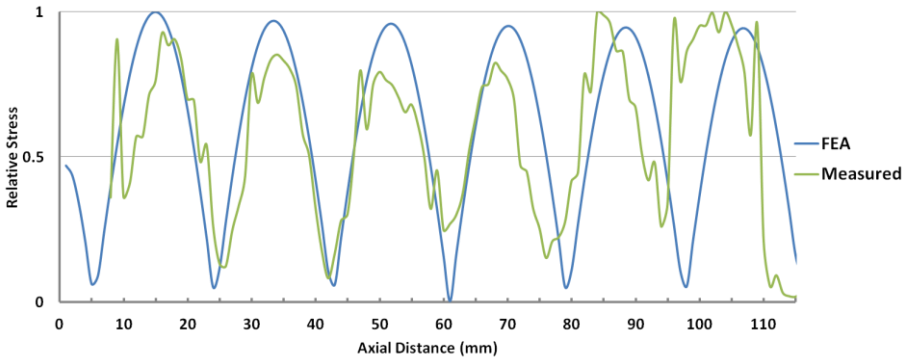

Fig. 6.22 Comparison of normalised axial stress profiles from the measured stress field and that predicted by FEA

Notable harmonics were detected in the measured data with a wavelength λ around 34 mm. The longitudinal wave speed, c, can be calculated from the longitudinal wavelength, λ, and frequency f by the equation:

$$c = \lambda f \qquad \textbf{6.4}$$

For isotropic materials, the longitudinal wave speed, c, is related to its Young's modulus, E, the Poisson's ratio, ν, and density, ρ, [236] and the equation is expressed as:

$$c = \sqrt{\frac{(1-\nu)E}{(1+\nu)(1-2\nu)\rho}} \quad \textbf{6.5}$$

By a combination of equations 6.4 and 6.5, the Young's modulus E can be obtained as

$$E = (\lambda f)^2 \rho \frac{(1+\nu)(1-2\nu)}{(1-\nu)} = 13.4\ MPa \quad \textbf{6.6}$$

where frequency $f = 19.6\times10^3$ Hz, density ρ =1020 kg/m^3, Poisson's ratio ν =0.495 and wavelength λ =0.034 m.

The Young's modulus from standard static compression and tensile tests was around 1 MPa. The dynamic modulus obtained from a reference using the nanoindentation tests was 13 MPa, which was correlated well with the result of 13.4 MPa obtained by a non-invasive ultrasonic field test. SE has frequency dependent behaviour, in which the dynamic response in high power ultrasonic applications cannot be described by the static modulus.

6.4.2 Error Analyses

Consider a laser beam entering the transparent sample of thickness T at an angle a to the x axis as shown in Fig. 6.23. When the laser beam encounters changes in the refractive index it will generally travel in a curved path. It is assumed that the beam travels in a straight line r from sample input position O to sample output position A given by:

$$z = \tan(a)x \quad \textbf{6.7}$$

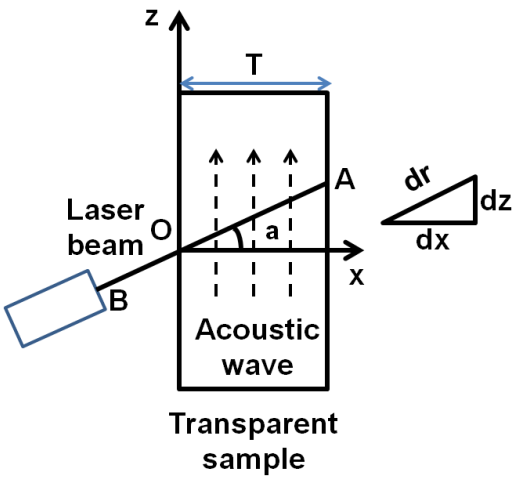

Fig. 6.23 Schematic diagram of the acoustic wave and laser beam

Total phase change was expressed as equation 5.14, where

$$dr = dz/\sin(a) \tag{6.8}$$

Integrating gives

$$I = \frac{2c}{\omega \sin a}\sin\left(\frac{\omega T \tan a}{2c}\right)\sin\left(\omega t + \theta_c - \frac{\omega T \tan a}{2c}\right) \equiv g(a,\omega,c,T)\sin\left(\omega t + \theta_c - \frac{\omega T \tan a}{2c}\right) \tag{6.9}$$

For the fixed frequency (19.6 kHz), speed of ultrasound (666.4 m/s) and sample thickness (0.026 mm), phase change depends on α through $g(a,\omega,c,T)$. In this case, an error of 1^0 in a will only give an error of 0.014% in $\varphi(t)$ and a variation of 5^0 will only give an error of 0.36% in $\varphi(t)$. This shows the measurement of the phase change is not sensitive to the angle a. Therefore, the setup using this technique for mapping stress field of this transparent sample is relatively simple with small errors on aligning the laser beam to the direction of propagation of ultrasonic field. It is clear from equation 6.9 that the error will increase linearly with T in the small a limit.

6.4.3 Discussion

It is evident that several high stress fields are present in Fig. 6.21, separated by a half wavelength from each other. The close correspondence between finite element analysis and measured stress data is clear. However, some discrepancies do exist especially at the far end of the specimen. Due to the impendence mismatch between the specimen and surrounding air, more ultrasonic energy was reflected at the interface, which increased the stress at the region of the interface in the specimen. Nevertheless, agreement between theoretical and experimental results is better over the majority of the specimen. It indicates that the internal stress field of transparent solid during ultrasonic excitation can be accurately characterised using such an scanning system with a simple setup. However, some limitations of this method can be summarised. Firstly, for ultrasonic field measurements the application of the LDV is limited since it acts to integrate the stress over the entire laser path. Moreover, it should be noted that it is not yet possible to derive acoustic stress or intensity at a specific point.

6.4.4 Conclusions

The work reported here describes a non-contacting and thus nonperturbing optical method for recording spatially distributed measurements of an acoustic field. The technique exploits the acousto-optic interaction to map the ultrasonic field in two-dimensions by traversing the optically beam across the ultrasonic field. Scanning LDV measurements enable construction of an image of the normalised stress field of a transparent solid when it is subject to ultrasonic vibration. The obtained stress field can be used to characterise the dynamic properties of the solid. The technique offers considerable potential for use in measuring the low frequency high power ultrasonic field and characterising the properties of the test sample. Favourable comparison has been obtained between measurement and FEA data. The acousto-optic study presented has demonstrated that it is possible to characterise ultrasonic fields of a transparent solid non-invasively. The ability of the scanning LDV system to rapidly record data from a grid through the ultrasonic field was a significant factor in the establishment of this method as a valuable tool for use in measurement of the stress field in a transparent solid subject to ultrasonic excitation.

6.5 Chapter Summary

The non-invasive ultrasonic field measurement methods have proved effective in mapping displacement, strain, stress and temperature fields of vibrating solids under free-field conditions. Additionally, the numerical models of ultrasonic fields show excellent correlation with experimental measurements. Hence, measurement methods and theoretical frameworks for the quantification and simulation of power ultrasonic fields exist. This combination offers the potential to confirm mutually both the experimental technique and the viability of numerical methods as a virtual prototyping tool.

7. Conclusions and Future Work

7.1 Conclusions

It is becoming increasingly important to understand how power ultrasound interacts with biological tissue during power ultrasonic surgery. The aim of this thesis was to quantitatively characterise the power ultrasonic effects on tissue. This was carried out in four stages. Firstly power ultrasonic horns were designed and manufactured. Next the material properties of the specimens were experimentally characterised before sample testing. Then experimental studies of the ultrasonic field on the surfaces of specimens were conducted using several non-invasive techniques. Finally, these experimental results were compared to numerical analysis and the damage mechanism of the specimen during ultrasonic loading was then assessed.

A review of the literature indicated that three main effects of ultrasonic interaction of biological tissue can be summarized as including direct mechanical effects, thermal effects and acoustic cavitation. The use of an ultrasonic horn in ultrasound based surgery for investigating the tissue damage by ultrasonic heating and cyclic loading is not well developed. Especially, for ultrasound and hard tissue interaction, the heat generated by ultrasonic waves can alter the mechanical properties of the hard tissue analogue and soften it to gum-like properties, in which cavitation probably occurs with simultaneous mechanical impact and thermal heating. This work focused on the study of ultrasonic wave propagation induced combined mechanical and thermal effects during ultrasonic surgical procedures. It presented detailed evaluation of power ultrasonic effects on hard and soft tissue by predictive models using numerical methods and experimental investigations using non-invasive detection.

Due to the complexity and nonuniformity of biological tissue, tissue mimic materials were manufactured and utilised instead of real tissue to obtain reliable information of ultrasound tissue interaction. The mechanical and thermal properties of tissue mimics were characterised to evaluate and simulate the biological tissue, in which static Young's modulus, heat conductivity and specific heat capacity were determined by compression/tensile tests, guarded heat flow meter method and differential scanning calorimetry respectively. Because of significant viscoelastic behaviour in application of ultrasonic loading on tissue mimics, dynamic mechanical analyses were performed to

record the frequency and temperature dependent viscoelastic properties. The time/frequency temperature superposition principle was applied to predict the material's behaviour at high frequencies, which are not directly measurable by dynamic mechanical analysis.

Two ultrasonic horns were designed using finite element methods and manufactured. The horns worked as the vibration input to load the test samples with sufficient vibration amplitude. The modal characteristics of the horns were confirmed using experimental modal analysis.

In this study, non-invasive ultrasonic field measurement techniques were introduced in the application of solids. This is the first application of ultra-high speed camera with digital image correlation technique for characterisation of power ultrasonic fields. This non-invasive technique has been proved as a successful alternative in power ultrasonic applications, in which loading frequency is over 20 kHz. Another technique combined the acousto-optic principle and laser interferometry in order to characterise the power ultrasonic stress field in transparent solids. Examination of ultrasonic waves propagating in transparent, isotropic and viscoelastic solids is particularly applicable to the very quick testing of the dynamic mechanical properties of transparent viscoelastic solids. Furthermore, non-contact thermal imaging technique by IR camera is a good choice for mapping temperature distribution of materials during power ultrasonic vibrating, which can be used for determination of internal heat generation induced by absorption of ultrasonic wave energy and understanding the damage mechanism of ultrasonic effects on solids. Due to the internal heat generated during power ultrasonic vibration, the materials are subject to mechanical and thermal loading simultaneously. Based on the quantitative characterisation of ultrasonic stress/strain and temperature fields in solids, the frequency and temperature dependent behaviour of materials were determined, which included a significant viscous effect of biological tissue or polymers in dynamic application.

Numerical models including finite element models and analytical models were defined by frequency dependent mechanical properties to predict and verify the experimental results. The results of numerical models matched well with experimental findings in the prediction of ultrasonic stress/strain fields. Therefore, static mechanical properties are not appropriate for characterisation of the dynamic behaviour of viscoelastic solid. Furthermore, finite element models for thermal analysis can be parameterized utilising thermal conductivity

and specific heat capacity to characterise heat transfer in materials and damping coefficient to determine the heat generation in materials. These thermal parameters were used in FEA models to obtain temperature distribution during ultrasonic wave propagation. The models have good correlations with experimental data captured using an IR camera.

During power ultrasonic loading, the damage to the material sample is accompanied by an accumulation of cyclic deformation and heating. When the accumulated heat softens the material to a gum-like pliable, which has a lower yield stress value than its initial, the cyclic deformation creates stress higher than the yield stress to make the strain becomes irreversible. Plastic deformation occurs in the materials initiating cracks and propagating existing cracks. Especially, as the temperate of the material rises to its glass transition temperature, when maximum damping induces lager amounts of heat to make plastic deformation more easily and melting occurs causing the solid to expand. Typically, the damage is associated with material damping and phase transition. No cavitation effect was found to contribute to solid material damage.

Through this work, the time/frequency temperature superposition principle was found to be a good predictor to analyse the frequency and temperature dependent behaviour of polymeric materials. The data from dynamic mechanical analyser is useful in generating the master curve to predict the polymers response in high frequency loading applications.

In power ultrasonic applications, three viscoelastic tissue mimic materials were categorized as follows: ER, a frequency and temperature dependent material; PUF, no obvious frequency and temperature dependency; SE, dependant on frequency but not temperature.

In the preparation of experimental study, the horn with triangular slots was designed using a finite element method. The technique of manufacturing the horn with triangular slots is a new method for designing an ultrasonic horn, which make it possible that the horn has a smaller input face and larger output face without the loss of surface uniformity and gain. The resonant response of the horn was checked by experimental modal analysis, which proves that the novel horn has a longitudinal mode around the predefined 20 kHz with an gain greater than 2. The uniformity of the output face was experimentally examined using 3D laser scanning vibrometer, which gave acceptable results for uniformity. Compared with conventional ones, the horn with triangular slots can work as a vibration amplifier with larger output face than input for contact with loading sample.

This study has provided confidence that the methodology could be applied to study tissue samples subjected to excitations typical of ultrasonic surgical devices, including those for orthopaedic bone cutting procedures. Full-field surface strain measurement has the potential to be used to predict regions where tissue damage can occur remote from the site where the ultrasonic surgical device is interacting directly with the tissue.

7.2 Suggestions for Further Work

The work presented in this thesis has identified further research which could be carried out. Future applications of this work within the context of power ultrasonic systems is three-fold: firstly, the non-invasive technique has potential to be extended to measure ultrasonic fields in biological tissues and more accurate tissue mimics; secondly, fully coupled mechanical and thermal finite element models could be developed to enable more accurate simulations and 3D FE models would be a great benefit. Finally, this work forms a platform from which further research into power ultrasonic surgery for cutting tissue could be launched.

7.2.1 Applications in Tissues and More Accurate Tissue Mimics

The use of DIC combined with thermal imaging has provided good correlation with FEA data in the location of damage sites in hard tissue mimic materials subject to power ultrasound excitation and offers opportunities to initiate a study for a range of biological tissues or more accurate tissue mimicking samples.

7.2.1.1 Hard Tissue and Mimics

In the future, to characterise the power ultrasonic effects on biological tissues, experimental investigations could be conducted using hard tissue with intricate shapes. The shape of the specimen has great effects on ultrasonic energy distribution. Full field strain and stress measurements and thermal imaging of complex tissue will provide more accurate and reliable experimental data for use during power ultrasonic surgery. Due to the limited image resolution of the high speed camera HTV-1, image captures of the tissue sample in an intricate shape with large surfaces will be performed separately in several times to cover the whole surface. Post image processing will be needed to combine these images into a single image for providing results of full field measurements.

Tissue mimicking materials which can closely mimic the mechanical and thermal properties of tissue play an important role in evaluating the effects of power ultrasound on hard tissues. 3D printing is a good technique for fabricating hard tissue mimics which accurately simulating the anatomy as well as the physical properties of tissue. The use of the additive manufacturing technologies makes the 3D printed bone tissue mimics possible. It has the ability to directly print porous bone mimics with desired shape, controlled chemical components and interconnected porosity. Instead of polymer based tissue mimics used in this study, a composite of hydroxyapatite and bioactive glasses could be manufactured via 3D printing process. Due to the bone is largely composed of the inorganic mineral hydroxyapatite, the 3D printed composite is advantageous for mimicking the mechanical and thermal properties of bone. According to a sliced virtual model of a bone sample, the granulated composite used as powder is printed into layers and formed into the customised structure. This accurate tissue mimics can be used to investigate its mechanical and thermal effects of ultrasound by the non-invasive techniques.

7.2.1.2 Soft Tissue Mimics

This work focussed on mechanical and thermal effects in the tissue mimics under ultrasonic loading. Further research could be carried out to investigate the cavitation effects in the process of ultrasonic surgery of soft tissue. Due to large amount of water in soft tissue, mechanical impact and heat generation will be highly dependent upon the cavitation field generated during power ultrasonic loading. To study the cavitation-induced damage to tissue, a tissue phantom with similar acoustic and mechanical properties to tissue could be developed.

The transparent agarose phantom with red blood cells introduced by Maxwell etc. [237] was found to be very sensitive indicator of cavitation damage. Experimental characterisation of cavitation could also be developed using non-invasive measurements. High speed imaging of the phantom could be performed while power ultrasound applied. The images of cavitation cloud generated in the cell phantom due to power ultrasonic excitation could be captured. Individual red blood cells could be observed in the agarose. Prior to ultrasound exposure, an image of the cell phantom could be recorded as the reference image and then consecutive images could be captured using high speed camera during ultrasound exposure. The movements of individual cells in the phantom caused by cavitation could be tracked and correlation based speckle tracking algorithm could be

developed to estimate the cell displacements. Cavitation damage could be identified and characterised based on the movement tracking of red blood cells in the phantom. Therefore, with the help of the cell tissue phantom, high speed imaging could be used to show the damage with the presence of cavitation.

7.2.2 Finite Element Updates

In this work, finite element studies of the heat generation in the specimen under ultrasonic loading were developed from two analytical steps. Firstly, damping losses per vibration cycle were calculated in the mechanical analysis. Then the damping losses became the heat source and were considered as the constant thermal input in thermal analysis to solve the heat equation and predict temperature distribution.

In the process of the ultrasound induced materials deformation, cyclic accumulation of heat flux transferred from the work under cyclic loading results in an increased temperature. The heat affects the mechanical properties. The heat generation per unit volume could be introduced as a source for a thermal-mechanical analysis. In further studies, the finite element model could be defined by the material data coupled with frequency and temperature dependent properties. A user-defined material model could be created by writing user subroutines with ABAQUS. Transient coupled temperature-displacement finite element analysis could be carried out to investigate thermo-mechanically coupled behaviours under power ultrasonic loading. The contribution of cyclic loading to internal heat generation could be addressed. The coupled model is more realistic even though it is computationally expensive due to involving handling of a large system of equations at every increment. The model could accurately simulate the actual situation in a time domain by providing mechanical deformation and thermal distribution simultaneously. Therefore, more accurate models could be developed to correlate the experimental and numerical data for improved simulation of ultrasonic surgical procedures.

A 3D finite element model with involving bone and soft tissue connections could be developed to solve the elastic wave equation and study the power ultrasound induced stress fields. The model could provide the results inside and on the surface of tissue. By modifying the coupling state, the boundary condition, and the mechanical characteristics of tissue, the model could be effectively used to analyse the ultrasonic tissue damages.

7.2.3 Involvement with Cutting Procedures

Damage of hard tissue in ultrasonic surgery could be discussed in more details by experimental characterisation of damage caused by a combination of cyclic loading induced fatigue and thermal damage and blade cutting induced tissue removal.

7.2.3.1 Experimental Ultrasonic Cutting

In this work, when tissue is only subject to longitudinal ultrasonic excitation, damage is closely related to stress distribution and thermal response due to heat generation by cyclic loading. With the effect of friction between the cutting edge and the material being cut, tissue damage in ultrasonic surgery could be considered mainly by separation of material bonds by stressing structural elements and frictional heats. Therefore, experimental investigations of ultrasonic cutting tissue should involve investigating the conventional cutting process and friction process in the presence of the superimposed ultrasonic vibration.

Conventional cutting applications are complex combinations including fracture, deformation and friction. Friction typically depends on the contacting area and sliding velocity. Superimposed with ultrasonic vibration, the mechanical interactions between contacting surfaces may be influenced. Apart from modifying mechanical interactions, friction is also related to the heat generation by the conversion of the mechanical vibration energy into thermal energy. Firstly, resonant cutting blades could be designed according to the horn design in this thesis. Then, thermal imaging technique could be used to monitor the temperature distribution around the cuts. Although it is difficult to obtain images from the contacting area using high speed camera, the displacements of the cutting blade and the fracture of the specimen during ultrasonic cutting could be monitored and calculated using DIC technique, which could be used to study the damaging process of the cut surface.

7.2.3.2 Finite Element Simulation of Ultrasonic Cutting

FE models for ultrasonic cutting of tissue could be developed to simulate the thermo-mechanical behaviour. Estimations of accurate mechanical and thermal properties of materials for inclusion in the models could be determined experimentally using the tests mentioned in this thesis. The hard/soft tissue could be modelled as linear homogenous isotropic elastic/viscoelastic-plastic materials and a shear failure criterion should be

applied for the failed element deletion. The cutting blade could be modelled as a rigid body for simplification in a 2D model. A velocity profile and vibrating displacement should be assigned to the blade in the boundary condition. Modelling the interaction between the cutting blade and the materials could be selected as Arbitrary Lagrangian Eulerian formulation, which could adopt an explicit integration solution for fast convergence.

References

1. Mason, W.P. and R.N. Thurston, *Physical Acoustics: Principles and Methods*1981: Academic Press.
2. Graff, K.F. *Process Applications of Power Ultrasonics - A Review*. in *1974 Ultrasonics Symposium*. 1974.
3. *Basics of power ultrasonics*. [cited 2012 Feburary 5]; Available from: http://www.powerultrasonics.com/content/basics-power-ultrasonics.
4. Thoe, T.B., D.K. Aspinwall, and M.L.H. Wise, *Review on ultrasonic machining.* International Journal of Machine Tools and Manufacture, 1998. **38**(4): p. 239-255.
5. Neppiras, E.A., *Ultrasonic welding of metals.* Ultrasonics. **3**(3): p. 128-135.
6. Lambert, B., *Ultrasonic cleaning aids to production.* Engineering (London), 1979. **219**(3): p. 329-331.
7. Lucas, M., et al., *Design and Characterisation of Ultrasonic Cutting Tools.* CIRP Annals - Manufacturing Technology, 2001. **50**(1): p. 149-152.
8. Dong, S., et al., *Development and application of ultrasonic surgical instruments.* Biomedical Engineering, IEEE Transactions on, 1997. **44**(6): p. 462-467.
9. Vaitekunas, J.J., F. Stulen, and E. Grood, *Cutting wax with an ultrasonically activated blade.* Engineering in Medicine and Biology Magazine, IEEE, 2008. **27**(4): p. 71-79.
10. Polyakov, V.A., *Ultrasonic cutting and welding in clinical surgery.* Sovetskaia Meditsina, 1972. **35**(6): p. 29-34. Rawson, F.H., Morris, P.S., 1993. Ultrasonic Cutting Apparatus. US Patent 5 226 343.
11. MacBeath, A., *Ultrasonic bone cutting*, in *Department of Mechanical Engineering*, 2006, University of Glasgow: Glasgow.
12. Drisko, C.L., et al., *Position paper: sonic and ultrasonic scalers in periodontics. Research, Science and Therapy Committee of the American Academy of Periodontology.* Journal of periodontology, 2000. **71**(11): p. 1792-801.
13. Kelman, C.D., *Pha/co-emulsification and aspiration. A new technique of cataract removal. A preliminary report.* American Journal of Ophthalmology, 1967. **64**: p. 23-35.
14. Aro, H., et al., *Ultrasonic Device in Bone Cutting: A Histological and Scanning Electron Microscopical Study.* Acta Orthopaedica, 1981. **52**(1): p. 5-10.
15. Flamm, E.S., et al., *Preliminary Experience with Ultrasonic Aspiration in Neurosurgery.* Neurosurgery, 1978. **2**(3): p. 240-245.
16. Hambley, R., Hebda, P.A., Abell, E., Cohen, B.A., Jegasothy, B.V., *Wound healing of skin incisions produced by ultrasonically vibrating knife, scalpel, electrosurgery, and carbon dioxide laser.* Journal of Dermatologic Surgery & Oncology, 1988. **14**(11): p. 1213-7.
17. Georghiou, G.P., et al., *Advantages of The Ultrasonic Harmonic Scalpel for Radial Artery Harvesting.* Asian Cardiovasc Thorac Ann, 2005. **13**(1): p. 58-60.
18. Feil, W., et al., *Ultrasonic Energy For Cutting, Coagulating, And Dissecting*2005: Thieme Medical Publishers, Incorporated.
19. Suslick, K.S., *Industrial applications of ultrasound*, in *Ultrasound: its chemical, physical, and biological effects*1988, VCH Publishers. p. 97-122.
20. O'Daly, B.J., et al., *High-power low-frequency ultrasound: A review of tissue dissection and ablation in medicine and surgery.* Journal of Materials Processing Technology, 2008. **200**(1-3): p. 38-58.
21. Rayleigh, J.W.S.B. and R.B. Lindsay, *The theory of sound*, 1976: Dover Publications.

22. Rayleigh, F., *Translated in Lindsay (1974).* Annals of Physical Chemistry, 1830. **20**: p. 290.
23. Galton, F., Nature, 1883. **27**(I3).
24. Koenig, R., Annals of Physical Chemistry, 1899. **69**: p. 626, 721.
25. Curie, J.-P. and P. Curie, *Translated in Lindsay (1973).* Academie des sciences Paris, 1880. **91**: p. 294.
26. Graff, K.E., *A History of Ultrasonics, Chapter 1*, in *Physical Acoustics*1981, Academic Press.
27. Sokolov, S., *Means for Indicating Flaws in Materials*, 1939, Sergey, Sokoloff: United States.
28. Mason, W.P., *Piezoelectricity, its history and applications.* The Journal of the Acoustical Society of America, 1981. **70**(6): p. 1561-1566.
29. Shoh, A., *Industrial Applications of Ultrasound - A Review I. High-Power Ultrasound.* Sonics and Ultrasonics, IEEE Transactions on, 1975. **22**(2): p. 60-70.
30. Neppiras, E.A., *Report on ultrasonic machining.* Metalworking Production, 1956. **100**: p. 1283-1604.
31. Wood, R.W. and A.L. Loomis, *The Physical and Biological Effects of High-frequency Sound-waves of Great Intensity*, in *Philosophical Magazine*1927. p. 417-436.
32. Wahl, P., *Put Sound Waves to Work in Your Shop*, in *Popular Science*March 1970.
33. Wikipedia contributors. *Ultrasonic welding*. [cited 2012 June 20]; Available from: http://en.wikipedia.org/w/index.php?title=Ultrasonic_welding&oldid=580962982.
34. Graff, K., *Macrosonics in industry: Ultrasonic soldering.* Ultrasonics, 1977. **15**(2): p. 75-81.
35. Kopeliovich, D. *Ultrasonic Processing*. [cited 2012 15 December]; Available from: http://www.substech.com/dokuwiki/doku.php?id=ultrasonic_processing.
36. Mason, W.P., *Physical Acoustics V15: Principles and Methods*1981: Elsevier Science.
37. Bar-Cohen, Y., et al. *Ultrasonic/sonic drilling/coring (USDC) for planetary applications*. 2001.
38. Cardoni, A., P. Harkness, and M. Lucas, *Ultrasonic rock sampling using longitudinal–torsional vibrations.* Ultrasonics, 2010. **50**(4–5): p. 447-452.
39. Tsujino, J., *Ultrasonic motor using a one-dimensional longitudinal-torsional vibration converter with diagonal slits.* Smart Materials and Structures, 1998. **7**(3): p. 345.
40. Sashida, T. and T. Kenjō, *An Introduction to Ultrasonic Motors*1993: Clarendon Press.
41. Ueha, S., Y. Tomikawa, and N. Nakamura, *Ultrasonic motors: theory and applications*1993: Clarendon Press.
42. Yi, Y., et al., *Development and analysis of a longitudinal and torsional type ultrasonic motor with two stators.* Ultrasonics, 2005. **43**(8): p. 629-634.
43. McCulloch, E., *Experimental and Finite Element Modelling of Ultrasonic Cutting of Food*, 2008, Unviersity of Glasgow.
44. Povey, J.W. and T.J. Mason, *Ultrasound in Food Processing*1998: Springer.
45. Arnold, G., et al., *Ultrasonic cutting of cheese: Composition affects cutting work reduction and energy demand.* International Dairy Journal, 2009. **19**(5): p. 314-320.
46. *Ultrasonic food cutting*. [cited 2012 November 15]; Available from: http://www.sonicsandmaterials.com/oem-foodcutting.htm.
47. Richards, W.T. and A.L. Loomis, *The Chemical Effects of High Frequency Sound Waves I. a Preminary Survey.* Journal of the American Chemical Society, 1927. **49**(12): p. 3086-3100.

48. Suslick, K.S., *The chemical effects of ultrasound.* Scientific American, 1989. **2**(260): p. 80-86.
49. Ritter, S., *Single-bubble Microreactor*. Chemical & Engineering News Archive, 2002. **80**(30): p. 11.
50. Flint, E.B. and K.S. Suslick, *The temperature of cavitation.* Science (New York, N.Y.), 1991. **253**(5026): p. 1397-1399.
51. Suslick, K.S., et al., *Acoustic cavitation and its chemical consequences.* Philosophical Transactions of the Royal Society of London. Series A: Mathematical, Physical and Engineering Sciences, 1999. **357**(1751): p. 335-353.
52. Mason, T.J., *Sonochemistry and sonoprocessing: the link, the trends and (probably) the future.* Ultrasonics Sonochemistry, 2003. **10**(4–5): p. 175-179.
53. Kristoffy, I., *Metal Forming With Vibrated Tools.* Journal of Engineering for Industry, 1969. **91**(4): p. 1168-1174.
54. Rozner, A.G., *Effect of Ultrasonic Vibration on Coefficient of Friction during Strip Drawing.* The Journal of the Acoustical Society of America, 1971. **49**(5A): p. 1368-1371.
55. Rodr ǵuez, G., et al., *Experimental study of defoaming by air-borne power ultrasonic technology.* Physics Procedia, 2010. **3**(1): p. 135-139.
56. Freitas, S., et al., *Continuous contact- and contamination-free ultrasonic emulsification—a useful tool for pharmaceutical development and production.* Ultrasonics Sonochemistry, 2006. **13**(1): p. 76-85.
57. O' Brien, W., *Assessing the Risks for Modern Diagnostic Ultrasound Imaging.* Japanese Journal of Applied Physics, 1998. **37**(Part 1, No. 5B): p. 2781-2788.
58. Gersten, J.W., *Effect of ultrasound on tendon extensibility.* American journal of physical medicine, 1955. **34**(2): p. 362-369.
59. ter Haar, G., *Therapeutic applications of ultrasound.* Progress in Biophysics and Molecular Biology, 2007. **93**(1–3): p. 111-129.
60. Shaw, A. and M. Hodnett, *Calibration and measurement issues for therapeutic ultrasound.* Ultrasonics, 2008. **48**(4): p. 234-252.
61. Chaussy, C. and E. Schmiedt, *Extracorporeal shock wave lithotripsy (ESWL) for kidney stones. An alternative to surgery?* Urologic radiology, 1984. **6**(1): p. 80-87.
62. Wikipedia contributors. *Extracorporeal shock wave lithotripsy*. [cited 2012 Febuary 2]; Available from: http://en.wikipedia.org/w/index.php?title=Extracorporeal_shock_wave_lithotripsy&oldid=536195339.
63. Lynn, J.G., et al., *A New Method for The Generation and Use of Focused Ultrasound in Experimental Biology.* The Journal of General Physiology, 1942. **26**(2): p. 179-193.
64. FRY, F.J., *Precision High Intensity Focusing Ultrasonic Machines for Surgery.* American Journal of Physical Medicine & Rehabilitation, 1958. **37**(3): p. 152-156.
65. Kennedy, J.E., *High-intensity focused ultrasound in the treatment of solid tumours.* Nat Rev Cancer, 2005. **5**(4): p. 321-327.
66. Kennedy, J.E., G.R. ter Haar, and D. Cranston, *High intensity focused ultrasound: surgery of the future?* British Journal of Radiology, 2003. **76**(909): p. 590-599.
67. Burov, A. *High-intensity ultrasonic vibrations for action on animal and human malignant tumours*. in *Dokl Akad Nauk SSSR*. 1956.
68. Wu, F., et al., *Extracorporeal high intensity focused ultrasound ablation in the treatment of 1038 patients with solid carcinomas in China: an overview.* Ultrasonics Sonochemistry, 2004. **11**(3–4): p. 149-154.
69. Mohan, R., R. Bains, and V. Bains, *Application of ultrasound in periodontics: Part I.* Journal of Indian Society of Periodontology, 2008. **12**(2): p. 29-33.

70. Vang, A., *VIBRATORY SURGICAL INSTRUMENTS*, United States Patent Office, Editor 1955: United State.
71. Giraud, J.-Y., et al., *Bone cutting.* Clinical Physics and Physiological Measurement, 1991. **12**(1): p. 1.
72. Gossot, D., et al., *Ultrasonic dissection for endoscopic surgery.* Surgical Endoscopy, 1999. **13**(4): p. 412-417.
73. Balamuth, L., *The application of ultrasonic energy in the dental field*, in *Ultrasonic techniques in biology and medicine*, B. Brown and D. Gordon, Editors. 1967, Ilife: London. p. 194-205.
74. Zinner, D.D., *Recent ultrasonic dental studies, including periodontia, without the use of an abrasive.* Journal of Dental Research, 1955. **34**(5): p. 748-749.
75. Plotino, G., et al., *Ultrasonics in Endodontics: A Review of the Literature.* Journal of Endodontics, 2007. **33**(2): p. 81-95.
76. Catuna, M.C., *Sonic energy: A possible dental application, Preliminary report of an ultrasonic cutting method.* Annals of dentistry, 1953. **12**: p. 100-101.
77. Balamuth, L., *Ultrasonics and Dentistry.* Sound: Its Uses and Control, 1963. **2**(2): p. 15-19.
78. Richman, R.J., *The use of ultrasonics in root canal therapy and root resection.* Journal of Dental Medicine, 1957. **12**: p. 12-18.
79. Postle, H.H., *Ultrasonic cavity preparation.* The Journal of Prosthetic Dentistry, 1958. **8**(1): p. 153-160.
80. Street, E.V., *A critical evaluation of ultrasonics in dentistry.* The Journal of Prosthetic Dentistry, 1959. **9**(1): p. 132-141.
81. Johnson, W.N. and J.R. Wilson, *The Application of the Ultrasonic Dental Unit to Scaling Procedures.* Journal of Periodontology, 1957. **28**: p. 264-271.
82. Laird, W.R.E. and A.D. Walmsley, *Ultrasound in dentistry. Part 1—biophysical interactions.* Journal of Dentistry, 1991. **19**(1): p. 14-17.
83. Martin, H., *Ultrasonic disinfection of the root canal.* Oral Surgery, Oral Medicine, Oral Pathology, 1976. **42**(1): p. 92-99.
84. Stock, C.J., *Current status of the use of ultrasound in endodontics*. Vol. 41. 1991. 175-82.
85. Walmsley, A.D., *Applications of ultrasound in dentistry.* Ultrasound in Medicine & Biology, 1988. **14**(1): p. 7-14.
86. Walmsley, A.D., W.R.E. Laird, and P.J. Lumley, *Ultrasound in dentistry. Part 2—periodontology and endodontics.* Journal of Dentistry, 1992. **20**(1): p. 11-17.
87. *Mectron Products Pizo Smart*. [cited 2012 Feburary 5]; Available from: www.mectron.com/piezo-smart.
88. Amaral, J.F., *The experimental development of an ultrasonically activated scalpel for laparoscopic use.* Surgical laparoscopy & endoscopy, 1994. **4**(2): p. 92-99.
89. Kinoshita, T., et al., *Experimental study on heat production by a 23.5-kHz ultrasonically activated device for endoscopic surgery.* Surgical Endoscopy, 1999. **13**(6): p. 621-625.
90. Kadesky, K.M., et al., *Proximity injury by the ultrasonically activated scalpel during dissection.* Journal of pediatric surgery, 1997. **32**(6): p. 878-879.
91. Feil, W., et al., *Ultrasonic Energy For Cutting, Coagulating, And Dissecting*2005: Thieme Medical Pub.
92. Flamm, E.S., et al., *Preliminary experience with ultrasonic aspiration in neurosurgery.* Neurosurgery, 1978. **2**(3): p. 240.
93. Wuchinich, D.G., et al., *Vibration apparatus preferably for endoscopic ultrasonic aspirator*, 1988, Google Patents.
94. Wuchinich, D.G., A. Broadwin, and R.P. Andersen, *Ultrasonic aspirator*, 1980, Google Patents.

95. *HARMONIC WAVE® Open Shears*. [cited 2012 Februrary 5]; Available from: http://www.ethicon.com/healthcare-professionals/products/energy-devices/harmonic-wave.
96. *Ablation Technologies Worldwide Market, 2008-2017: Products, Technologies Markets, Companies and Opportunities*, 2008, MedMarket Diligence, LLC.
97. Volkov, M. and I. Shepeleva, *The use of ultrasonic instrumentation for the transection and uniting of bone tissue in orthopaedic surgery.* Reconstruction surgery and traumatology, 1974. **14**: p. 147.
98. Polyakov, V., *Ultrasonic Bonding of Bones and Cutting of Live Biological Tissues*1974: Mir Pub.
99. Grasshoff, H. and M. Beckert, *Osteotomy with ultrasonics].* Beiträge zur Orthopädie und Traumatologie, 1981. **28**(6): p. 299.
100. Horton, J.E., T.M. Tarpley, and J.R. Jacoway, *Clinical applications of ultrasonic instrumentation in the surgical removal of bone.* Oral Surgery, Oral Medicine, Oral Pathology, 1981. **51**(3): p. 236-242.
101. Fuji Technology Press, *Low-invasive Bone Cutting with Ultrasonic Scalpel*, in *Techno Japan*2001. p. 41.
102. Robiony, M., et al., *Piezoelectric bone cutting in multipiece maxillary osteotomies.* Journal of oral and maxillofacial surgery : official journal of the American Association of Oral and Maxillofacial Surgeons, 2004. **62**(6): p. 759-761.
103. Beziat, J.L., et al., *Ultrasonic osteotomy as a new technique in craniomaxillofacial surgery.* International journal of oral and maxillofacial surgery, 2007. **36**(6): p. 493-500.
104. Chaichana, K., et al., *Novel use of an ultrasonic bone-cutting device for endoscopic-assisted craniosynostosis surgery.* Child's Nervous System, 2013: p. 1-6.
105. Matsuoka, H., et al., *Recapping hemilaminoplasty for spinal surgical disorders using ultrasonic bone curette.* Surgical Neurology International, 2012. **3**.
106. Schaller, B.J., et al., *Piezoelectric Bone Surgery: A Revolutionary Technique for Minimally Invasive Surgery in Cranial Base and Spinal Surgery? Technical Note.* Neurosurgery, 2005. **57**(4): p. E410 10.1227/01.NEU.0000176700.77461.C9.
107. *Piezosurgery medical*. [cited 2012 Feburary 5]; Available from: http://www.piezosurgery.com.
108. Chan, K.K., et al., *A new motor-driven surgical probe and its in vitro comparison with the cavitron ultrasonic surgical aspirator.* Ultrasound in Medicine & Biology, 1986. **12**(4): p. 279-283.
109. Cimino, W.W. and L.J. Bond. *Physics of ultrasonic surgery using tissue fragmentation*. in *Ultrasonics Symposium, 1995. Proceedings., 1995 IEEE*. 1995.
110. Cimino, W.W. and L.J. Bond, *Physics of ultrasonic surgery using tissue fragmentation: Part I.* Ultrasound in Medicine & Biology, 1996. **22**(1): p. 89-100.
111. Bond, L.J. and W.W. Cimino, *Physics of ultrasonic surgery using tissue fragmentation: Part II.* Ultrasound in Medicine & Biology, 1996. **22**(1): p. 101-117.
112. Khambay, B.S. and A.D. Walmsley, *Investigations into the use of an ultrasonic chisel to cut bone. Part 1: forces applied by clinicians.* Journal of Dentistry, 2000. **28**(1): p. 31-37.
113. Khambay, B.S. and A.D. Walmsley, *Investigations into the use of an ultrasonic chisel to cut bone. Part 2: Cutting ability.* J Dent, 2000. **28**(1): p. 39-44.
114. Emam, T.A. and A. Cuschieri, *How safe is high-power ultrasonic dissection?* Annals of surgery, 2003. **237**(2): p. 186.

115. Koch, C., et al., *Determination of temperature elevation in tissue during the application of the harmonic scalpel.* Ultrasound in Medicine & Biology, 2003. **29**(2): p. 301-309.
116. Goldberg, S.H., et al., *Thermal Tissue Damage Caused by Ultrasonic Cement Removal from the Humerus.* The Journal of Bone & Joint Surgery, 2005. **87**(3): p. 583-591.
117. Humphrey, V.F., *Ultrasound and matter—Physical interactions.* Progress in Biophysics and Molecular Biology, 2007. **93**(1–3): p. 195-211.
118. Barnett, S.B., et al., *The sensitivity of biological tissue to ultrasound.* Ultrasound in Medicine & Biology, 1997. **23**(6): p. 805-812.
119. Schafer, M.E. and B. Arbisser. *Quantification of acoustic exposure during cataract surgery*. in *Ultrasonics Symposium, 2004 IEEE*. 2004.
120. Rosenschein, U., et al., *Experimental ultrasonic angioplasty: Disruption of atherosclerotic plaques and thrombi in vitro and arterial recanalization in vivo.* Journal of the American College of Cardiology, 1990. **15**(3): p. 711-717.
121. Brown, B.H., et al., *Medical Physics And Biomedical Engineering*1999: San Val, Incorporated.
122. Sun, Y., *Ultrasound characterization of structure and density of coral as a model for trabecular bone*, 2000, Worcester Polytechnic Institute.
123. Laugier, P. and G. Haïat, *Introduction to the Physics of Ultrasound*, in *Bone Quantitative Ultrasound*, P. Laugier and G. Haïat, Editors. 2011, Springer Netherlands. p. 29-45.
124. Kohles, S.S., et al., *Ultrasonic wave velocity measurement in small polymeric and cortical bone specimens.* J Biomech Eng, 1997. **119**(3): p. 232-6.
125. Rho, J.Y., *Ultrasonic characterisation in determining elastic modulus of trabecular bone material.* Medical and Biological Engineering and Computing, 1998. **36**(1): p. 57-59.
126. Rooney, J.A., *Shear as a Mechanism for Sonically Induced Biological Effects.* The Journal of the Acoustical Society of America, 1972. **52**(6B): p. 1718-1724.
127. Frost, H.M. and E.E. Fill, *Interactions between a Vibrating Object and the Surface of a Soft Solid.* The Journal of the Acoustical Society of America, 1971. **50**(1A): p. 112-112.
128. MCGuinness. G., et al., *Surgical Cutting and Ablation by Energy Based Devices: Principles and Applications*, in *International Conference on Advanced Manufacturing Systems and Technology*2011: Mali Losinj, Croatia.
129. Barnett, S.B., et al., *Current status of research on biophysical effects of ultrasound.* Ultrasound in Medicine & Biology, 1994. **20**(3): p. 205-218.
130. Goldman, D.E. and T.F. Hueter, *Tabular Data of the Velocity and Absorption of High-Frequency Sound in Mammalian Tissues.* The Journal of the Acoustical Society of America, 1956. **28**(1): p. 35-37.
131. Graf, R., *Ultrasound-Assisted Liposuction: An Analysis of 348 Cases.* Aesthetic Plastic Surgery, 2003. **27**(2): p. 146-153.
132. Brooks, A.T., et al., *Effect of an ultrasonic device on temperatures generated in bone and on bone-cement structure.* The Journal of Arthroplasty, 1993. **8**(4): p. 413-418.
133. Klapper, R.C., et al., *Ultrasonic technology in revision joint arthroplasty.* Clinical Orthopaedics and Related Research, 1992(285): p. 147-154.
134. Dominici, J.T., et al., *Analysis of Heat Generation Using Ultrasonic Vibration for Post Removal.* Journal of Endodontics, 2005. **31**(4): p. 301-303.
135. Nicoll, B.K. and R.J. Peters, *Heat Generation During Ultrasonic Instrumentation of Dentin as Affected by Different Irrigation Methods.* Journal of Periodontology, 1998. **69**(8): p. 884-888.

136. Apfel, R.E., *Acoustic cavitation prediction.* The Journal of the Acoustical Society of America, 1981. **69**(6): p. 1624-1633.
137. Pecha, R. and B. Gompf, *Microimplosions: Cavitation Collapse and Shock Wave Emission on a Nanosecond Time Scale.* Physical Review Letters, 2000. **84**(6): p. 1328-1330.
138. Fong, S.W., et al., *Numerical analysis of a gas bubble near bio-materials in an ultrasound field.* Ultrasound in Medicine & Biology, 2006. **32**(6): p. 925-942.
139. Lawrence, N. and S.E. Cox, *The Efficacy of External Ultrasound-Assisted Liposuction: A Randomized Controlled Trial.* Dermatologic Surgery, 2000. **26**(4): p. 329-332.
140. Coleman, A.J., et al., *Acoustic cavitation generated by an extracorporeal shockwave lithotripter.* Ultrasound in Medicine & Biology, 1987. **13**(2): p. 69-76.
141. Brock, M., I. Ingwersen, and W. Roggendorf, *Ultrasonic aspiration in neurosurgery.* Neurosurgical Review, 1984. **7**(2-3): p. 173-177.
142. Brujan, E.A., *The role of cavitation microjets in the therapeutic applications of ultrasound.* Ultrasound in Medicine & Biology, 2004. **30**(3): p. 381-387.
143. Mostafa, F. and F.G. James, *Probing the dynamics of tissue at low frequencies with the radiation force of ultrasound.* Physics in Medicine and Biology, 2000. **45**(6): p. 1449.
144. Lauterborn, W. and W. Hentschel, *Cavitation bubble dynamics studied by high speed photography and holography: part one.* Ultrasonics, 1985. **23**(6): p. 260-268.
145. Harvey, G., *An investigation into the simulation and measurement of high intensity ultrasonic systems*, 2009, The university of Strathclyde.
146. Stockbridge, A., *Fiber Optic Hydrophones (April 2011).*
147. O' Leary, R., *An investigation into the passive materials utilised within the construction of piezoelectric composite transducers*, 2003, University of Strathclyde.
148. Wikipedia contributors. *Hydrophone.* [cited 2012 Febuary 2]; Available from: http://en.wikipedia.org/w/index.php?title=Hydrophone&oldid=539707484.
149. Marselli, S., et al., *Porous piezoelectric ceramic hydrophone.* The Journal of the Acoustical Society of America, 1999. **106**(2): p. 733-738.
150. Smith, W.A. *The role of piezocomposites in ultrasonic transducers*. in *Ultrasonics Symposium, 1989. Proceedings., IEEE 1989*. 1989.
151. Ramesh, R., H. Kara, and C.R. Bowen, *Characteristics of piezoceramic and 3–3 piezocomposite hydrophones evaluated by finite element modelling.* Computational Materials Science, 2004. **30**(3–4): p. 397-403.
152. Bowen, L., et al., *Design, fabrication, and properties of sonopanelTM 1–3 piezocomposite transducers.* Ferroelectrics, 1996. **187**(1): p. 109-120.
153. Kawai, H., *The piezoelectricity of poly (vinylidene fluoride).* Japanese Journal of Applied Physics, 1969. **8**(7): p. 975-976.
154. Wells, P.N.T., *Ultrasonic imaging of the human body.* Reports on Progress in Physics, 1999. **62**(5): p. 671.
155. Preston, R.C., et al., *PVDF membrane hydrophone performance properties and their relevance to the measurement of the acoustic output of medical ultrasonic equipment.* Journal of Physics E: Scientific Instruments, 1983. **16**(8): p. 786.
156. Fay, B., et al., *Frequency response of PVDF needle-type hydrophones.* Ultrasound in Medicine & Biology, 1994. **20**(4): p. 361-366.
157. Morris, P., et al., *A Fabry--P[e-acute]rot fiber-optic ultrasonic hydrophone for the simultaneous measurement of temperature and acoustic pressure.* The Journal of the Acoustical Society of America, 2009. **125**(6): p. 3611-3622.

158. Raman, C.V. and N.S. Nath, *The diffraction of light by high frequency sound waves: Part I-V.* Proceedings Indian Academy of Science, 1935/36. **2, 3**: p. 406-412, 413-420; 75-84, 119-125, 459-465.
159. Schneider, B. and K.K. Shung, *Quantitative analysis of pulsed ultrasonic beam patterns using a schlieren system.* Ultrasonics, Ferroelectrics and Frequency Control, IEEE Transactions on, 1996. **43**(6): p. 1181-1186.
160. Kudo, N., et al., *A simple Schlieren system for visualizing a sound field of pulsed ultrasound.* Journal of Physics: Conference Series, 2004. **1**(1): p. 146.
161. Zipser, L. and S. Lindner. *Visualisation of vortexes and acoustic sound waves*. in *17th Int. Congress on Acoustics*. 2001. Rome.
162. Mattei, C. and L. Adler, *Ultrasonic Field Reconstruction from Optical Interferometric Measurements*, in *Review of Progress in Quantitative Nondestructive Evaluation*
D.O. Thompson and D.E. Chimenti, Editors. 1997, Springer.
163. Henderson, B.K., et al., *Elasto-optic technique for measurement of elastic wave propagation in solids.* Experimental Mechanics, 2002. **42**(3): p. 338-343.
164. Julianna, C.S., et al., *Ultrasonic atomization of tissue and its role in tissue fractionation by high intensity focused ultrasound.* Physics in Medicine and Biology, 2012. **57**(23): p. 8061.
165. Barthelat, F., et al., *Dynamic torsion testing of nanocrystalline coatings using high-speed photography and digital image correlation.* Experimental Mechanics, 2003. **43**(3): p. 331-340.
166. Tiwari, V., Williams, S., Sutton, M., and McNeil, S. *Application of digital image correlation in impact testing*. in *SEM Annual Conference & Exposition on Experimental and Applied Mechanic*. 2005. Portland, Oregon.
167. Kirugulige, M.S., Tippur, H.V., Denny, T.S. , *Measurement of transient deformations using digital image correlation method and high-speed photography: application to dynamic fracture.* Applied Optics, 2007. **46**(22): p. 5083-5096.
168. Helfrick, M.N., et al., *3D digital image correlation methods for full-field vibration measurement.* Mechanical Systems and Signal Processing, 2011. **25**(3): p. 917-927.
169. Siebert, T., R. Wood, and K. Splitthof, *High speed image correlation for vibration analysis.* Journal of Physics: Conference Series, 2009. **181**(1): p. 012064.
170. Wang, W.Z., et al., *Frequency response functions of shape features from full-field vibration measurements using digital image correlation.* Mechanical Systems and Signal Processing, 2011. **28**: p. 333-347.
171. Huttula, A.S., et al., *The Effect of Ultrasonic Post Instrumentation on Root Surface Temperature.* Journal of Endodontics, 2006. **32**(11): p. 1085-1087.
172. *Piezoelectric Ceramics Properties and Applications, UK*. Assessed on 8th June 2012; Available from: http://www.morgantechnicalceramics.com/resources/piezoelectric-ceramics-properties-and-applications/.
173. da Silva, J.B., N.N. Franceschetti, and J.C. Adamowski, *Numerical Analysis of a High Power Piezoelectric Transducer Used in the Cutting and Welding of Thermoplastic Textiles,* in *ABCM Symposium Series in Mechatronics*2006. p. 142-149.
174. Rayleigh (Strutt) J. W. , *The Theory of Sound*1945, New York.
175. Peshkovsky, S.L. and A.S. Peshkovsky, *Matching a transducer to water at cavitation: Acoustic horn design principles.* Ultrasonics Sonochemistry, 2007. **14**(3): p. 314-322.
176. Cardoni, A. and M. Lucas, *Enhanced vibration performance of ultrasonic block horns.* Ultrasonics, 2002. **40**(1–8): p. 365-369.

177. Volkov, S.S., I.N. Garanin, and Y.V. Kholopov, *Choice of Waveguide Material for Ultrasonic Welding.* Russian Ultrasonics, 1998. **28**(3).
178. Reddy, J.N., *An Introduction to the Finite Element Method*2006: McGraw-Hill Education.
179. R. J. Allemang, *Vibrations: Experimental Modal Analysis*, 1999, University of Cincinnati.
180. Ewins, D.J., *Modal testing: theory, practice, and application*2000: Research Studies Press.
181. Ploytech. Accessed 18th August 2011; Available from: www.polytec.com.
182. Wiksell, H., et al., *Miniaturised ultrasonic aspiration handpiece for increased applicability.* European Journal of Ultrasound, 2000. **11**(1): p. 41-46.
183. Khambay, B.S. and A.D. Walmsley, *Investigations into the use of an ultrasonic chisel to cut bone. Part 2: cutting ability.* Journal of Dentistry, 2000. **28**(1): p. 39-44.
184. Kim, K., et al., *Surgical pitfalls of an ultrasonic bone curette (SONOPET) in spinal surgery.* Neurosurgery, 2006. **59**(4 Suppl 2): p. ONS390-3; discussion ONS393.
185. Duck, F.A., *Physical properties of tissue: A comprehensive reference book*1990: Academic Press.
186. Fung, Y.C., *Bio-viscoelastic solids*, in *Biomechanics:Mechanical Properties of Living Tissues*1981, Springer Verlag: New York. p. 196-260.
187. Kutz, M., *Standard handbook of biomedical engineering and design*2003: McGraw-Hill Companies, Inc.
188. Ruan, J.M., J.P. Zhou, and B.Y. Huang, *Biomaterials (in Chinese)*2004, Beijing: Science Press.
189. Takegami, K., et al., *Polyacrylamide gel containing egg white as new model for irradiation experiments using focused ultrasound.* Ultrasound in Medicine & Biology, 2004. **30**(10): p. 1419-1422.
190. Ellis, B. and R. Smith, *Polymers a property database*. second edition ed2009: CRC Press.
191. James, E.M., *Polymer data handbook*1999: Oxford university press.
192. *Materials data book*, 2003: Cambridge university engineering department.
193. Sawbones Europe. Available from: www.sawbones.com.
194. British Standards Institution 2003, *Plastics-Determination of compressive properties*, in *BS EN ISO 64:2003*.
195. International Organization for Standardization 2009, *Plastics-Determination of thermal conductivity and diffusivity-Part1:General principles*, in *ISO 22007-1:2009*.
196. British Standards Institution 2005, *Plastics-Differential scanning calorImetry (DSC)-Part 4: Determination of specific heat capacity*, in *BS ISO 11357-4:2005*.
197. TA Instruments. Available from: www.tainstruments.com.
198. Shaw, M.T. and W.J. MacKnight, *Introduction to Polymer Viscoelasticity*2005: Wiley.
199. Sperling, L.H., *Introduction to Physical Polymer Science*2005: Wiley.
200. Menard, K.P., *Dynamic Mechanical Analysis: A Practical Introduction*2008: CRC Press.
201. Ng, W.C., *Study of Vibration and Viscoelastic Heating of Thermoplastic Parts Subjected to Ultrasonic Excitation*1996: Ohio State University.
202. Ferry, J.D., *Viscoelastic Properties of Polymers*. 3rd ed1980, New York: Wiley.
203. Lu, H., G. Huang, and F. Wang, *Measurements of Viscoelastic Properties of Polymers using Flat Punch Indenter*, in *2007 SEM Annual Conference & Exposition on Experimental and Applied Mechanics*2007.
204. Fang, H.Y., *Foundation Engineering Handbook*1991: Chapman & Hall.

205. Johansson, L., et al., *Surface acoustic wave induced particle manipulation in a PDMS channel—principle concepts for continuous flow applications.* Biomedical Microdevices, 2012. **14**(2): p. 279-289.
206. Macioce, P., *Viscoelastic damping 101.* SV Sound Vib, 2003. **37**(4): p. 8-10.
207. Accessed 12th October 2011; Available from: www.lavision.de/en.
208. Pan, B., Qian, K., Xie, H., Asundi, A., *Two-dimensional digital image correlation for in-plane displacement and strain measurement: a review.* Measurement Science and Technology, 2009. **20**(6): p. 062001.
209. Eberl, C., D. Gianola, and K. Hemker, *Mechanical Characterization of Coatings Using Microbeam Bending and Digital Image Correlation Techniques.* Experimental Mechanics, 2010. **50**(1): p. 85-97.
210. Eberl, C., et al. *Digital Image Correlation and Tracking with Matlab*. 2006 Accessed 12th September 2011; Available from: http://www.mathworks.com/matlabcentral/fileexchange.
211. Reu, P.L. and T.J. Miller, *The application of high-speed digital image correlation.* The Journal of Strain Analysis for Engineering Design, 2008. **43**(8): p. 673-688.
212. Shimadzu HPV-1. Available from: www.shimadu.com.
213. Speedlight: Nikon SB 900. Available from: www.nikon.com.
214. Sutton M.A., Orteu J.J., and Schreier H.W., *Image correlation for shape, motion and deformation measurements*2009: Springer.
215. Xue, H.Q., E. Bayraktar, and C. Bathias, *Fatigue behaviour and energy dissipation of a nodular cast iron in ultrasonic fatigue loading.* Journal of Achievements in Materials and Manufacturing Engineering, 2006. **18**(1-2): p. 251-254.
216. Flir T425. Available from: www.flir.com.
217. Meyendorf, N.G.H., et al., *Thermo-acoustic fatigue characterization.* Ultrasonics, 2002. **40**(1–8): p. 427-434.
218. Harvey, G. and A. Gachagan, *Noninvasive field measurement of low-frequency ultrasonic transducers operating in sealed vessels.* Ultrasonics, Ferroelectrics and Frequency Control, IEEE Transactions on, 2006. **53**(10): p. 1749-1758.
219. Brillouin, L., *Diffusion of Light and of X-rays by a Transparent Homogeneous Body.* Ann. Phys. (Paris), 1922. **17**: p. 88.
220. Debye, P. and F.W. Sears, *On the Scattering of Light by Supersonic Waves.* Proceedings of the National Academy of Sciences, 1932. **18**(6): p. 409-414.
221. Lucas R. and Biquard P., *Optical properties of solid and liquid medias subjected to high-frequency elastic vibrations.* JourNAL Phys., 1932. **71**: p. 464-477.
222. Phariseau P., *On the diffraction of light by progressive supersonic waves.* Proc. Ind. Acad. Sci., 1956. **44**: p. 165-170.
223. Torras-Rosell, A., S. Barrera-Figueroa, and F. Jacobsen, *Sound field reconstruction using acousto-optic tomography.* The Journal of the Acoustical Society of America, 2012. **131**(5): p. 3786-3793.
224. Urzhumov Y. A., *Sub-wavelength Electromagnetic Phenomena in Plasmonic and Polaritonic Nanostructures: from Optical Magnetism to Supper-resolution*, 2007, The University of Texas at Austin.
225. R. W. Damon, W. T. Maloney, and D. H. McMahon, *Interaction of light with ultraound: phenomena and applications*, in *Physical Acoustics Principles and Methods*, W.P.M.a.R.N. Thurston, Editor 1970, Academic Press: New York. p. 273-366.
226. Paufler, P., *Photoelastic and Electro-Optic Properties of Crystals.* Crystal Research and Technology, 1982. **17**(8): p. 972-972.
227. Merkulov, L.G., *Design of Ultrasonic Concentrations.* Soviet Physis Acoustics, 1957. **3**(3): p. 230-238.

228. Trabucho, L. and J.M. Viaño, *A derivation of generalized saint venant's torsion theory from three-dimensional elasticity by asymptotic expansion methods.* Applicable Analysis, 1988. **31**(1-2): p. 129-148.
229. W. Weaver, J., S.P. Timoshenko, and D.H. Young, *Vibration Problems in Engineering*1990: John Wiley & Sons.
230. Sawbones Europe. *Solid Rigid Polyurethane Foam*. Available from: www.sawbones.com.
231. Sawbones Europe. *Short-Fiber-Filled Epoxy Sheets*. Available from: www.sawbones.com.
232. Bougherara, H., et al., *Finite element investigation of hybrid and conventional knee implants.* International Journal of Engineering, 2009. **3**(3): p. 257.
233. Wacker Chemicals Ltd. *Elastosil RT 601*. Available from: www.sawbones.com.
234. Hartsuijker, C. and J.W. Welleman, *Engineering Mechanics: Volume 2: Stresses, Strains, Displacements*2007: Springer.
235. Abboud, N., Mould, J., Wojcik, G., Vaughan, D., Powell, D., Murray, MacLean, C. *Thermal generation, diffusion and dissipation in 1-3 piezocomposite sonar transducers: finite element analysis and experimental measurements*. in *IEEE International Ultrasonics Symposium Proceedings*. 1997.
236. Achenbath, J.D., *Wave Propagation in Elastic Solids*1987, Dodrecht, Netherlands: Elsevier.
237. Maxwell, A.D., et al., *A tissue phantom for visualization and measurement of ultrasound-induced cavitation damage.* Ultrasound in Medicine & Biology, 2010. **36**(12): p. 2132-2143.

Appendix 1

The Fabrication of PAA Gel Phantom

The PAA gel phantom was made based on the research of *Takegami, 2004*:

Ingredients	Concentration in phantom
Degassed water	44.50%
Fresh egg white	30%
40% w/v acrylamide	24.80%
10% w/v APS	0.50%
TEMED	0.20%

However, some changes were made for this project.

Ingredients	Concentration in phantom
Degassed water	44.50%
Fresh egg white	30%
40% w/v acrylamide+ 2% w/v N,N'-Methylene-bis-Acrylamide (*powder*)	24.80%
10% w/v APS (*powder*)	0.50%
TEMED	0.20%

Too much egg white results in an opaque gel, while too little causes low sensitivity and low optical contrast.

The directions:

All preparations take place at room temperature, as followed:

1. Stir fresh egg white and degassed water together by using magnetic stirrer until mixture appears uniform in color and consistency.
2. Remove the bubbles or foam from the top of the liquid mixture by using a pipette.
3. Add the acylamide solution to the mixture, stir and then remove the foam.
4. Stir APS and TEMED to catalyze the polymerization of the acrylamide.
5. Pour the mixture to the mold and allow the mixture to polymerize for 20-30 mins.

Notice: the mixture will solidify when APS meets TEMED, so please make sure that any of these two is added as the last step.

Appendix 2

Publications

Journal papers

1. D. WANG, M. Lucas, K. E. Tanner, “Characterising the Strain and Temperature Fields in a Surrogate Bone Material Subject to Power Ultrasonic Excitation”, Strain, 49: 409-419.

Conference papers

2. D. Wang, M. Lucas, K. E. Tanner, “Surrogate Bone Materials for Assessing the Effects of Ultrasonic Surgical Devices”, 24th European Conference on Biomaterials, Dublin, 2011

3. D. Wang, M. Lucas, K. E. Tanner, “Surrogate Bone Materials for Assessing the Effects of Ultrasonic Surgical Devices”, UK Society for Biomaterials Annual Conference, Glasgow, 2010